NUMERICAL INVESTIGATION OF FREAK WAVE EFFECTS ON OFFSHORE STRUCTURES

By

Mengshi Sun

A thesis submitted in fulfilment of the requirements for the degree of

Doctor of Philosophy

Department of Naval Architecture, Ocean and Marine Engineering

University of Strathclyde

March, 2017

Declaration

This thesis is the result of the author's original research. It has been composed by the author and has not been previously submitted for examination which has led to the award of a degree.

Mengshi Sun

Signature: Date:

Abstract

The freak wave is extremely dangerous to offshore structures due to its unexpected high wave height and strong nonlinearity. Although increasingly more attention is paid to the investigations of freak wave, the principle of its generation mechanism and the factors that contribute to its occurrence remain unclear. Also, few efforts were exerted to investigate the interactions between offshore structures and a freak wave such as wave run-up and slamming force. In this present work, both the two dimensional (2D) and three dimensional (3D) numerical wave tanks are established based on Navier-Stokes equations for viscous, incompressible fluid by CFD commercial software FLUENT.

At first, the regular waves are generated numerically. Two different wave generation methods, paddle wave making method and the source function wave making method, are introduced. The paddle wave-making method is a physical wave generation technology which is to imitate the wave makers in the laboratory. The source function wave-making method is discussed later and the empirical formulas of the source size and source intensity are introduced. The numerical wave elevations are compared with the linear analytical results.

Second, the freak waves are generated numerically. According to Longuet-Higgins wave model theory, the wave free surface can be represented by the linear sum of the individual wave components with different frequencies and random phases. Improving this wave model, the wave components have their phase adjusted, so that a large amount of energy is located at the focus position at a given time. Then two more efficient and realistic freak wave models are presented, combining wave models and phase modulation wave models, respectively. Finally, the numerical results of the shift of freak wave train focusing position and focusing time are analysed, and the time history of wave elevations are compared with the analytical results.

Third, a 3-D numerical wave tank is established to perform the interactions between a freak wave train and a single cylinder or a pair of two cylinders. How the focused wave parameters, including wave steepness, frequency bandwidth,

focused position and the distance between the two cylinders, affect the freak wave run-up and total slamming forces on the cylinders are investigated.

Finally, the hydrodynamic behaviour of a rectangular body in roll motions under both freak wave excitation and internal flow sloshing is investigated in a CFD numerical wave tank. In this study, three different freak wave conditions are considered, and two different water levels are investigated.

The comparisons of numerical regular wave elevations and first order analytical results show that the current CFD numerical wave tank based on computational fluid dynamic commercial software FLUENT has a good capacity in sea water waves simulation. The focused wave parameters, such as frequency bandwidth and input wave steepness, have an obvious effect on the nonlinear behaviour of a focused wave group. This nonlinear behaviour will not only downstream shift the focused position and focused time, but also change the wave elevation at the focused position largely. The increased nonlinear behaviour of a focused wave group will increase the wave run-up along a fixed vertical cylinder at the incident wave facing direction largely. The bigger nonlinear behaviour of a focused wave group can result in larger rolling motion amplitude for a floating rectangular body, however the anti-rolling behaviour is obvious for the low filling case.

Acknowledgements

First, I would like to show my gratitude to my supervisor Prof. Atilla Incecik for his encouragement and valuable advice on my project. Six years ago, I would not have an opportunity to study aboard without his encouragement and help.

Second, I would like to thank my parents, family and friends for their support and care. My mother Cong, my father Jiye, my brother Zilong, you are the most important people in my life and I will always love you. My dearest grandmother, you are always in my heart. Junpeng, Chunqi, Duo, Xinyi, Zijian and Eddie, thank you to let me having friends is one of the happiest things in my life.

Finally, I would like to express my gratitude to all my friends in Glasgow. I would like to thank Dr Lei, who helped me a lot in the CFD study. We had a memorable researching Christmas in 2015. Many thanks to my roommate Enqian and all my friends and colleagues in the department of NAOME for their assistance during my PhD.

I would also like to thank the University of Strathclyde Faculty of Engineering for provision of the ARCHIE-WeSt high performance computing facilities. The CFD results were obtained using the EPSRC funded ARCHIE-WeSt High Performance Computer (www.archie-west.ac.uk). EPSRC grant no. EP/K000586/1.

Contents

List of Figures

List of Tables

1 Introduction

1.1 Background

The freak wave (also called extreme wave, rouge wave, huge wave) is an extremely giant water wave in ocean and may appear in all the sea areas. Freak waves present considerable danger for several reasons: they are rare, unpredictable, may appear suddenly or without warning, and can impact on structures with tremendous force.

In oceanography, freak waves are more precisely defined as waves whose height is more than twice the significant wave height (H_s), which is itself defined as the mean of the largest third of waves in a wave record. Therefore, freak waves are not necessarily the biggest waves found in the sea; they are, rather, usually large waves for a given sea state (The Economist, 2009).

Offshore structures such as wind turbine foundations, marine renewable energy devices, offshore platforms, floating breakwaters and floating vessels are widely built and utilised in coastal and offshore engineering. Because of climate change, the risk of having more severe extreme events is likely to increase in the future. So, the offshore structures are more likely to be exposed to harsh environmental conditions like freak waves. The freak waves are relatively large and spontaneous ocean surface waves, and they are extremely dangerous to offshore structures sue to its unexpected high wave height and strong nonlinearity. Thus, the accurate evaluation of such impact forces and corresponding structure responses is important for structure safety and disaster prevention. The research on the impact of extreme waves on offshore structures and the corresponding responses has vital significance for structural design and safety assessment. For the extreme wave and offshore structure interaction problems, the wave impacts are characterized by nonlinear phenomena, distorted free surface and large amplitude structure responses for floating bodies. This nonlinear analysis is very complicated. Although increasingly more attentions are paid to the investigation of freak wave, the principle of its generation mechanism and the factors that contribute to its

occurrence remain unclear. Also, few efforts were exerted to investigate the interactions between offshore structures and freak wave such as wave run-up and slamming force.

With the development of computer technology, numerical simulation methods are widely used in all areas of research. The world has realised great achievements in numerically simulated waves, and the interactions between waves and offshore structures. Compared with real physical experiments, the numerical wave tank has the advantages of low costs, easy application, easy transformation, and accurate measurement among others (Tang and Yuan, 2001).

It should be mentioned that, as for as problems associated with freak waves concerned, the nonlinear VOF models are not widely applied in the numerical simulations. This work is motivated by the requirement of developing a nonlinear model to investigate the complex nonlinear freak wave and offshore interaction issues, including the freak wave run-up and floating body response under freak wave groups. The numerical simulation works are established based on fully nonlinear Navier-Stokes and VOF equations for viscous, incompressible fluid by CFD commercial software FLUENT.

1.1.1 Freak Wave Observations

The first scientific evidence of the existence of freak waves came with the recording of a rogue wave by Gorm platform in the central North Sea in 1984. A stand-out wave was detected with a wave height of 11m in a relatively low sea state. However, the wave that caught the attention of the scientific community was digital measurement of the "Draupner wave" (Haver, Sverre, 2003), a rogue wave at the Draupner platform in the North Sea on January 1, 1995, with a maximum wave height of 25.6 meters (84 ft.) and maximum wave amplitude of 18.5meters (61 ft.), shown in Figure 1.1.

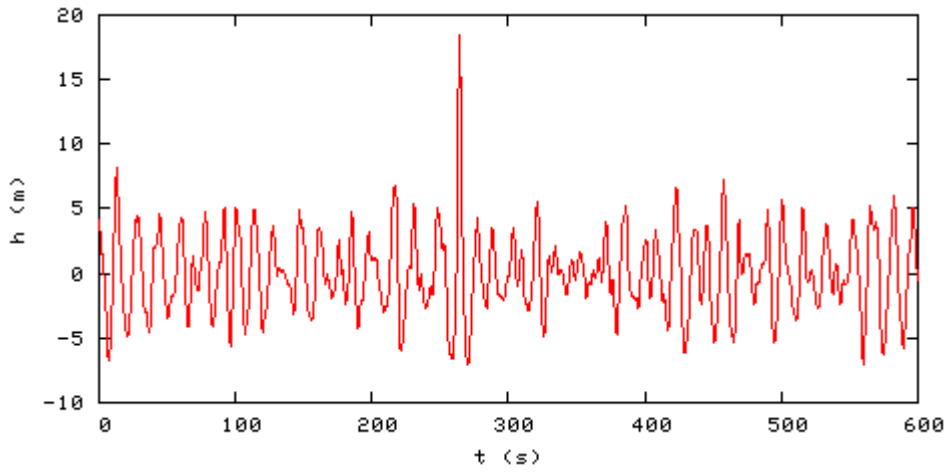

Figure 1.1 The Draupner Wave, a single giant wave measured on New Year's Day 1995, finally confirmed the existence of freak waves. (Haver, Sverre, 2003)

1.1.2 Physical Mechanisms of the Freak Wave

The physical mechanisms of the freak wave phenomenon are introduced clearly by Kharif (2003). It is worth to introduce various theories as to why freak wave events occur. One general category of theories is based on "wave focusing" in which wave convergence or focus at a point due to variable currents, e.g. Peregrine (1986), Peregrine et al. (1998), and White and Fornberg (1998).

Another category of theories is based on nonlinear wave-wave interactions, primarily associated with Benjamin-Feir instabilities, e.g. Stansberg (1993, 1998), Trulsen and Dysthe (1996), Yasuda and Mori (1994), and Osborne (1999).

A third general category of theories is based on the simple argument that Fourier wave components in a random sea may superimpose at a point to produce an abnormally large transient wave. This approach has formed the basis of many laboratory studies of extreme waves, for example by Rapp and Melville (1990), Kim et al. (1992), Taylor and Haagsma (1994), Baldock and Swan (1994), Chaplin (1996), Johannessen and Swan (1997), Clauss and Kuhnlein (1997), Clauss and Steinhagen (1999), and Clauss (1999).

1.1.3 Freak Wave Definition

Extreme wave was traditionally defined by a ratio of $H_{max}/H_s>2$ (Skourup et al., 1996). The analysis was based on 12-year wave elevation measurements in the North Sea. During this period, 400 extreme waves were selected. The measured wave heights for the 400 individual extreme waves were all more than two times the significant wave height $H_{max}/H_s>2$ and their crest amplitudes were all more than 1.1 times the significant wave height $A_{max}/H_s>1.1$. Taylor (2007) analysed the shape of the Draupner Wave of 1st January 1995. The Draupner wave is also called New Year's wave which was the first rouge wave to be detected by a measuring instrument, happening at the Draupner platform in the North Sea off the coast of Norway on 1 January 1995. The maximum wave height of New Year's wave is $H_{max}=25.63$m and the maximum wave crest height is $A_{max}=18.5$m. The extreme wave ratio of $H_{max}/H_s=2.15$.

In the linear approximation, a random wave field can be considered as a Gaussian process. Under this assumption, a mathematical definition of a freak wave event can be expressed by $H_{max}>2.0H_s$, H_{max} being the maximum wave height of the freak wave event. Accounting to nonlinearities in the process, a refined definition tends to raise the limit of the freak wave height to $H_{max}\geq 2.2H_s$. The latter limit of $2.2H_s$ is now commonly accepted.

1.2 Research Aims

Based on the background and motivation of current research, the main objectives are as follows:

1) The two dimensional and three-dimensional numerical wave tanks are established based on Navier-Stokes equations for viscous, incompressible fluid by computational fluid dynamic commercial software. The wave generation, wave absorption and method to capture the free surface will be introduced. The focused wave groups allocated by different focused wave parameters are generated in numerical wave tanks.

2) The regular waves are generated by two different wave making methods. The computational wave elevation results need to be compared with the analytical results. The accuracy of the numerical wave generation should be validated. In a three-dimensional numerical wave tank, the results of regular wave run-up around a vertical cylinder surface are compared with the experimental data and the analytical first order diffraction theory results. The regular wave force impacting on the cylinder surface need to be compared with the Morrison's equation. The validation of a rectangular body rolling response under different regular wave conditions is conducted by comparing the numerical simulation and experimental rolling RAO.

3) Parametric studies are conducted to investigate the effect of focused wave factors, including frequency bandwidth, freak wave steepness, wave scattering and focused position, on wave run-up around vertical cylinders. The effects of focused wave parameters on rectangular body rolling response under freak wave are investigated. The influence of internal tank sloshing on the floating body global response under freak wave is also analysed.

1.3 Thesis Outline

The layout of the thesis is described as follow;

In chapter 2, a literature review of the freak wave event and of its experimental and numerical simulations is given. The usage of CFD numerical wave tank technique in ship and offshore structure hydrodynamic analysis is introduced. The freak wave observation, the physical mechanisms and freak wave definition are introduced.

In chapter 3, two numerical wave generation methods and numerical wave absorption technique are introduced first. After that, two regular wave trains are generated numerically by two different wave making methods, and the wave elevation profiles are compared with the first order analytical

results. The validation of the current numerical method is regular wave simulation is proved.

In chapter 4, based on the Longuet-Higgins random wave model, a large amount of wave energy can be gathered in a fixed position at a predetermined time by modulation the phase angle for each individual wave component. The basic focused wave model and three different effective freak wave models are compared. Twenty different focused wave groups allocated by different frequency bandwidth and freak wave steepness are generated in a two-dimensional numerical wave tank. The effect of focused wave parameters on the freak nonlinear behaviour is investigated.

In chapter 5, the regular wave running-up on a fixed vertical cylinder is validated at first. The results of regular wave run-up around the vertical cylinder surface are compared with both the experimental data and analytical results. After the validation, different freak wave trains running-up on a vertical cylinder and a pair of two cylinders are investigated. The effect of focused wave parameters on the wave run-up intensity and horizontal wave forces are analysed.

In chapter 6, an experiment study of investigating liquid sloshing in a 2-D rectangular tank is reproduced numerically at first. The numerical simulations of a rectangular body rolling response RAO are compared with the experimental results. The effect of focused wave parameters, including frequency bandwidth and peak frequency, on the global floating body response under freak wave trains is investigated. Finally, the influence internal sloshing loads on a rectangular body rolling response under freak wave are analysed.

In chapter 7, conclusions and discussions of this work are given.

2 Literature Review

In this chapter, a critical review of the previous related studies in the subject of freak wave interacting with offshore structures are presented, aiming to identify the capacities and limitations of the previous mathematical models in dealing with the subject.

2.1 Wave Run-up

One of offshore engineers' interests is to measure wave run-up on both fixed and floating platforms. This amplification of incident wave can result in wave overtopping of the platform deck. Furthermore, under the platforms, the rapid rise of water level can result in wave impact or slamming loads on the structures. The design of offshore structures needs an accurate prediction of maximum wave run-up elevation to maintain sufficient air gap below the platform deck.

Physical wave tank testing is one of the most common methods to model wave structure interaction problems. The most obvious strength of physical test is that the real hydrodynamic data can be measured and collected. To research wave run-up on circular cylinders, many laboratory experiment studies were conducted.

Galvin and Hallermeier (1972) carried out experimental measurements of wave heights very near the surface of cylinders of selected cross sections. When a wave passed a vertical cylinder, its shape, including its height, was affected by the presence of the cylinder and viscous dissipation in the wake of the cylinder. Parameter $\pi X/L$ describes the wave scattering and parameter H/X describes the wake effects and parameter $K=UT/X$ describes the eddy shedding. The experiment results showed that when $K=4$, the wave viscous effect was obvious.

Niedzwecki and Duggal (1992) performed a small-scale experimental study to investigate wave run-up on rigid full-length and truncated circular cylinders under regular and random sea conditions. An empirical equation was presented to make preliminary estimates of wave run-up on truncated circular cylinders.

And an approximate formula for predicting the time-dependent wave force on a truncated cylinder was also presented.

Nielsen (2003) carried out an experiment study of regular wave run-up along platform columns. A rigid vertical circular column and a rigid vertical square column with rounded corners two different models were considered and wave elevations within a radial distance around the cylinder were monitored at different locations. The positions where the wave elevations are computed around the circular and square columns are shown in Figure 2.1. The experiment results showed that, in incident wave direction, wave run-up elevation was large on wave measurement points near cylinder surface, and wave run-up ability increased with an increase of incident wave steepness. Furthermore, the experimental wave run-up results are compared with several numerical results. The different numerical methods include first order diffraction theory, second-order diffraction theory, frequency domain method and time domain method. The comparison results show that the second order diffraction theory simulates a more realistic result than the first order diffraction theory in regular wave run-up evaluation.

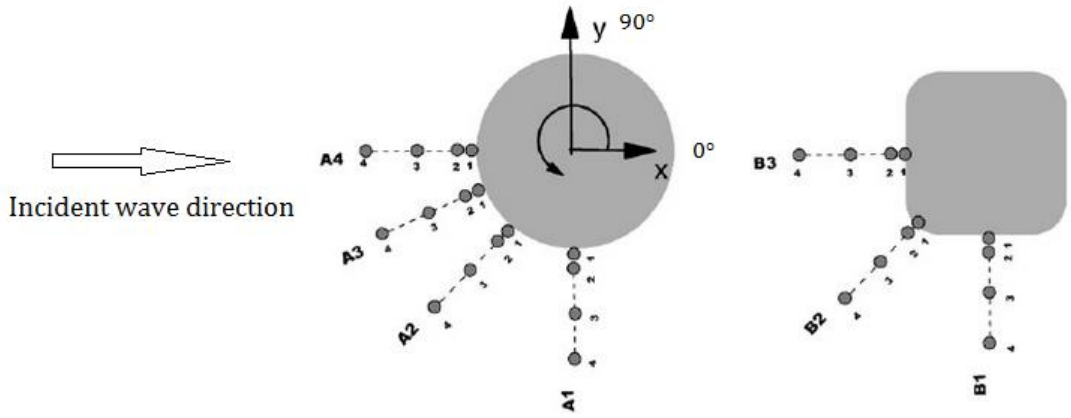

Figure 2.1 Arrangements of the wave probes (Niesen,2003)

Morris-Tomas et al. (2004) investigated an experiment of wave run-up on a fixed vertical surface piercing circular cylinder. Figure 2.2 illustrates the wave run-up on front side of column. And Figure 2.3 shows the wave run-up resulting from an incident wave impinging on a vertical surface piercing column. The

study focused on two important parameters wave steepness and body slenderness. How the two parameters affecting the wave run-up were investigated. Using a regression analysis involving a separation of ka and kA dependence, the importance of higher-order wave steepness effects on wave run-up was demonstrated. In long waves, the third-harmonic component was shown to contribute up to 8 percent of the wave run-up.

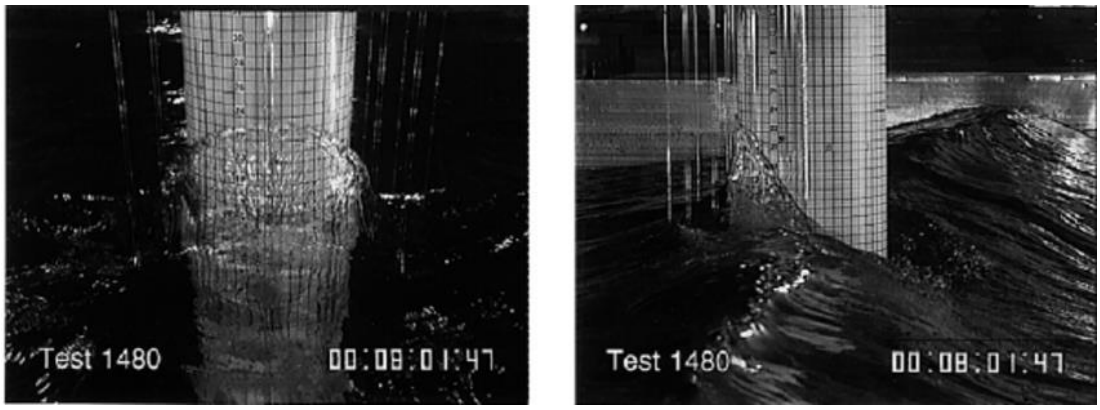

Figure 2.2 Wave run-up on front side of column (Morris-Tomas et al., 2004)

Figure 2.3 Illustration of the wave run-up resulting from an incident wave impinging on a vertical surface piercing column (Morris-Tomas et al., 2004)

To find an alternative method to evaluate the wave cylinder interactions, the analytical methods are developed. Generally, there are two different analytical methods to investigate the hydrodynamic force on cylinder offshore structures. The first one is Morison's equation, which is proposed by Morison et al. (1950).

The Morison's equation is a semi-empirical equation to calculate the regular wave forces interacting with a slender cylinder. The total force is combined a linear inertial component and a non-linear drag component. The Morison's equation is always used under a condition D/L≤0.15, in which D is the cylinder diameter and L is regular wave length. In this wave and cylinder size condition, the wave diffraction can be ignored. When the cylinder diameter and wave length ratio D/L>0.15, the wave diffraction cannot be ignored and diffraction theory is used to evaluate the wave force on cylinder, which is proposed by MacCamy and Fuchs (1954). In diffraction theory, the total wave potential is combined with incident wave potential and diffracted wave potential, and it is based on an assumption that the wave steepness is small.

It is acknowledged that the increased wave steepness raises the nonlinear behaviour of regular wave, and many researches show that the calculation maximum wave elevations are always underestimated based on linear diffraction theory (Niedewecki and Duggal, 1992). Many authors use second-order diffraction theory to study the nonlinear interaction of regular waves with a vertical cylinder.

Stansberg and Kristiansen (2005) investigated the free-surface wave elevation within a radius distance around fixed vertical columns and the validity of second-order modelling of the wave-column interaction in steep waves were addressed. The side view of wave run-up on a vertical cylinder from a experiment photo is shown in Figure 2.4. The simulation results showed that linear modelling significantly underestimated the crest amplification, while the second-order correction represented a significant improvement well in waves with moderate steepness. In high steep waves, first-harmonic amplitudes were underestimated but second-harmonics were overestimated.

Figure 2.4 Photo from experiment for wave run-up, T=15s, H=35m Side view (Stansberg and Kristiansen, 2005)

Kriebel (1992, 1998) investigated the wave run-up and wave force on cylinders. The results showed that the linear diffraction theory underestimated the maximum wave forces about 5% to 15%, and the measured maximum wave elevation was larger than the linear analytical results 44%. The results of second-order diffraction theory for wave run-up elevation around the cylinder and wave force have a good agreement with the experimental data.

For the high-nonlinear hydrodynamic problems of wave breaking, green water and violent floating body motion, the CFD method can be utilised. Different from second-order diffraction theory which is based on truncated perturbation expansion, computational fluid dynamic is totally a nonlinear method to simulate the flow by solving the Navier-Stokes equations directly. When considering the wave run-up on cylinder problems, the multiphase technique to track the complicated free surface deformations around the cylinder is needed. The tracking multiphase methods include volume of fluid (VOF) method (Harlow, 1965) and the Level-Set (LS) method (Takewaki, 1985), and both are based on Eulerian formulation. The Smooth Particle Hydrodynamics (SPH) method (Gingold and Monaghan, 1977) is based on a concept to decompose the fluid domain into numerous freely moving discrete fluid particles by a grid-free Lagrangian formulation. The CFD method has many advantages. It can be used in all flow regimes in ship and offshore engineering. The overturning flows and

fluid viscous behaviours can be considered. Further, the scaling restriction is not needed anymore in CFD analysis. With the development of the computational technology and the improvement in the efficiency of the numerical simulation models, computational expenses is not going to be a barrier for the CFD development in ocean engineering,

Westphalen et al. (2005) introduced a numerical method to analyse the interaction of a vertical cylinder in regular waves with Commercial CFD software Ansys CFX 22 and STAR-CCM+. Two different regular wave situations were considered and the calculated wave forces results on vertical cylinder were compared with physical experiment data. The calculated and experiment results showed a good agreement. Using the FVM solver the horizontal force results predicted for a slender cylinder showed a secondary load cycle.

Repalle et al. (2007) examined the wave run-up on a square cylinder using experimental and numerical methods. The Experiments were performed in a wave tank with 1:66 scaled model of a square column. Numerical simulation was conducted using the commercial software FLUENT. It was found that the results for wave run-up from numerical simulation and experiments were in good agreement and were consistently greater than linear diffraction theory.

The use of an alternative method for prediction of wave run-up around a Gravity-Base Structure is conducted by Danmeier et al. (2008). The results from a second-order diffraction code WAMIT and a fully nonlinear CFD program (ComFLOW) are compared to assess the importance of nonlinearities. The numerical simulation of nonlinear wave run-up profile from ComFLOW is shown in Figure 2.5. The results showed that the wave run-up behaviour around the GBS depends on incident wave steepness and wave length. The computational results showed that when the incident wave has a small wave steepness, linear wave component dominates the wave run-up. With the increased wave steepness, the wave elevation around the cylinder becomes shaper and narrower, and the wave trough becomes much more flat, which contributes from the increased high nonlinear wave behaviour.

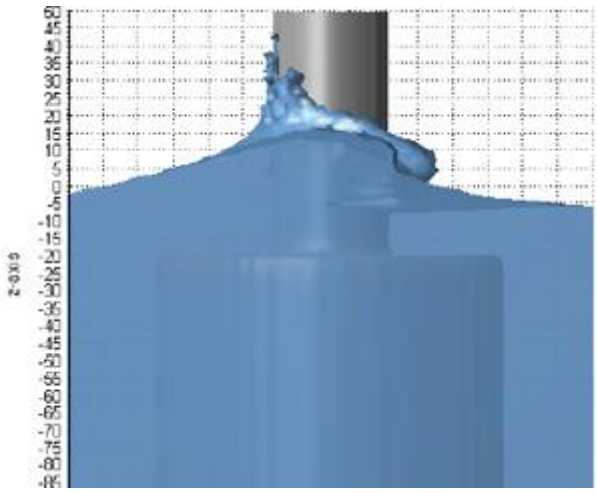

Figure 2.5 Nonlinear wave run-up profile from ComFLOW (Danmeier et al., 2008)

Lwanowski et al. (2009) investigated the wave run-up around a semi-submersible by the same CFD numerical tool ComFLOW. In the numerical study, four different wave gauges are set around the cylinder surface, and at the lower deck six fluid pressures are set to check the hydrodynamic pressures. The VOF method is used to track the water free surfaces, and short wave, medium wave and long wave three different regular wave conditions are considered. The visualization of wave run-up along the platform's front column is shown in Figure 2.6. By comparing the experimental results, it shows that the current CFD method is suitable to simulate regular wave running-up on semi-submersible cylinders problems, and some nonlinear hydrodynamic phenomenon like wave slamming and wave turning over are observed.

Figure 2.6 Long wave running-up on semi-submersible (Lwanowski et al., 2009)

An open source numerical wave tank based on the OpenFOAM software was setup and tested to solve the Navier–Stokes equations by Rajagopalan and Nihous (2016). This work focused on submerged plates because of their simple geometry, their importance as a design component (e.g., heave plates), and the broad availability of published experimental results. Two-dimensional plates in an oscillatory flow, as well as three-dimensional circular disks and square plates undergoing forced oscillations were simulated in conditions where the nonlinearity of hydrodynamic viscous drag and inertia forces can be probed easily. The effect of plate thickness as well as the ability of the numerical simulations to predict wave radiation damping at shallow plate submergence were also considered. Overall, force coefficient predictions were very satisfactory when compared to experimental data, and generally exhibited less scatter. The influence of both Keulegan–Carpenter number and frequency parameter on the hydrodynamic force could be assessed as well from these numerical simulations as from past laboratory experiments.

Lin et al. (2017) conducted a hydrodynamic simulation of wave run-up heights and wave loads on three types of wind turbine foundations by using a RANS solver and employing k-ε turbulent closure. Due to the contribution of the present CFD model, a semi-empirical formula was calibrated based on velocity stagnation head theory for crest kinematics. Eventually, the results indicated that the difference among the maximum normalized run-up heights of these support structures was smaller for lower wave steepness than those for higher wave steepness. In contrast, it was shown that the difference among the wave loads of these foundations was larger for lower wave steepness than those for higher wave steepness. A calibrated run-up parameter was also obtained by means of numerical simulation and found that the value of calibrated run-up parameter became smaller accompanied with larger values of wave steepness and the maximum normalized run-up height. It was relevant that the tendency of run-up heights was positively correlated with higher nonlinearity, whereas an opposite trend was observed in the relationship between larger calibrated run-up parameter and lower nonlinearity.

2.2 Freak Wave

In order to research the hydrodynamic characteristics of extreme waves, many laboratory experiment studies were investigated. The wave focusing approach is used mostly in previous experimental work in physical wave tank, such as Baldock et al. (1996), Pelinovsky et al. (2000), Kriebel and Alsina (2000) and Clauss (2002). Some details are going to be shown later.

Baldock et al. (1996) made an experimental investigation in which many water waves were focused at one point in space and time to generate a large transient freak wave. Figure 2.7 shows the formation of a focused wave group and the wave elevations close to the focal point at three locations. Both the measured water surface elevation and water particle underlying kinematics were compared with first- and second- order solutions. Experiment results showed that the wave focusing can result in highly nonlinear extreme wave group, and the nonlinearity was related to the input amplitude and wave group frequency bandwidth. The nonlinearity also gave rise to the downstream shifting of the focus point.

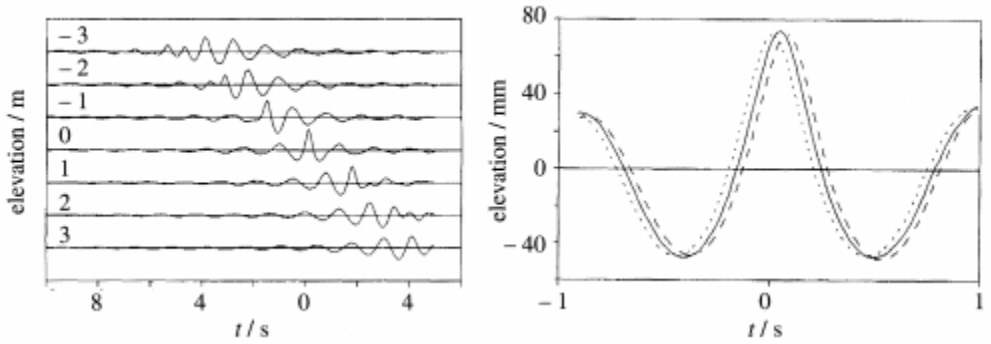

(a) (b)

Figure 2.7 (a) Formation of a focused wave group. The number indicated on the left-hand side corresponds to the position along the length of the wave flume, x (m). (b) Wave focusing close to the focal point at three locations. (Baldock et al., 1996)

Kim et al. (1990) presented the results of recent research on laboratory synthesis of extreme waves and experimental investigation of wave-fluid

particle kinematics just prior to breaking using laser Doppler anemometry. An extreme wave was generated and their kinematics was measured. The transient wave kinematics under the crest was shown to be much more severe above the still water level and somewhat less severe below. The experimental extreme transient wave velocity filed is shown in Figure 2.8.

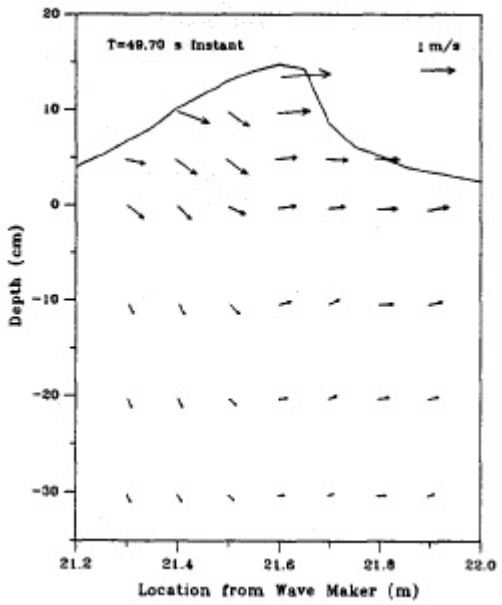

Figure 2.8 Extreme transient wave velocity field (Kim et al., 1990)

Kriebel and Alsina (2000) aligned the traditional wave focusing extreme wave generation method. Laboratory experiments were conducted to embed a large transient wave within a random sea as a means of simulating freak wave in a wave tank. The wave energy spectrum was separated into two parts, the first part energy was used to generate background random sea and the second part energy was distributed to generate extreme wave. The results showed that a realistic freak wave train can be made by only allocating 15% to 20% total wave energy for freak wave part generation based on freak wave definition of a ratio $H_{max}/H_S>2$.

Cox and Ortega (2002) performed a small-scale laboratory experiment to quantify a transient wave overtopping a horizontal deck fixed above the free surface. The experimental setup is shown in Figure 2.9. A short transient wave was chosen to produce an extreme wave. The flap-type wave-maker signal

consisted of two cycles of a T_1=1.0s sinusoidal wave followed by two and a half cycles of a T_2=1.5s sinusoidal wave with larger amplitude. The experimental results showed that the effect of the structure on the free surface at the leading edge increases the total wave height by 6% and the free surface height relative to an observer on the deck by 20%. Immediately below the deck, the maximum velocity is 2.5 times greater than the corresponding velocity without the deck and 2.1 times larger than the maximum crest velocity measured without the deck.

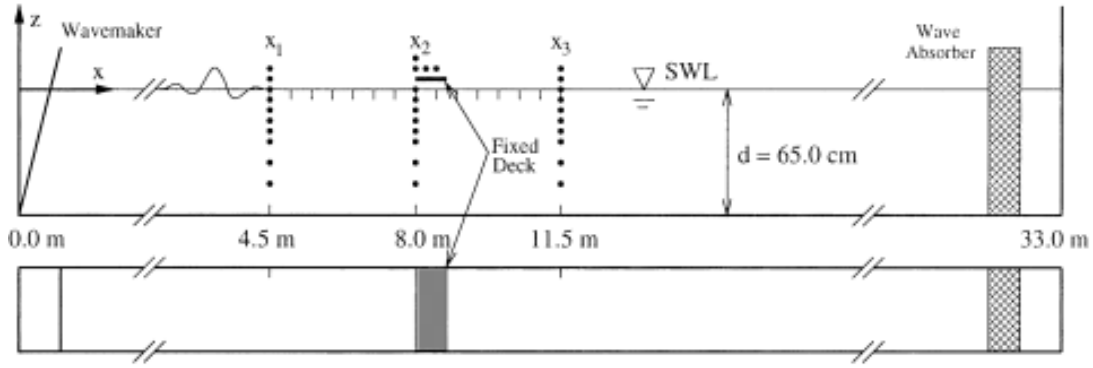

Figure 2.9 Elevation and plan view of experimental setup (Cox and Ortega, 2002)

Clauss et al. (2002, 2003) did a numerical study of the seakeeping behaviour of a semisubmersible GAV 4000 in a reported rouge wave, the Draupner New York Wave embedded in irregular sea states. The numerical time-domain investigation using a panel-method and potential theory is compared to frequency-domain results. For time-domain analysis, the commercial code TiMIT is used to provide the motions and forces on the wetted body of the semisubmersible in rouge waves as time series. Corresponding response amplitude operators are also calculated with WAMIT, a program system for zero-speed problems. The research results showed that WAMIT and TiMIT results compare quite well as far as significant and maximum motions and forces are evaluated by a frequency-domain analysis. Also, the time-domain analysis of the dynamics of the selected semisubmersible agrees satisfactorily with experimental results.

Li et al. (2012) and Ji et al. (2015) performed a wave basin experiment to investigate the interactions between multi-directional focused wave and

vertical bottom-mounted cylinder. The work is only focused on the extreme wave run-up phenomenon. The experimental results showed that the focused wave parameters, including wave steepness, frequency bandwidth, a directional spreading index, have significant impacts on the wave run-up on a cylinder. The maximum wave run-up happens at the front of the cylinder, and the minimum run-up depends on the directional parameters occurring at attack angle range [135°, 180°]. The wave run-up increase at the front part of the cylinder as the relative dimension ka increases, but at the back cylinder, it showed an opposite tendency. The focused wave run-up increases as the wave steepness increases.

With the development of advanced computer techniques, the numerical wave tank can provide more detailed insights into wave hydrodynamics than traditional experiment. The pressure and velocity fields in the numerical wave tank are easily measured. In recent years, more efforts are made in numerical wave tank technologies and it has become a new method to investigate the freak waves.

Clauss et al. (2005) introduced different approaches for numerical wave tanks and all numerical wave tanks were used to simulate rouge wave trains. The first kind numerical wave tank was based on potential theory with Finite Element discretization (Pot/FE). The second kind numerical wave tank was based on Reynolds-Averaged Navier-Stokes Equations (RANSE) using the Volume of Fluid (VOF) method for describing the free surface. For the NWT using the VOF method three different commercial RANSE codes (CFX, FLUENT, COMET) were applied to calculate wave propagation. In order to simulate the Jonswap wave spectrum, two different methods of coupling potential theory and RANSE/VOF-solver were presented. Potential theory was used to simulate the propagation of the wave train from the start toward a given position in the wave tank or until wave breaking was encountered at a given time step. So, that the velocity field and the contour of the free surface were handed over as boundary or initial values to RANSE/VOF-solver and the simulation process continued.

Sun et al. (2008) analysed the efficient freak wave generation models in his work. Based on improved Longuet-Higgins wave model, four wave focusing

models for freak wave generation were presented first. The efficient freak wave generation models include extreme wave model, extreme wave mode plus regular wave model, phase interval modulation wave focusing model and number modulation wave focusing model with the same phase. By using different energy distribution techniques in the four models, the freak wave events were obtained with different maximum wave height by significant wave height ratios in finite space and time. After that the author carried out a numerical simulation of 2-D freak wave event based on enhanced high order spectral (HOS) numerical method and validated by comparison of numerical results with experimental and analytical results (Baldock et al., 1996).

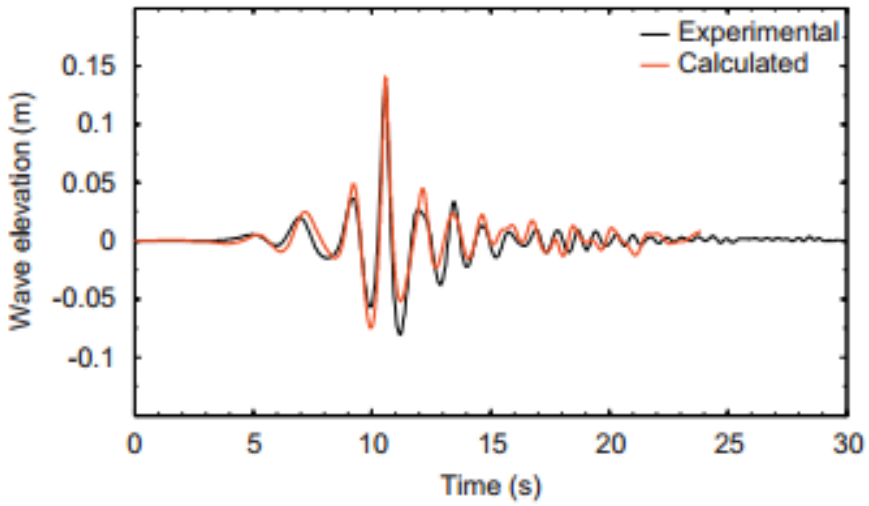

Figure 2.10 Comparison of experimental wave elevation and calculated wave elevation at the wave probe in the numerical wave tank (Liang et al., 2011)

Liang et al. (2011) described how the generation of single extreme wave was investigated. Based on commercial CFD software Fluent, VOF method was used to capture the fee surface. First, an experimental irregular wave train was decomposed into certain number of small-amplitude waves. Fourier series expansion was performed to determine the amplitude and phase angle of each wave component. And then a hydrodynamic transfer function was used to calculate the amplitude of the wave-maker motion associated with each wave component. During the numerical simulation, calculated horizontal velocity profiles of the extreme wave at different moments were analysed and compared

with experimental results. The comparisons of experimental extreme wave elevation and numerical calculated extreme wave elevation are shown in Figure 2.10.

Zhao et al. (2012) introduced further development of a constrained interpolation profile (CIP)-based Cartesian grid method to model nonlinear interactions between extreme waves and a floating body. In the 2D numerical wave tank, three kinds of waves (regular wave focused wave and combined regular and focused wave) were generated. The numerical wave tank was based on improved CIP-based Cartesian grid method in which the THIN/WLIC scheme was used for interface capturing. Computations were compared with experimental results, and agreement was achieved. In (2014), Zhao et al. extended the 2D numerical wave tank to a 3D model to investigate the green water running-up on a floating body under freak wave conditions. Cao and Wan (2014) presented a new CFD code which was based on the open source package OpenFOAM, and Zhao (2012)'s work was reproduced numerically. The accuracy of the present numerical solver naoe-FOAM-SJTU for dealing with the problem of extreme wave interaction with floating body was proved.

Westphalen et al. (2012) developed a fully nonlinear method to investigate the design in different conditions at full scale by computational fluid dynamic method. The generation and behaviour of extreme focused wave groups were conducted in the numerical wave tank. Nonlinear effects of these extreme waves were shown and the implications for a numerical wave tanks were discussed. The double frequency force oscillation on the horizontal cylinder and the secondary load cycle for the vertical cylinder were observed, which might cause severe damage due to the ringing of the structure after being passed by the wave.

Deng et al. (2016) investigated the generation of freak waves using a new focusing model, which considered the effects of wave reflection. In the developed model, the wave spectrum energy was divided into three parts: one for random waves, one for forward transient waves, and one for backward reflected waves. The numerical simulations were compared with those of

simulations based on Kriebel's focusing model. The comparisons showed that the developed model can generate extremely high waves in an accurate and repeatable manner. The primary advantage of the developed model was that both the forward transient waves and the backward reflected waves contained only half the energy of the transient waves in Kriebel's focusing model, making it much better at easing wave breaking. In addition, the numerical simulations indicated that wave reflection could be a possible factor that contributed to the formation of freak waves. Figure 2.11 shows the comparisons of focal position and focal moments with different focusing model. The large fluctuations on the actual focal positions and moments are with Kriebel's focusing model, which is a disadvantage for generating freak waves at a specific point to investigate its impact on marine structures.

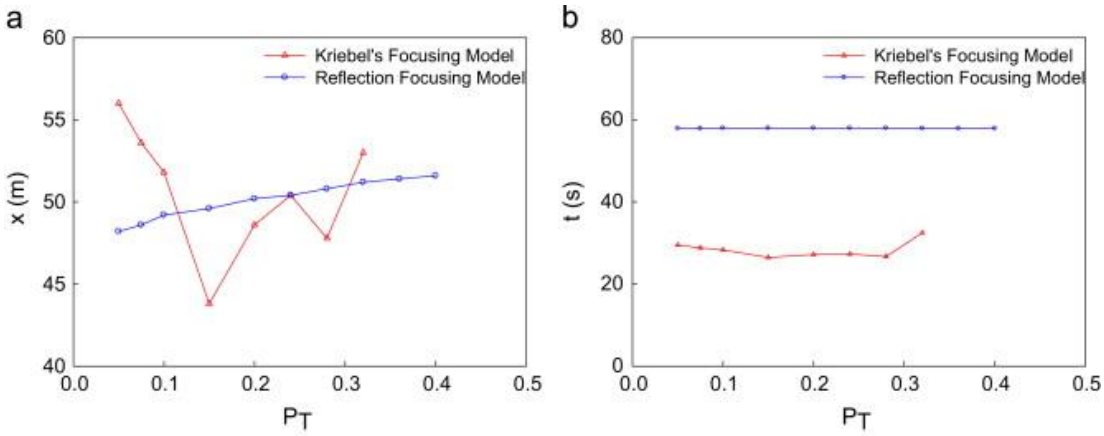

Figure 2.11 Comparisons of focal position and focal moment with different focusing model (Deng et al., 2016)

Qin et al. (2017) investigated the freak wave structure interactions by applying an implicit iterative algorithm in a 2-D numerical wave flume. In this numerical wave flume, three simulations were performed, including a regular wave impact against a rigid wall, a laboratory-scale freak wave impact against elastic wall, and the deck-house impact caused by a full-scale freak wave. Visual snapshots were taken to show the entire wave slamming phenomena. Fluid pressures adjacent to the wall were reported to indicate the influence of hydroelasticity. The displacement of the vertical wall and the deck-house wall from a semi-submersible barge are analysed with the fast Fourier transformation (FFT) and

wavelet transformation method. The total forces of fluid acting on the elastic wall and rigid wall are shown in Figure 2.12. The plot indicated that the total wave force on the rigid wall has a smooth times series and the force on the elastic wall oscillates severely, which is quite similar to distinctions of the fluid pressures of the wall models due to the hydroelastic effect.

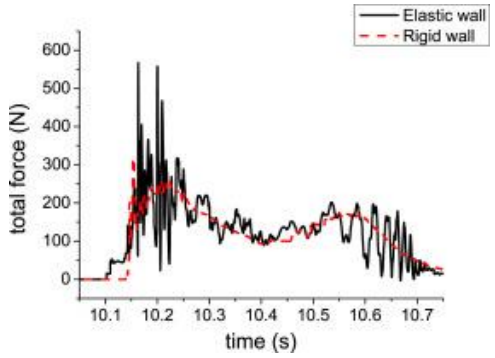

Figure 2.12 Comparisons of the total force time series between the elastic wall and rigid wall (Qin et al, 2017)

2.3 Sloshing

The offshore engineering and LNG production develops very fast in recent decades. The coupled motion response excited by internal flow and external wave excitation becomes the most important research interests in LNG industry. The sloshing in the internal tank has a large effect on the LNG ship motion, and the ship motion response also has an obvious effect on the excited sloshing. It is very important to develop a numerical method to investigate the coupled effect of the ship motion response and the sloshing excitation.

Many experimental and numerical researches about the sloshing tank have been conducted. Kim et al. (2004) did an investigation on the violent sloshing flows with impact occurrences solved using a finite difference method. Two- and three-dimensional prismatic tanks with and without internal members are considered, and the concepts of buffer zone and time averaging are applied for computing impact pressures on the side wall, chamfer, and ceiling. The research results showed that the resent numerical method showing fair numerical efficiency and stability in the prediction of impact pressure. This method can be applied for actual designs of liquid cargo tanks for ships and FPSOs.

Yang et al. (2006) simulated both internal sloshing liquid of a LNG carrier and outer sea waves around the ship by VOF method simultaneously. An incompressible Euler/Navier Stokes discretized by finite element methods was solved for both internal and outside regions. An arbitrary Lagrangian-Eulerian (ALE) was used to treat the motions of ship. However, the turbulent effects were neglected in the work. The computational comparisons

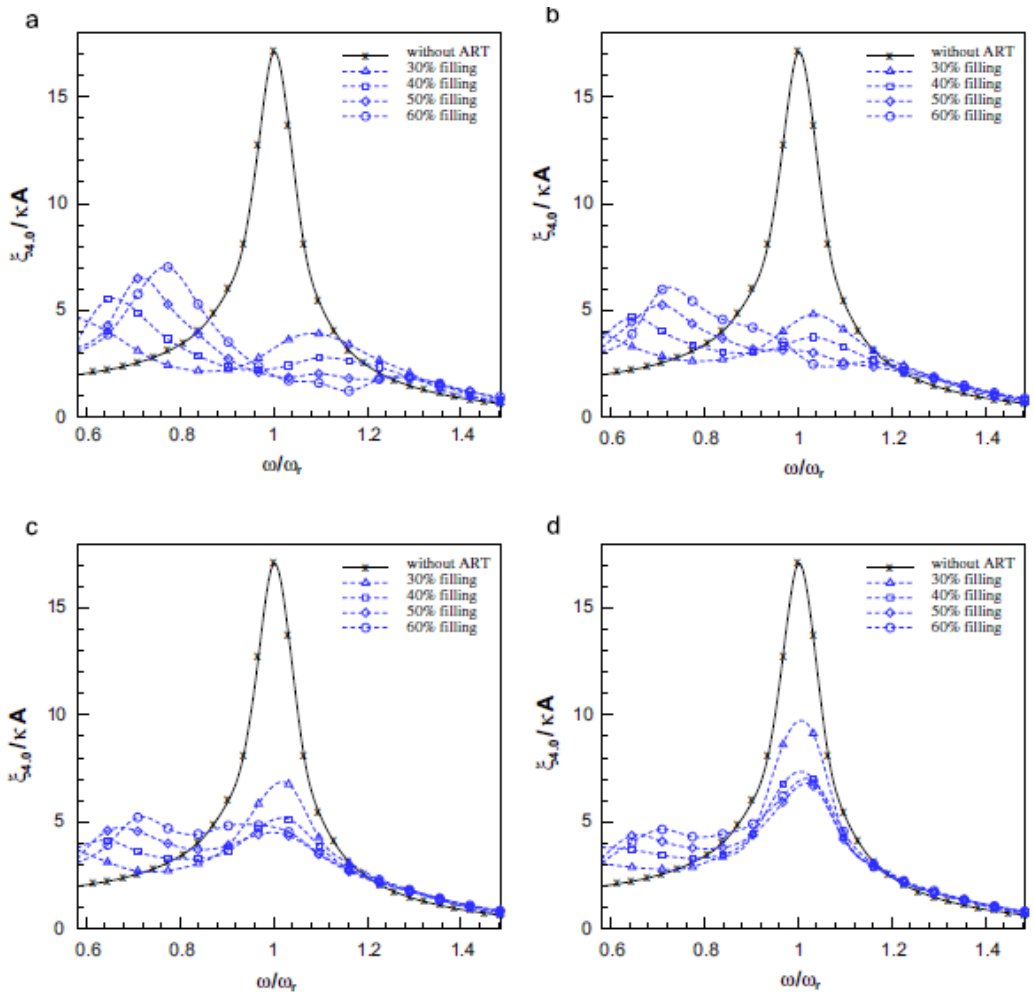

Figure 2.13 Comparisons of roll RAOs for different filling and wave slope. (a) A/L=0.01, (b) A/L=0.015, (c) A/L=0.02 and (d) A/L=0.025 (Kim et al., 2007)

Kim et al. (2007) developed an effective numerical model to investigate the coupled effects on ship motion under wave excitation coupled sloshing excitation. In the numerical model, the linear ship motion was solved using an impulse-response-function (IRF) method, while the nonlinear sloshing flow was simulated using a finite-difference method. By converting the frequency-domain

solution to the time domain, the computational effort was much less than the simulated conducted from the time domain analysis directly. The computational results showed that the nonlinearity of sloshing flow played an important role in the coupling effects, and the motion responses were sensitive to the filling height in the internal tank. An accurate computation of the retardation function was critical in the IRF formulation. The computational results were sensitive to some parameters, e.g. infinite-frequency added mass, roll-damping coefficient, and proper restoring. The nonlinearity of sloshing flow played an important role in the coupling effects. The sloshing-induced forces and moments were not linear with respect to motion amplitude. Therefore, in the coupled problem, the motion amplitude was not linearly proportional to wave amplitude. As the wave amplitude becomes larger, the wave-excitation component becomes more significant. The rolling RAO curves for different filling conditions and wave slopes are shown in Figure 2.13.

S. Lee et al. (2007) studied the coupling effects on ship motion and sloshing. A barge-type FPSO was investigated by using WAMIT for ship motion and by finite difference method with SURF scheme for liquid sloshing. However, since the ship motions were predicted by potential theories, there were many limitations on these methods, e.g. viscous effects were neglected and breaking waves and green water on deck cannot be dealt with. Based on the same numerical theory, Jiang et al. (2015) investigated the coupled motion of a three-dimensional simplified LNG-FPSO ship with two partially-filled prismatic tanks. A typical grid system in AP tank for 20% filling condition is shown in Figure 2.14. Numerical simulations showed that the coupling effect was significant at low-filling conditions in Beam Sea and the typical anti-rolling characteristics can be observed in such cases. The ship motion response showed strong sensitivity to incident wave steepness, especially around the natural frequencies for ship motion and sloshing motion respectively. The sloshing impact loading had no significant coupling effect on global ship response.

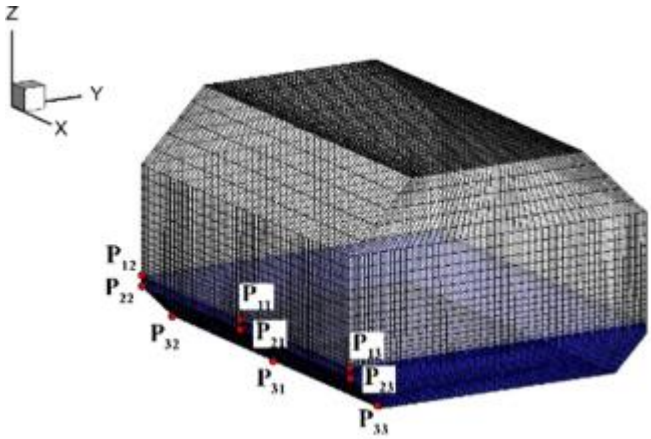

Figure 2.14 A typical grid system in AP tank for 20% filling condition (S. Lee et al. 2007)

Medeiros et al. (2008) presented some results of an experimental study on the effect of the sloshing on the motion of the floating units. The experimental tank model is shown in Figure 2.15. The roll motion of the model with fixed cargo was measured and compared with WAMIT, which showed very good agreement between the experimental and the numerical results. The research results showed that the main effect of sloshing was on the roll motion of the model. When the wave frequency was close to the resonant liquid motion, the sloshing reduced the roll motion remarkably.

Figure 2.15 The model in the tank (Medeiros et al., 2008)

Khezzar et al. (2009) presented the steps involved in designing a test rig to study water sloshing phenomenon in a rectangular container subjected to impulsive impact. Two water levels of 50% and 75% full as well as two driving weights of 2.5 and 4.5 kg were used. The experimental study was supplemented

by a computational fluid dynamics study to investigate the fluid motion inside the tank. The main purpose of this study was to examine the CFD capacity to predict the behaviour of the free surface of the fluid during the container motion. The research results showed that the flow visualization of simulation and experimental results showing a good agreement.

Lee et al. (2010) developed a Moving Particle Semi-implicit (MPS) method for a 2-D incompressible flow simulation to investigate the violent free-surface motions interacting with floating vessels containing inner liquid tanks. The initial configuration for simulating motions of a 2-D rectangular barge is shown in Figure 2.16. In this study, many efficient and robust algorithms had been developed to improve the overall quality and efficiency in solving various highly nonlinear free-surface problems. The computational results showed that the roll amplitudes can be significantly reduced due to the presence of the sloshing tank when the excitation frequencies were away from the lowest sloshing natural frequencies. The reduction rate depended on the fill ratio, and more reduction at 25% fill ratio than that at 50% fill ratio. When the excitation frequencies were close to the lowest sloshing natural frequencies, the maximum roll angles could be slightly increased due to the liquid cargo.

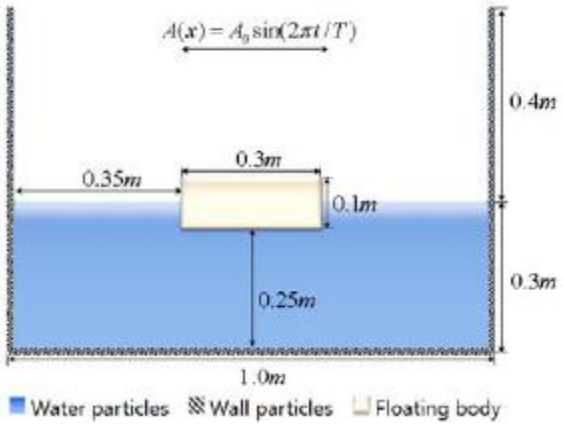

Figure 2.16 Initial configurations for simulating motions of 2-D rectangular barge (Lee et al., 2010)

Lee and Kim (2010) investigated the coupling and interactions between ship motions and inter-tank sloshing by a potential-viscous hybrid method in the time domain. Figure 2.17 shows the snapshot of motion-sloshing coupled animation in the time domain. In this time-domain simulation, a potential-theory-based 3D diffraction/radiation panel program in the frequency domain was used to calculate the hydrodynamic coefficients and wave forces. Then the corresponding simulations of motions in the time domain were carried out using the convolution-integral method. The liquid sloshing in a tank was simulated in the time domain by a Navier-Stokes solver. A finite difference method with SURF scheme assuming the single-valued free-surface profile was applied for the direct simulation of liquid sloshing. The computed sloshing forces and moments were then applied as external excitations to the ship motion. The developed computer programs were applied to a barge-type floating production storage and offloading (FPSO) hull equipped with two partially filled tanks. The research results showed that the most pronounced coupling effects on roll motions are the shift or split of peak frequencies.

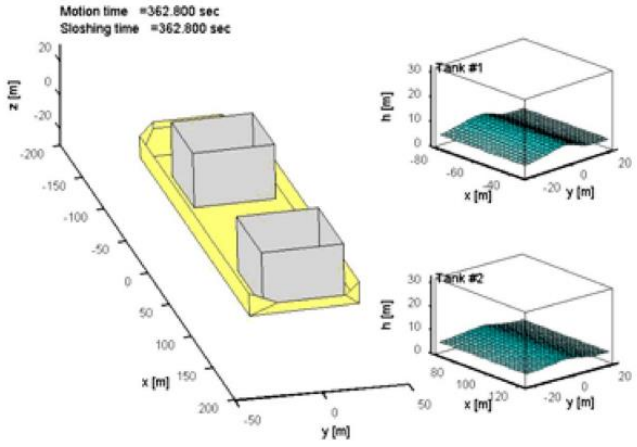

Figure 2.17 Snapshot of motion-sloshing coupled animation (37% beam waves) in the time domain (Lee and Kim, 2010)

Shen and Wan (2012) developed a fully coupled numerical method to simulate the KVLCC2 tank coupled with sloshing under waves by using their own unsteady RANS solver, naoeFoam-SJTU. The computational results showed that in the condition of wave length equal to 1.1 times ship length, the sloshing had

little effect on the heave and pitch motions, not only for head wave but also for beam wave. However, the sloshing had notable effects on the roll motion in beam waves. After comparing different wave heights and different filling ratios of LNG tanks, the results indicated that instead of increasing, the tank sloshing reduced the roll amplitude of ship motion, especially for the largest wave height, H=0.18m. Roll motion of 60% filled tank was slightly smaller than 30% filled.

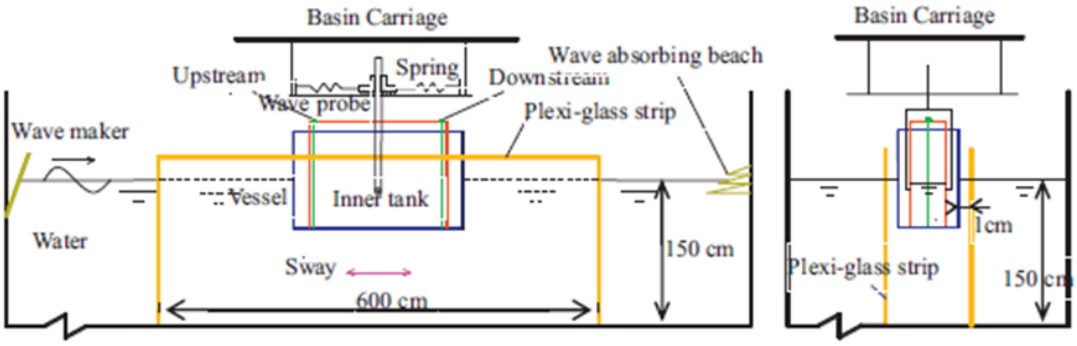

(a) (b)

Figure 2.18 Schematic of the experimental setups; the wave probe located at the upstream of the tank is defined as “upstream”, and the wave probe at the downstream of the tank id defined as “downstream”. (a) Front view and (b) side view (Zhao et al., 2014)

Zhao et al. (2014) developed coupled numerical model considering nonlinear sloshing flows and the linear ship motions based on a boundary element method. The front view and side view of schematic of the experimental setups are shown in Figure 2.18. Only the 2-D hydrodynamic performance of a tank containing internal fluid under regular wave in sway response was investigated by the developed time-domain analysis method, and the computational results were compared with the experimental data. The research results showed that the internal sloshing amplitude is found to change nonlinearly when the incident wave height varies. The asymmetry of the internal surface elevation relative to the still water surface becomes obvious as the wave height grows. Both the internal sloshing and the ship motions exhibit amplitude modulation

phenomenon. The frequency of the amplitude modulation envelope was determined by the difference between the incident wave frequency and the natural frequency of the internal sloshing. The internal sloshing-induced force was π behind the external wave forces at the natural frequency, which was one possible reason to explain why the internal sloshing exhibits significant reduction effects on the global motions at the natural frequency.

3 Numerical Wave Tank

3.1 General Remarks

With the development of computer technology, numerical simulation methods are widely used in all areas of research. The world has realised great achievements in numerically simulated waves, and the interactions between waves and offshore structures. The numerical wave generation technology introduced in my thesis is based on the CFD method. Compared with real physical experiments, the numerical wave tank has the advantages of low costs, easy application, easy transformation, and accurate measurement among others (Tang and Yuan, 2001).

In this present work, both the two dimensional (2D) and three dimensional (3D) numerical wave tanks are established based on Navier-Stokes equations for viscous, incompressible fluid by CFD commercial software FLUENT. The VOF method is used to capture the free surface. Paddle wave generation method and added mass term wave generation methods are compared and analysed in regular and focused wave generation. Momentum source terms are added in the governing equations in dissipation domain to reduce wave reflection.

In general, a CFD analysis should always pass through the following basic steps:

1. Problem identification and pre-processing
    - Definition of the modelling goals
    - Identification of the domain
2. Solver execution
    - Set-up of the numerical model
    - Computation and monitoring of the solution
3. Post-processing
    - Examination of the results
    - Consideration of model revisions

3.2 Wave Generation Method

Nowadays, wave generation can be classified into two types according to their wave generation principles. One type is the physical wave generation technology, which is used to imitate the wave makers in the laboratory, such as the paddle wave generation method and piston wave generation method. The other type of wave generation method is purely numerical and includes the velocity inlet method, source function method and momentum function method. In the following chapter, only the paddle wave generation method and source function method will be introduced.

3.2.1 Paddle Wave-making Method

Paddle wave making is the first and most common method in a wave tank laboratory. In a numerical wave tank, the same concept can be used. To derive the paddle wave generating formulae, length of paddle under water is defined as l. The paddle amplitude at water surface is E, and the wave propagating direction is positive. The regular wave amplitude is a. The wave length is λ. The wave period is T, and the wave number is k. The wave frequency is ω.The water surface is at $x = 0$ and the static paddle position is at $y = 0$. (Tao and Yuan, 2001)

The paddle amplitude at a specific water depth is:

$$e(y) = 0; 0 \leq y \leq (h - l)$$

$$e(y) = \frac{E}{l}(y - h + l); (h - l) < y \leq h \tag{3.2.1}$$

Horizontal movement of paddle is

$$x = e(y) \cdot sin\, \omega t \tag{3.2.2}$$

Horizontal velocity of paddle

$$u = \frac{dx}{dt} = \omega \cdot e(y) \cdot cos\, \omega t \tag{3.2.3}$$

Based on small amplitude wave assumption, i.e. $\lambda \gg a$, denote ϕ to be velocity potential, u and v to be horizontal and vertical velocity of wave at wave paddle respectively, then

$$\frac{\partial \phi}{\partial x} = u = \omega \cdot e(y) \cdot cos\, \omega t \quad (x = 0) \tag{3.2.4}$$

$$\frac{\partial \phi}{\partial y} = v \quad (x = 0) \tag{3.2.5}$$

Velocity potential satisfies Laplace equation

$$\frac{\partial^2 \phi}{\partial x^2} + \frac{\partial^2 \phi}{\partial y^2} = 0 \tag{3.2.6}$$

The boundary condition in this case is as follows:

Vertical velocity at seabed is zero:

$$v = \frac{\partial \phi}{\partial y} = 0 \quad (y = 0) \tag{3.2.7}$$

The free surface boundary condition:

$$\frac{\partial^2 \phi}{\partial t^2} + g \cdot \frac{\partial \phi}{\partial y} = 0 \quad (y = h) \tag{3.2.8}$$

General solution to the velocity potential of wave propagation is derived based on Fourier method:

$$\phi = C_0 \frac{\omega}{k_0} cosh(k_0 y)\, sin(k_0\, x - \omega t) - \sum_{n=1}^{\infty} C_n \frac{\omega}{k_n} cos(k_n y)\, e^{-k_n x} cos(\omega t) \tag{3.2.9}$$

Solve the derivative of ϕ and substitute it in free surface boundary condition can yield:

$$-C_0\omega\, cosh(k_0 y)\, sin(k_0\, x - \omega t) - \sum_{n=1}^{\infty} C_n \omega\, cos(k_n y) e^{-k_n x}\, cos(\omega t)\, (\frac{\omega^2}{k_n} + g\, tan(\, k_n y))\Big|_{y=h} = 0 \tag{3.2.10}$$

The dispersion relation is further derived as:

$$\omega^2 - k_0 g\, tanh(k_0 h) = 0 \tag{3.2.11}$$

$$\omega^2 + k_n g\, tan(k_n h) = 0 \tag{3.2.12}$$

For (3.2.12), there is an infinite number of k corresponding to a specific ω, which is denoted as k_n. k_n lies in $(n\pi - \frac{\pi}{2})/h \sim n\pi/h$ interval. C_0 and C_n in (3.2.9) is solved based on boundary conditions. Substitute (3.2.9) to (3.2.4) and multiply by $cosh(\, k_0 y)$, followed by integrating:

$$C_0 \int_0^h cosh^2\,(k_0 y) dy + \sum_{n=1}^{\infty} C_n \int_0^h cosh(k_0 y)\, cos(k_n y)\, dy = \int_0^h e(y)\, cosh(k_0 y)\, dy = 0 \tag{3.2.13}$$

The dispersion relation (3.2.11) and (3.2.12) can validate the equation $\int_0^h cosh(k_0 y)\, cos(k_n y)\, dy = 0$, therefore:

$$C_0 = 2k_0 \frac{\int_0^h e(y)\, ch(k_0 y) dy}{k_0 h + sinh(\, k_0 h)\, cosh(k_0 h)} \tag{3.2.14}$$

The result of C_0 is obtained by integrating (3.2.1):

$$C_0 = \frac{2E}{k_0 l} \cdot \frac{k_0 l\, sinh(k_0 h) - cosh(k_0 h) + cosh(k_0 h - k_0 l)}{k_0 h + sinh(k_0 h)\, cos(k_0 h)} \tag{3.2.15}$$

The same approach can be applied to solve C_n:

$$C_n = \frac{2E}{k_n l} \cdot \frac{k_n l \sinh(k_n h) + \cosh(k_n h) - \cosh(k_n h - k_n l)}{k_n h + \sinh(k_n h)\cos(k_n h)} \tag{3.2.16}$$

Furthermore, wave function in front of wave paddle is derived based on calculating average displacement of water particle in vertical direction from (3.2.7):

$$\begin{aligned} \eta(x,t) &= \int \frac{\partial \varphi}{\partial y} dt \Big|_{y=h} \\ &= C_0 \sinh(k_0 h)\cos(k_0 x - \omega t) \\ &+ \sum_{n=1}^{\infty} C_n \sin(k_0 y) e^{-k_0 x} \sin(\omega t) \end{aligned} \tag{3.2.17}$$

The first part of right hand side of the equation above is propagating wave and second part is standing wave. Standing wave can be neglected after moving away from wave paddle. The wave amplitude is also observed as:

$$A = C_0 \sinh(k_0 h) \tag{3.2.18}$$

Substitute (3.2.15) with C_0 value:

$$A = \frac{2E}{k_0 l} \sin(k_0 h) \cdot \frac{k_0 l \sinh(k_0 h) - \cosh(k_0 h)\cosh(k_0 h - k_0 l)}{k_0 h + \sinh(k_0 h)\cos(k_0 h)} \tag{3.2.19}$$

Therefore, two hydrodynamic transmission functions are obtained:

$$\begin{aligned} T(\omega) = \frac{A}{E} &= \frac{2\sin(k_0 h)}{k_0 l} \\ &\cdot \frac{k_0 l \sinh(k_0 h) - \cosh(k_0 h) + \cosh(k_0 h - k_0 l)}{k_0 h + \sinh(k_0 h)\cos(k_0 h)} \end{aligned} \tag{3.2.20}$$

$$\begin{aligned} T_1(\omega) = \frac{A}{\tilde{\theta}} &= \frac{2\sin(k_0 h)}{k_0} \\ &\cdot \frac{k_0 l \sinh(k_0 h) - \cosh(k_0 h) + \cosh(k_0 h - k_0 l)}{k_0 h + \sinh(k_0 h)\cos(k_0 h)} \end{aligned} \tag{3.2.21}$$

(3.2.20) demonstrates the relation between wave amplitude and paddle amplitude, namely the amplitude-frequency characteristics of paddle wave generator which is the core control mechanism. In (3.2.21), $\tilde{\theta}$ is paddle amplitude and satisfied the scenario in small amplitude wave theory below. The equation is applied in favour of defining paddle movement in the dynamic mesh model.

3.2.2 Source Function Wave-making Method

3.2.2.1 Basic Functions

Based on the Continuity equation (A.2.3) and the Navier-Stokes equation (A.2.4) which are introduced in Appendix A, the source function wave-making methods can be classified into three ways. One method is to add forcing functions in the momentum equations. The forcing function can be applied with stress on a free surface of water or in the source function region. Another method is to add a mass source function in the continuity equation in a wave generation domain. In general, the mass source can be a point, a line, or a volume. The third method is the combination of the momentum source and the mass source. In this thesis, only the added mass source wave-making method will be introduced.

For a two-dimensional numerical wave tank, the added source term definition can be presented as:

$$\frac{\partial u}{\partial x}+\frac{\partial v}{\partial y}=s(x,y,t) \qquad in\ 2d\ \Omega \tag{3.2.22}$$

$$s(x,y,t)=\begin{matrix} s_s(y,t) & x=x_s \\ 0 & x\neq x_s \end{matrix} \tag{3.2.23}$$

where

$x_s =$ the horizontal position of the source region

The $s(x,y,t)$ is the added mass term in the mass conservation function in the source region, which is defined as Ω. If the mass term is added in the continuity equation in the source region, the free surface above the source region will

change gradually. Theoretically, two trains of surface gravity wave will travel with the same wave length and period but in the opposite direction.

3.2.2.2 Source Region Size and Position:

In the real numerical simulation process, a finite region is collected as the source region. For two dimensional simulations, the source region is always defined as a rectangular region. In the present work, the rectangular source is used. The position of the source region is regarded as the numerical wave-making position. The minimum region is a computation cell size. The source height is H_s and width is L_s. The distance from the region top side to the free water surface is e. In theory, the smaller L_s value makes better wave profile results. If L_s is larger than 20 percent of the target wave length, the modelling result may lead to extreme inaccuracy, as at that moment the wave cannot be defined and generated in position $x = x_s$. In the present work, the source region width is the width of one computation cell. After selecting a proper source region width, a suitable value e, the distance from the region top side to the water free surface, is also of great importance. If e is quite small, which means the mass source region is close to the water free surface, this may lead to computation divergence. In contrast, the increase of value e may decrease the modelled wave amplitude above the source region, which will unlikely meet the target wave profile requirement. For the regular wave simulation, e is set equal to one target wave height, but for irregular and focusing wave simulations, the e value should have further validation.

3.2.2.3 Source Intensity

In theory, proper mass source intensity can generate any target wave. The relationship between source intensity and target wave profile is the main topic in this chapter. The source region is set as a layer of rectangle cells positioned with a distance from the water free surface directly to the wave tank bottom. The width of the source region is small relative to the target wave length, so that the wave-making position can be regarded as the centre of the source region and two wave trains will be generated at the same time with identical wave length and period. On the premise of an assumption that all the increase and

decrease in mass from the added mass term in the continuity equation contributes to the wave generation, in every cell domain in the mass region, the relationship between generated wave horizontal velocity and source intensity for two-dimensional numerical wave tanks can be defined as:

$$s_s(y,t)\Delta x\Delta y\Delta t = 2u(x_s,y,t)\Delta t\Delta y \tag{3.2.24}$$

Such that,

$$s_s(y,t) = \frac{2u(x_s,y,t)}{\Delta x} \tag{3.2.25}$$

In the above two equations, $u(x_s,y,t)$ is the water particle horizontal velocity above the source region. Δx and Δy are horizontal length and vertical length of the cell.

For a linear regular wave,

$$u(x_s,y,t) = a\omega\frac{coshk(y+h)}{sinhkh}cos(kx_s-\omega t) \tag{3.2.26}$$

With the wave profile,

$$\eta = acos(kx-\omega t) \tag{3.2.27}$$

3.3 Wave Absorption Technique

An absorption zone is set at the end of the tank domain, aiming for wave energy absorption and preventing wave reflection. The artificial viscous wave absorption method is not sensitive to wave frequency. In other words, it is effective for wave absorption of various frequencies. The idea behind the artificial viscous wave absorption method in the numerical wave tank is to simulate the real wave tank by adding additional terms in the momentum equations. Note that the zone size affects the wave absorption result and the damping zone length is always larger than one wave length.

For the two-dimensional case, the momentum equations (ANSYS FLUENT 14.5 User's Guide, 2012) in the absorption domain are defined as:

$$\frac{\partial u}{\partial t}+u\frac{\partial u}{\partial x}+v\frac{\partial u}{\partial y}=-\frac{1}{\rho}\frac{\partial p}{\partial x}+\upsilon\left(\frac{\partial^2 u}{\partial x^2}+\frac{\partial^2 u}{\partial y^2}\right)-\mu(x)u \tag{3.3.1}$$

$$\frac{\partial v}{\partial t}+u\frac{\partial v}{\partial x}+v\frac{\partial v}{\partial y}=g-\frac{1}{\rho}\frac{\partial p}{\partial y}+\upsilon\left(\frac{\partial^2 v}{\partial x^2}+\frac{\partial^2 v}{\partial y^2}\right)-\mu(x)v \tag{3.3.2}$$

$\mu(x)$ is the damping coefficient and the intensity is

$$\mu(x)=\alpha(\frac{x-x_s}{x_e-x_s})^2 \tag{3.3.3}$$

where

$\alpha=$ damping control parameter

$x_s=$ the start point of the wave absorption domain

$x_e=$ the ending point of the wave absorption domain

3.4 Regular Wave Simulation Setup and Results

The CFD numerical simulation of the regular wave is conducted in this section. Two different wave making methods, the paddle wave making method and source function wave making method, are considered here. The results demonstrate a good agreement between the numerical and analytical results. The accuracy of the numerical simulation is also affirmed. Finally, the two wave making methods are compared.

3.4.1 Paddle Wave-making Results

The detailed configuration of the numerical wave tank is shown in Figure 3.1. The wave tank is 30m long in total and the length of the wave damping domain is 6m – located at the wave tank end. The water depth is 5m in total in this case. The tank dimensions are defined based on the target wave properties. In this case, the wave period T=2s, and the corresponding wave length is 6.24m in deep water conditions. As the figure shows, the upper part of the wave tank, which is above the initial free surface, is the air phase and the lower part is the water phase. The boundary AB, BC, CD, DE, EF and GF is set to be wall. The

boundary AH and HG are set to be the pressure inlet. The paddle is also set to be the non-slip wall boundary condition.

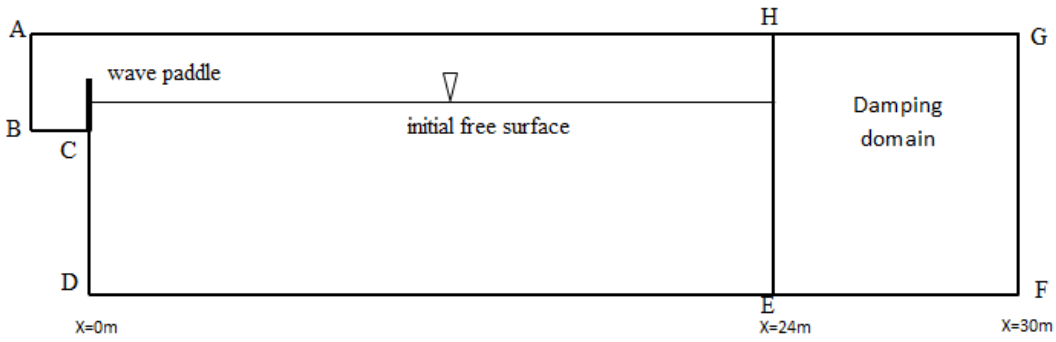

Figure 3.1 The detailed configuration of paddle wave making numerical wave tank

The design and creation of the grid is an important factor in the CFD simulation and can have a lasting effect on the calculation results. The CFD pre-processing geometry creation and meshing software GAMBIT is used in the present study. Therefore, several points should be considered:

- Which type of grids can be used, a quadrilateral/hexahedron, a triangle/tetrahedron or a hybrid grid cell type?
- How can numerical diffusion be avoided?
- How complex is the geometry and the flow?
- Is sufficient computer memory available for a certain number of cells and models?

Most relevant to the choice of the grid is to minimise numerical diffusion. Thus, ideally the flow should be aligned with the mesh which can be achieved by using quadrilateral or hexahedral mesh. When the flow is complex or the shape of the geometry is complicated, the use of triangular or tetrahedral mesh is recommended.

In this case, a distinction should be made between the static domain and the dynamic domain. In the wave generation domain, to simulate the paddle motion, the triangle mesh is selected to increase the dynamic mesh accuracy. In the working domain and the damping domain, to reduce the CFD computational

expenses, the structured quadrilateral mesh is used. More mesh elements are set near the free surface for a smoother wave elevation profile, as shown in Figure 3.2 and Figure 3.3.

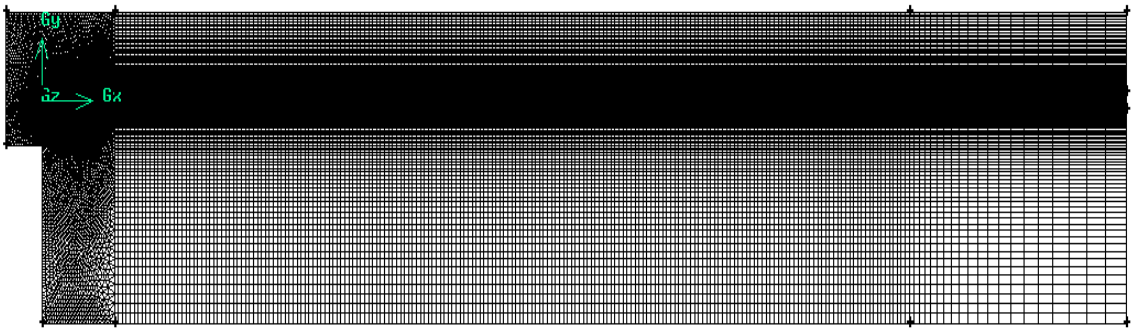

Figure 3.2 The global meshing configuration of the numerical wave tank

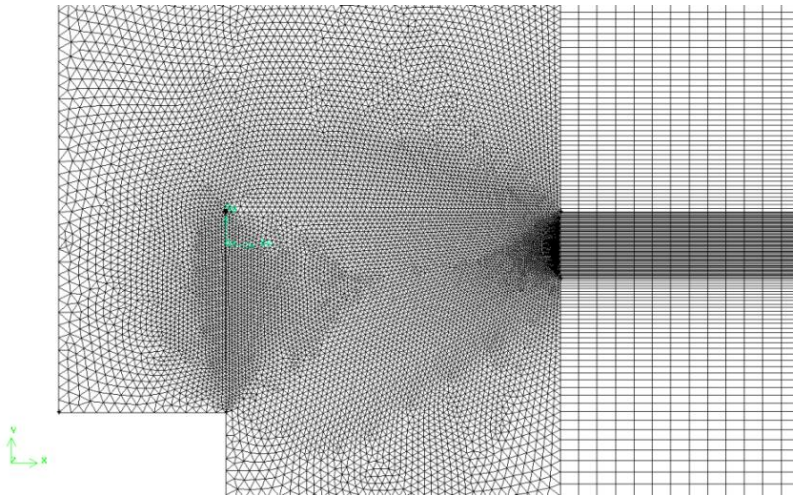

Figure 3.3 The meshing configuration around the paddle and free surface

In the paddle wave-making simulation, the pressure-based, unsteady solver is used. The Geo-reconstruct Scheme is utilised for reconstructing the free surface. A second-order upwind discretization is used for better accuracy and the Pressure-Implicit with Splitting of Operators (PISO) algorithm with a neighbour correction is chosen. A non-iterative time-advancing scheme is used as the time-steeping algorithm. The User Defined Functions (UDFs) are integrated to control the predetermined paddle motion.

In favour of observing wave height at different locations along the wave propagating direction, as well as verifying the wave absorption effect in the

damping domain, the time history of the wave elevation profile is measured to compare with the linear analytical results, shown from Figure 3.4 to Figure 3.11, at different locations along the wave tank within 30 minutes. It is obvious that the regular wave profiles simulated in the numerical wave tank have good agreement with the analytical results. The numerical waves are in phase with the analytical wave profiles. When waves propagate gradually away from the wave paddle, the wave elevation demonstrates a higher order effect. Compared with the first order analytical results, the CFD simulated wave has a higher wave crest and a lower wave trough, seen in Figure 3.5 and Figure 3.6. At the wave elevation gauge x=10m, the average simulated regular wave crest is 0.114m, which is 14% larger than the first order linear analytical results. However, the computational diffusion is inevitable in the numerical wave tank, as the simulated regular wave elevation reduced slightly after a three-wave length distance from the wave paddle.

In terms of the wave absorption effect in the damping domain, Figure 3.10 and Figure 3.11 show the CFD simulated wave elevations measured at locations x=27m and x=29m. The damping effect is excellent from the figures where the wave amplitude reduces from approximately 0.05m to 0.0005m. After the wave passes the damping domain, it will interact with the right boundary of the numerical wave tank and then reflect by passing the damping domain again. Thus, it can be concluded that there will be negligible reflection effect, and therefore the damping zone performs well with absorbing wave energy.

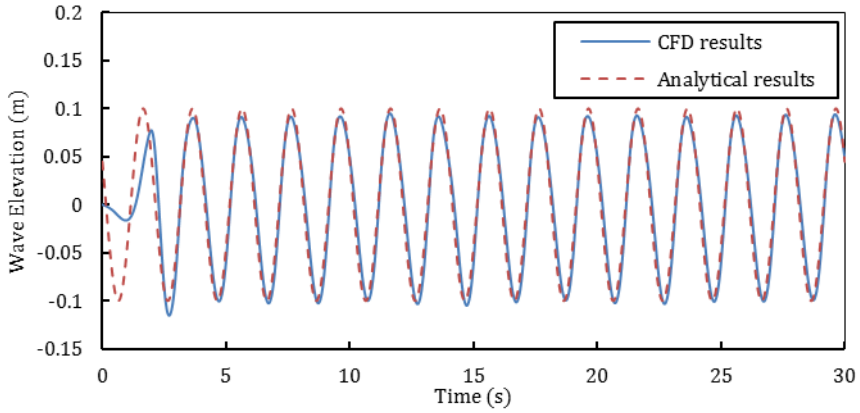

Figure 3.4 The numerical time history of wave elevation measured at x=2m compared with linear analytical results

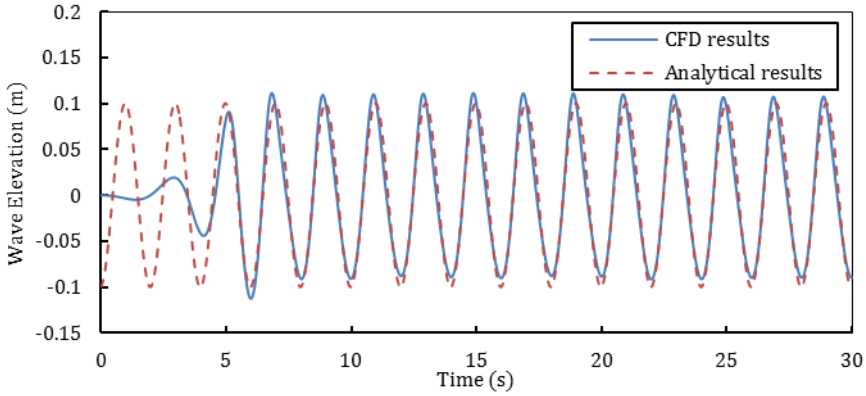

Figure 3.5 The numerical time history of wave elevation measured at x=6m compared with linear analytical results

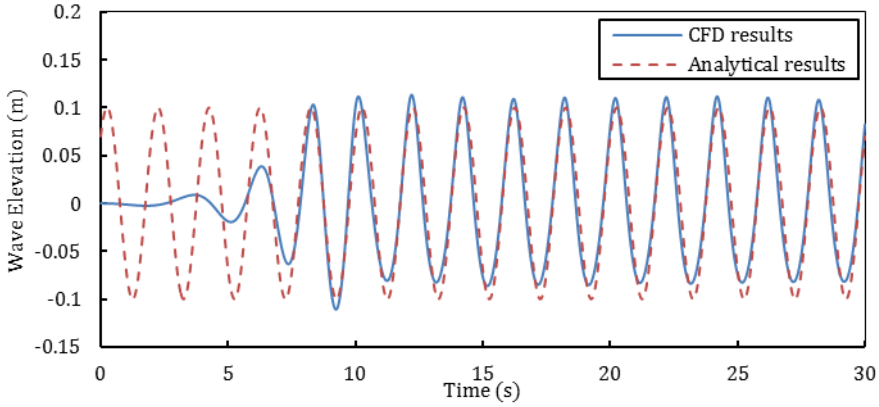

Figure 3.6 The numerical time history of wave elevation measured at x=10m compared with linear analytical results

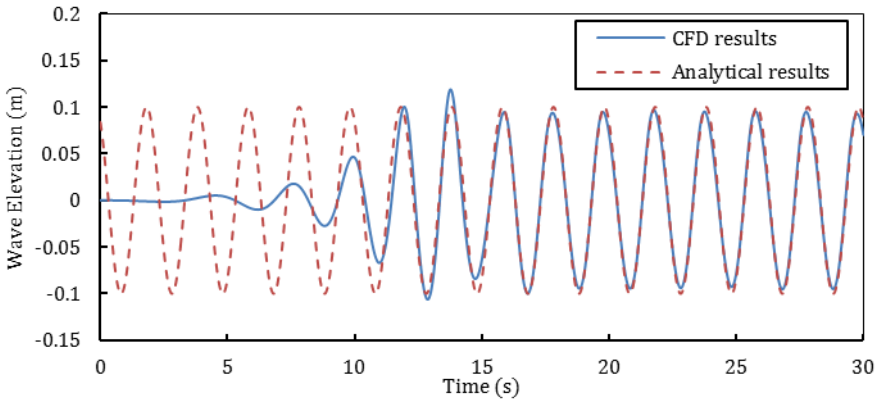

Figure 3.7 The numerical time history of wave elevation measured at x=15m compared with linear analytical results

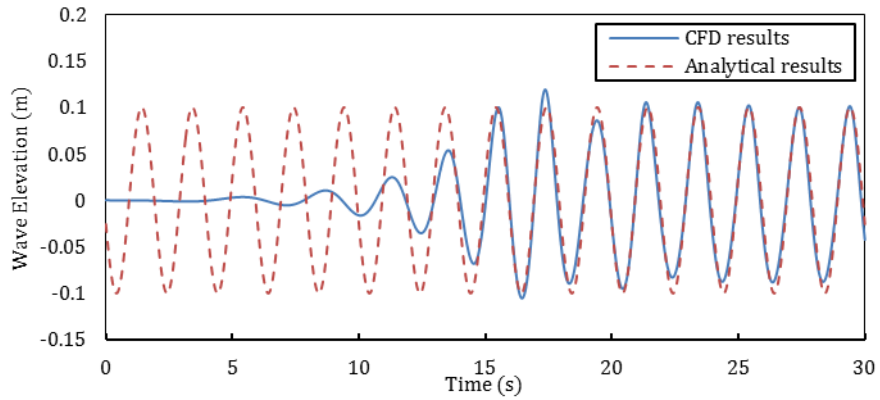

Figure 3.8 The numerical time history of wave elevation measured at x=20m compared with linear analytical results

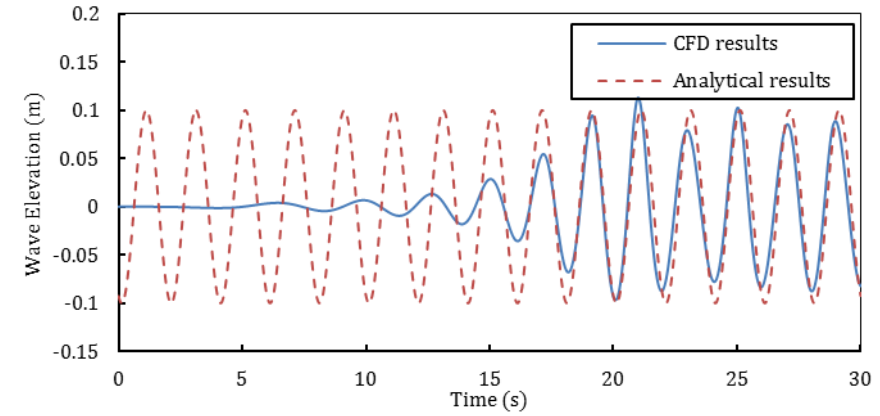

Figure 3.9 The numerical time history of wave elevation measured at x=25m compared with linear analytical results

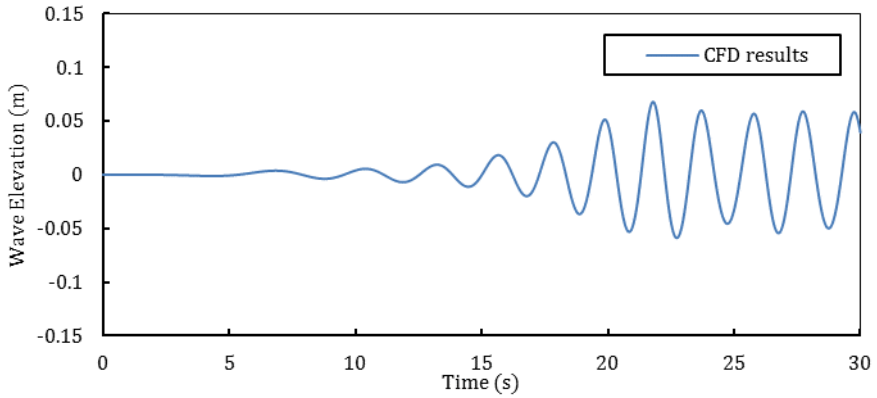

Figure 3.10 The numerical time history of wave elevation measured at x=27m

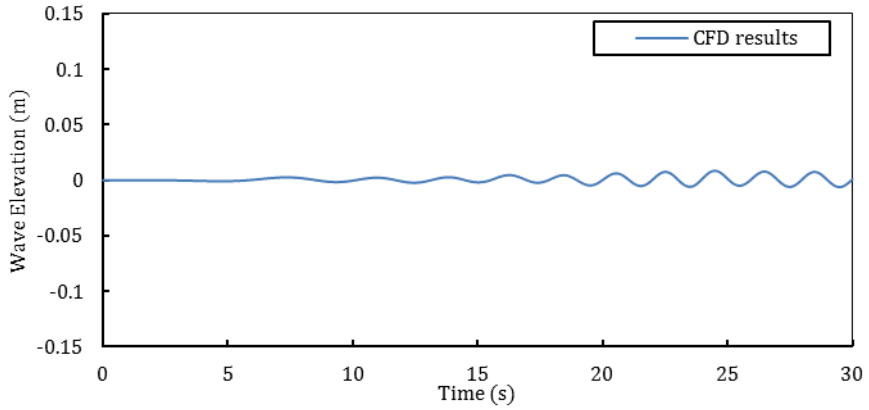

Figure 3.11 The numerical time history of wave elevation measured at x=29m

The wave contours of the numerical wave tank at different four moments are shown from Figure 3.12 to Figure 3.15.

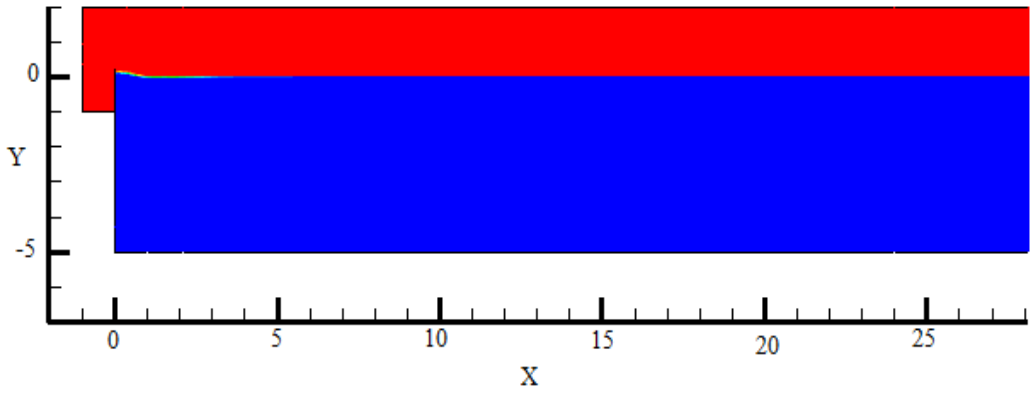

Figure 3.12 Wave contour at time t=5s

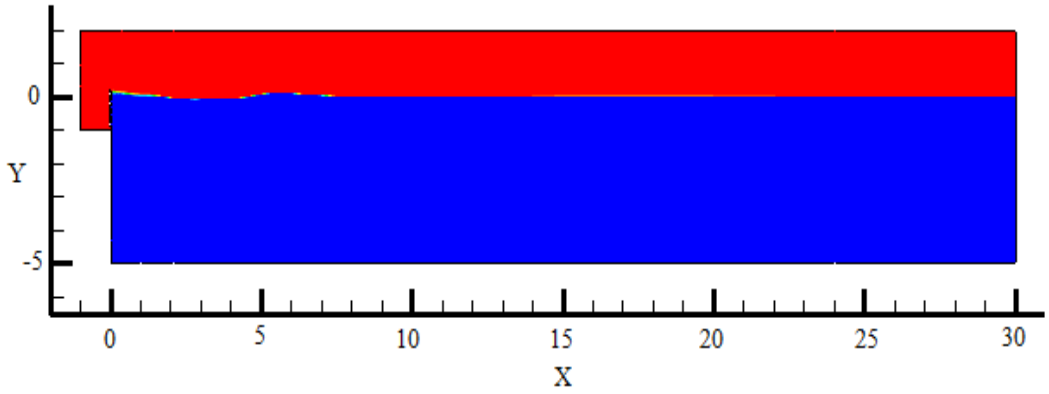

Figure 3.13 Wave contour at time t=10s

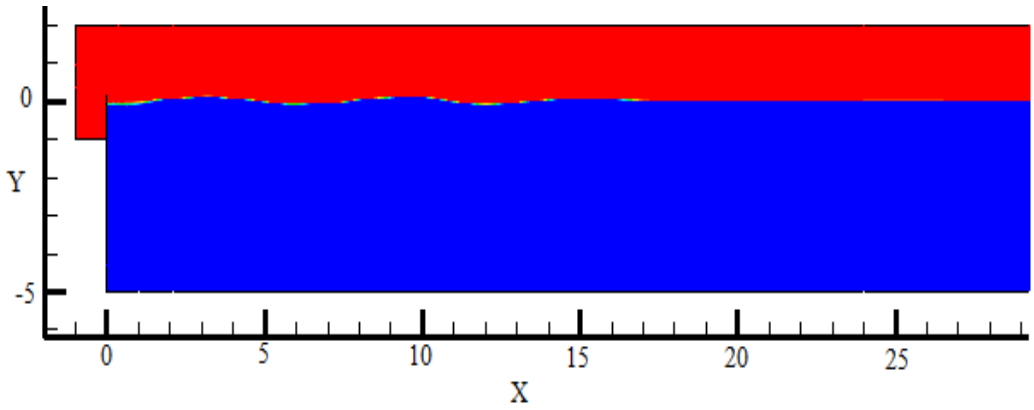

Figure 3.14 Wave contour at time t=15s

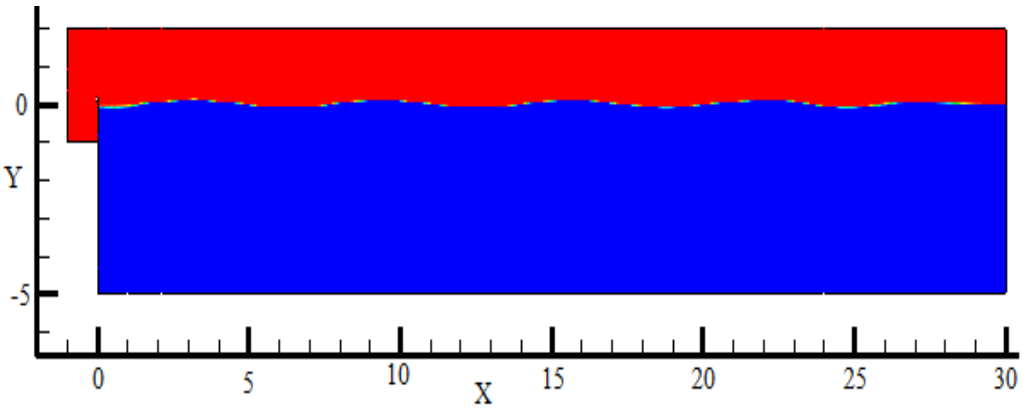

Figure 3.15 Wave contour at time t=20s

3.4.2 Source Function Wave-making Results

In this part, a period T = 9s deep regular wave is simulated by the mass function wave-making method. The detailed configuration of the numerical

wave tank is shown in Figure 3.16. The boundary AB and BC is set to be symmetry and all the other boundaries are the same as the paddle wave-making wave tank. The coordinate origin O is located at the left side of the wave tank. Considering the target wave length, the wave tank is 700m long in total, and the length of the damping domain is 150m. The total water depth is 100m, and the distance between the water free surface and top boundary is 30m. A rectangle source domain is used, which is placed 4.22m below the free surface with a width of 3.2m.

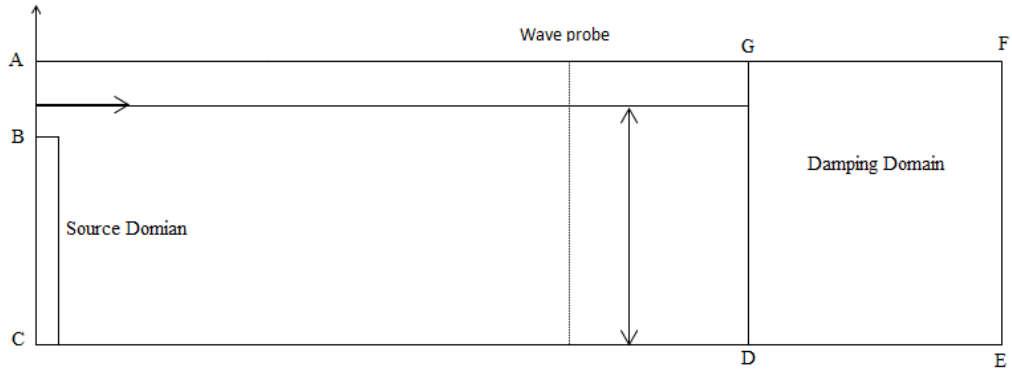

Figure 3.16 The detailed configuration of source function wave-making numerical wave tank

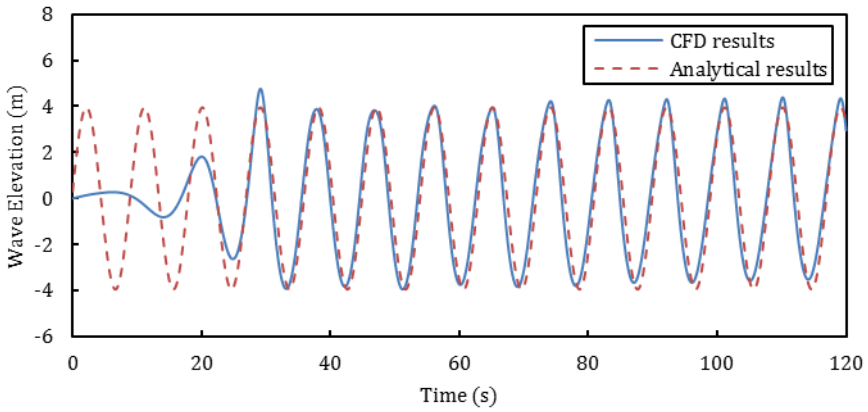

Figure 3.17 The numerical time history of wave elevation measured at x=250m compared with linear analytical results

The wave elevation comparison is shown in Figure 3.17 at location x = 250m. The comparison results show that the wave elevation profiles computed from the current CFD method and derived from the linear wave theory have a good

agreement. It should be noted that the computational regular wave crest is higher and the wave trough is much shallower than the linear sine wave profile result. The phenomenon is similar with the paddle wave-making method.

3.5 Conclusions

The implementation of the numerical method has been discussed in this chapter. In order to investigate the wave structure interaction issues by the Computational Fluid Dynamic method, the development of the CFD numerical wave tank technique is the primary work.

The general regular wave theory is introduced first. Based on the linear regular wave theory, the higher order regular wave theory, the irregular wave theory and the extreme wave theory could be developed. Following that, two different wave generation methods are discussed. The paddle wave-making method is a physical wave generation technology which imitates the wave makers in the laboratory. The wave generation formula is derived by a small amplitude wave assumption. Then, the source function wave-making method is discussed. The empirical formula of the source size and source intensity has been summarized. Finally, the regular wave computational simulation setup and results are discussed. The numerical wave elevations are all compared with the linear analytical results, and a good agreement is achieved.

In the following chapters, the extreme wave will be generated based on the numerical wave tank technique discussed in this chapter, and the wave structure interaction issues will be investigated further.

4 Freak Wave Models and Numerical Simulations

4.1 General Remarks

In this chapter, the freak wave models are introduced. According to Longuet-Higgins wave model theory, the wave free surface can be represented by the linear sum of the individual wave components with different frequencies and random phases. Improving this wave model, the wave components have their phase adjusted so that a large amount of energy is located at a focused position and at a given time. Following this, two more efficient and realistic freak wave models are presented: the combined wave models and phase modulation wave models, respectively.

Finally, a 2-D numerical wave tank is established based on the numerical wave tank theory introduced in the previous chapter. In this numerical wave tank, 12 different freak wave events are generated numerically, and the effect of focused wave parameters on the nonlinearity of the freak wave train is investigated. The parametric studies include the shift of freak wave train focusing position and focusing time, and a comparison of numerical time histories of wave elevations with the analytical results.

4.2 Random Wave Model Theory

Based on the Longuet-Higgins wave model theory, the realistic sea surface in space and time $\eta(x,t)$ can be expressed by the linear sum of the individual wave component with different wave amplitude, different wave frequency and random phase angle in the usual way as:

$$\eta(x,t) = \sum_{i=1}^{N} a_i * cos(k_i x - \omega_i t + \tau_i) \tag{4.2.1}$$

Where

a_i = wave amplitude (m) for group component i

k_i = wave number (rad/m) for group component i

ω_i = circular wave frequency (rad/s) for group component i

$\tau_i =$ the phase of the wave component

$i = 1,2 \ldots N$ represents the wave component

To generate a random wave train, the phases of each wave component τ_i are selected in the usual way by randomly selecting a number between 0 and 2π using the random number function in Mathcad.

In 1968 and 1969, an extensive wave measurement program called the Joint North Sea Wave Project JONSWAP was carried out. Analysis of the data yielded a spectrum formulation for fetch-limited wind generated seas (Hasselmann et al., 1973). Based on the given significant wave height and wave spectrum period, the formulation can be represented as:

$$s(\omega) = \frac{320 * H_{1/3}^2}{T_p^4} * \omega^{-5} * exp\left(\frac{-1950}{T_p^4} * \omega^{-4}\right) * \gamma^Y \tag{4.2.2}$$

$$Y = exp[-\left(\frac{\left(\omega - \omega_p\right)^2}{2\sigma^2\omega_p^2}\right)] \tag{4.2.3}$$

where

$\gamma = 3.3$ peakness factor

$\omega_p = \frac{2\pi}{T_p}$ circular frequency at spectral peak

$\sigma =$ a step function of ω

If $\omega < \omega_p$ then: $\sigma = 0.07$.

And $if\ \omega > \omega_p$ then: $\sigma = 0.09$

For a given wave spectrum, most wave energy is gathered in the frequency range $(\omega_{min}, \omega_{max})$. During the analysis, the total wave component number is M. Thus, the frequency is divided into M components equally and the frequency interval for each component is $\Delta\omega = (\omega_{max} - \omega_{min})/M$. According to the wave

spectrum definition, for each frequency component, the relative wave amplitude is $a_i = \sqrt{2 * s(\omega_i) * \Delta\omega}$ and $\Delta\omega$ is the uniform spacing between frequencies.

Jonswap is selected as the target wave spectrum in the analysis. For the random wave modelling, the relative spectrum parameters are selected as follows. Significant wave height is $H_s = 0.1$m and peak wave period is $T_p = 2$s. The total simulating time is $60T_p$ and the time interval during the simulation is 0.05s. The wave frequency range is from $f_{min} = 0.1f_p$ to $f_{max} = 4f_p$. The wave component number $M = 100$.

The random initial phase τ_i is shown in Figure 4.1 and the wave amplitude a_i is shown in Figure 4.2. By substituting a_i and τ_i into equation (4.2.1), the time histories of the analytical irregular wave train are shown in Figure 4.3 and Figure 4.4 at the position $x = 0$m and $x = 10$m, respectively.

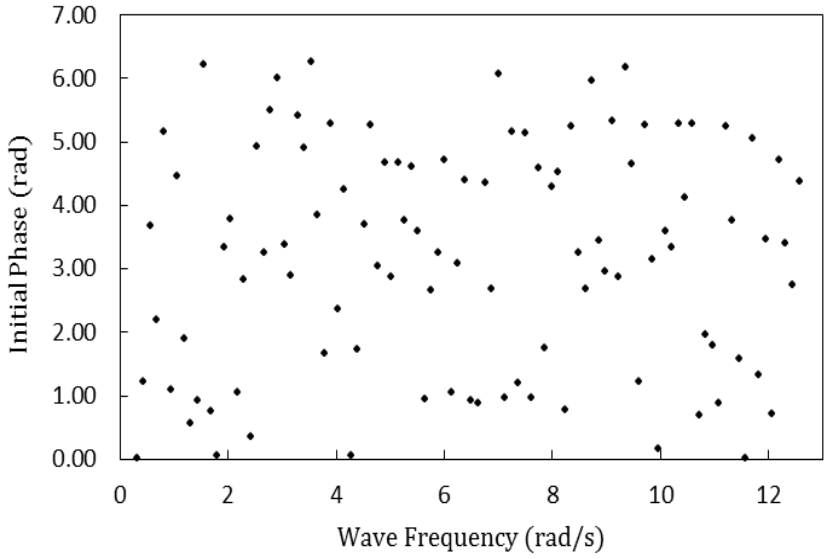

Figure 4.1 Random initial phase related to each wave frequency component

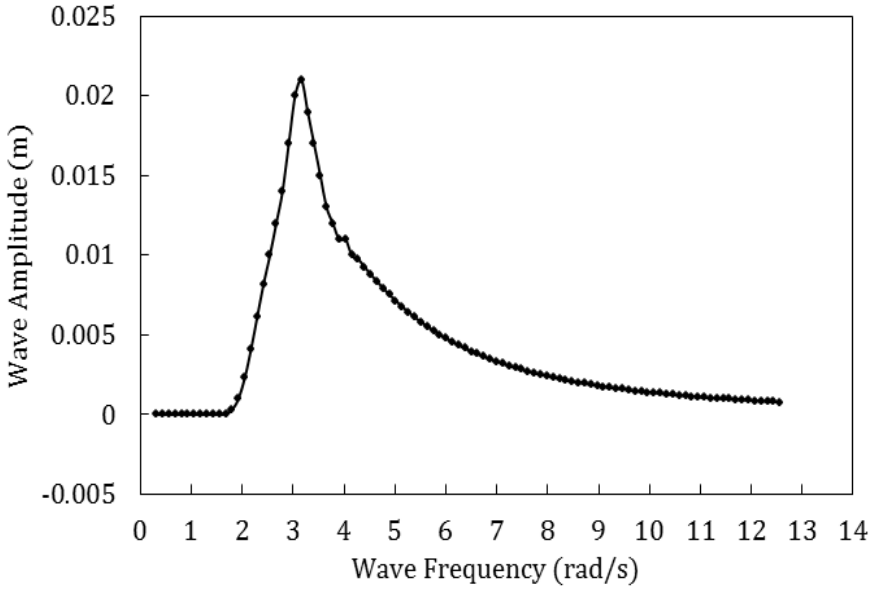

Figure 4.2 Wave amplitude related to each wave frequency component

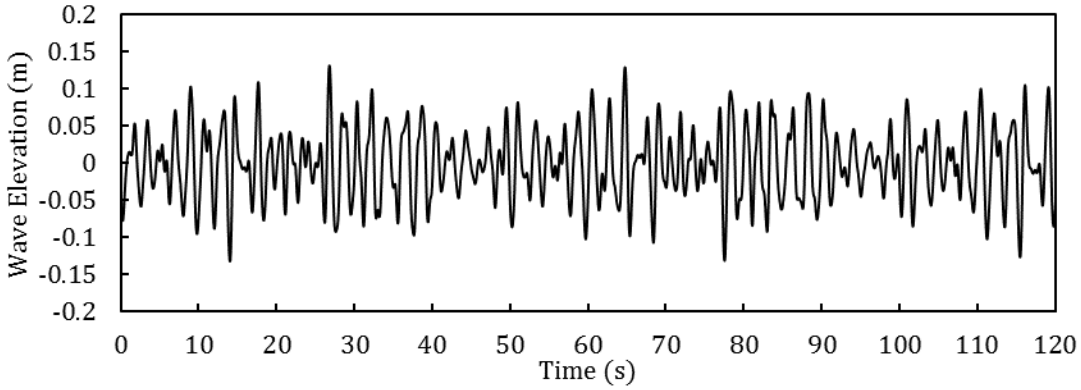

Figure 4.3 Time history of analytical random wave elevation at x=0m

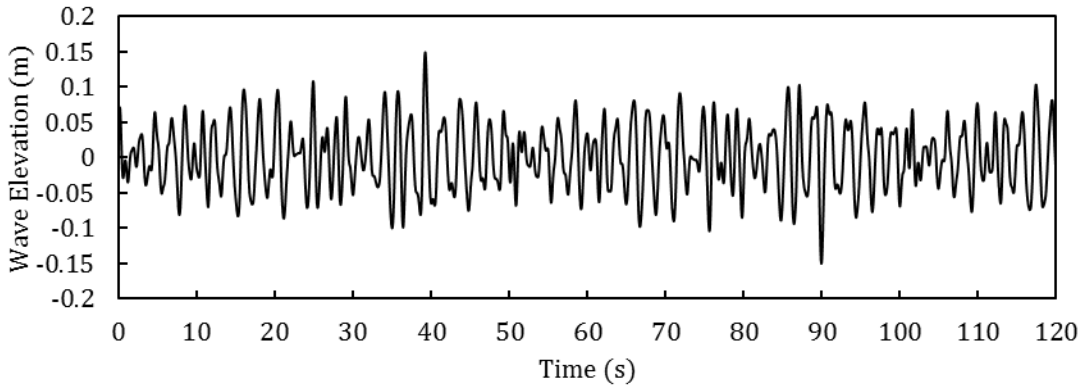

Figure 4.4 Time history of analytical random wave elevation at x=10m

4.3 Freak Wave Modelling Theory

4.3.1 Basic Freak Wave Model

Improving the random wave theory stated above, modulation of the phase angle for each individual wave component can gather the large amount of wave train energy in a fixed position at a fixed moment. The linear sum of individual wave components is assumed to be the most effective method to model freak waves.

Wave number and wave frequency satisfies the wave dispersion relationship as $\omega_i^2 = gk_i tanhk_i d$. The mechanism of 2D wave focusing theory is related to the wave dispersion relationship. Among the wave components, short waves with small velocities travel in front of the waves with large velocities at the initial time. During the wave propagation, large waves will overtake the short waves. Adjusting the random phase angles can superpose all the waves at a fixed time and in a fixed position. At the same time, the wave energy will gather theoretically. The wave peaks superposition in a fixed time and position can be represented mathematically as:

$$\cos(k_i x - \omega_i t + \tau_i) = 1 \tag{4.3.1}$$

The phase angle of i^{th} wave component can be expressed as

$$\tau_i = k_i x - \omega_i t - 2\pi m, m = 0,1,2, \ldots \tag{4.3.2}$$

Then, contriving the phases, the wave elevation of the freak event at focused position x_c and focused time t_c is given by:

$$\eta(x,t) = \sum_{i=1}^{M} a_i * cos(k_i(x - xc) + \omega_i(t - t_c)) \tag{4.3.3}$$

The above freak wave modelling formula is considered the most basic model method which assumes that all the wave components in the wave train gather together in the focused position and time. The freak wave is generated from the same wave spectrum and relative parameters as used in random wave modelling. Significant wave height is $H_s = 0.1\text{m}$ and peak wave period is $T_p =$

2s. The total simulating time is $30T_p$. The time interval during the simulation is 0.05s and the total number of discrete points in the irregular wave train is 1200. The wave frequency range is from $f_{min} = 0.1f_p$ to $f_{max} = 4f_p$. Based on the wave theory stated above, the complicated freak wave train profile is composed of 100 small amplitude waves and the predetermined focused position and focused time are $x_c = 0$m and $t_c = 40$m. The analytical focused wave elevation profile is shown in Figure 4.5.

At the focused point, all waves are combined at time $t = t_c$ and the water surface looks like a single large wave with a high wave amplitude given by $\eta(x_c, t_c) = \sum a_i$. The water surface is quiescent before the focal time, and after the large single transient wave passes, the water free surface becomes quiescent again. During the wave propagation period at the focal place and time, the situation of the transient wave only emerging but without a random background surface is unrealistic.

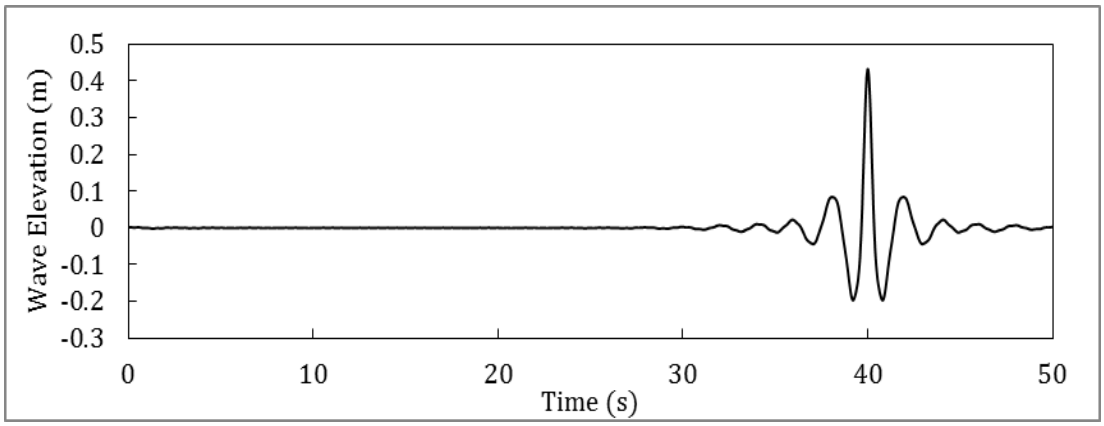

Figure 4.5 Time series of analytical wave elevation at the focused point

Today, there is still no exact definition of a freak wave event. But it is known that the rare freak waves follow the Rayleigh probability distribution of wave heights. The Rayleigh distribution is based on the superposition of linear wave components and reveals that the most probable maximum wave height in a random sea H_{MAX} is related to the significant wave height H_s given by:

$$\frac{H_{MAX}}{H_s} = 0.707\sqrt{lnM} \tag{4.3.4}$$

Normally, the definition of a freak wave is a large wave whose ratio maximum wave height by significant wave height is a factor in a range of (2-2.2). In the linear approximation, the random wave field can be regarded as a Gaussian process. Under the Gaussian process assumption, a mathematical definition of a freak wave can be considered as $H_{max} \geq 2.0H_s$. Considering the nonlinearities in the process, a refined definition is to increase the limit of the freak wave height to $H_{max} \geq 2.2H_s$. In this paper, the ratio $H_{max} \geq 2.2H_s$ and $A_{max} \geq 1.1H_s$ are considered as the definition of a freak wave event.

In the freak wave model, the ratio $H_{max}/H_s = 3.15$ which is much more than the definition in Chapter 2.2. Further, the water surface derived from this freak wave model is quiescent before and after the focused time, which is unrealistic.

4.3.2 Efficient Freak Wave Model

4.3.2.1 Combining Wave Models

The generation of a more realistic freak wave event is also based on the same superposition technique introduced above. However, the total wave energy is not only used for the freak wave generation, but also a portion of wave energy used to generate the surrounding waves.

4.3.2.1.1 Combining Wave Model One: Random Wave + Transient Wave

The first combination wave model is stated by Kriebel and Alsina (2000), who did a real wave tank experimented by splitting the wave spectrum into two parts to model a real freak wave. The first part is used to model surrounding random waves and the other one is for transient extreme waves. The mathematical method specifies the relative percentage of the total wave energy at each frequency, which will go to each part. P_r is the percentage of energy which denotes the random waves, and P_t is the corresponding percentage contributing to the transient wave. These two parameters are related as $P_r + P_t = 1$.

When the spectrum energy percentage is chosen, the free surface is obtained by combining random wave profiles and transient wave profiles by:

$$\eta(x,t) = \sum_{i=1}^{N} a_{ri} * cos(k_i x - \omega_i t + \tau_i) + \sum_{i=1}^{N} a_{ti} * cos(k_i(x - x_c) + \omega_i(t - t_c)) \quad (4.3.5)$$

In the above formula, the phase angles for the transient parts are zero and the phase angle values are selected randomly between 0 and 2π to generate the random waves. The wave amplitudes for the random and transient wave parts are represented as:

$$a_{ri} = \sqrt{2 * P_r * s(\omega_i) * \Delta\omega}$$

$$a_{ti} = \sqrt{2 * P_t * s(\omega_i) * \Delta\omega} \quad (4.3.6)$$

The percentages of spectrum energy for random and transient waves P_r and P_t are two values from 0% to 100%. For the situation $P_r = 0\%$, all wave energy will contribute to the transient wave generation and there will be no surrounding background waves. Further, for the situation $P_r = 100\%$, all wave energy will contribute to the random wave modelling and wave height will not exceed the freak height definition. The target for this part is to determine the percentage of energy for each part to achieve the freak wave which can represent a more realistic sea state.

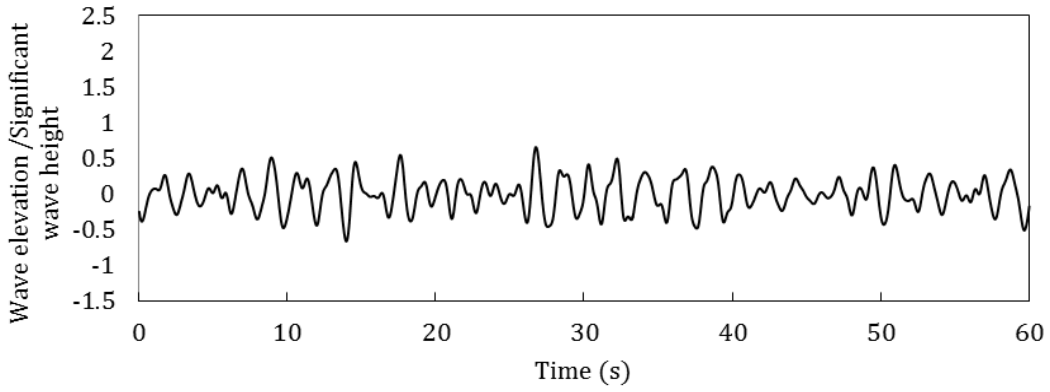

Figure 4.6 Time history of analytical wave elevation at the focused point when $P_t = 0\%$

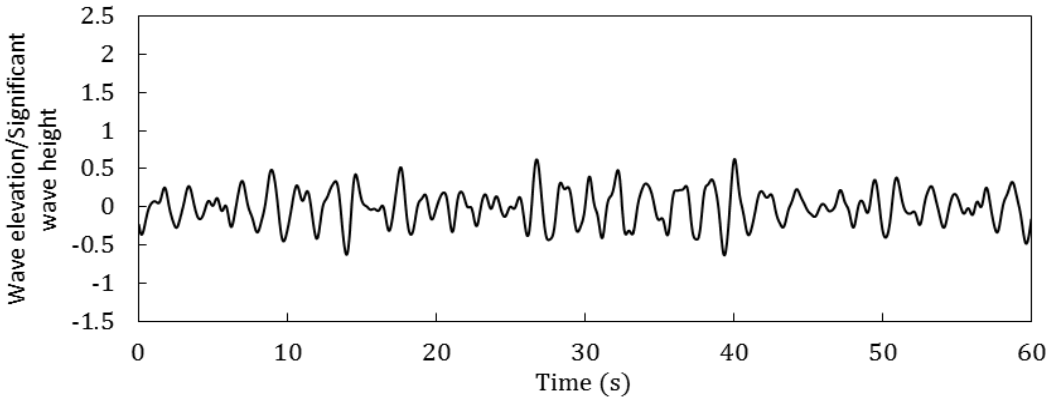

Figure 4.7 Time history of analytical wave elevation at the focused point when Pt= 10%

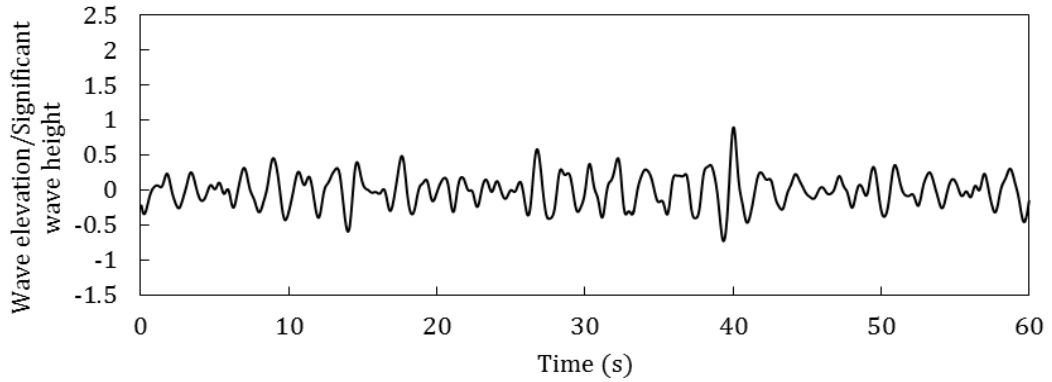

Figure 4.8 Time history of analytical wave elevation at the focused point when Pt= 20%

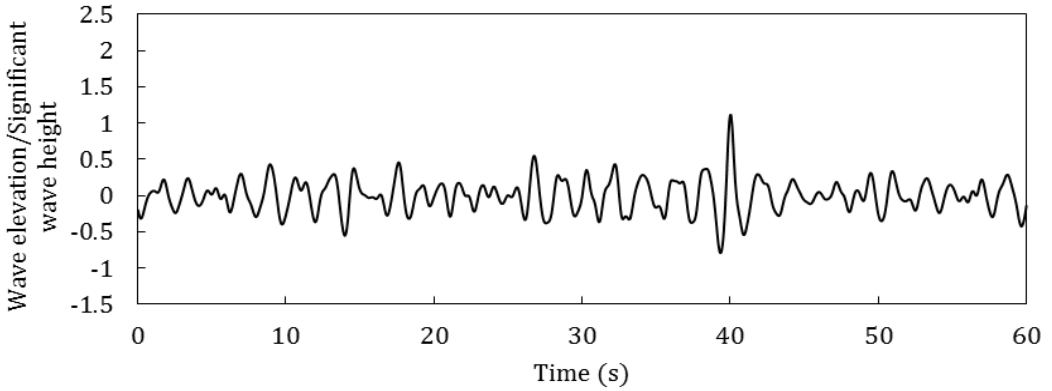

Figure 4.9 Time history of analytical wave elevation at the focused point when Pt= 30%

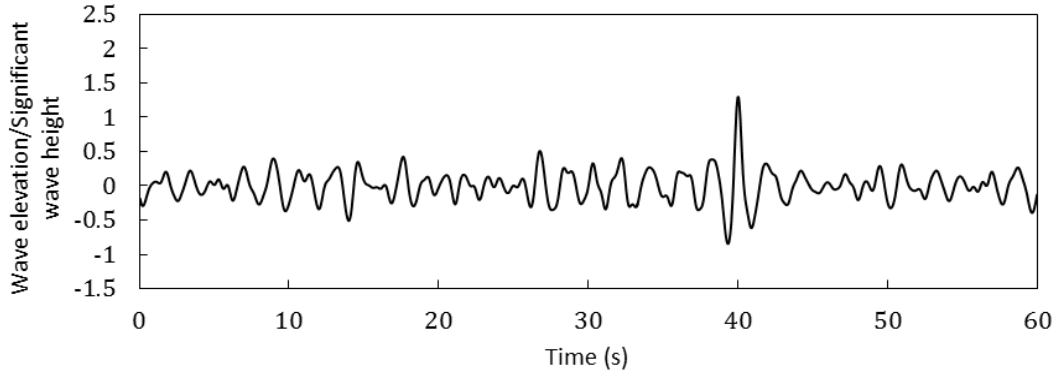

Figure 4.10 Time history of analytical wave elevation at the focused point when Pt= 40%

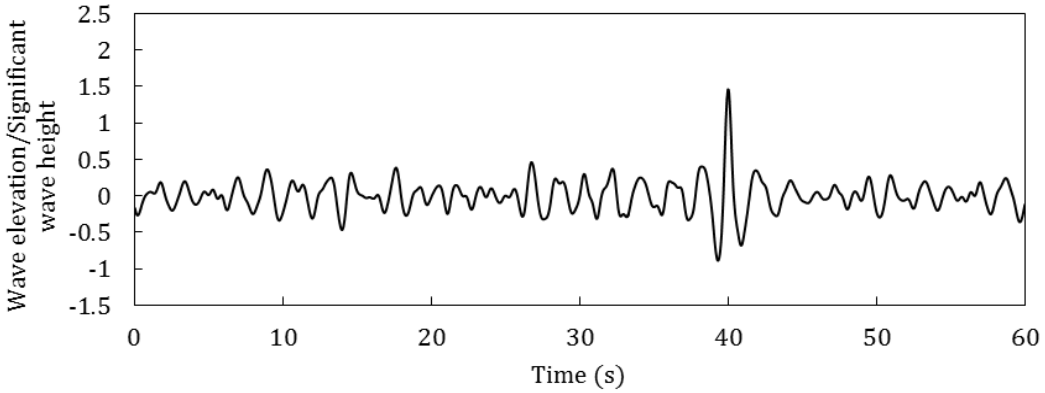

Figure 4.11 Time history of analytical wave elevation at the focused point when Pt= 50%

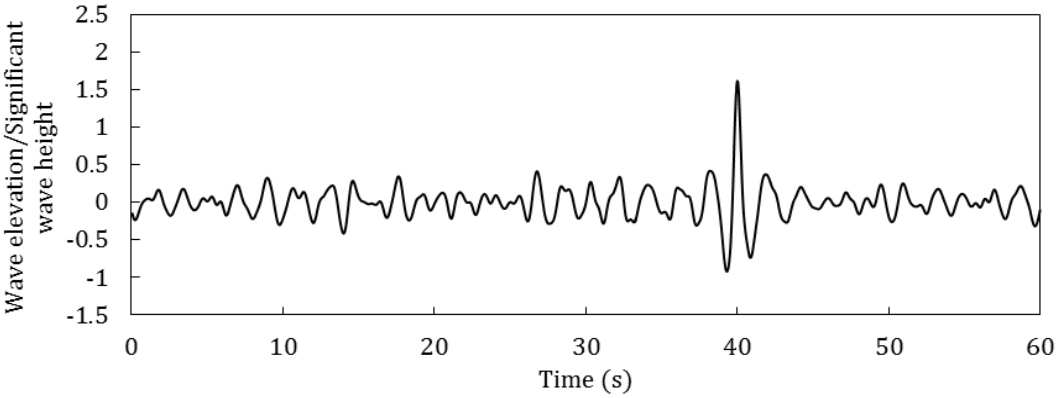

Figure 4.12 Time history of analytical wave elevation at the focused point when Pt= 60%

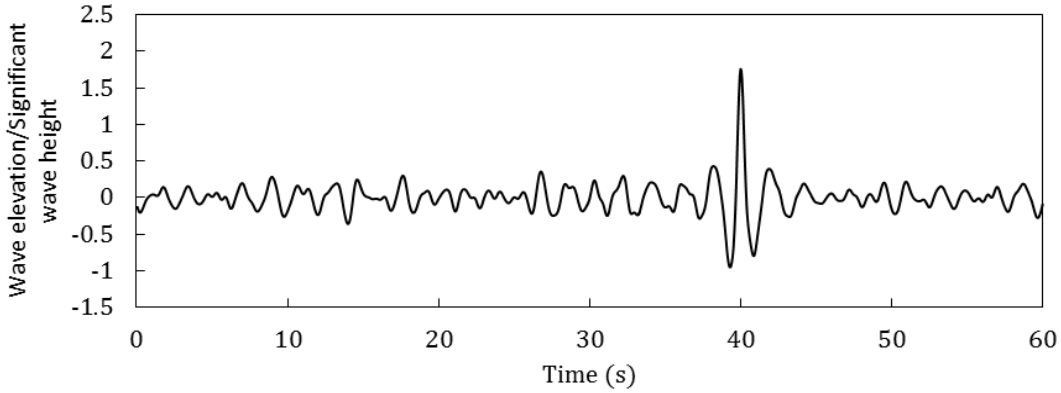

Figure 4.13 Time history of analytical wave elevation at the focused point when Pt= 70%

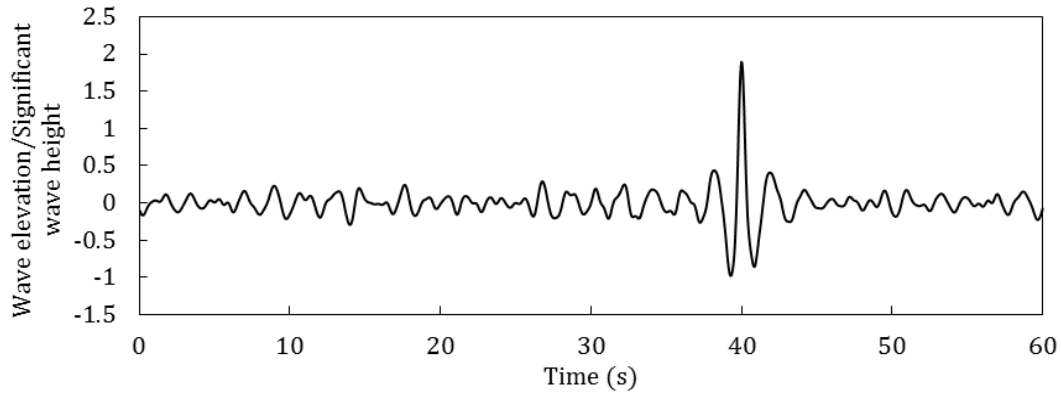

Figure 4.14 Time history of analytical wave elevation at the focused point when Pt= 80%

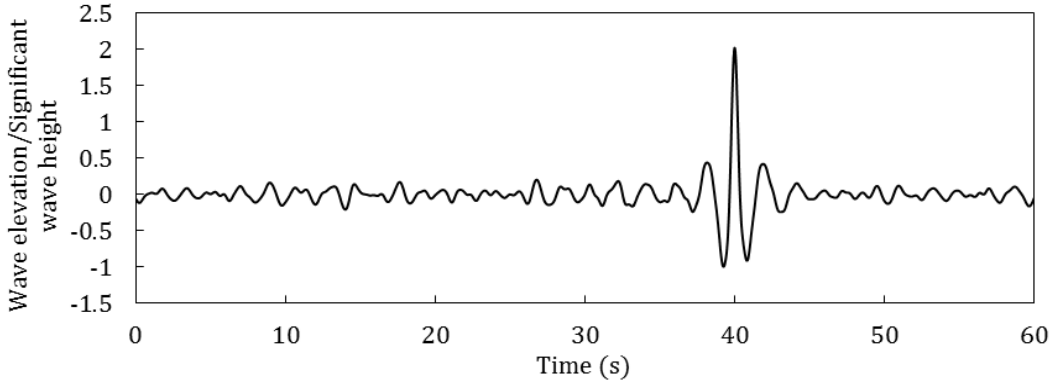

Figure 4.15 Time history of analytical wave elevation at the focused point when Pt= 90%

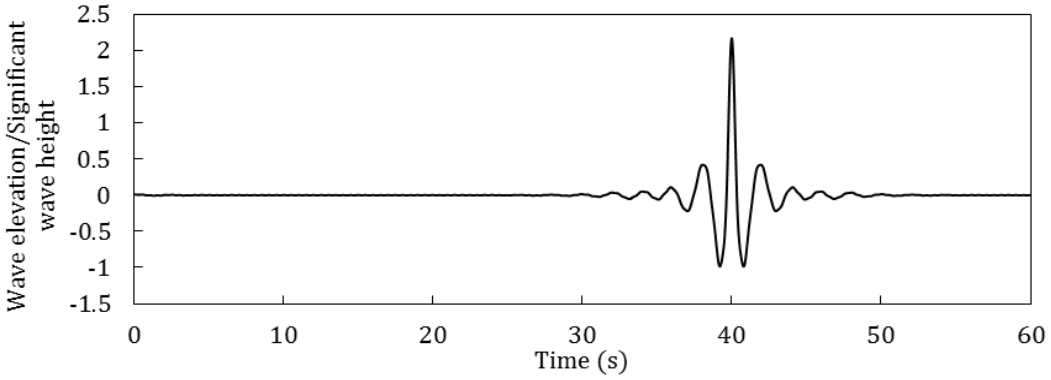

Figure 4.16 Time history of analytical wave elevation at the focused point when Pt= 100%

The analytical results illustrated from Figure 4.6 to Figure 4.16 show how the wave elevation is transferred from realistic random sea states to an unrealistic sea state with the increase of P_t from 0% to 100% with an interval of 10%. The sea state seems much more unrealistic when P_t exceeds 40%. At that time, the maximum wave height by significant wave height ratio is larger than 2.2.

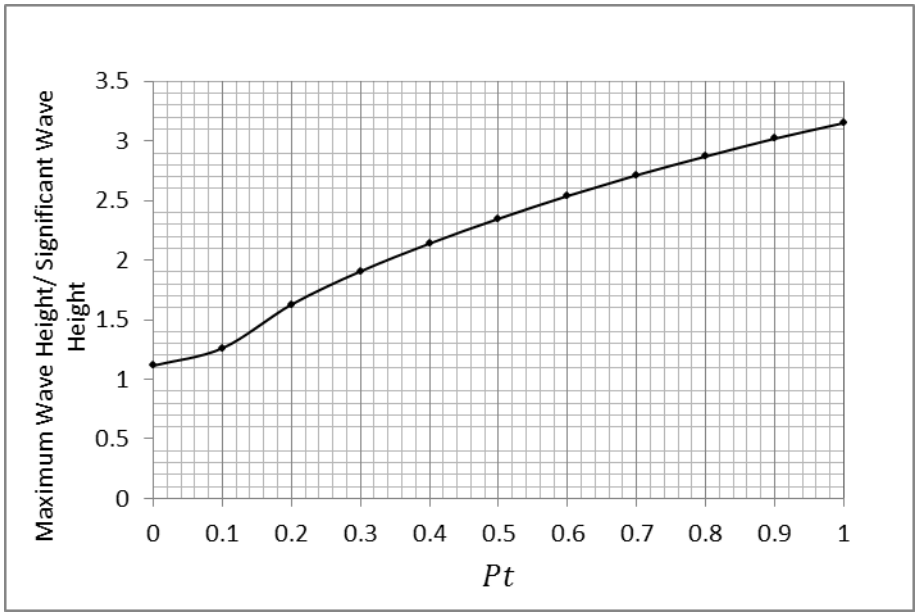

Figure 4.17 The ratio H_{max}/H_s with different energy percentage P_t

The ratio H_{max}/H_s at different transient wave energy percentage P_t is shown in Figure 4.17. For the case $P_t = 0$, all the wave energy goes into the random wave modelling and no wave energy is used for the freak wave generation. However,

for the case $P_t = 1$, the entire wave energy goes into the freak part simulation. With the increase of P_t, the ratio H_{max}/H_s grows from 1.115 to 3.151. When $P_t < 0.2$, the random sea dominates the sea state as the ratio maximum wave height by significant wave height is smaller than 1.627. However, when P_t is larger than 0.5, the focused transient wave dominates the entire sea state and the ratio H_{max}/H_s is 2.348. When the transient focused percentage P_t is 0.4, the maximum wave height and significant wave height ratio is 2.139, which is adjusted to the freak wave definition.

4.3.2.1.2 Combining Wave Model Two: Regular Wave + Transient Wave

Differing from the above combination model, the second efficient focused wave modelling method is a combination of transient focused wave and a regular wave to generate a realistic freak wave sea state. The model specifies the relative percentage of the total wave spectrum energy at each frequency, which will go to each part. P_a is the percentage of energy which denotes the regular wave and P_t is the corresponding percentage contributing to the transient waves. These two parameters are related as $P_a + P_t = 1$. Once the percentages are selected, the wave free surface is obtained by adding a regular wave profile to the transient wave series as such:

$$\eta(x,t) = P_a a_p \cos\big(k_p(x - x_c) - \omega_p(t - t_c)\big) + P_t \sum_{i=1}^{N} a_i * \cos(k_i(x - x_c) + \omega_i(t - t_c)) \tag{4.3.7}$$

For the random wave modelling part, the wave amplitude for each frequency component is $a_i = \sqrt{2 * P_t * s(\omega_i) * \Delta\omega}$ and $\Delta\omega$ is the uniform spacing between frequencies. For the regular wave part, the wave amplitude a_p is half the significant wave height, which is $H_s/2$. The wave number and wave frequency are calculated from the spectrum peak period $T_p = 2$s.

The percentages of spectrum energy for regular and transient waves P_a and P_t are two values from 0% to 100%. For the situation $P_a = 0\%$, all wave energy will contribute to the transient wave generation and there will be no

surrounding background regular waves. Further, for the situation $P_a = 100\%$, all wave energy will contribute to the regular wave modelling. The modelling result would be a regular wave train, but there is no obvious transient focused wave. The time series of analytical wave elevations are shown from Figure 4.18 to Figure 4.28, and the mathematical water free surface elevation is normalized by the significant wave height in these figures.

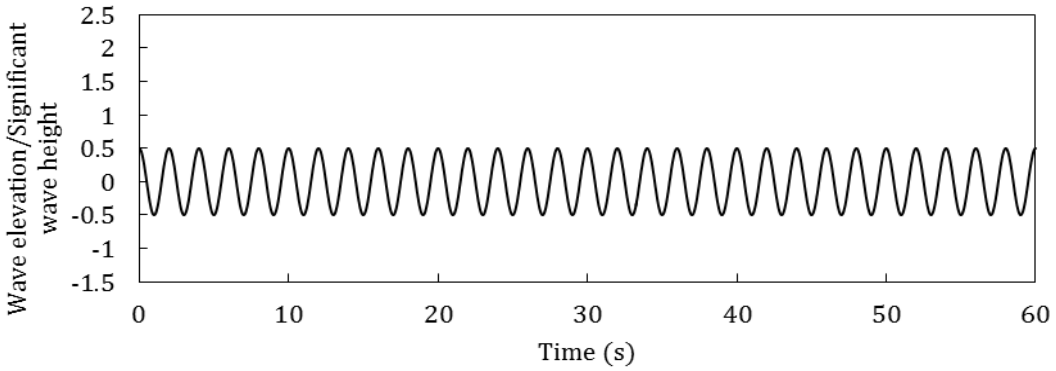

Figure 4.18 Time history of analytical wave elevation at the focused point when Pt= 0%

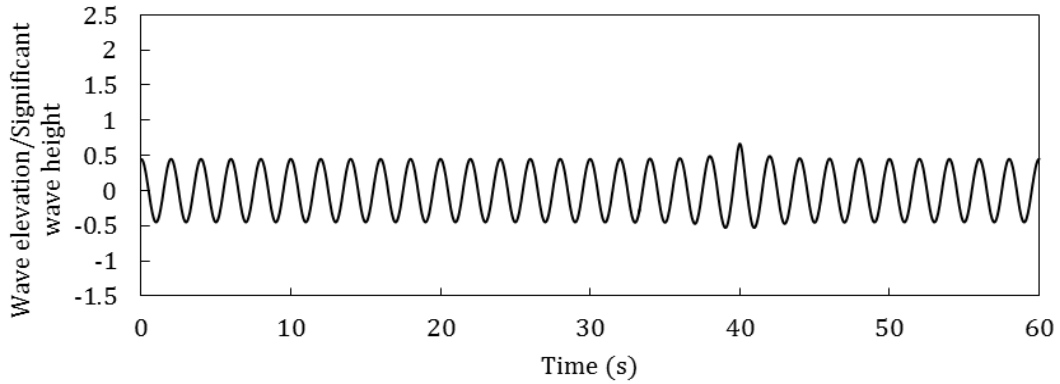

Figure 4.19 Time history of analytical wave elevation at the focused point when Pt= 10%

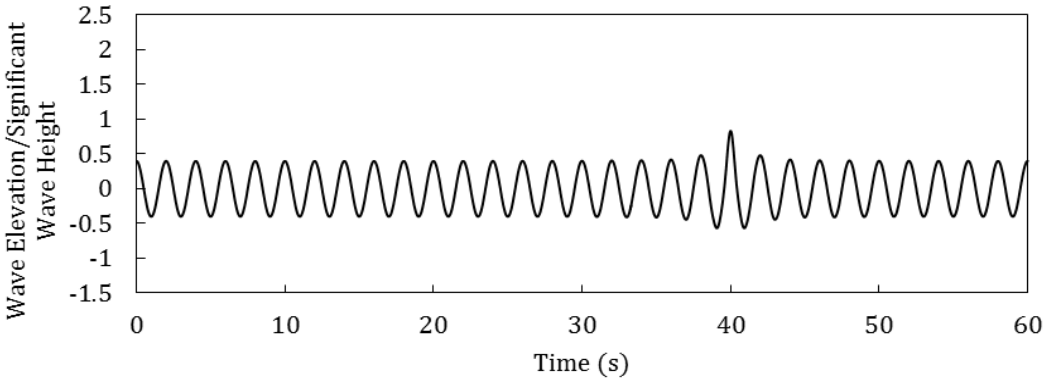

Figure 4.20 Time history of analytical wave elevation at the focused point when Pt= 20%

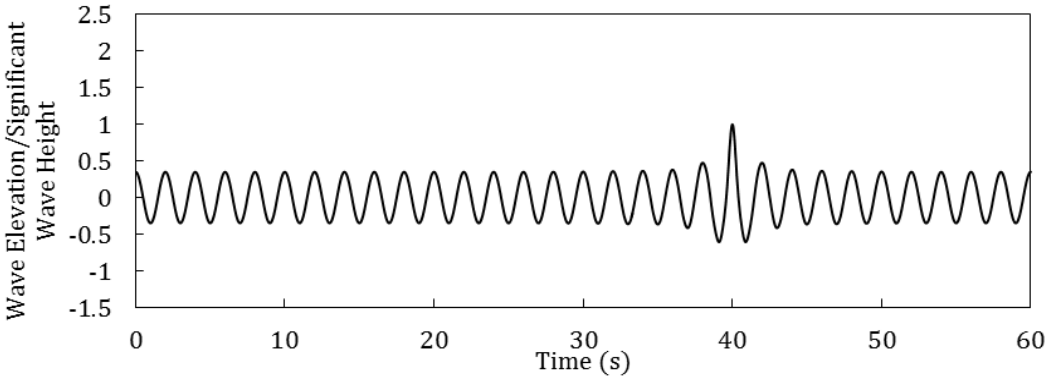

Figure 4.21 Time history of analytical wave elevation at the focused point when Pt= 30%

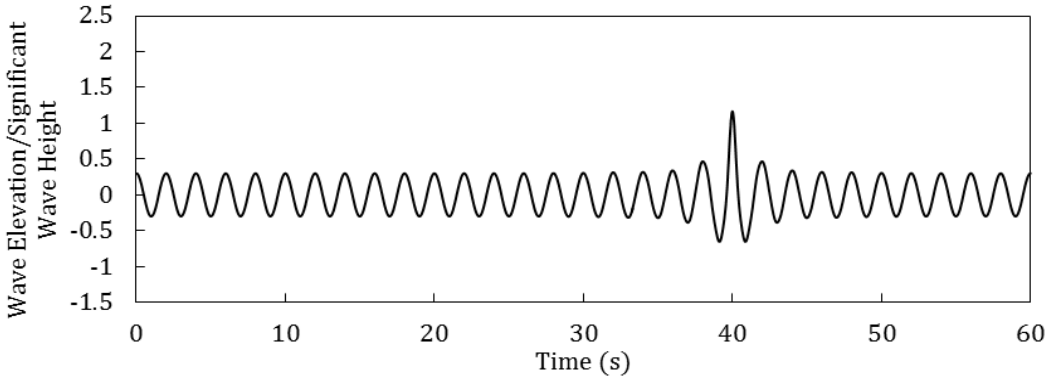

Figure 4.22 Time history of analytical wave elevation at the focused point when Pt= 40%

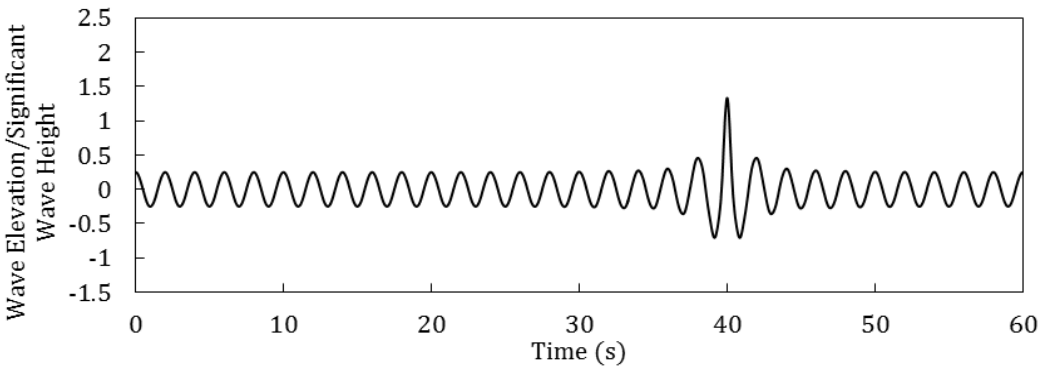

Figure 4.23 Time history of analytical wave elevation at the focused point when Pt= 50%

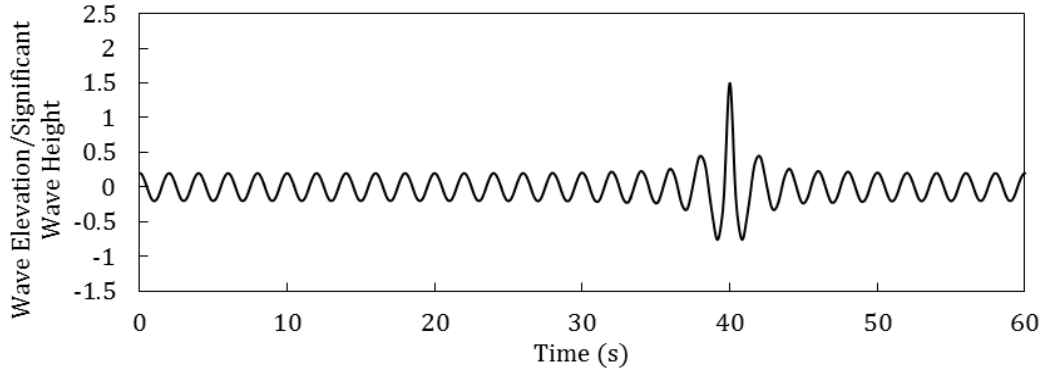

Figure 4.24 Time history of analytical wave elevation at the focused point when Pt= 60%

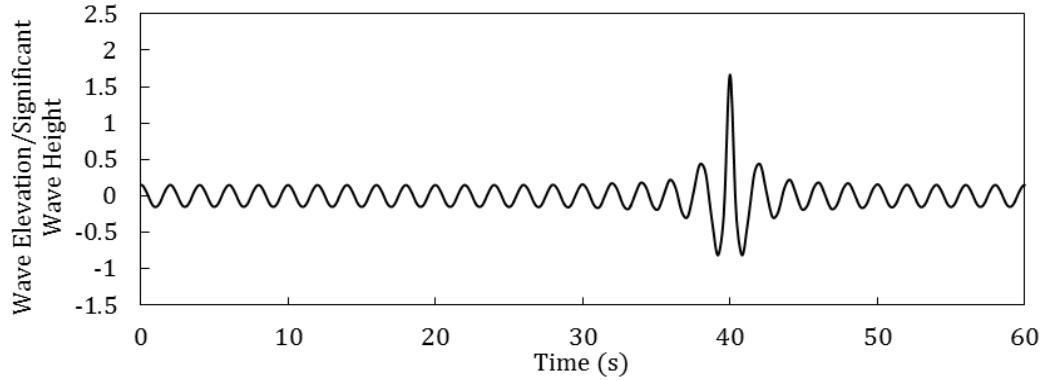

Figure 4.25 Time history of analytical wave elevation at the focused point when Pt= 70%

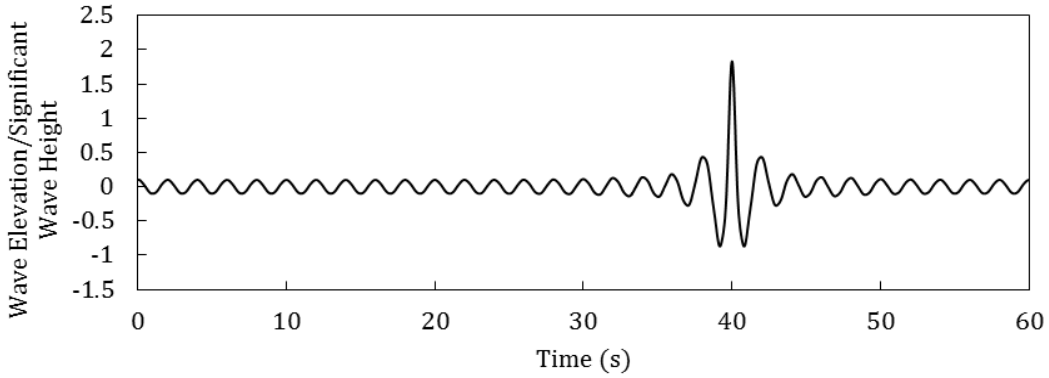

Figure 4.26 Time history of analytical wave elevation at the focused point when Pt= 80%

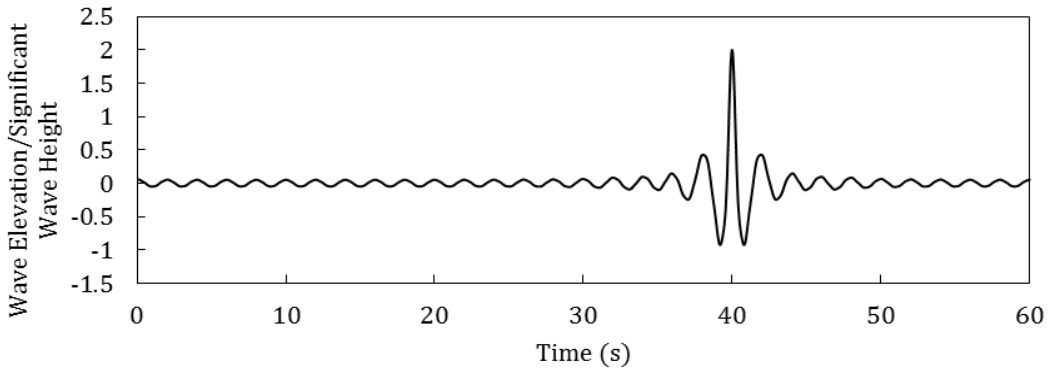

Figure 4.27 Time history of analytical wave elevation at the focused point when Pt= 90%

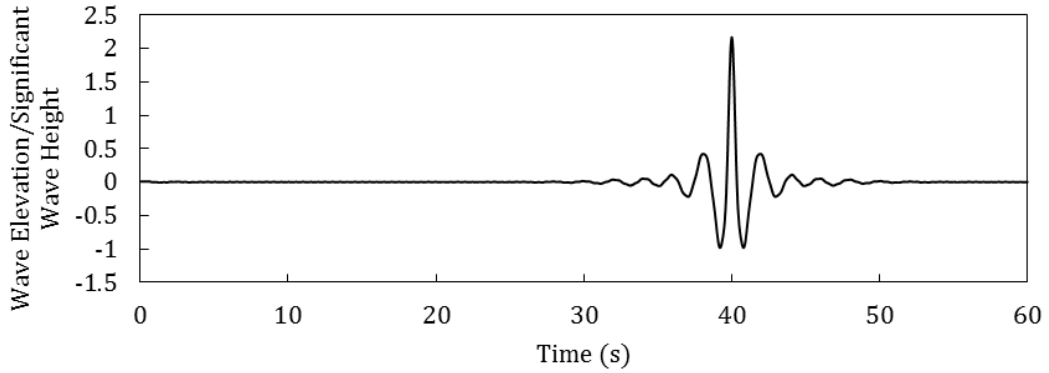

Figure 4.28 Time history of analytical wave elevation at the focused point when Pt= 100%

The ratios of maximum wave height by significant wave height H_{max}/H_s are shown in Figure 4.29 by different wave spectrum energy percentage distributions. In the case $P_t = 0$, the entire wave spectrum energy contributes to the regular wave modelling, while in the case $P_t = 100\%$, the wave free surface reduces to the total focused wave modelling. The statistical value (H_{max}/H_s) increases with the growth of P_t. When the random percentage $P_t = 0.6$, the freak wave train is generated with a maximum wave height equalling to $2.258H_s$ and this satisfies freak wave event definition $H_{max} = 2.2H_s$.

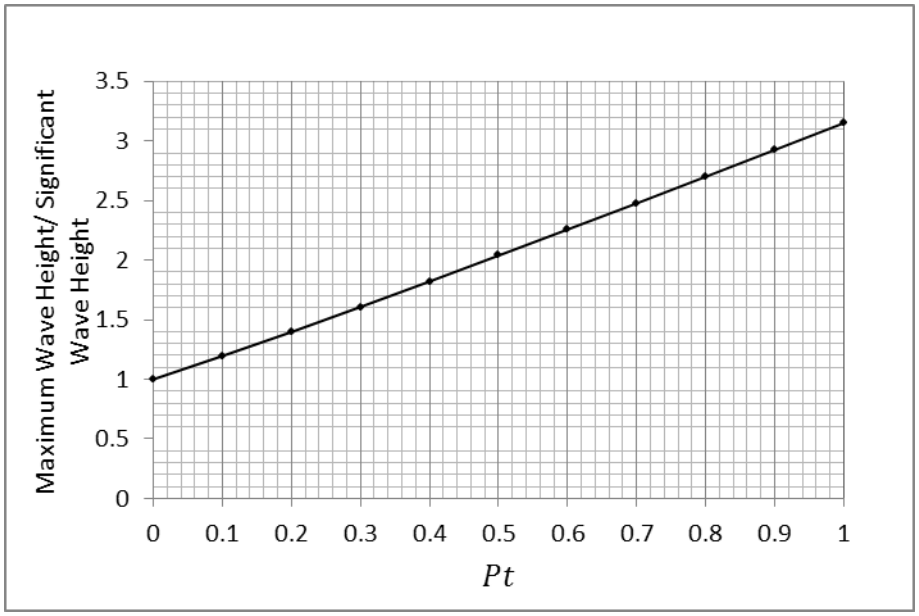

Figure 4.29 The ratio H_{max}/H_s with different energy percentage Pt

4.3.2.2 Focused Wave Models of Initial Phase Adjusting:

Another freak wave modelling method is presented by adjusting the initial phase angle interval. The mathematical model is based on the initial freak wave superposition method and the more realistic sea state is generated by modulation of the initial phase angle interval.

By adjusting the phase angles of different wave components, the wave energy can be gathered in the limited space at a predetermined time. This modulation is based on the choice of initial phase angle. Each wave component of irregular wave train has random phases between 0 and 2π. By reducing the random number interval, the probability of a large amount of energy gathering in a

space at a determined time increases. The wave surface profile is the same as the irregular wave profile:

$$\eta(x,t) = \sum_{i=1}^{N} a_i * cos(k_i(x - x_c) - \omega_i(t - t_c) + \tau_i) \tag{4.3.8}$$

Where the number τ_i is assumed to be a random number in a range of [0, α] and the number α is an interval of [0, 2π]. Figure 4.30 and Figure 4.35 show how the wave elevation is transferred from an unrealistic freak sea state to the realistic sea state as the initial phase interval decreases. Generally, the analytical wave elevation profile is like the random plus transient combination model.

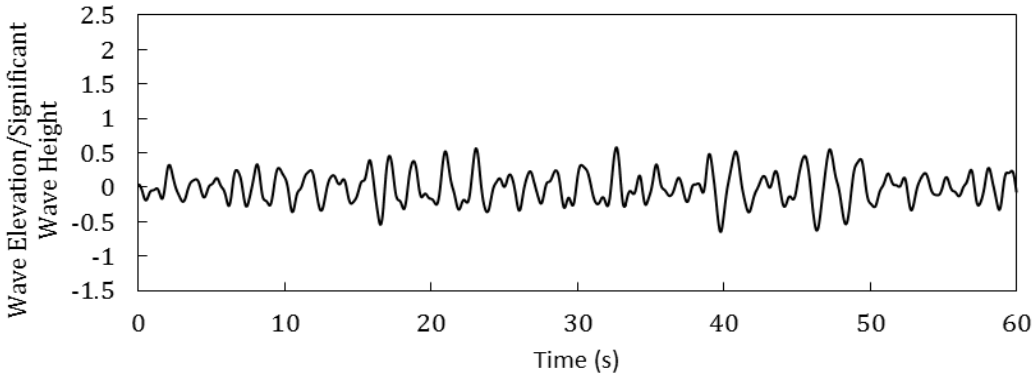

Figure 4.30 Time history of analytical wave elevation at the focused position with α=2π

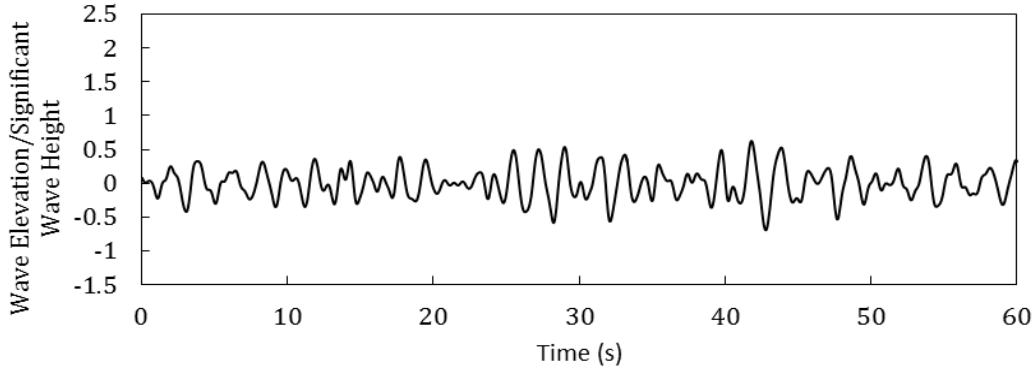

Figure 4.31 Time history of analytical wave elevation at the focused position with α=1.6π

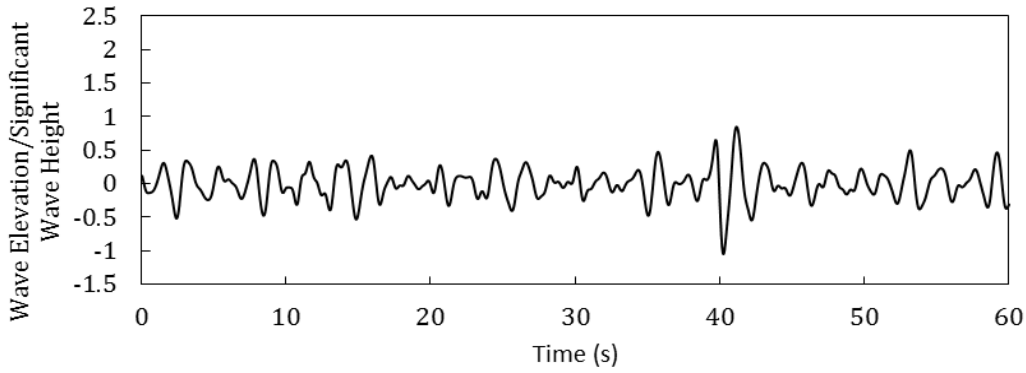

Figure 4.32 Time history of analytical wave elevation at the focused position with $\alpha=1.2\pi$

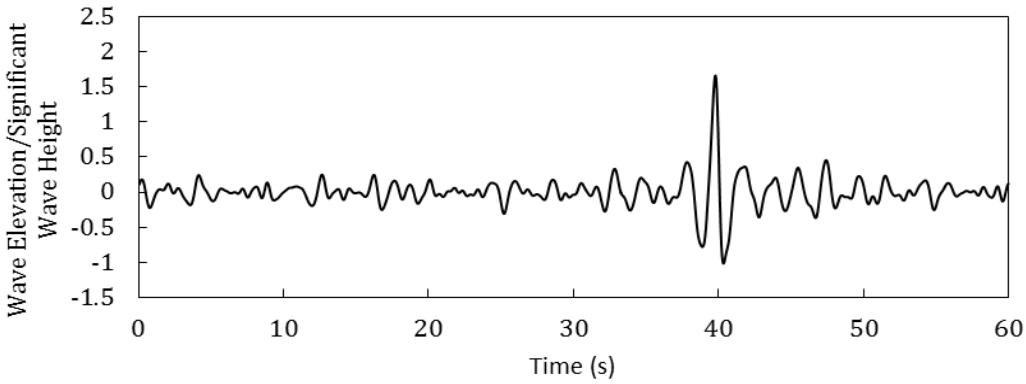

Figure 4.33 Time history of analytical wave elevation at the focused position with $\alpha=0.8\pi$

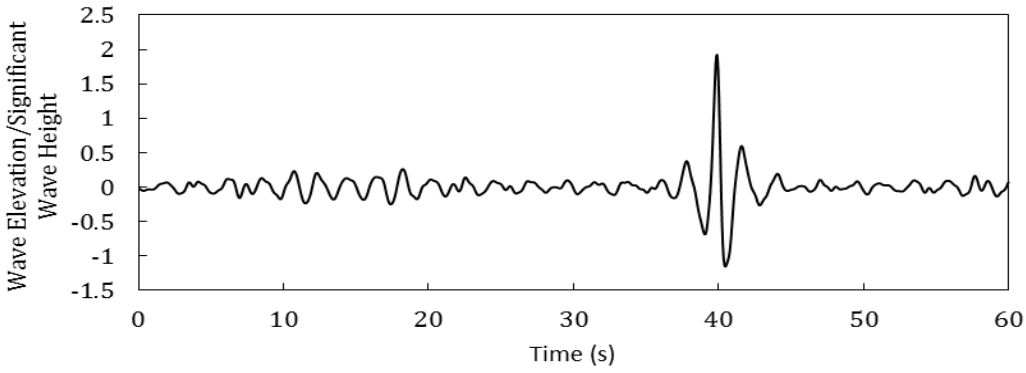

Figure 4.34 Time history of analytical wave elevation at the focused position with $\alpha=0.4\pi$

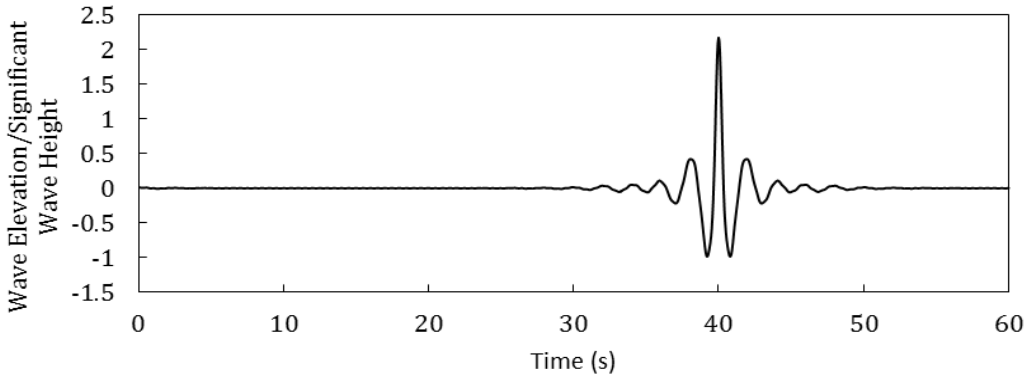

Figure 4.35 Time history of analytical wave elevation at the focused position with α=0π

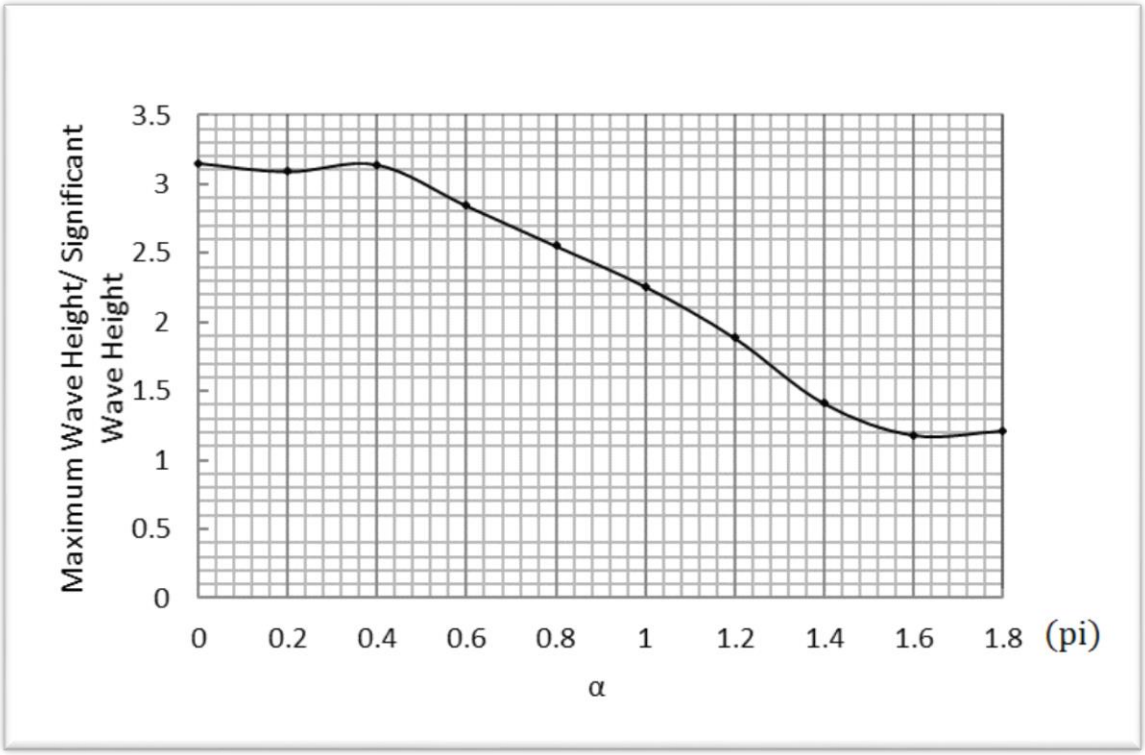

Figure 4.36 Ratio H_{max} /H_s with an interval of 0.2π

Figure 4.36 illustrates the ratio (H_{max}/H_s) of analytical freak waves corresponding to the different initial phase intervals. When $\alpha = 0$, the phase angle belongs to the range of [0, 0] and the freak wave model is the same as the extreme wave model. When $\alpha = 2\pi$, the phase angle belongs to the range of [0, 2π] and the freak wave model is the same as the random wave model. For the cases of $\alpha < 1.2\pi$, the random phases gather together so that the combination of

wave energy can result in the generation of a freak wave. With the increase of the initial phase interval, the ratio (H_{max}/H_s) reduces. In the above figure, when $\alpha = \pi$, the ratio maximum wave height by significant wave height is 2.257, which is slightly larger than $2.2H_s$.

4.4 Freak Wave Numerical Simulation

In this part, a two-dimensional numerical wave tank is established. The source function wave-making method is used to simulate freak wave events computationally. Finally, the numerical results are compared with the analytical ones to discuss the nonlinear characteristics of a freak wave train.

4.4.1 Freak Wave Generation Theory

The generation of linear regular waves by source function wave-making methods has been introduced in Chapter 3.3. The source intensity equation (3.2.23) is not only used for regular wave generation, but is also appropriate for freak wave generation. In theory, proper mass source intensity can generate any target wave. The freak wave free surface, which is focused at x_c and at a moment t_c, has been expressed in Equation (4.3.3). The corresponding freak wave horizontal velocity can be represented as:

$$u(y,t) = \sum_{i=1}^{M} a_i * \omega_i * \frac{coshk_i(y+h)}{sinhk_i h} * \cos\big(k_i(x-xc) - \omega_i(t-tb)\big) \tag{4.4.1}$$

With the source intensity:

$$s_s(y,t) = \frac{2u(x_s,y,t)}{\Delta x} \tag{4.4.2}$$

4.4.2 Input Extreme Wave Conditions

This work contains the freak wave groups from four different frequency bandwidths conditions which are shown in Table 4.1. In each wave group, the wave component number $M = 29$. During the numerical modelling, the individual wave has the same wave amplitude and the wave frequency is uniformly distributed in the frequency range. For each specific frequency range

wave group, there are three different input wave amplitudes to analyse the freak wave breaking conditions. They are 0.09m, 0.18m and 0.36m respectively. Concerning the peak wave number ($k = 1.006$) in the 29 individual wave components, the corresponding freak wave steepness values are 0.02866, 0.05732 and 0.11465 respectively.

Table 4.1 Freak wave modelling input conditions

Case	Frequency range (Hz)	Input Amplitude (m)
A1	0.15-0.85	0.09
A2		0.18
A3		0.36
B1	0.2-0.8	0.09
B2		0.18
B3		0.36
C1	0.25-0.75	0.09
C2		0.18
C3		0.36
D1	0.35-0.65	0.09
D2		0.18
D3		0.36

4.4.3 Geometric Model

The detailed configuration of the numerical wave tank is shown in Figure 4.37. A two-dimensional geometric model is made in Gambit which is Fluent's pre-processing and mesh generation software. The coordinate origin O is located at the left side of the free surface in the numerical tank. The tank is 40m long in total and the length of the dissipation zone is 10m. The wave tank depth is 10m and the height above the free surface is 3m. At x=20m, a major wave probe is set to measure the time series of the wave elevation. An example of meshing

configuration is shown in Figure 4.38. The meshing convergence test is conducted in the following part to select a suitable mesh for the further analysis. As the mass source wave generation method is used in the regular and focused wave simulation in this part, the structured mesh is used to reduce the CFD modelling time. More mesh elements are set near the free surface to capture a smoother wave elevation profile. Along the wave propagation direction, more meshes are set around the main wave measurement position in order to capture the downstream shifting intensity of the focused wave group.

The pressure-based, unsteady solver is used in Fluent. The geo-reconstruct scheme is utilised for reconstructing the free surface. A second-order upwind discretization is used for better accuracy and the Pressure-Implicit with splitting of Operators (PISO) algorithm with a neighbour correction is chosen. A non-iterative time advancing scheme is used as the time-stepping algorithm.

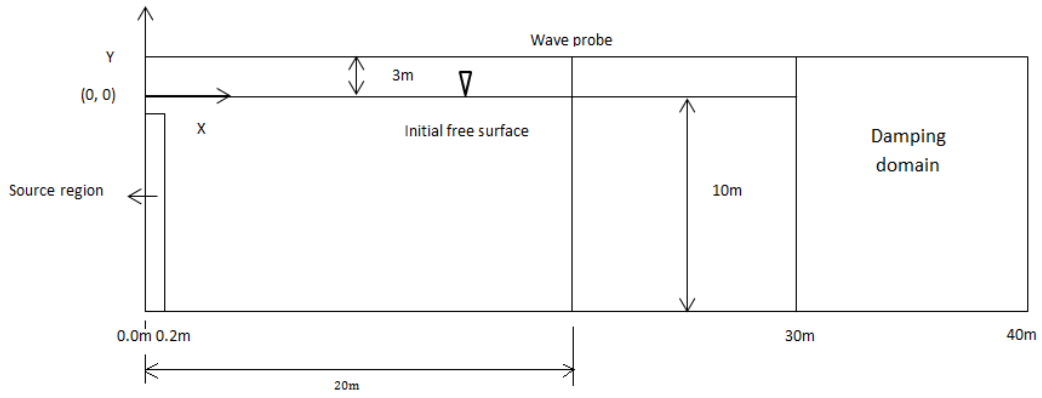

Figure 4.37 Sketch of 2-D numerical wave tank

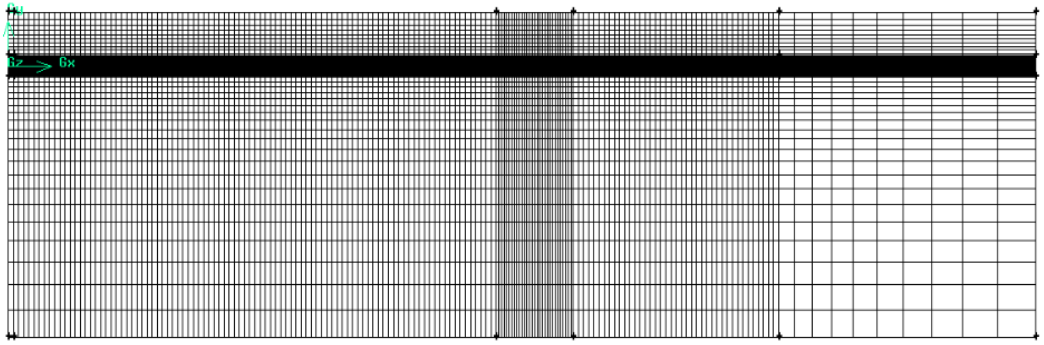

Figure 4.38 Meshing configuration of the computational domain

4.4.4 Results and Analysis

4.4.4.1 Grid Convergence Test

To validate the mesh convergence of the computation domain, three different meshes are used to simulate a regular wave train, which has the same wave amplitude of 0.08m and a wave period of 2s. The mesh details are shown in Table 4.2. The different mesh conditions are only considered in the working domain.

Table 4.2 Mesh conditions for grid convergence test

Mesh	Cell Size in x-direction	Cell number around free surface	Computational time（CPU hours）
Mesh 1	3%λ= 0.28m	20	2h 35min
Mesh 2	2.5%λ= 0.2m	30	3h 42min
Mesh 3	2%λ= 0.12m	40	6h 18min

Figure 4.39 shows the comparisons of time histories of wave elevations measured at x=20m. The regular wave crest is underestimated by Mesh 1. However, the time histories of wave elevation simulated by Mesh 2 and Mesh 3 can achieve a good agreement. The increase of mesh number from Mesh 2 to

Mesh 3 will not change the simulation results significantly, and both regular wave elevations converge to 0.0792m.

In order to capture the wave elevation free surface exactly, a small time-step (1/100 of the wave period) is used over this numerical simulation time. The comparisons of computational CPU hours are shown in Table 4.2. By increasing the cell size in the x-axis direction and the cell number around the free surface, the whole computational time 35s increases from 2 hours and 35 minutes to 6 hours and 18 minutes. The total CPU hours spent in Mesh 3 case is almost 2.5 times larger than the CPU hours spent in Mesh 1 case.

By considering the regular wave elevation convergence results and the computational CPU hours, Mesh 2 is used for further analysis. The 12 different focused wave groups will be simulated in this numerical wave tank.

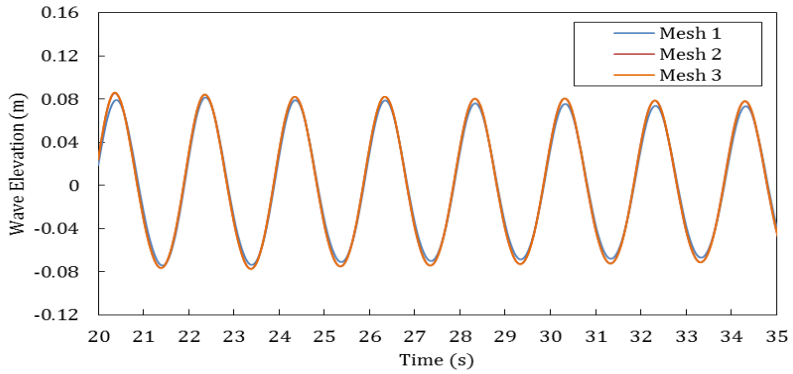

Figure 4.39 Comparisons of regular wave elevation in three mesh conditions

4.4.4.2 Evaluation of a Focused Wave Train

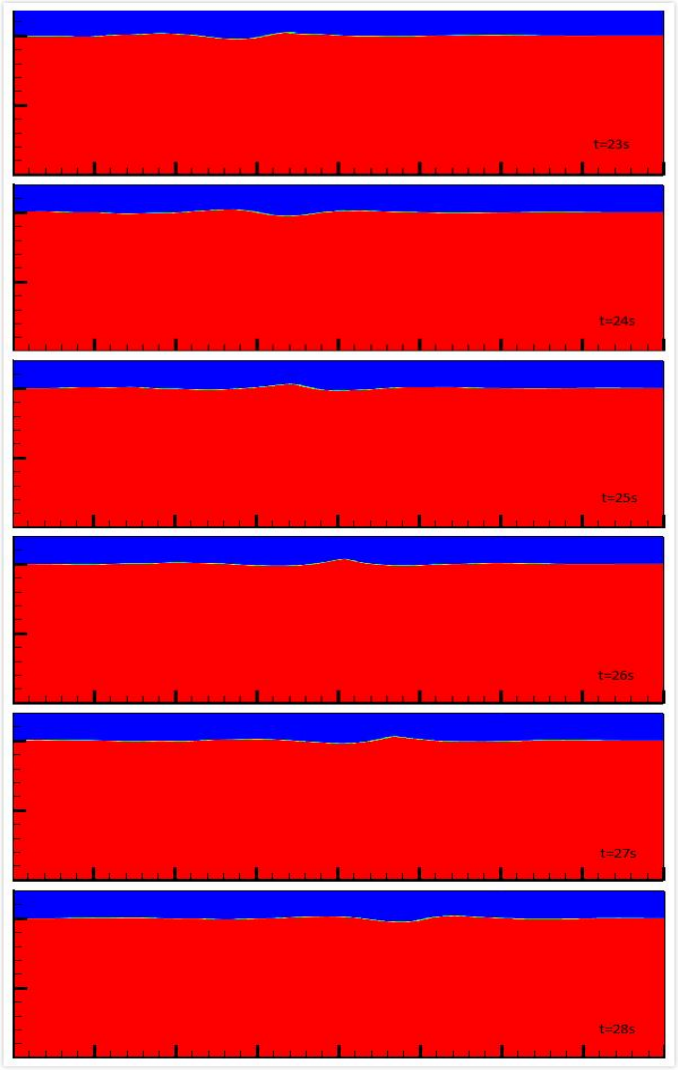

Figure 4.40 Numerical wave tank contours from t=23s to t=28s

The wave contours of the freak wave case D3 are shown in Figure 4.40. Six different moments are selected to illustrate the big wave generation procedure. The contours show that the freak wave train focuses at t=26s when the maximum wave amplitude appears.

The evolution of a freak wave train travelling in a numerical wave tank is shown from Figure 4.41 to Figure 4.48. In these figures, the freak wave case B2 is selected here. The time series of wave surface profiles are shown and measured at eight different wave probes. They are x=5m, x=8m, x=12m, x=18m, x=20m, x=22m, x=24m and x=28m along the wave travelling direction, respectively. It

is found that during the propagation of the 29 waves, the large waves chase up to the small waves in front of the focused position. When all the waves meet in the focal place, a large amplitude wave is generated and the wave energy gathers there. After that moment, the wave amplitude begins to reduce.

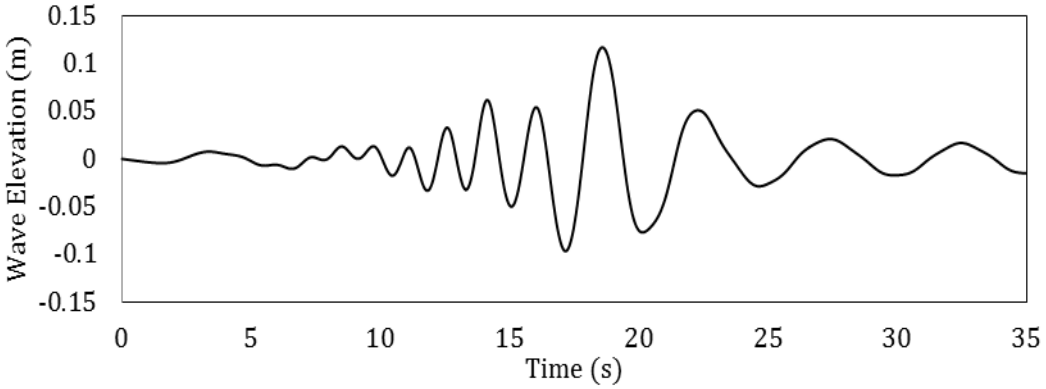

Figure 4.41 Wave elevation measured at x=5m for freak wave case B2

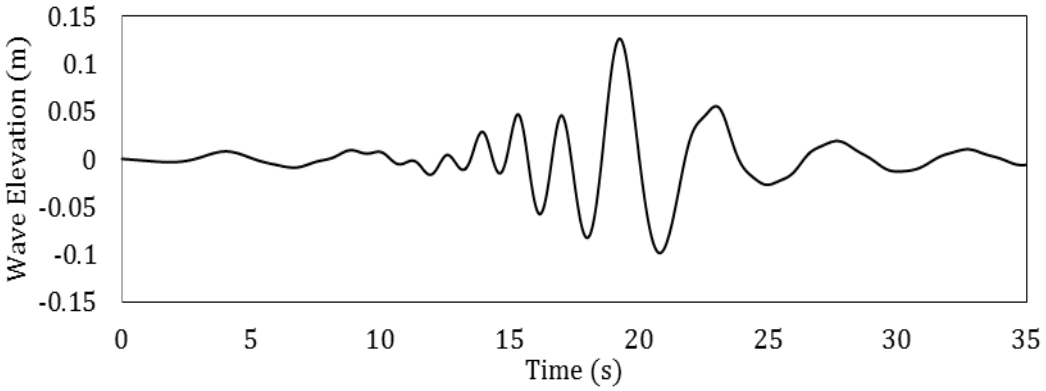

Figure 4.42 Wave elevation measured at x=8m for freak wave case B2

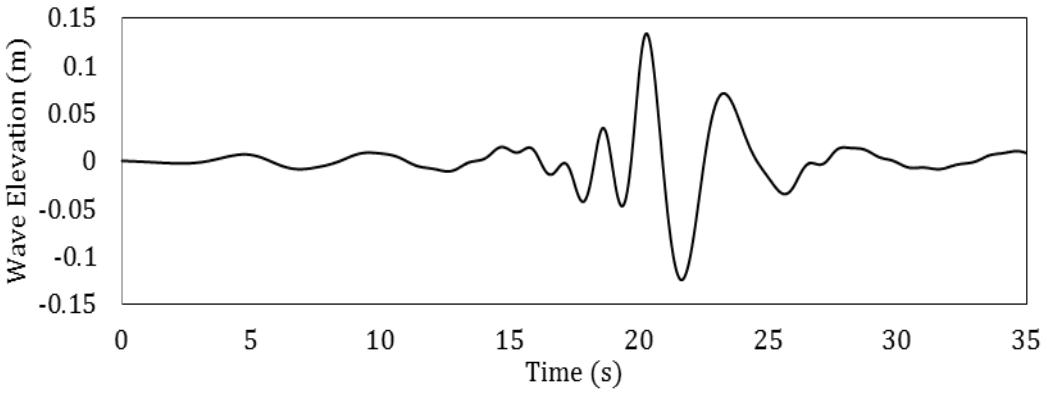

Figure 4.43 Wave elevation measured at x=12m for freak wave case B2

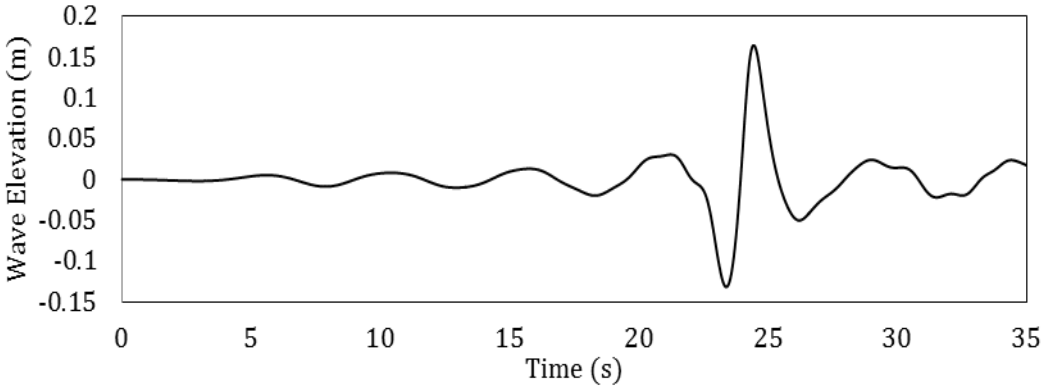

Figure 4.44 Wave elevation measured at x=15m for freak wave case B2

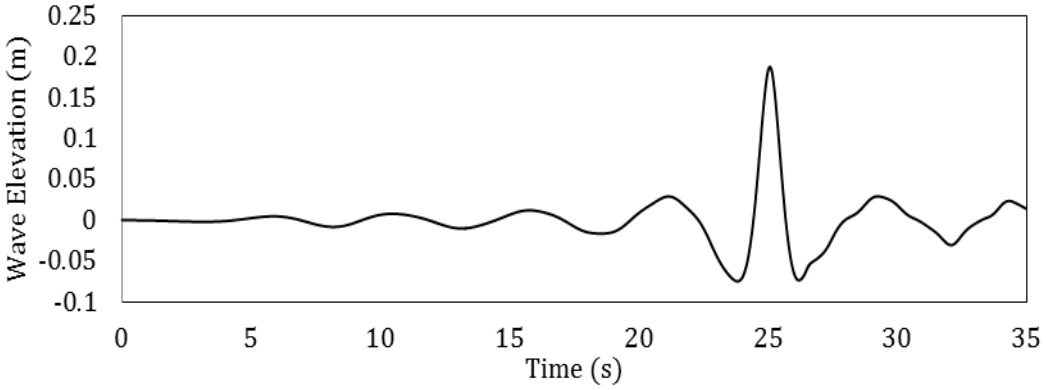

Figure 4.45 Wave elevation measured at x=20m for freak wave case B2

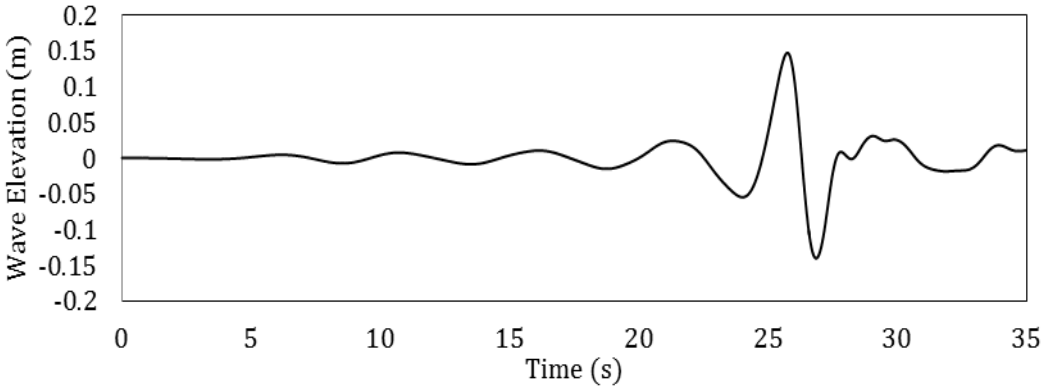

Figure 4.46 Wave elevation measured at x=22m for freak wave case B2

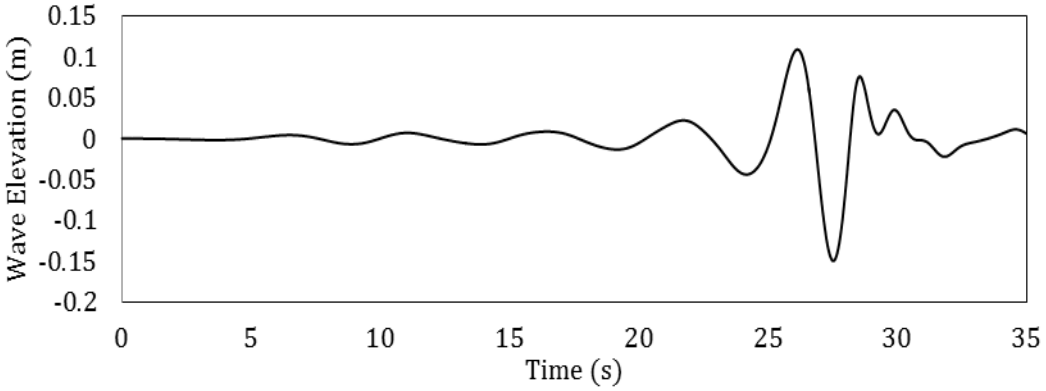

Figure 4.47 Wave elevation measured at x=24m for freak wave case B2

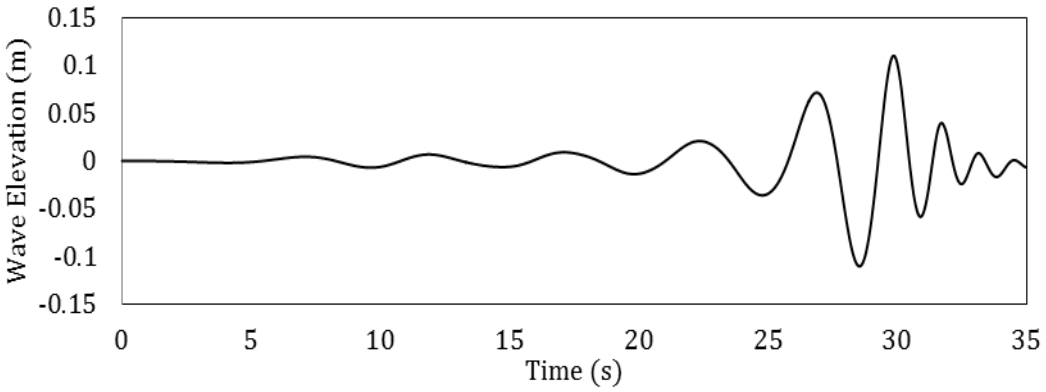

Figure 4.48 Wave elevation measured at x=28m for freak wave case B2

4.4.4.3 Focused Position and Time

As the linear wave theory is used to model the freak wave, the superposition wave theory assumes that all wave components focus at the predetermined focused positon x_c and at the predetermined focal time t_c. However, the ignorance of wave-wave nonlinear interaction can result in the shifting of the real focal position and the corresponding focal time. The real focal position and focal time should be measured before further analysis.

Baldock et al. (1996) conducted experimental research to analyse the nonlinear characteristics of a focused wave group and his results showed that the intensity of shifting ability was closely related to the wave group frequency bandwidth and the input amplitude. In the present work, the real focal position and the corresponding focused time are measured for all the 12 different cases. How the frequency bandwidth and input amplitude affect the focal positon

shifting intensity will be compared and discussed. In order to make the measurements, several wave gauges are set around the predetermined focal position to calculate the time histories of wave elevation with the same distance interval of 0.1m in the x-axis. The real focal position is determined by comparing the simulated data when the maximum wave elevation appears.

Figure 4.49 and Figure 4.50 show the results of the CFD modelling real focal position and focal time for the 12 different cases. From the simulation results, it is found that the extreme wave train focused position and the corresponding focused time are related to the nonlinear behaviour of wave-wave interaction in the wave group.

For any three cases with the same frequency bandwidths, the downstream shifting of focal position and focal time grows with the increase of the input wave freak amplitude, as an increase of input amplitude results in a growth of freak wave nonlinear behaviour. Although the focal position and focal time shifting trend are the same in case A, B, C and D, the shifting intensities are different.

The nonlinear behaviour for a freak wave group is not only related to the input amplitude, but the frequency range for a wave group is one other important parameter to consider. For the small input amplitude cases A1, B1, C1 and D1, due to the nonlinear characteristics of the wave group not being obvious, the frequency bandwidth does not noticeably affect the focal position. However, for cases A3, B3, C3 and D3, the frequency bandwidth affects the wave group nonlinear behaviour dramatically. For case A3, the frequency range is from 0.15Hz to 0.85Hz, and the real wave group focal position downstream shifts 0.6m to the position x=20.6m. For case D3 with same input amplitude of 0.36m, the frequency difference is 0.3Hz ranging from 0.35Hz to 0.65Hz and the corresponding wave length is from 3.695m to 12.745m. The frequency range reduction increases the wave group nonlinear behaviour and the wave group focal position is downstream, shifting 6 meters from the predetermined positon x=20m to x=26m. The data provided in Figure 4.49 and Figure 4.50 show that the position and timing of a focusing event is dependent upon the nonlinearity

of the wave group. In each case, the wave focusing position and focusing time increases with a growth of input amplitude and decrease of frequency range.

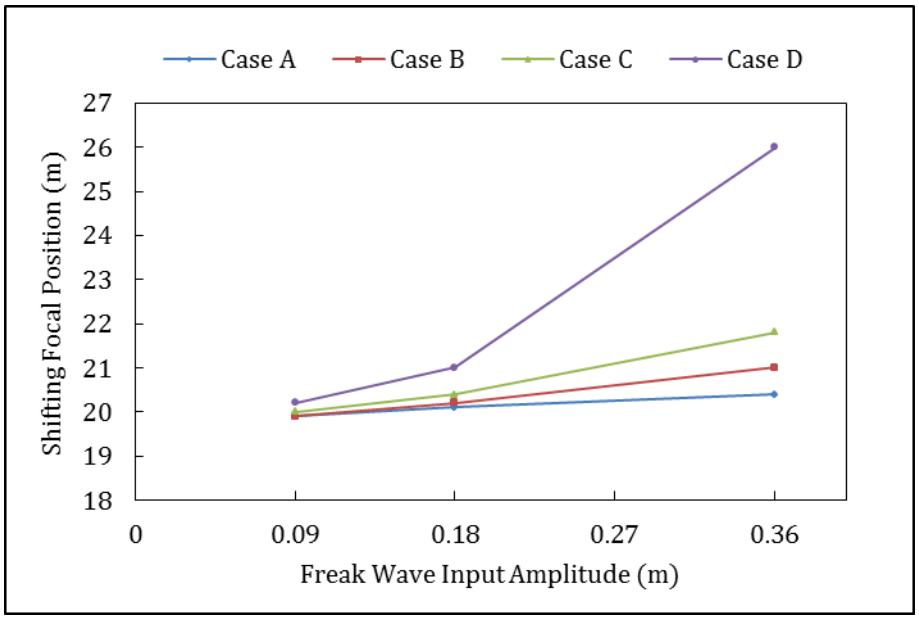

Figure 4.49 Numerical downstream shifting of the focused position

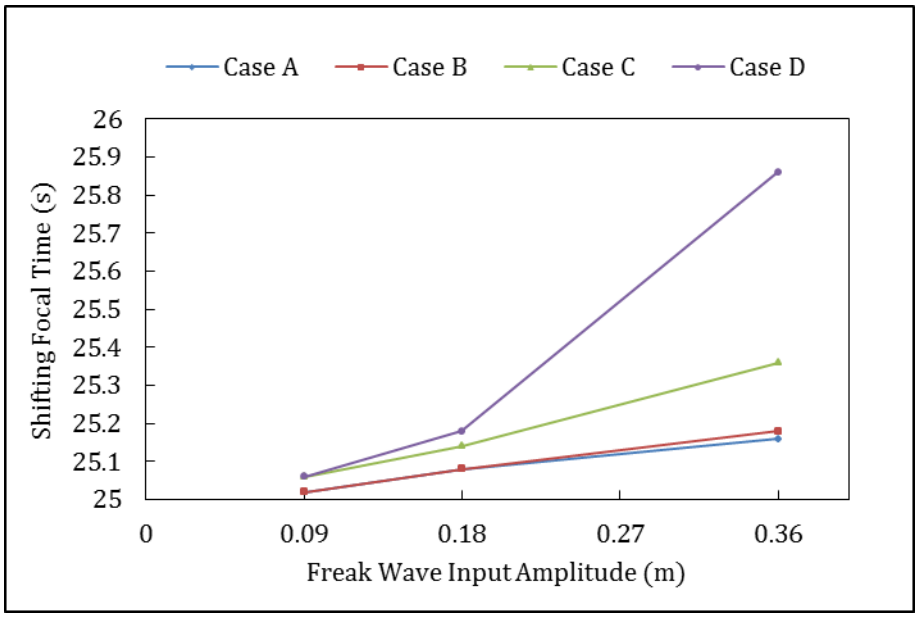

Figure 4.50 Numerical downstream shifting of the focused time

4.4.4.4 Surface Elevation at Focused Position

The nonlinear behaviour of a freak wave train will not only affect the real focal position and time, but also results in a change of wave surface elevation. Figure 4.51, Figure 4.52, Figure 4.53 and Figure 4.54 show the time history of wave

elevations for the small input amplitude cases A1, B1, C1 and D1. The computational results have a similar tendency as the analytical results. For the board-banded case A1, the computational maximum wave elevation is 0.0888m, and the corresponding result is 0.098m for the narrow-banded case D1. In these cases, as the input freak wave amplitude is small, the nonlinear wave-wave interaction behaviour is not obvious in the freak wave groups and the nonlinear behaviour can be ignored.

For the other four cases with the same input amplitude of 0.18m, the computational wave surface profiles measured at the focused location are compared with the linear analytical results as shown in Figure 4.55, Figure 4.56, Figure 4.57 and Figure 4.58. The increase of the input amplitude results in obvious nonlinear behaviour of the wave group, which leads to an increase in wave elevation compared with the linear wave theory. Although for all the four cases, the computational wave elevations measured at the focal position are all larger than the results derived from the linear sum of the wave amplitude method; this wave elevation increase is only 0.2% for the board-banded case A2. However, for the narrow-banded case C2 and D2, the increases in wave elevation are 8% and 10%, respectively.

For the four cases with the same input amplitude of 0.36m, the time histories of the wave elevation are shown in Figure 4.59, Figure 4.60, Figure 4.61 and Figure 4.62. The increased input amplitude results in large nonlinear wave-wave interaction issues in a freak wave group, and the nonlinear behaviours of the freak wave are obvious. Because much more wave energy is gathered in the higher order harmonic, the computational maximum wave elevations are all much larger than the linear analytical results. The wave crest measured at the focal position is narrower and higher, and the adjacent wave troughs are wider and shallower than the linear results.

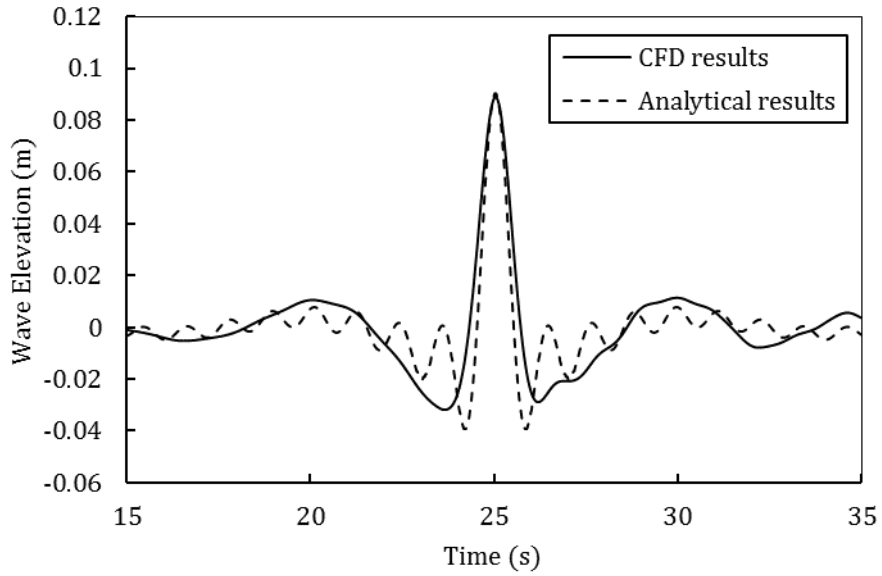

Figure 4.51 Wave elevation comparisons for freak wave case A1

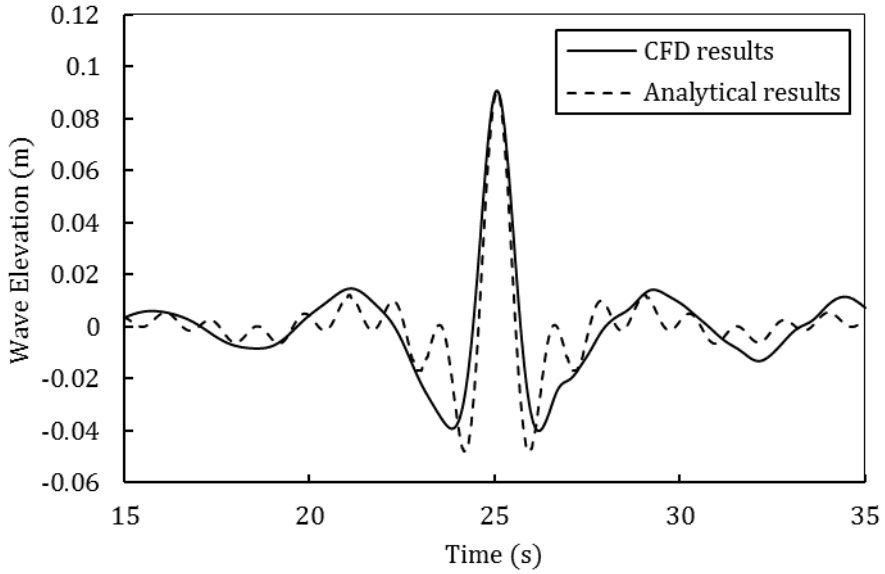

Figure 4.52 Wave elevation comparisons for freak wave case B1

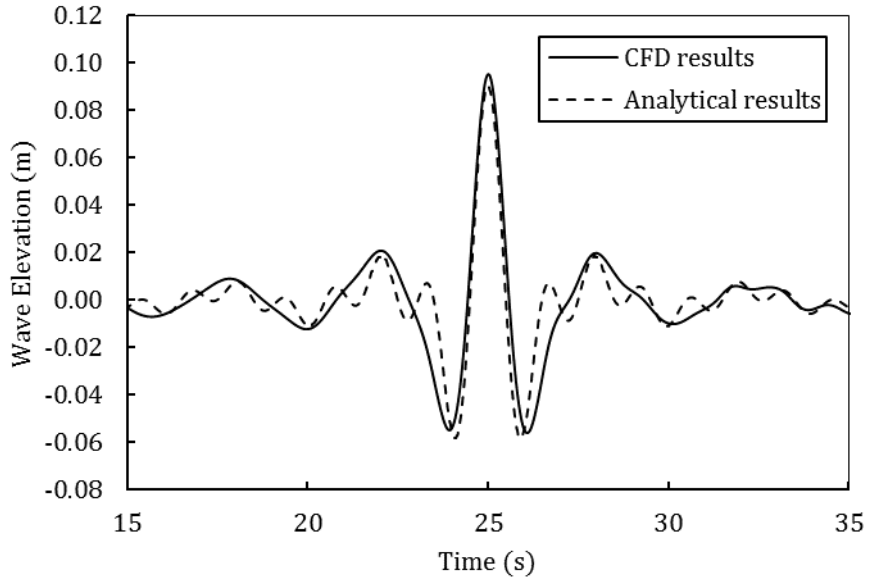

Figure 4.53 Wave elevation comparisons for freak wave case C1

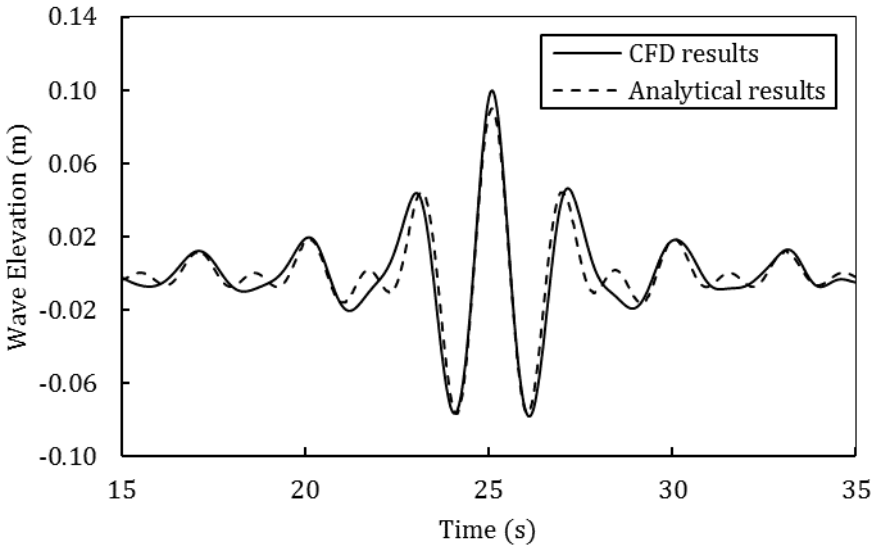

Figure 4.54 Wave elevation comparisons for freak wave case D1

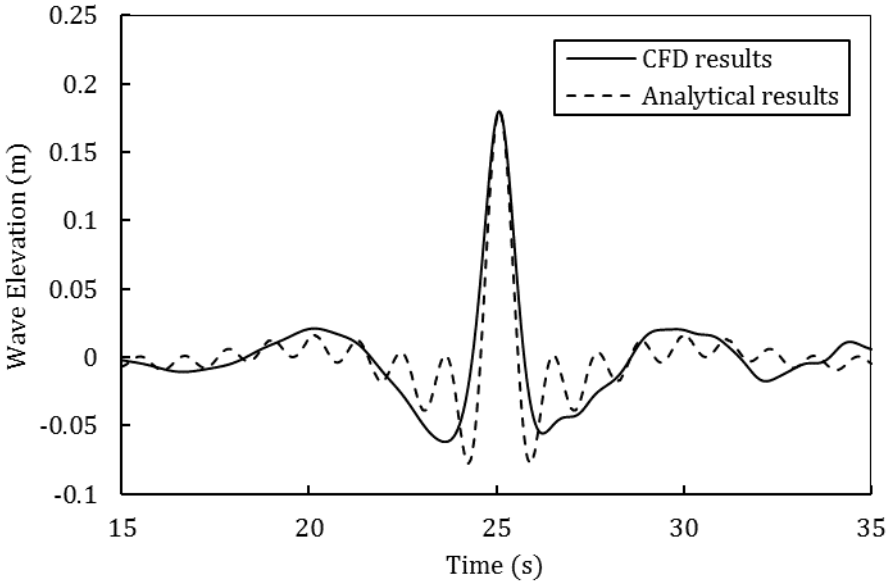

Figure 4.55 Wave elevation comparisons for freak wave case A2

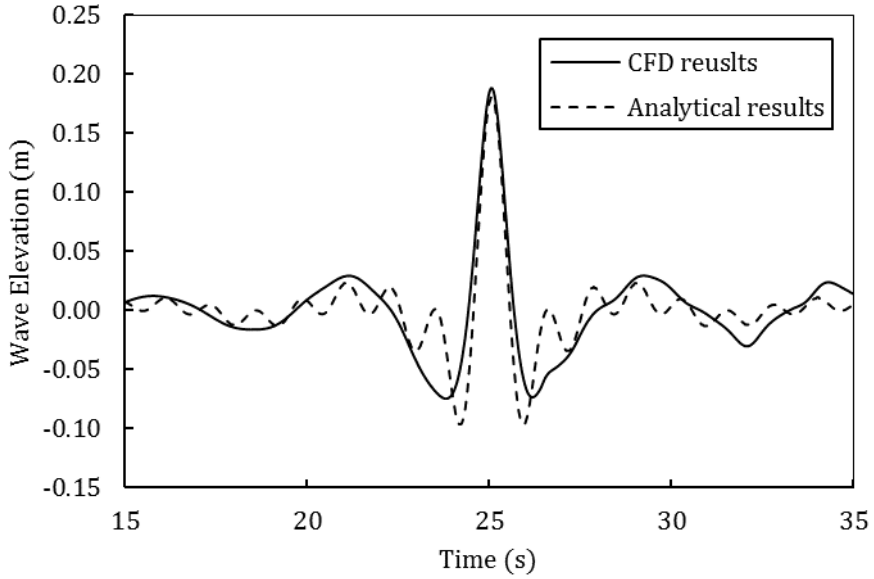

Figure 4.56 Wave elevation comparisons for freak wave case B2

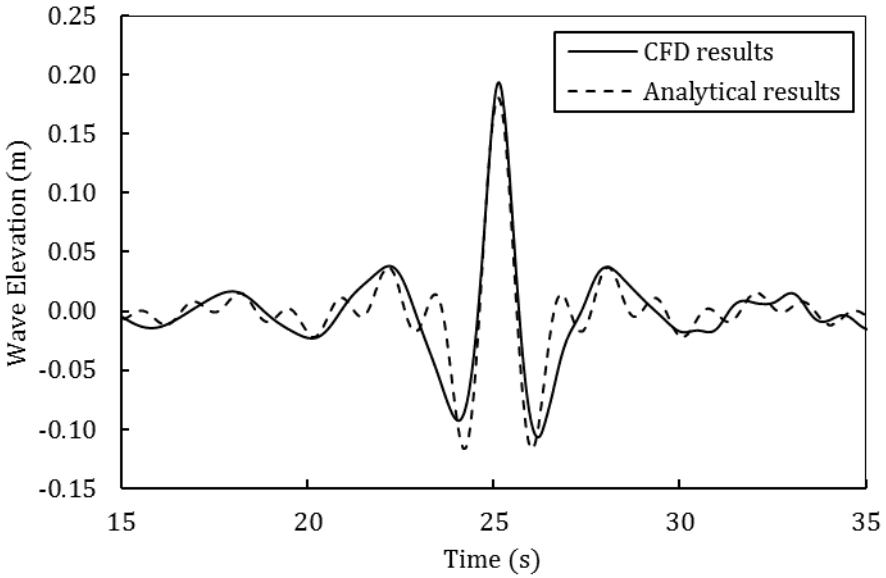

Figure 4.57 Wave elevation comparisons for freak wave case C2

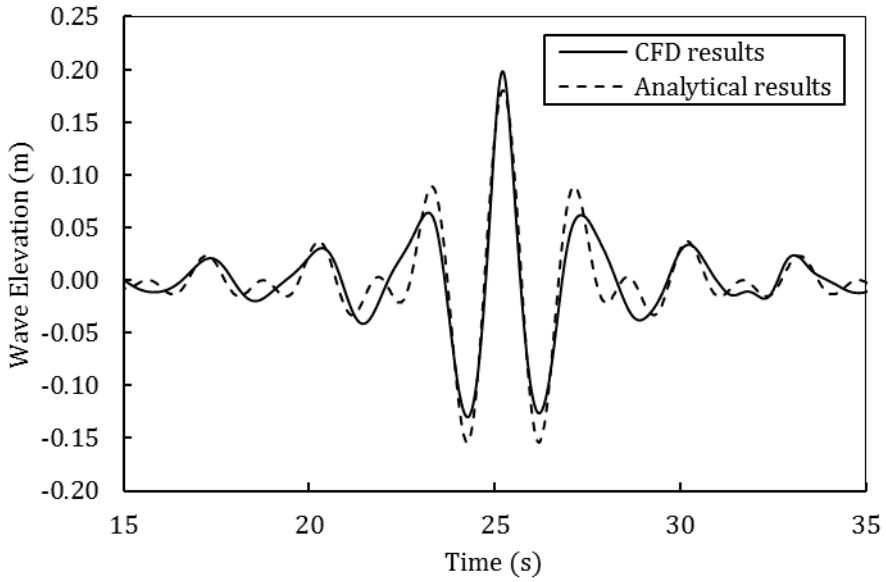

Figure 4.58 Wave elevation comparisons for freak wave case D2

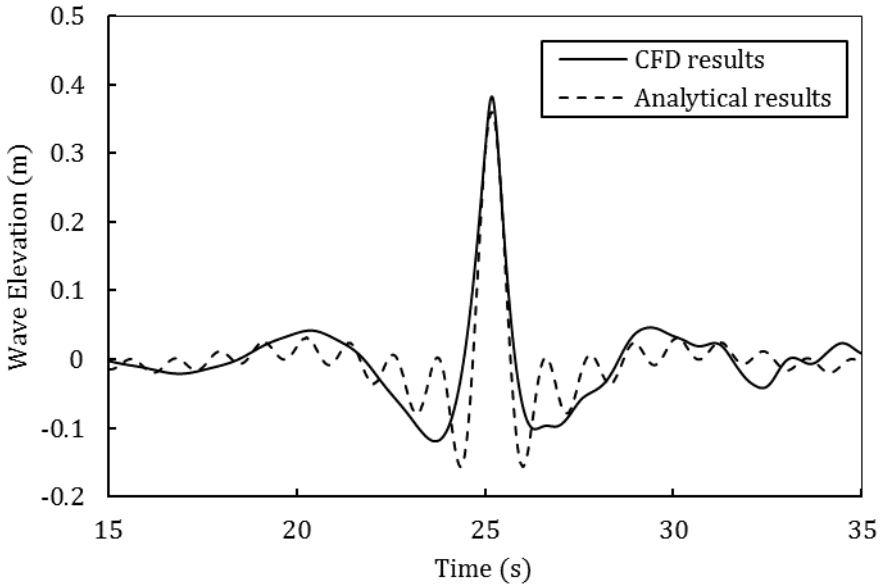

Figure 4.59 Wave elevation comparisons for freak wave case A3

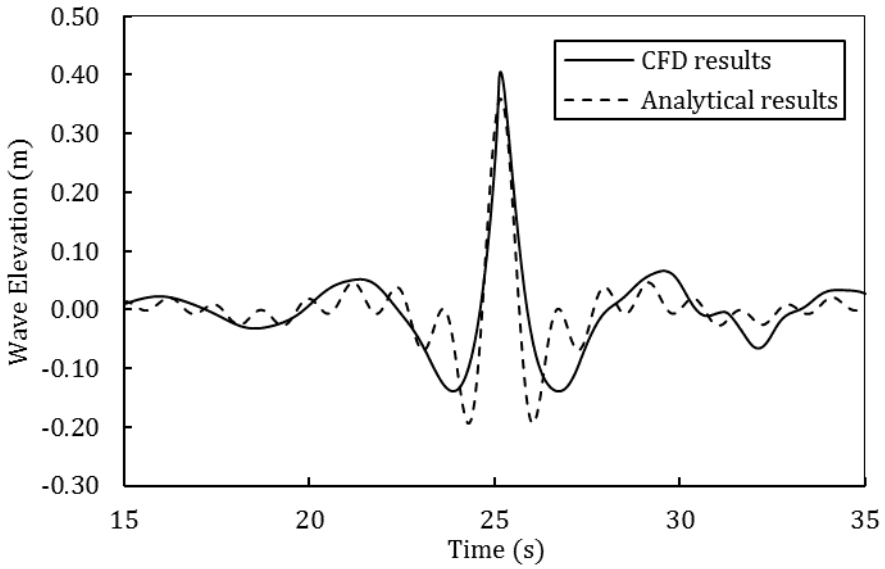

Figure 4.60 Wave elevation comparisons for freak wave case B3

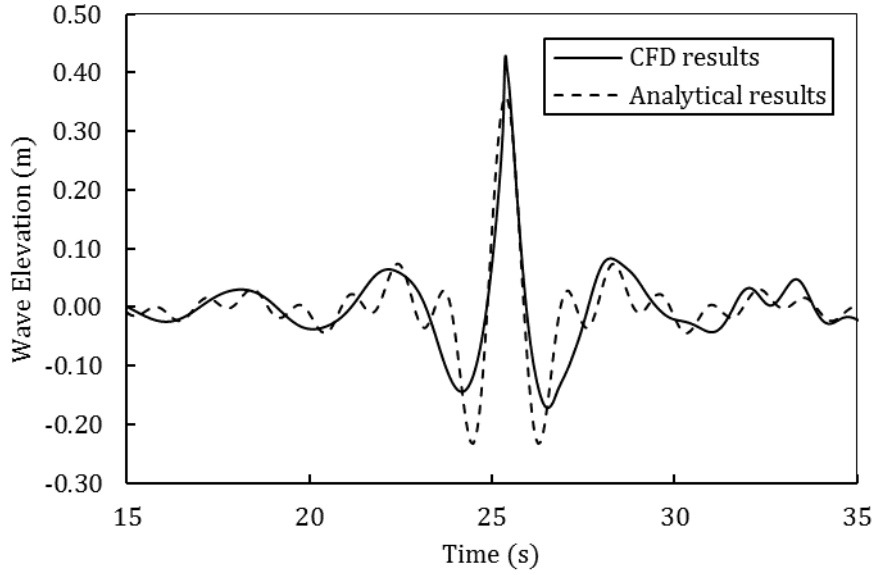

Figure 4.61 Wave elevation comparisons for freak wave case C3

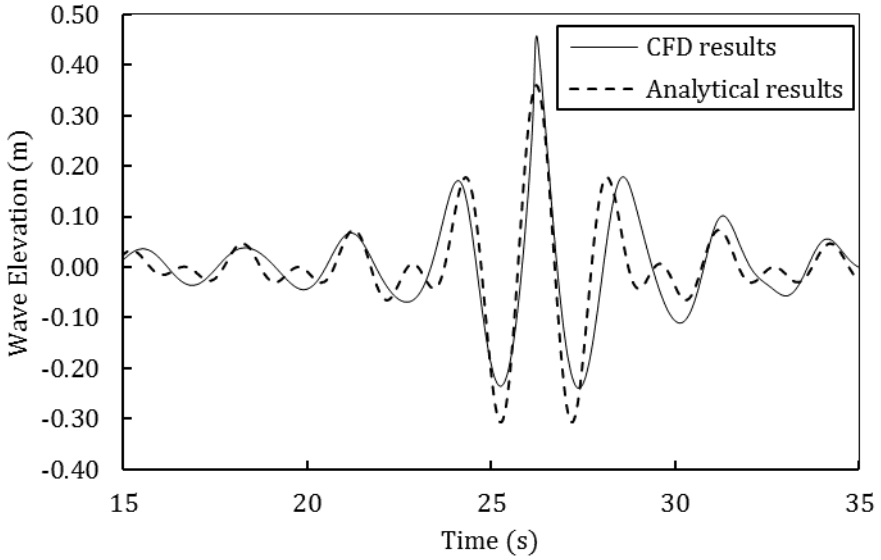

Figure 4.62 Wave elevation comparisons for freak wave case D3

4.5 Conclusions

The freak wave model is introduced in this section. According to the Longuet-Higgins model, an irregular wave train is presented with a component of 100 regular waves with different wave numbers and different frequencies. Based on the wave amplitude superposition technique, entire wave components can gather in a fixed position at a predetermined time by modulating the initial

phase for each wave component. In the freak wave model, all the wave spectrum energy is used for the transient big wave generation.

Further, three more efficient and realistic wave models for generating a freak wave in a numerical tank are introduced. Because the wave heights of the freak wave event in a real sea follows the Rayleigh distribution and the water surface elevation generally follows a Gaussian distribution, the definition of a freak wave event is determined to be $H_{max} > 2.2H_s$.

Finally, a freak wave train is simulated numerically in a 2-D numerical wave tank, and 12 different cases are conducted. In each freak wave train, there are 29 individual wave components with the same amplitude. The 12 cases are allocated by different input amplitudes and frequency bandwidths. The numerical results show that the increased input amplitude and the reduced frequency bandwidth can result in a growth of nonlinear behaviour of a freak wave group, which will not only shift the focal position and focused time, but also change the wave surface profile compared with the linear analytical results. When the nonlinear behaviour increases, much more wave energy gathers in the higher order harmonic, which result in the computational maximum wave elevations being much larger than the linear analytical results.

5 Freak Wave Run-up on Vertical Cylinders

5.1 General Remarks

The design of offshore structures need an accurate prediction of wave scattering and maximum wave run-up elevation around the offshore structures to maintain sufficient air gaps below the platform decks. The wave run-up is always underestimated by linear diffraction theory, especially in extreme conditions.

At first, a 3-D numerical wave tank is established with the source function wave making method to investigate a regular wave run-up on fixed vertical cylinder problems. The numerical wave run-up results are compared with experimental data, which was conducted by Nielsen (2003), to validate the accuracy of the current CFD numerical method.

Following this, the 3-D numerical wave tank is performed to investigate the interactions between a freak wave train and a vertical fixed cylinder. Two cylinder sizes in total are considered. The numerical results show that the focused wave parameters, including wave steepness, frequency bandwidth and focal position, had significant impact on the wave run-up on a cylinder.

Finally, the 3-D numerical wave tank is performed to investigate the interactions between a focused wave group and a pair of two cylinders. The results show that the focused wave parameters, including wave steepness, frequency bandwidth and distance between cylinders, had significant impact on the wave run-up on a cylinder.

5.2 Validation of Regular Wave Run-up on a Vertical Cylinder

5.2.1 Experimental Test

In the present work, the results of a numerical wave run-up on a fixed vertical cylinder are compared with experimental data conducted by Nielsen (2003). A full-scale test is set up for the simulation. In the experiment, the circular cylinder diameter is D=16m and the cylinder draft is 24m. 16 different wave elevation measurement points in total are set around the cylinder surface, as

illustrated in Figure 5.1 and Table. 5.1, and the radial distances are measured from the cylinder centre.

Table 5.1 Wave measurement point position

Row	Direction (degree)	Radial distances (m) point no. 1,2,3 and 4
A1	270	8.05, 9.47, 12.75 and 16
A2	225	8.05, 9.47, 12.75 and 16
A3	202.5	8.05, 9.47, 12.75 and 16
A4	180	8.05, 9.47, 12.75 and 16

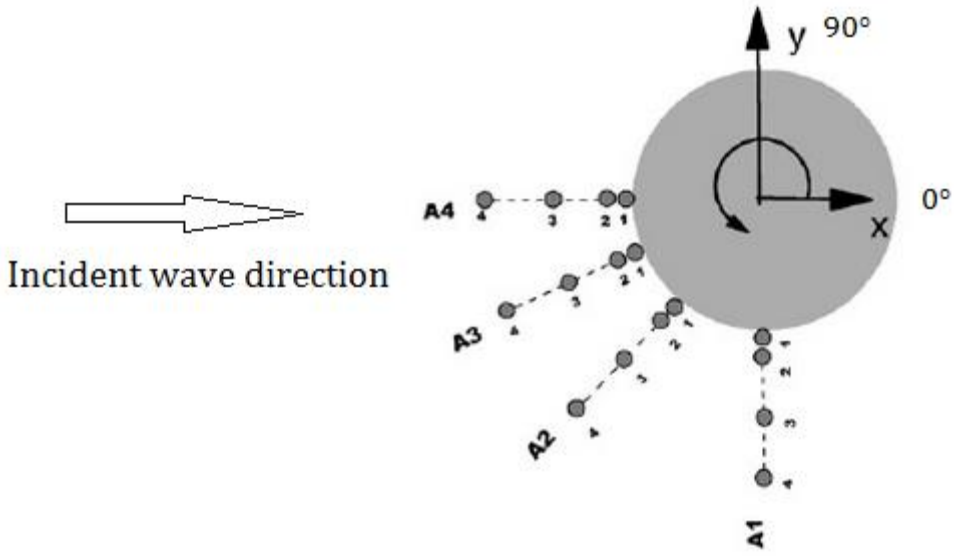

Figure 5.1 Wave measurement point positions

A regular wave is selected as the target incident wave in this present work. The wave parameter is shown in Table 5.2. The regular wave period is T=9s and the corresponding wave length is λ=126.5m for a deep-water condition.

Table 5.2 Wave parameter

Wave	Height H(m)	Period T(s)	Steepness H/ λ
M1	4.22	9	0.0333/1
M2	7.9	9	0.0625/1

5.2.2 Incident Wave Generation

To investigate regular wave run-up around a vertical cylinder, incident waves must be generated in the 3-D numerical wave tank first.

5.2.2.1 Numerical Tank Configuration

The coordinate origin O is located at the left side of the free surface in the numerical tank. The wave tank is 506 meters long in total and the dissipation region length is 126.5m, located at the end position. A source region is placed at the front side 4.22m below the free surface with a width of 3.2m. The total height of the wave tank is 120m and the water depth is 100m. The numerical tank configuration is shown in Figure 5.2.

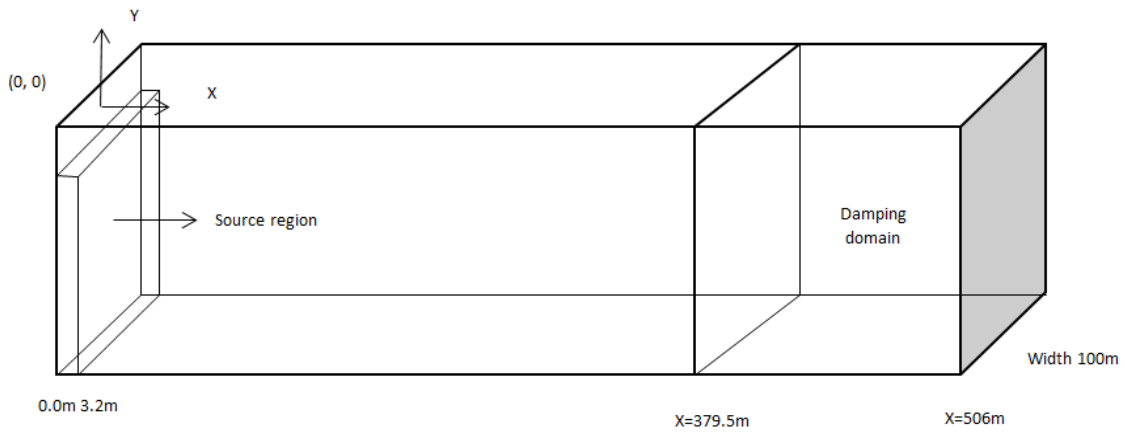

Figure 5.2 3-D Numerical wave tank configurations

5.2.2.2 Numerical Results

Figure 5.3 and Figure 5.4 show the comparison of time histories of wave elevation simulated by the present CFD method and linear wave theory. It is found that the wave elevation profiles simulated by the numerical method and derived from linear theory show a good agreement. A difference worth mentioning is that the CFD-simulated regular wave trough is shallower and much more flat than the linear theory results. For the high wave steepness case of M2, the numerical simulated wave elevation is much narrower than the linear theory results. The average wave crests of M1 and M2 during the effective time are 2.2m and 3.97m

and both are slightly larger than target wave amplitudes of 2.11m and 3.95m. The experiment measured average wave amplitudes of 1.97m and 3.91m.

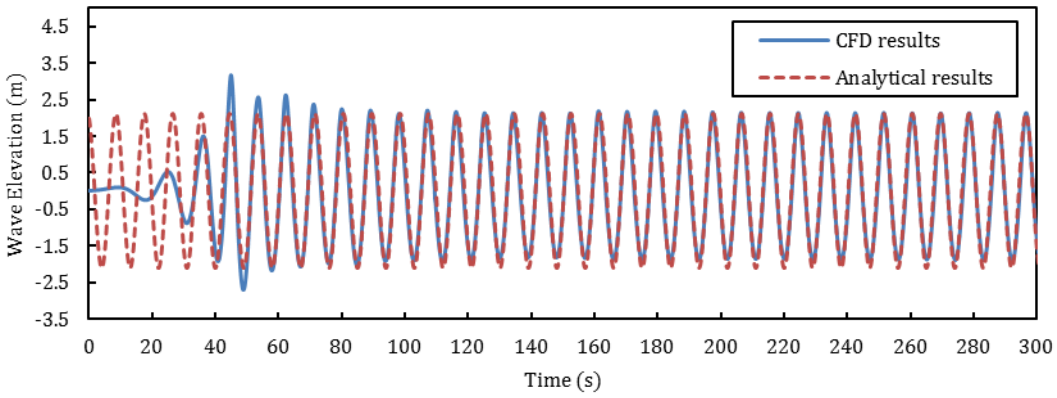

Figure 5.3 Comparisons of time history of wave elevation simulated by present CFD method and linear wave theory for regular wave M1

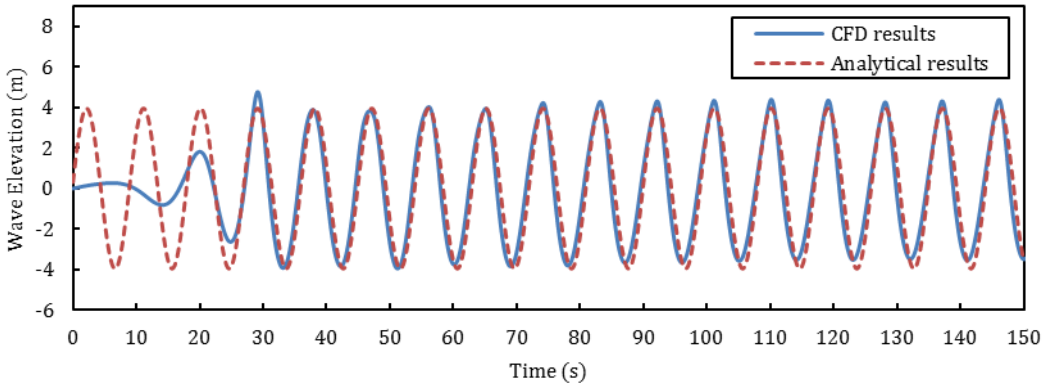

Figure 5.4 Comparisons of time history of wave elevation simulated by present CFD method and linear wave theory for regular wave M2

5.2.3 Convergence Test

The mesh convergence test is investigated with three different meshes by comparing the horizontal wave forces impacting on the cylinder. The global meshing configuration is shown in Figure 5.5, and the detailed meshing configuration around the cylinder surface is shown in Figure 5.6. The structured hexagonal mesh is used in the present case, which will not only reduce the computation time but also produce a smooth free surface. In order to test mesh convergence, three different meshes are established to calculate the wave force on cylinders listed in Table 5.3.

The horizontal wave force impacting on the vertical cylinder by three different grid sizes is shown in Figure 5.7, and only the wave case M1 is used for the convergence test. It is shown that the horizontal wave force converges to 6340kN. Mesh 3 is used for further analysis to obtain a robust numerical result.

Table 5.3 Three mesh conditions for grid convergence test

Mesh	Cell Size In X-Direction	Cell Number Around Free Surface	Cell Number Around Cylinder Surface
Mesh-1	3%λ= 3.84m	30	900
Mesh-2	2.5%λ= 3.2m	35	1600
Mesh-3	2%λ= 2.56m	40	2500

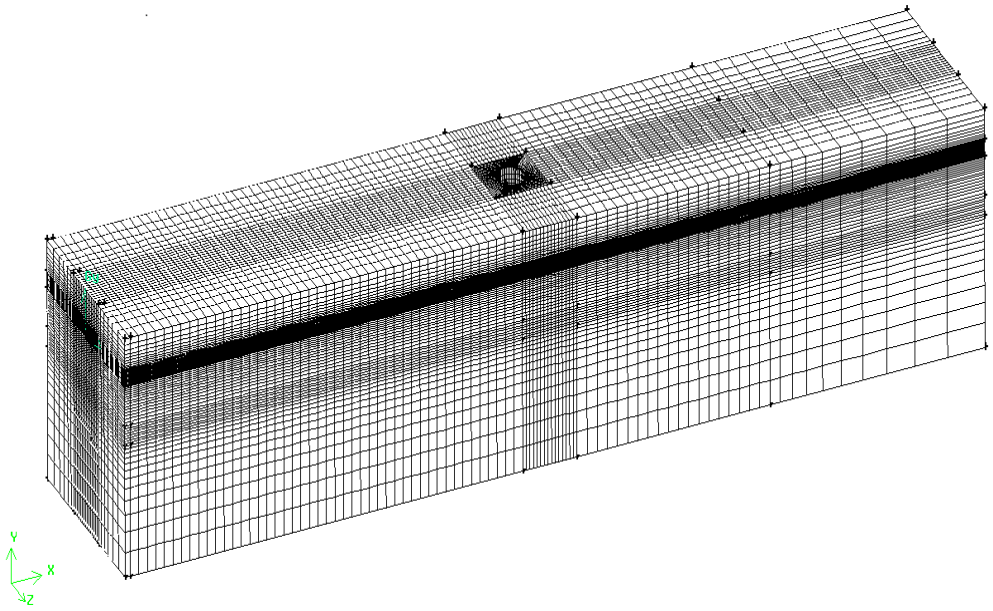

Figure 5.5 Global mesh configurations of the 3D numerical wave tank

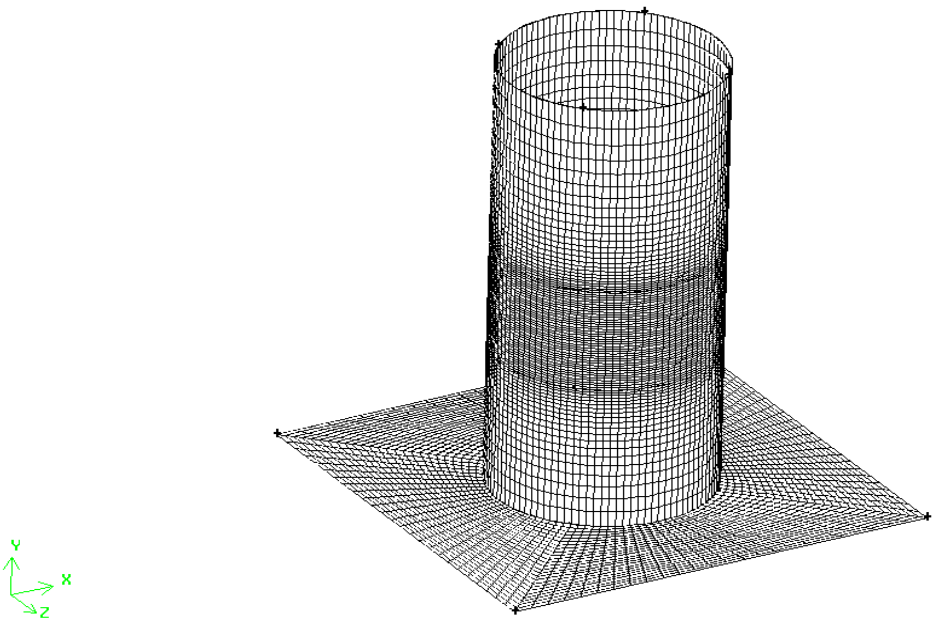

Figure 5.6 Detailed mesh configurations around the cylinder surface

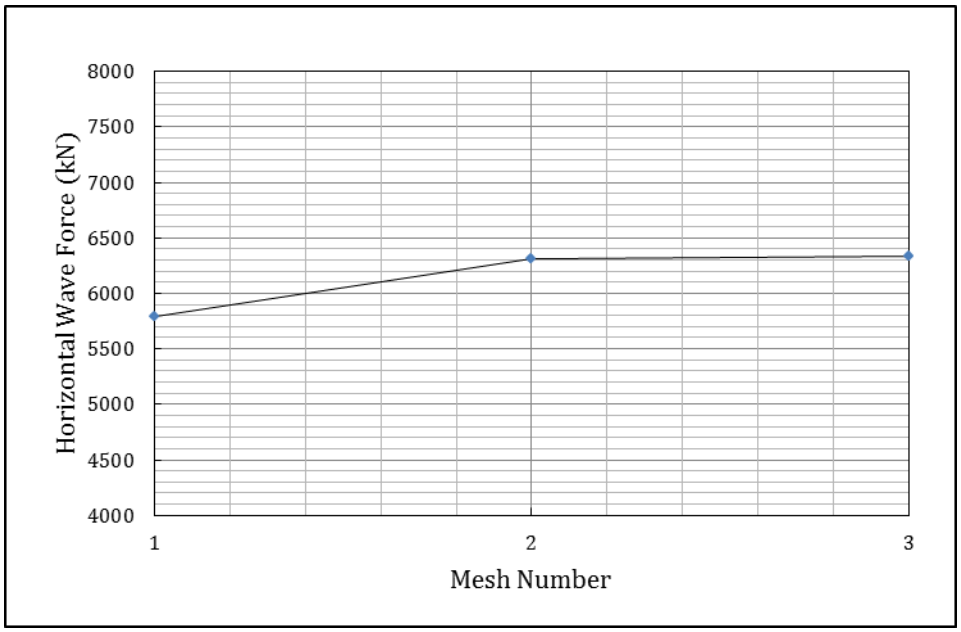

Figure 5.7 Horizontal wave forces on the vertical cylinder in three different mesh conditions

5.2.4 Horizontal Wave Force

Time histories of horizontal wave force impacting on the vertical cylinder for incident regular waves M1 and M2 are shown in Figure 5.8 and Figure 5.9, respectively. The effective simulation time starts at t=95s, and ten periods are considered. The mean value of the computational maximum wave horizontal force is 6340kN for regular wave M1.

In order to validate the accuracy of the CFD modelling result, Morrison's equation is used to compare wave horizontal forces impacting on the cylinder, which is often used to calculate wave loads on circular cylindrical structural members of fixed offshore structures when viscous forces matter. Morrison's equation tells us that the horizontal force dF on a strip pf with length dz of a vertical rigid circular cylinder can be written as:

$$dF = \rho \frac{\pi D^2}{4} dz C_m \dot{u} + \frac{\rho}{2} C_D D dz |u| u \tag{5.2.1}$$

The formula was published by Morison et al. (1950) as a result of force measurements on piles due to the action of progressive waves. ρ is the water density, D is the cylinder diameter, and u and $\dot{u}$ are the horizontal undisturbed fluid velocity and acceleration at the midpoint of the strip, respectively. The inertia coefficient C_m and drag coefficient C_D are determined to be 2 and 1.2, respectively, in this case. In the Morrison equation, the first part is called the mass (inertia) term, which concerns the pressure on the cylinder and the extra force caused by the change in pressure due to the presence of the cylinder. The second part is called the drag force, which concerns the viscous effects. The maximum wave force derived from the Morrison equation is $F_{mass(max)} =$ 6278N for regular wave case M1, which has a good agreement with the computational results.

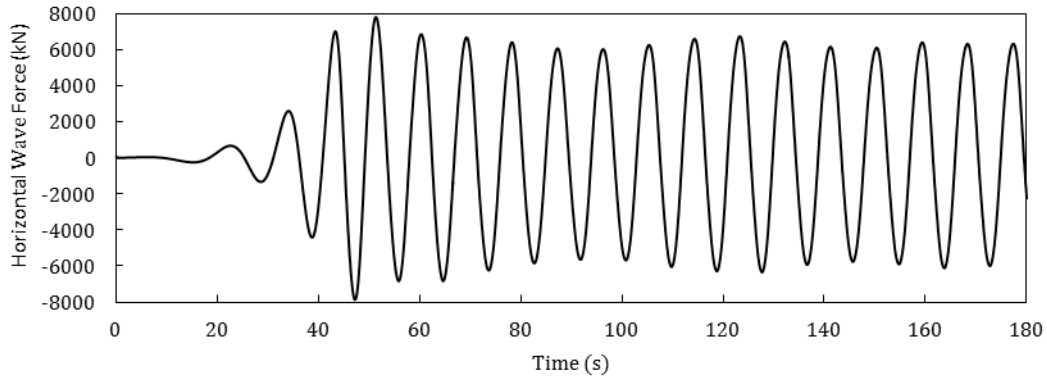

Figure 5.8 Numerical time history of horizontal wave force impacting on the vertical cylinder for regular wave M1

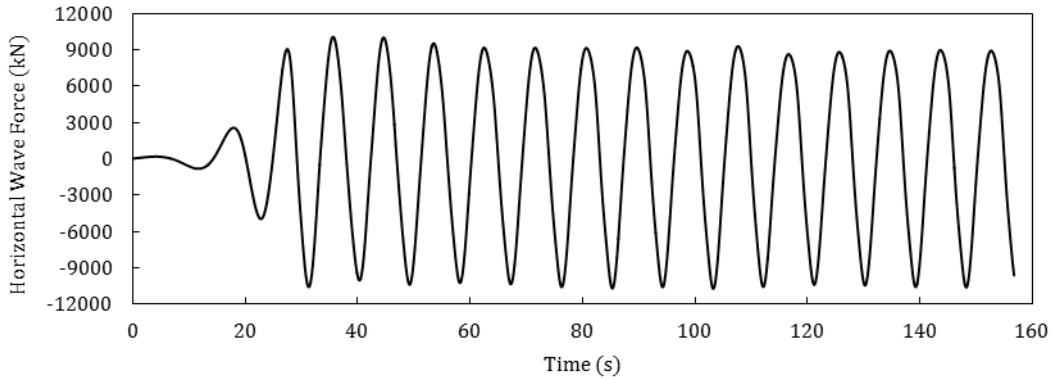

Figure 5.9 Numerical time history of horizontal wave force impacting on the vertical cylinder for regular wave M2

5.2.5 Wave Run-up

Figure 5.10 shows the free surface elevation when the regular wave M2 runs up the cylinder. At t=82.7s, the maximum wave run-up happens along the cylinder surface.

Figure 5.11 and Figure 5.12 show the time histories of wave elevations at wave measurement point A14 for the low wave steepness case M1 and high wave steepness case M2. The wave elevation profile for case M1 is smooth while, during a wave period time, an obvious small wave crest happens near a wave elevation trough for wave M2. With the increase of incident wave height, the nonlinear effect of a regular wave becomes stronger.

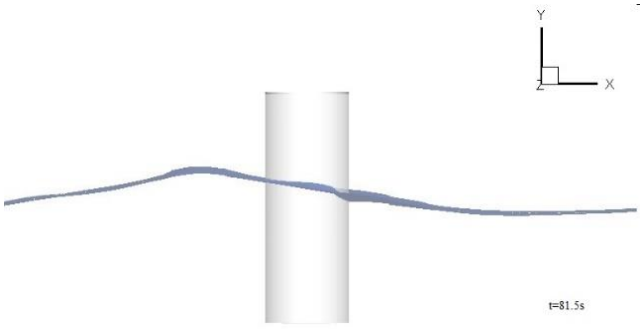

(a)

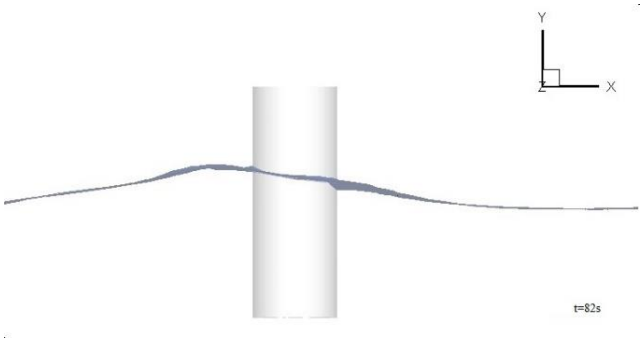

(b)

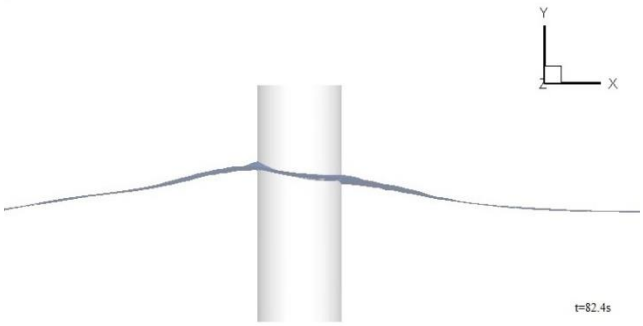

(c)

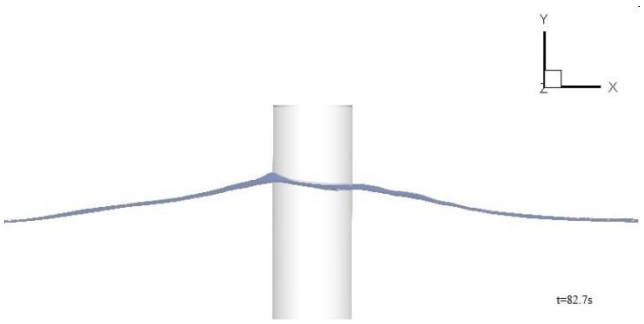

(d)

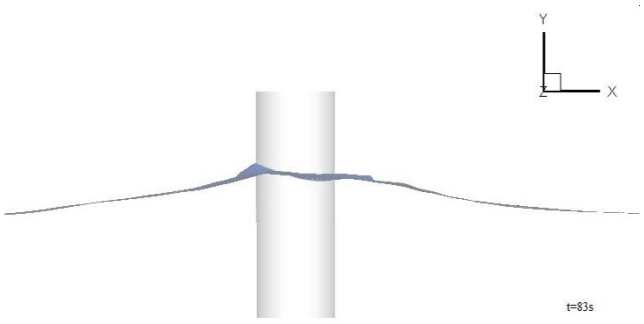

(e)

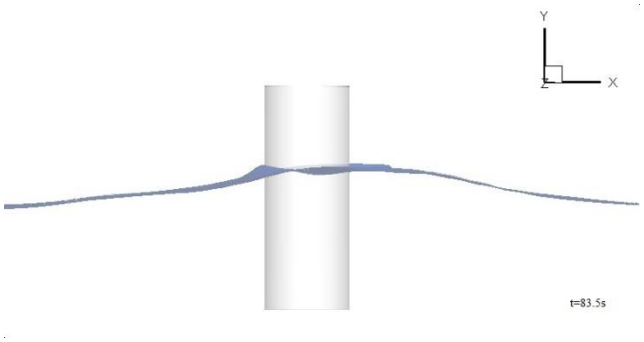

(f)

Figure 5.10 Six snapshots of wave surface when regular wave M2 running-up on the cylinder

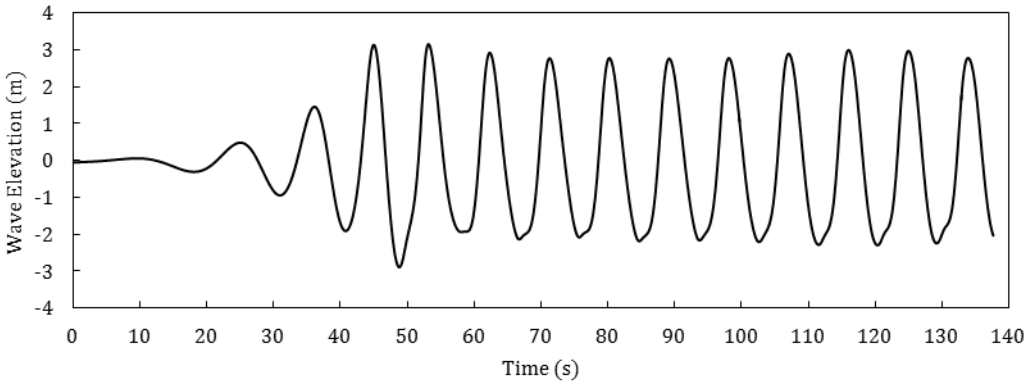

Figure 5.11 Time history of wave elevation at wave measurement point A14 for low steepness case M1

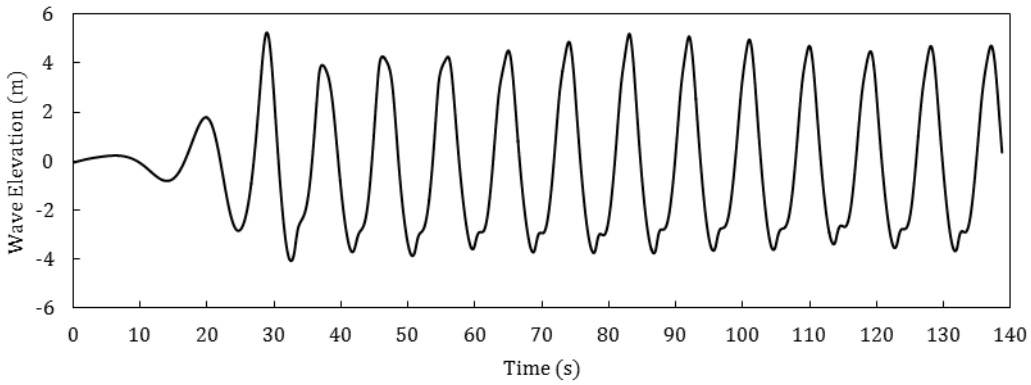

Figure 5.12 Time history of wave elevation at wave measurement point A14 for high steepness case M2

The first order diffraction theory was first introduced by MacCamy and Fuchs (1956). The first order diffraction theory is used to calculate wave loads on a vertical circular cylinder extending from water free surface to the seabed. Different from Morrison's equation, which is used to calculate wave loads exerted on a relative small size cylinder, the first order diffraction theory is used as a relative large size cylinder causing the reflection and diffraction of the incident wave.

According to small amplitude wave theory, the velocity of the wave incident on the rigid cylinder is:

$$\phi_I = -\frac{gH}{2\omega} * \frac{cosk(y+d)}{coshkd} * e^{i(kx-\omega t)} \tag{5.2.2}$$

Where g is the gravity acceleration, H is the wave height, ω is the wave frequency, $\omega=2\pi/T$, T is the wave period, k is the wave number, $k=2\pi/\lambda$, λ is the wave length, d is the water depth, t is the time. The equation for plane incident wave can be expressed as an infinite series using the polar co-ordinates r and θ:

$$\phi_I = -\frac{gH}{2\omega} * \frac{cosk(y+d)}{coshkd} * \sum_{m=0}^{\infty} \in_m i^m cosm\theta \, J_m(kr)(kr)e^{-i\omega t} \tag{5.2.3}$$

Where $J_m(kr)$ are Bessel functions of the first kind of orders 0, 1,2…m, ϵ_0=1 for m=0 and ϵ_m=2 for m≥1.

A cylindrical wave is reflected from the cylinder and may be described by the velocity potential ϕ_R:

$$\phi_R = -\frac{gH}{2\omega} * \frac{cosk(y+d)}{coshkd} \sum_{m=0}^{\infty} \in_m i^m cosm\theta \, [J_m(kr) + iY_m(kr)]e^{-i\omega t} \tag{5.2.4}$$

Where A_m are constants and $Y_m(kr)$ are Bessel functions of the second kind.

The total potential ϕ is the sum of the incident and reflected potentials:

$$\phi = -\frac{gH}{2\omega} * \frac{cosk(y+d)}{coshkd} \sum_{m=0}^{\infty} [\in_m i^m cosm\theta \, J_m(kr) + A_m cosm\theta H_m^1(kr)]e^{-i\omega t} \tag{5.2.5}$$

Where $H_m^{(1)}(kr) = J_m(kr) + iY_m(kr)$ is the Hankel function of the first kind.

$$A_m = -\in_m i^m \frac{J'_m(ka)}{H'^{(1)}_m(ka)} \tag{5.2.6}$$

For m=0, 1, 2 3…, where $J'_m(ka)$ and $H'^{(1)}_m(ka)$ are the derivatives of $J_m(kr)$ and $H_m^{(1)}(kr)$ at $r=a$ Therefore, the total potential is:

$$\phi = -\frac{gH}{2\omega} * \frac{cosk(y+d)}{coshkd} \sum_{m=0}^{\infty} \in_m i^m \left[J_m(kr) - \frac{J'_m(ka)}{H'^{(1)}_m(ka)} H^{(1)}_m(kr) \right] cosm\theta e^{-i\omega t} \tag{5.2.7}$$

The water surface elevation η and the dynamic pressure at the surface of the cylinder are calculated using the total velocity potential and the linear Bernoulli equation:

$$p = -\rho g y + \rho \frac{\partial \phi}{\partial t} \tag{5.2.8}$$

So, that the water surface elevation can be expressed as:

$$\eta = \frac{H}{2} \sum_{m=0}^{\infty} \in_m i^{m+1} [J_m(kr) - \frac{J'_m(ka)}{H'^{(1)}_m(ka)} H^{(1)}_m(kr)] cosm\theta e^{-i\omega t} \tag{5.2.9}$$

The comparison between current CFD simulation, experiment and first order diffraction results of wave run-up on a cylinder are shown in Figure 5.13 and Figure 5.14 for two incident waves, M1 and M2. ζ is the mean maximum wave crest; A is the incident wave amplitude, $A = H/2$; r is the radial distance from the cylinder centre to wave measurement point, and a is the radius of the cylinder. The ratio r/a represents the distance between the wave measurement point and the cylinder centre. In the present work, the incident wave amplitudes for cases M1 and M2 are 2.2m and 3.79m, respectively, in the CFD simulation. The effective simulation time starts at time t=70s, and ten time periods are considered in total.

The present CFD simulation and experiment wave run-up results around a vertical cylinder show a good agreement with each other. The first order diffraction theory underestimates wave run-up dramatically. In the experiment, the maximum wave run-up appeared at row A3 and wave measurement point A_{32} in both M1 and M2. However, the maximum wave run-up is measured at row A4 and wave measurement point A_{41} in the CFD simulation which is opposite to the

incident wave direction and closest to the cylinder surface. Some other numerical simulation results were also compared with the experiment data in the original Nielsen's work(2003). Their results illustrated the same tendency as the current CFD method in which the maximum wave run-up occurs in the wave flow direction and is measured in a wave measurement point closest to the cylinder surface.

Except for the wave measurement points in row A3, the CFD measured wave run-up amplitudes are almost all slightly larger than the experimental data for the regular wave case M1. This can be attributed to the incident regular wave amplitudes used in the CFD simulation being larger than the regular waves used in the experiment.

With the increase of incident wave height, the nonlinear characteristics become stronger. The maximum CFD simulated wave run-up ratio is 1.53 for case M1 and the corresponding ratio is 1.69 for case M2, with both measured at wave point A_{41}.

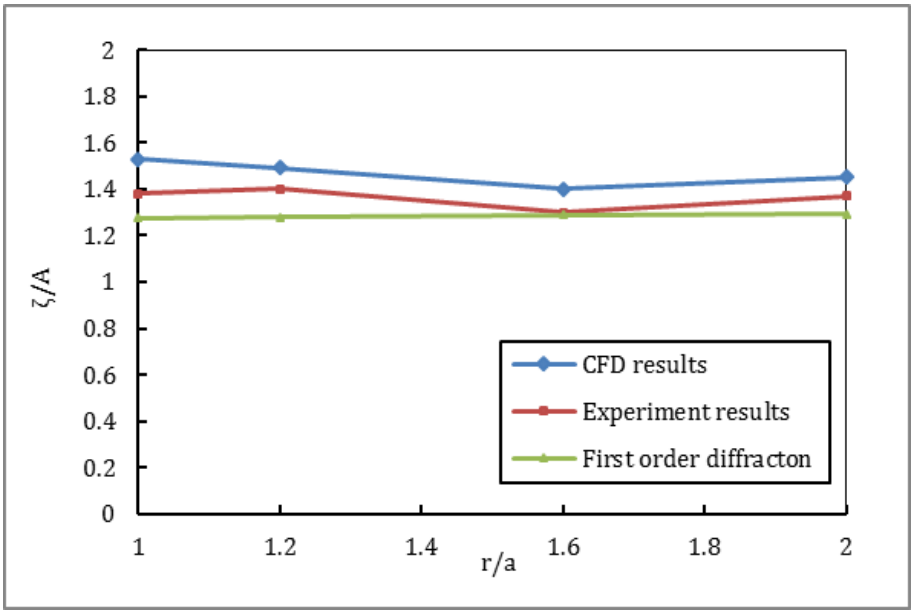

(a) Line A4

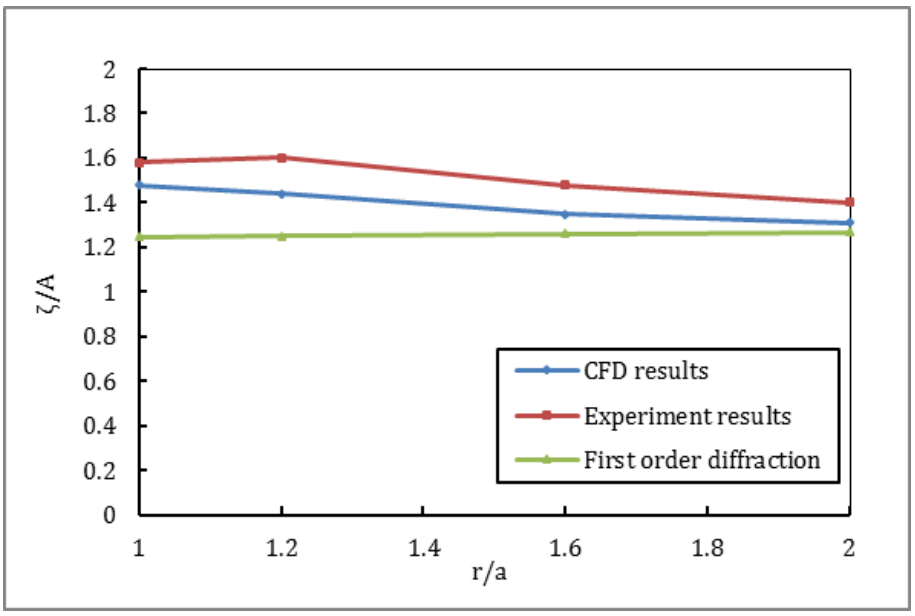

(b) Line A3

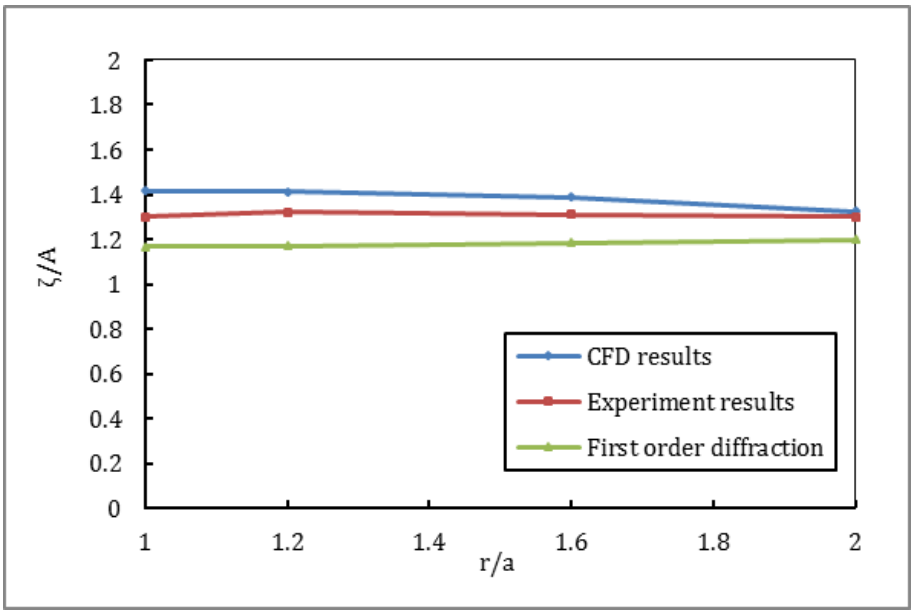

(c) Line A2

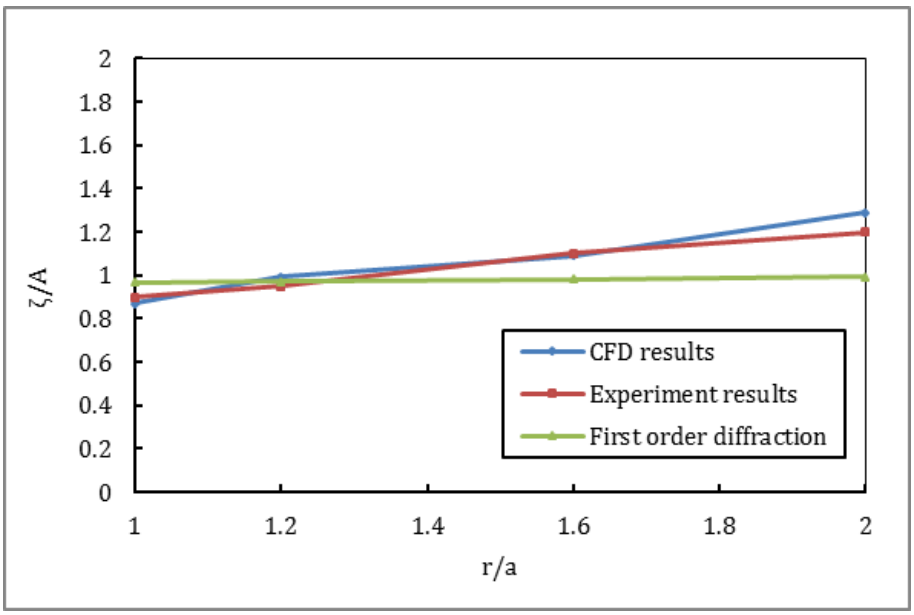

(d) Line A1

Figure 5.13 Comparisons of wave run-up ratio in four incident wave directions for regular wave M1

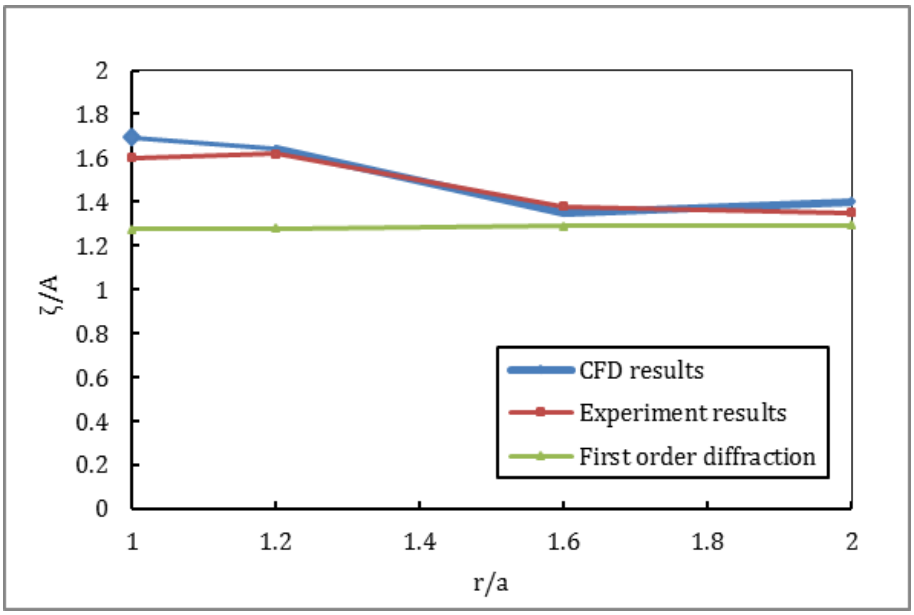

(a) Line A4

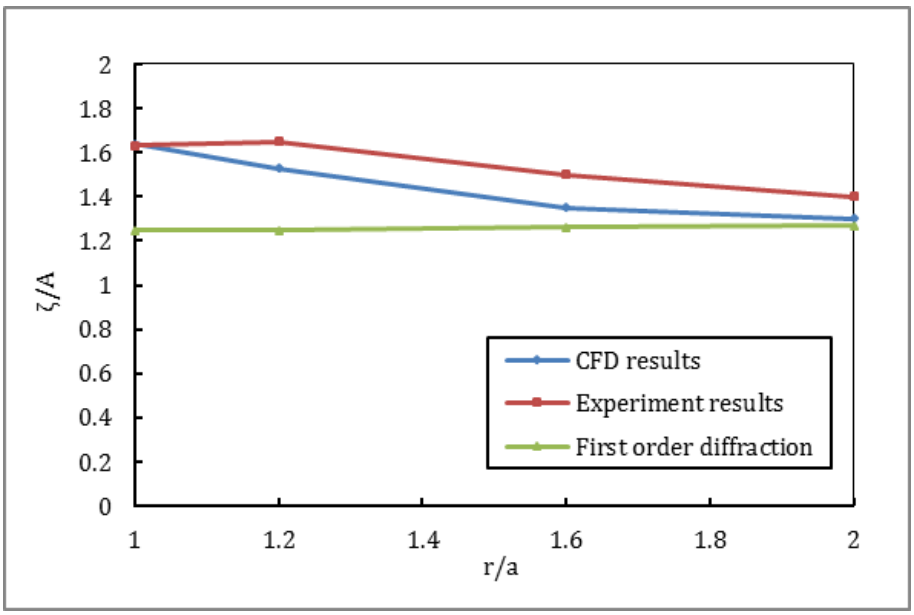

(b) Line A3

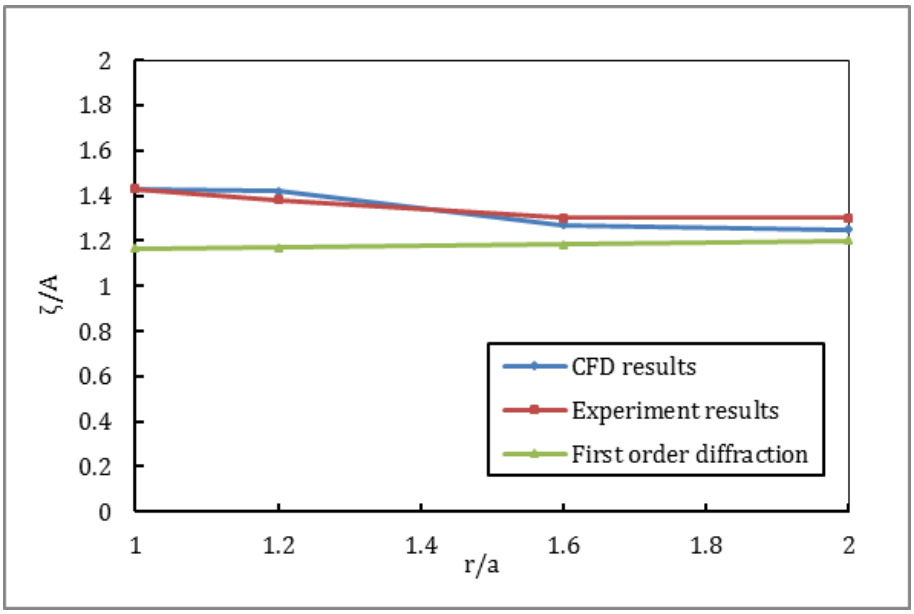

(c) Line A2

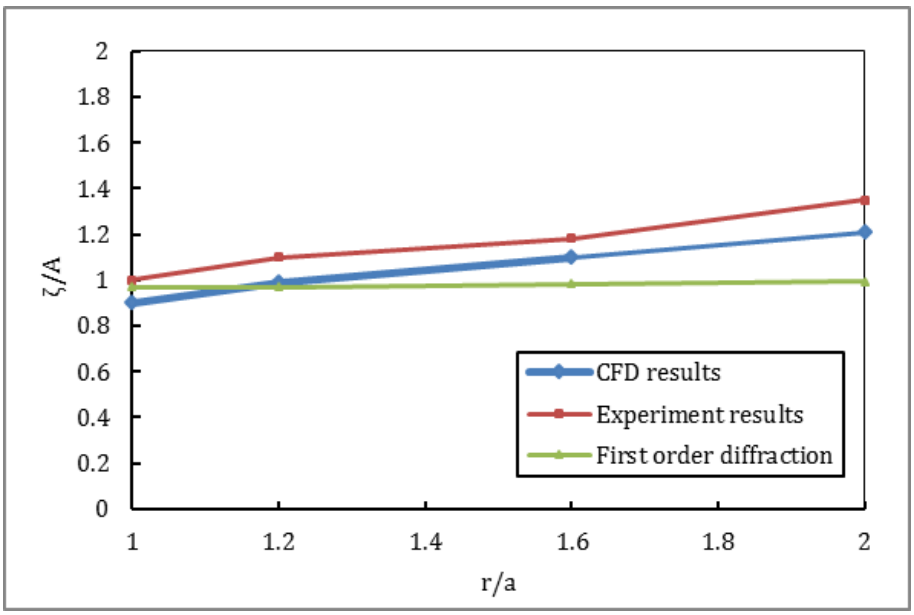

(d) Line A1

Figure 5.14 Comparisons of wave run-up ratio in four incident wave directions for regular wave M2

5.3 Freak Wave Run-up on a Single Cylinder

After validating the accuracy of the current CFD method to simulate the regular wave run-up on a vertical cylinder, a freak wave run-up on a vertical cylinder is investigated in this section. In particular, how the focused wave parameters, including wave steepness, frequency bandwidth and focused position impact on the wave run-up on a cylinder are analysed.

5.3.1 Geometric Model

The detailed configuration is shown in Figure 5.15. The coordinate origin O is located at the left side of the numerical wave tank at the free surface level. The tank is 40 meters long in total and a 10 meters long dissipation domain is located at the end of the wave tank. A source domain is 0.4m below the free surface with a width of 0.2m, placed at the front side of the numerical wave tank. The water depth is 10m and the height above the free surface is 3m. At the position x=20m, a vertical cylinder is fixed with a drought of 3m. To investigate the effect of wave scattering on freak wave run-up on a vertical cylinder and wave-structure interaction characteristics, cylinders with two different sizes are

considered. For the small size model, the cylinder has a diameter of 0.812m. For the large size model, the cylinder has a diameter of 1.56m.

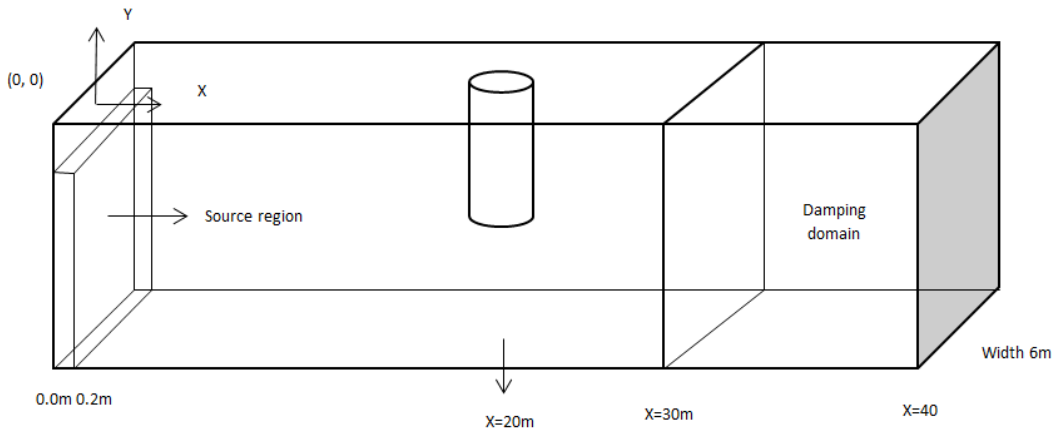

Figure 5.15 Detailed configuration of the numerical wave tank

Figure 5.16 shows the sketch of a numerical test set-up. A total of twenty different wave gauges are used to measure the wave elevations around the cylinder in five different incident wave directions. The freak wave propagates from left to right. The radial distances are shown in Table 5.4 and Table 5.5 for the small size cylinder and large size cylinder, respectively. The radial distance is measured from the cylinder centre.

Table 5.4 Radial distance from wave measurement point to cylinder centre for small size cylinder

Row	Direction (degree)	Radial distances (m) point no. 1,2,3 and 4
A	180	0.812, 0.65, 0.4872 and 0.426
B	225	0.812, 0.65, 0.4872 and 0.426
C	270	0.812, 0.65, 0.4872 and 0.426
D	315	0.812, 0.65, 0.4872 and 0.426
E	360	0.812, 0.65, 0.4872 and 0.426

Table 5.5 Radial distance from wave measurement point to cylinder centre for large size cylinder

Row	Direction (degree)	Radial distances (m) point no. 1,2,3 and 4
A	180	1.56, 1.248, 0.912 and 0.819
B	225	1.56, 1.248, 0.912 and 0.819
C	270	1.56, 1.248, 0.912 and 0.819
D	315	1.56, 1.248, 0.912 and 0.819
E	360	1.56, 1.248, 0.912 and 0.819

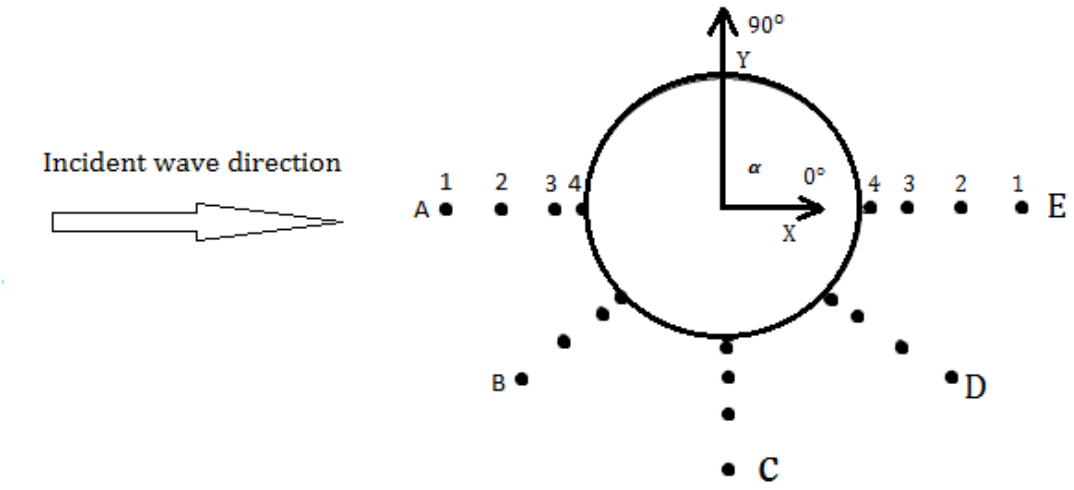

Figure 5.16 Sketch of numerical test set-up

5.3.2 Input Freak Wave Parameter

The different freak wave cases allocated by different input parameters, including input wave steepness, frequency bandwidth, cylinder size, and focused positions, are shown in Table 5.6. For case D3, the freak wave train is focused at the cylinder centre, and in cases D4 and D5, the freak wave train are focused at the cylinder's front side and back side, respectively.

Table 5.6 Input freak wave parameters

Case	A (m)	Δf (Hz)	ka	Focused position
A1	0.09	0.7	0.406	Cylinder Centre
A2	0.18	0.7	0.406	Cylinder Centre
A3	0.36	0.7	0.406	Cylinder Centre
B1	0.09	0.6	0.406	Cylinder Centre
B2	0.18	0.6	0.406	Cylinder Centre
B3	0.36	0.6	0.406	Cylinder Centre
C1	0.09	0.5	0.406	Cylinder Centre
C2	0.18	0.5	0.406	Cylinder Centre
C3	0.36	0.5	0.406	Cylinder Centre
D1	0.09	0.3	0.406	Cylinder Centre
D2	0.18	0.3	0.406	Cylinder Centre
D3	0.36	0.3	0.406	Cylinder Centre
D4	0.18	0.3	0.406	Front
D5	0.18	0.3	0.406	back
E1	0.09	0.3	0.781	Cylinder Centre
E2	0.18	0.3	0.781	Cylinder Centre
E3	0.36	0.3	0.781	Cylinder Centre

5.3.3 Freak Wave Generation in a 3-D Numerical Wave Tank

The computational results introduced in Chapter 6 show that the wave focused position and the corresponding focal time change because of the high nonlinear behaviour in a freak wave group. It is noted that the phenomenon is still obvious in a 3-D freak wave numerical simulation. In the freak wave structure

interaction computations, the adjustment of the added mass term in the governing mass function is necessary to control the wave group focal positions. Figure 5.17, Figure 5.18, Figure 5.19 and Figure 5.20 show the time histories of wave elevation measured at x=20m in the 3-D numerical wave tank after adjusting the added mass term in the source function for freak wave cases A2, B3, C2 and D1. The 3-D and 2-D computational wave elevations have a good agreement for all cases, which validates the accuracy of the current 3-D numerical wave tank.

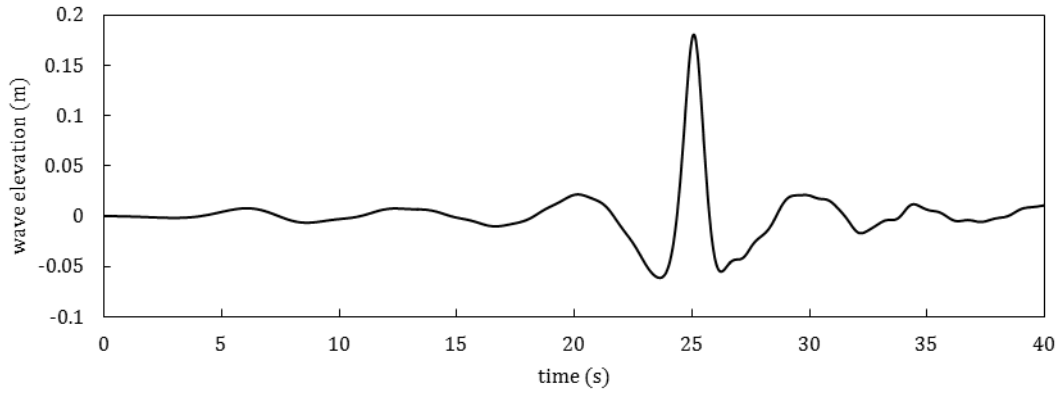

Figure 5.17 Wave elevation measured at x=20m for freak wave case A2

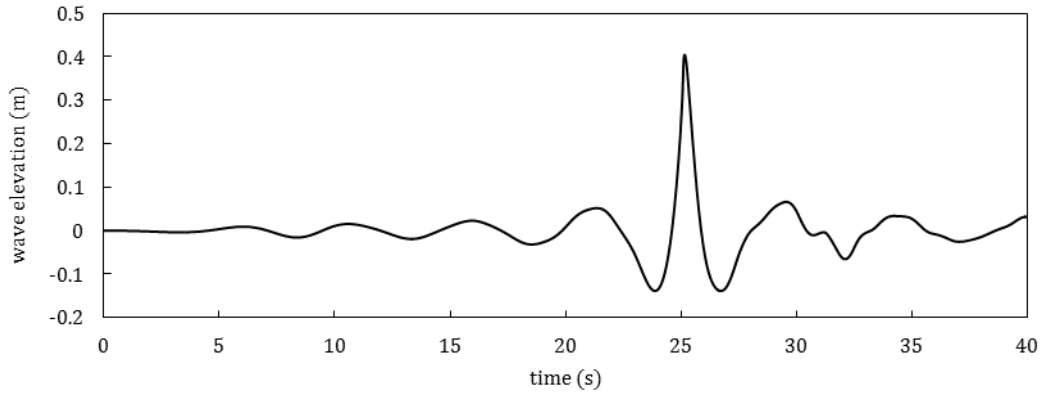

Figure 5.18 Wave elevation measured at x=20m for freak wave case B3

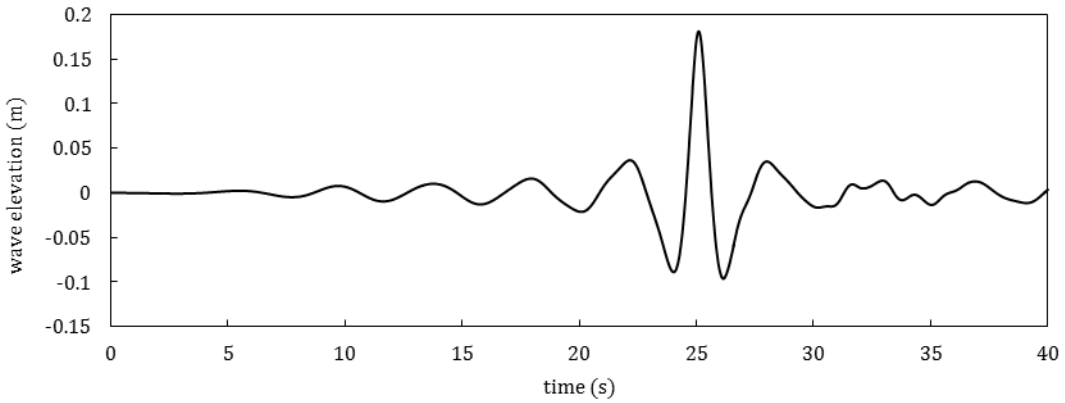

Figure 5.19 Wave elevation measured at x=20m for freak wave case C2

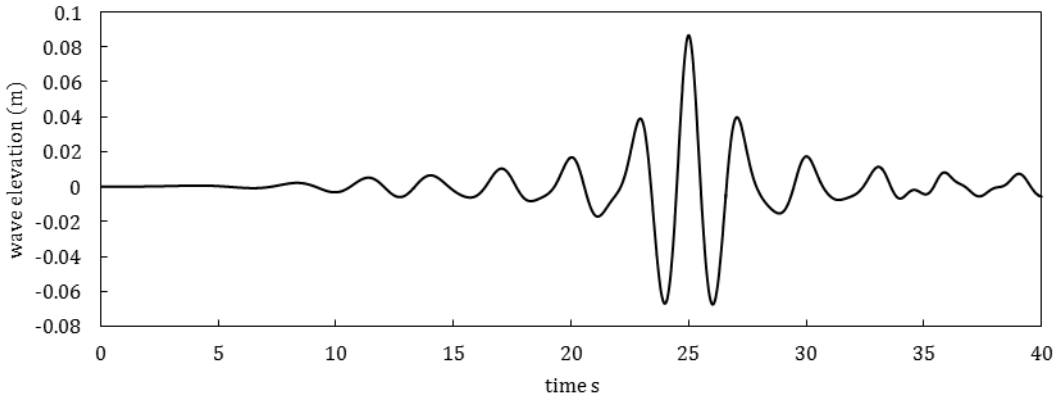

Figure 5.20 Wave elevation measured at x=20m for freak wave case D1

5.3.4 Results and Discussion

The wave run-up induced by wave structure interaction is an important factor in the design stage of offshore ocean structures. In this chapter, the wave run-up ratios are defined as:

$$R = \frac{A - A_o}{A_o} \tag{5.3.1}$$

Where

A_o = amplitude of incident wave

A = measured wave amplitude around a vertical cylinder

It should be noted that the maximum wave amplitude in a focused wave train is selected as A and A_o in the above equation to investigate the maximum wave run-up around the cylinder surface.

5.3.4.1 Wave Run-up Tendency

Figure 5.21 shows the time histories of wave elevation measured at 20 different wave gauges at different incident wave directions (referred as α in Figure 5.16) around the cylinder for case E1. Concentrating on the extreme wave run-up on the cylinder, only the maximum wave amplitudes in a freak wave train are considered. Figure 5.22, Figure 5.23 and Figure 5.24 show the maximum wave run-up with varying radial distances from cylinder centre in five different incident wave directions for case E1, case B3 and case D2.

In all the three cases, the wave run-up tendency in Line A and Line B is almost the same. The wave elevation increases with the freak wave train propagating to the cylinder surface, but in Line C and Line D, the wave elevation decreases with the freak wave train propagating to the cylinder surface. It is obvious that the wave run-up in direction α =180° is highest, especially at wave gauge a4, where the severe damage to the offshore structures occurs. In wave direction α=315°, the wave run-up ratio has the lowest values in all the three cases.

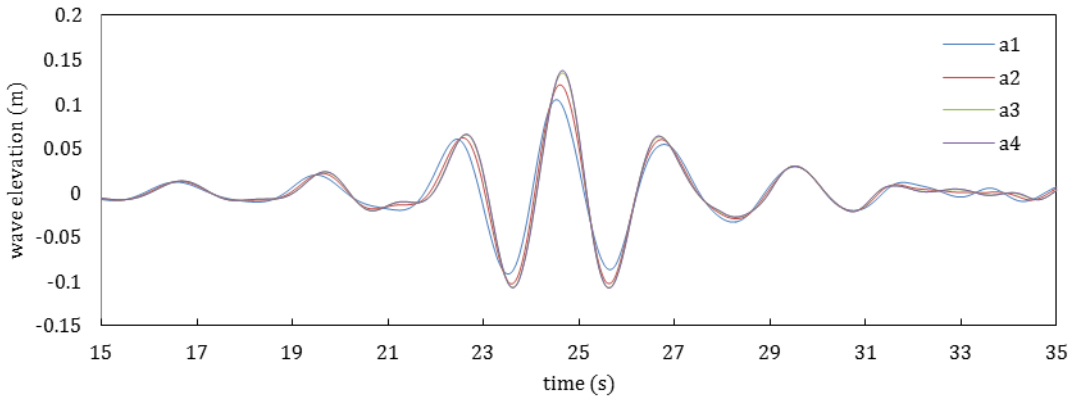

(a) Row A

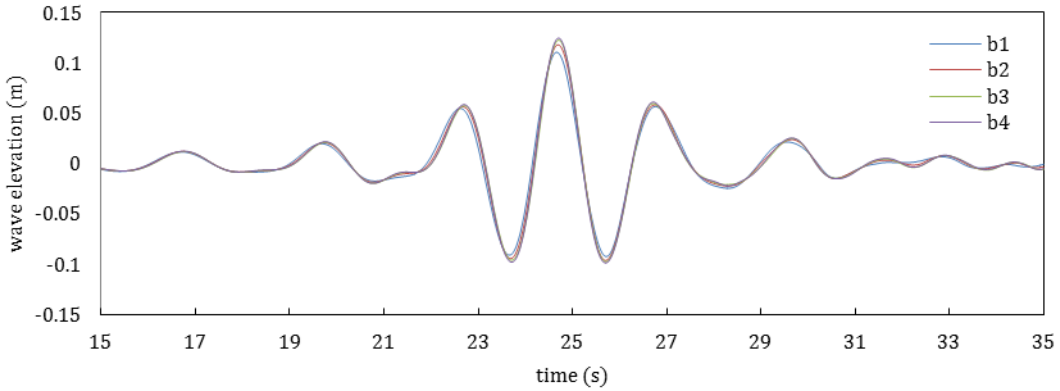

(b) Row B

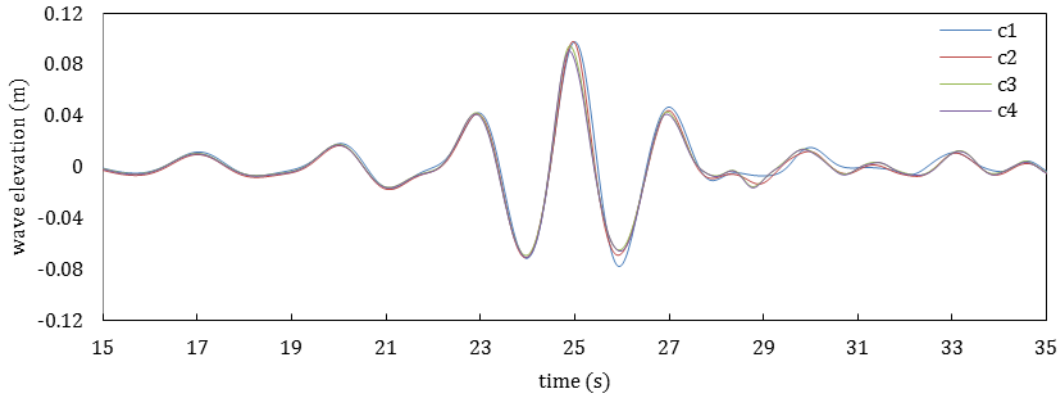

(c) Row C

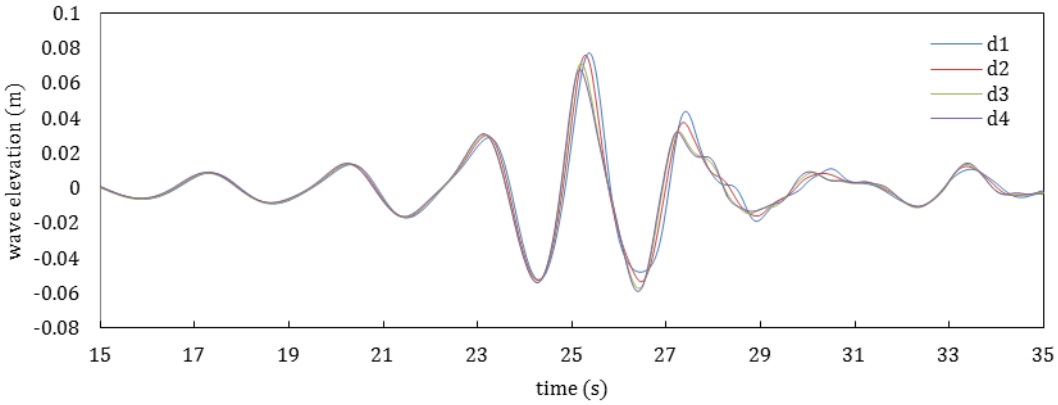

(d) Row D

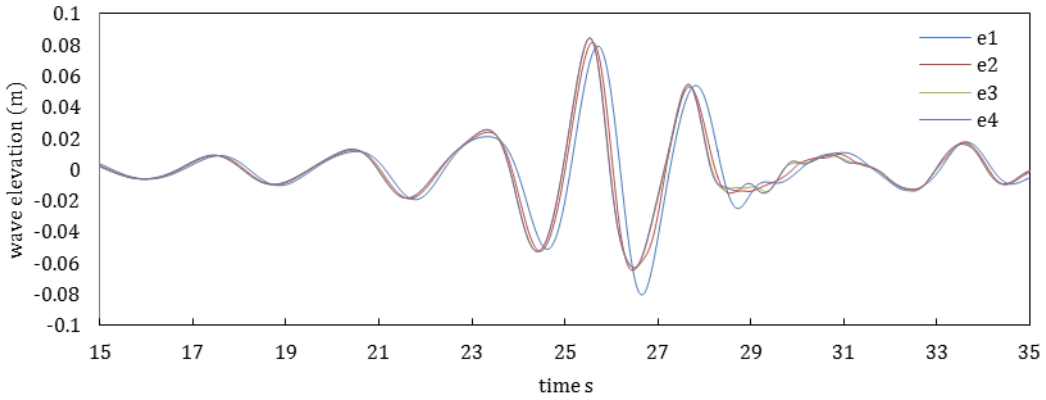

(e) Row E

Figure 5.21 Wave elevation measured at twenty different wave gauges at different incident wave directions for case E1

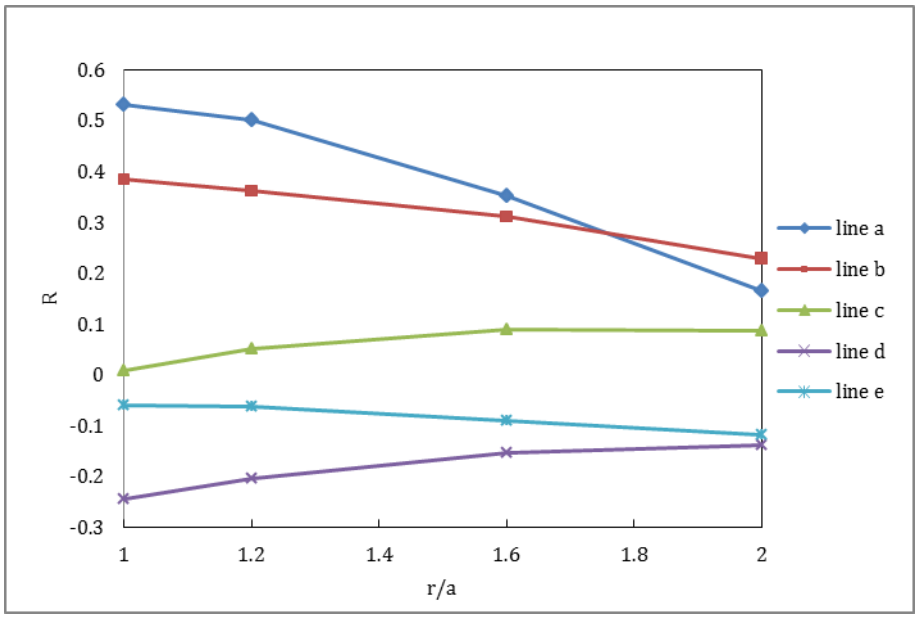

Figure 5.22 The maximum wave run-up for case E1

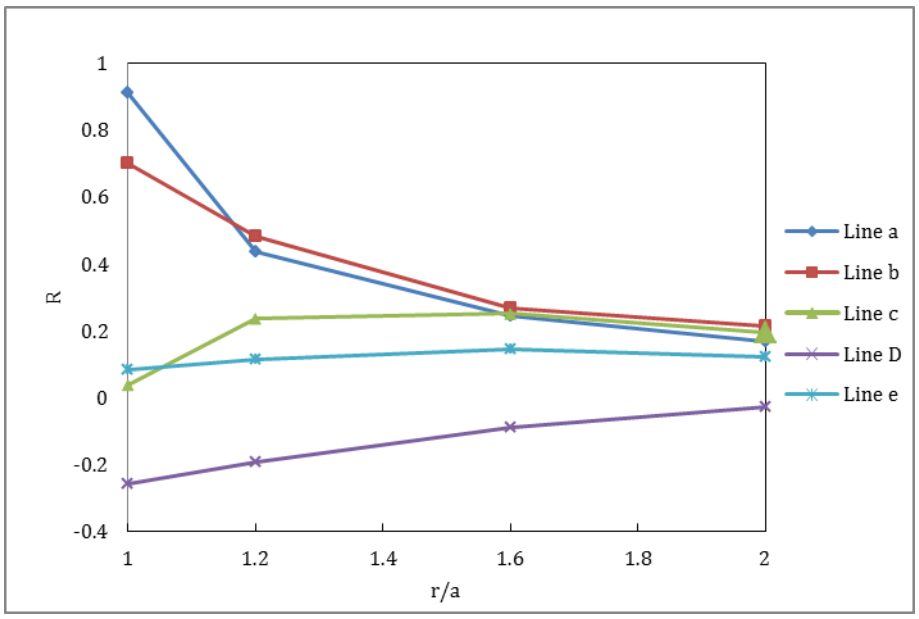

Figure 5.23 The maximum wave run-up for case B3

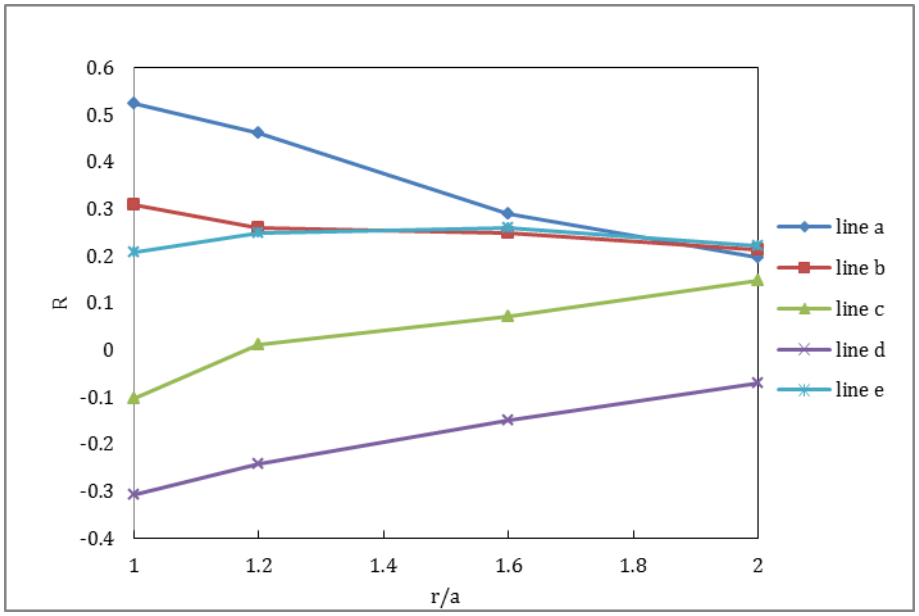

Figure 5.24 The maximum wave run-up for case D2

5.3.4.2 Wave Run-up at Wave Point a4

The wave run-up measured at the wave point a4 is investigated by comparing three important parameters: wave steepness, wave scattering parameter and wave group frequency bandwidth. The wave run-up at wave point a4, where the maximum wave elevation happens, should be emphasized as a big wave can result in severe damage to offshore structures.

5.3.4.2.1 Effect of Wave Steepness and Wave Scattering on Freak Wave Run-up at Point a4

Figure 5.25 illustrates the variation of wave run-up at point a4 with different values for input wave steepness, kA. The computational results show that increased wave steepness raises the wave run-up dramatically. This phenomenon is identical to the regular wave run-up of a circular cylinder. The increased wave amplitude results in a growth of nonlinear behaviour and this will gather more wave energy into higher order wave components. Looking at the computational results of case D and case E, the increased wave scattering raises the wave run-up ratios.

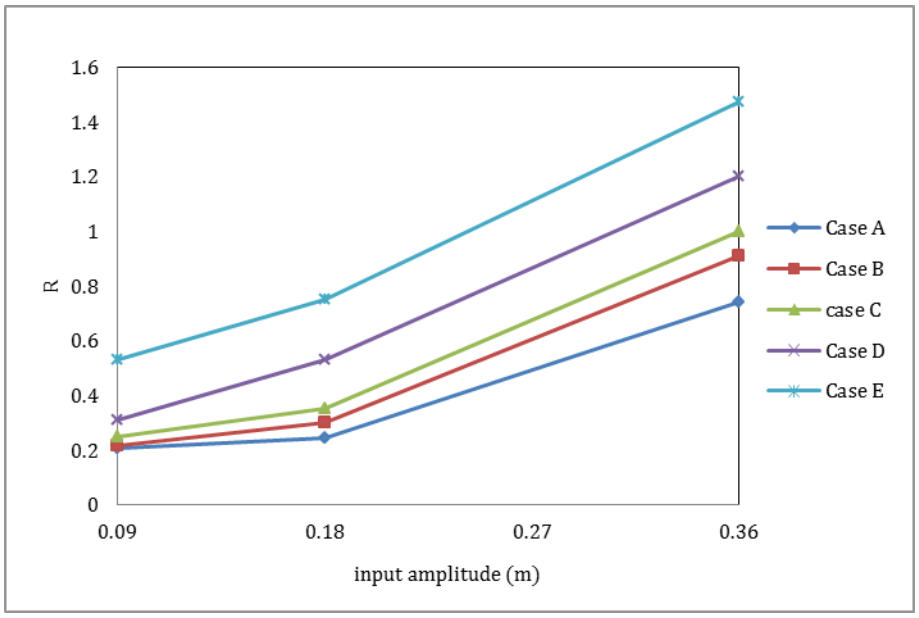

Figure 5.25 Variation of wave run-up at point a4 with different input wave steepness kA

5.3.4.2.2 Effect of Frequency Bandwidth on Freak Wave Run-up at Point a4

Figure 5.26 shows the variation of wave run-up at point a4 with different frequency bandwidth Δf values. The 12 computational results are allocated into three groups, and any four cases have the same input amplitude but different frequency bandwidths in each group. The numerical results show that the increased frequency bandwidth reduces the freak wave run-up ratio. This phenomenon is not obvious in the small input amplitude case, which is shown in by blue, while it is quite clear in the cases with large input amplitudes.

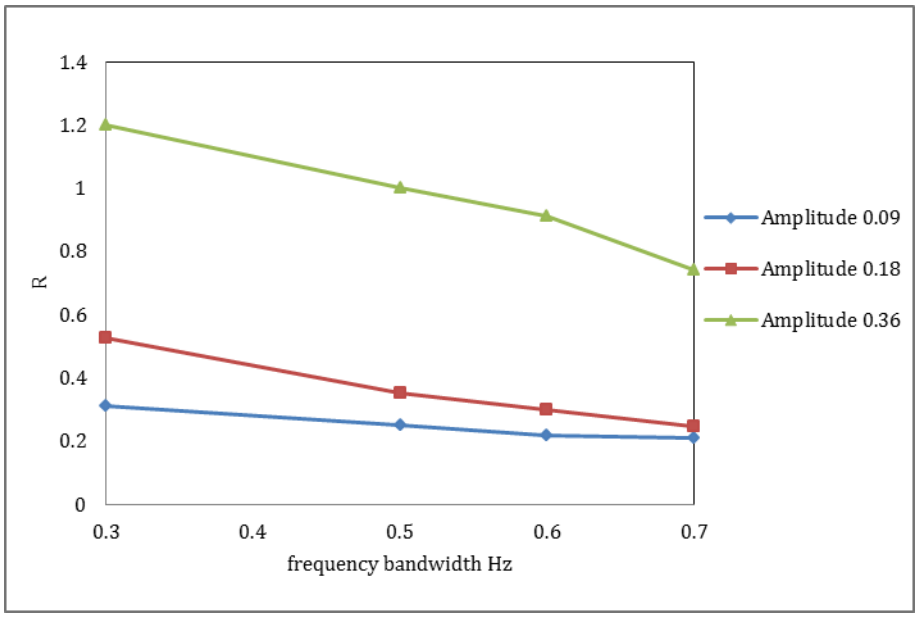

Figure 5.26 Variation of wave run-up at point a4 with different frequency bandwidth Δf

5.3.4.3 Wave Run-up around the Cylinder Surface

After investigating the effect of focused wave parameters on the wave run-up on a vertical cylinder at the wave gauge a4, the research moves to comparing the maximum wave run-up around the cylinder surface.

Figure 5.27, Figure 5.28 and Figure 5.29 show the variations of wave run-up around the cylinder with different degrees of input wave amplitudes for case B, case D and case E. The results obtained from chapter 4 have shown that the wave steepness is a general parameter to express the nonlinear behaviour of a freak wave group.

The computational results show that the steeper the wave, the larger the wave run-up at α =180° and 225°, and the smaller the wave run-up at the position near α =315° in all the 12 cases. In other words, the difference between the maximum and minimum wave run-up in five wave gauges around the cylinder surface rises with increased input amplitude. At the back side of the cylinder surface, where the wave gauge e4 is set, the increased wave steepness raises the wave run-up largely in case B, case D and case E.

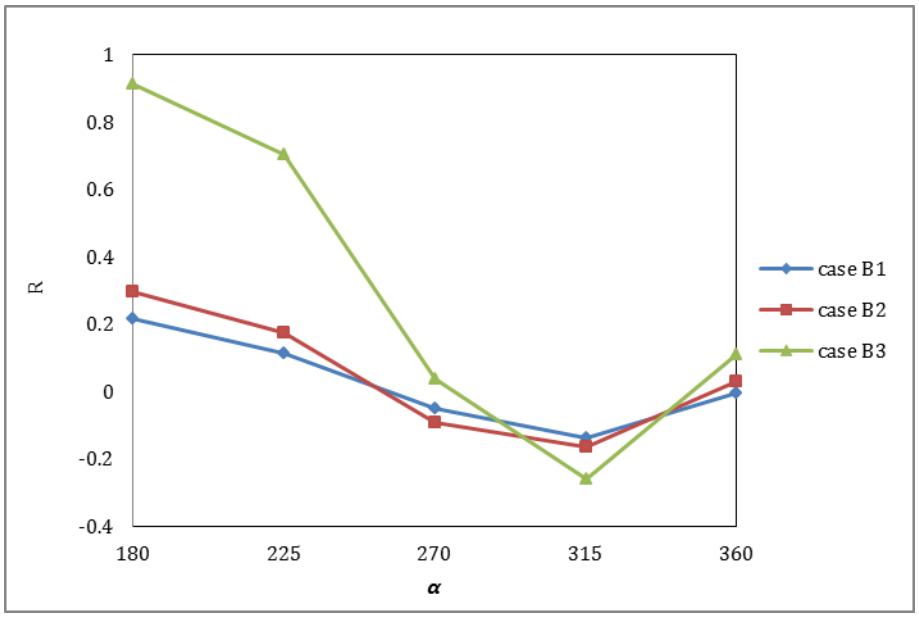

Figure 5.27 Variations of maximum wave run-up with different degrees of input wave amplitude around cylinder for case B

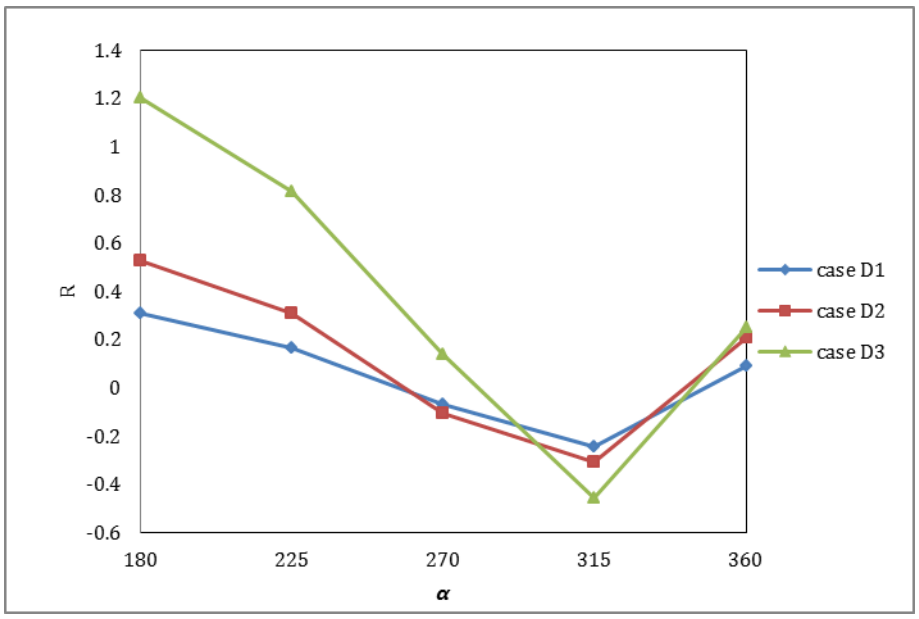

Figure 5.28 Variations of maximum wave run-up with different degrees of input wave amplitude around cylinder for case D

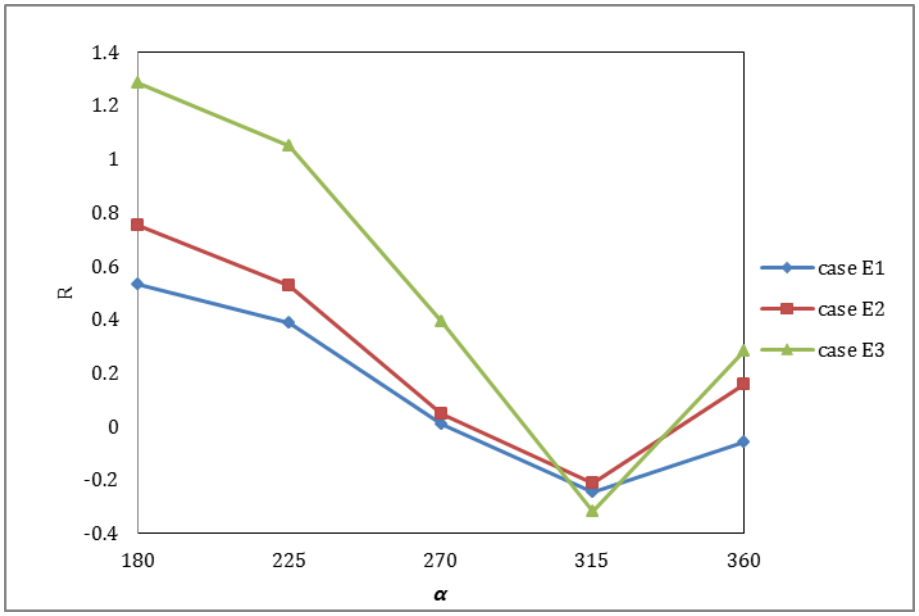

Figure 5.29 Variations of maximum wave run-up with different degrees of input wave amplitude around cylinder for case E

5.3.4.4 Wave Field around the Cylinder

Figure 5.30 shows a visualization of the wave run-up around a cylinder at the focused time to illustrate how the freak wave run-up wraps. The narrow-

banded case D3 is selected as the example. Due to the highly nonlinear phenomenon, the jet-like wave run-up and a highly nonlinear wave structure interaction behaviour is clearly observed.

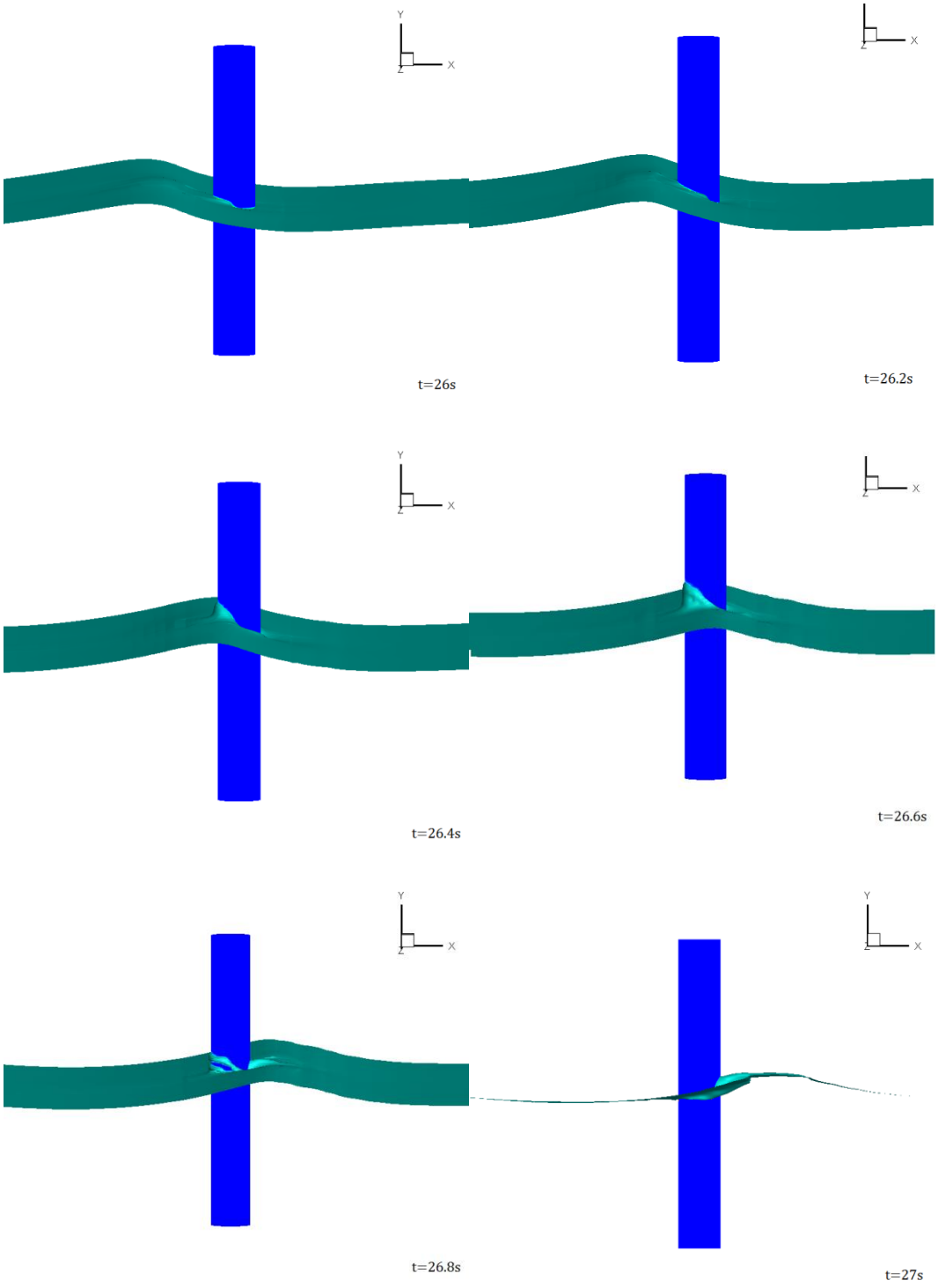

Figure 5.30 Visualization of freak wave run-up around a cylinder (wave propagates from left to right)

5.3.4.5 Effect of Focused Position on Freak Wave Run-up

Figure 5.31 and Figure 5.32 show the comparison of time histories of wave elevation measured at wave point a4 and e4 for three freak wave groups focusing at different positions. The freak wave case D4 focuses at the cylinder front side at x=19.54m. For case D2, the focal position is x=20m, and the focused position of freak wave case D5 is at the cylinder back side x=20.46m. The computational results show that at a4, the closer the wave group focused position moves to the front cylinder, the larger the maximum wave run-up appears. At wave gauge e4, the closer the wave group focused position moves to the front cylinder, the smaller the maximum wave run-up occurs.

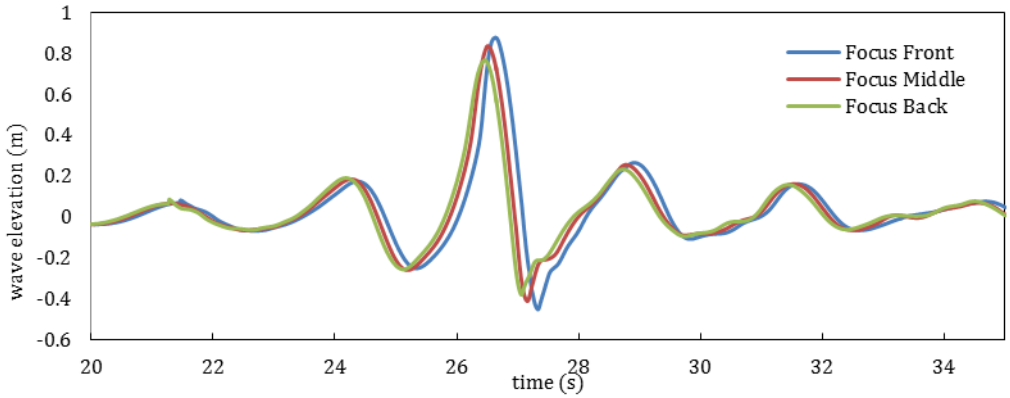

Figure 5.31 Comparisons of wave elevation measured at a4 for three freak wave group focusing positions

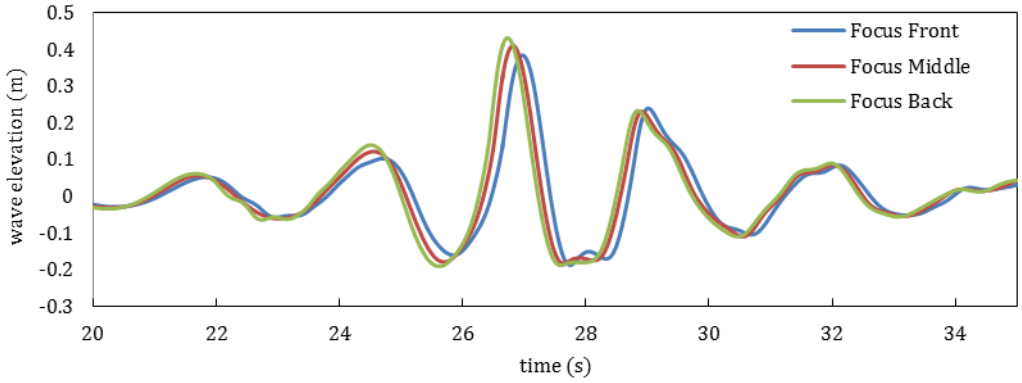

Figure 5.32 Comparisons of wave elevation measured at e4 for three freak Wave group focusing positions

5.3.4.6 Horizontal Freak Wave Force

The accurate prediction of the wave loading on structures is extremely important for design purposes. To analyse the freak wave impacting on a vertical cylinder, a non-dimensional parameter is used to present the normal and transverse forces. The non-dimensional normal force F_x and transverse force F_y can be expressed in a standard form:

$$F_x = \frac{f_x}{\rho g A a^2}$$

$$F_y = \frac{f_y}{\rho g A a^2} \tag{5.3.2}$$

Where, f_x and f_y are the experimental significant normal and transverse wave forces, respectively. On the cylinder, ρ is the water density; g is the gravitational acceleration; A is the incident wave amplitude and a is the radius of the cylinder.

5.3.4.6.1 Effect of Wave Steepness on Freak Wave Force

Figure 5.33 shows the variations of non-dimensional focused normal wave force on a cylinder for cases with different values of wave steepness. The computational results show that increased wave steepness raises the freak wave normal forces dramatically for cases D and E, while this phenomenon is not obvious for case B.

5.3.4.6.2 Effect of Frequency Bandwidth on Wave Force

Figure 5.34 illustrates the variation of freak wave force for cases with different frequency bandwidths. The computational results show that the increased frequency bandwidth reduces the nonlinear behaviour of a freak wave group, which decreases the wave normal force further. The freak wave non-dimensional normal force for narrow frequency banded case D3 is 5.5, and the non-dimensional normal force is 3.8 for board frequency banded case B3 with the same input amplitude.

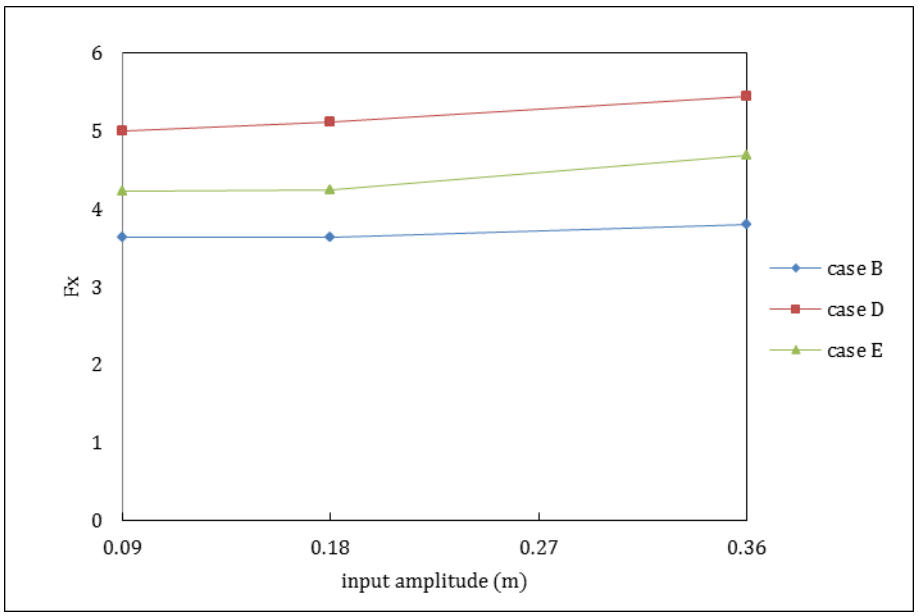

Figure 5.33 Variations of non-dimensional focused normal wave force on cylinder for cases with different wave steepness

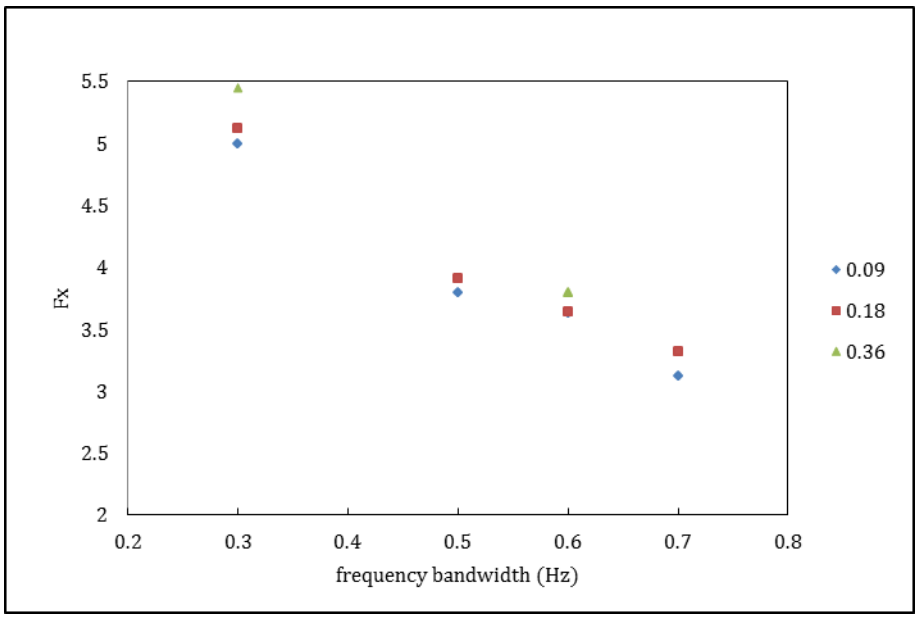

Figure 5.34 Variations of non-dimensional focused normal wave force on cylinder for cases with different frequency bandwidth

5.3.4.6.3 Effect of Focused Position on the Freak Wave Normal Force

Figure 5.35 illustrates the time history of horizontal wave force on the cylinder for freak wave case D2, case D4 and case D5. The computational results show that when the focal position of the freak wave group moves from the front

cylinder side to the back-cylinder side, the maximum horizontal freak wave forces increase.

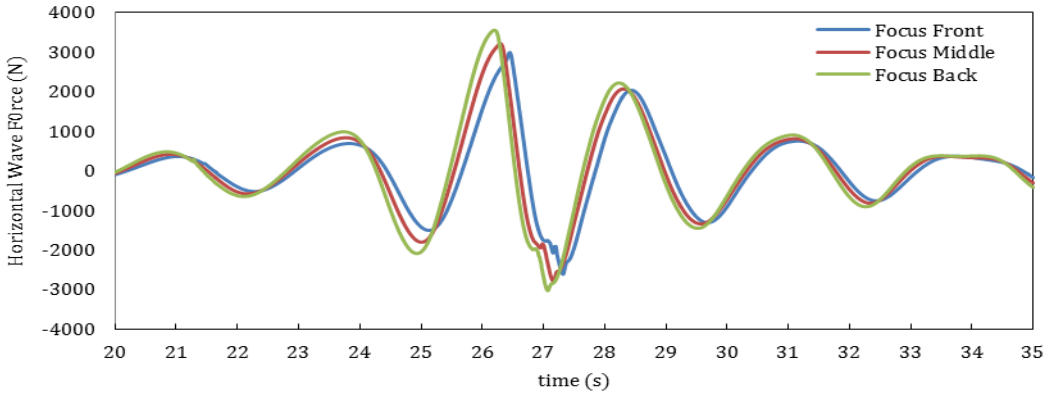

Figure 5.35 Time history of horizontal wave force on cylinder for three different focusing positions

5.4 Freak Wave Run-up on a Pair of Two Cylinders

After researching a freak wave running up a vertical cylinder, the interactions between a focused wave group and a pair of cylinders are investigated. In particular, how the focused wave parameters, including wave steepness, frequency bandwidth and focused position, impact the wave run-up on a cylinder are analysed.

5.4.1 Geometric Model

The detailed configuration of a pair of cylinders in the numerical wave tank is shown in Figure 5.36, and the meshing configurations are shown in Figure 5.37 and Figure 5.38. A pair of vertical cylinders is fixed in the wave tank with two different radial distances. Only the small size cylinders are considered in these cases, and the middle position between the two cylinders is located at x=20m.

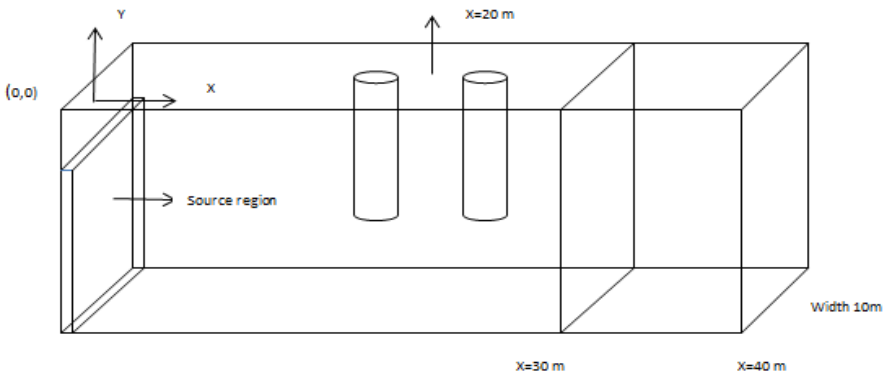

Figure 5.36 Detailed configuration of a pair of two cylinders

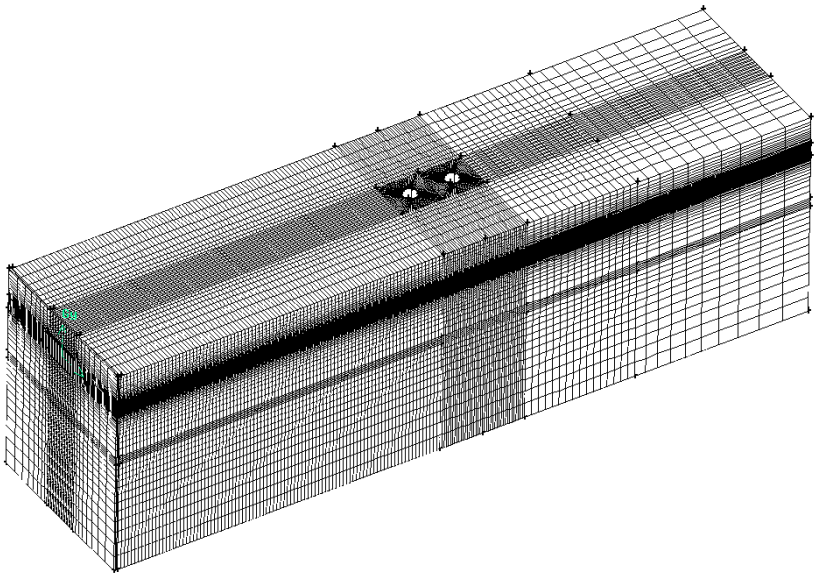

Figure 5.37 Global meshing configuration of the numerical wave tank

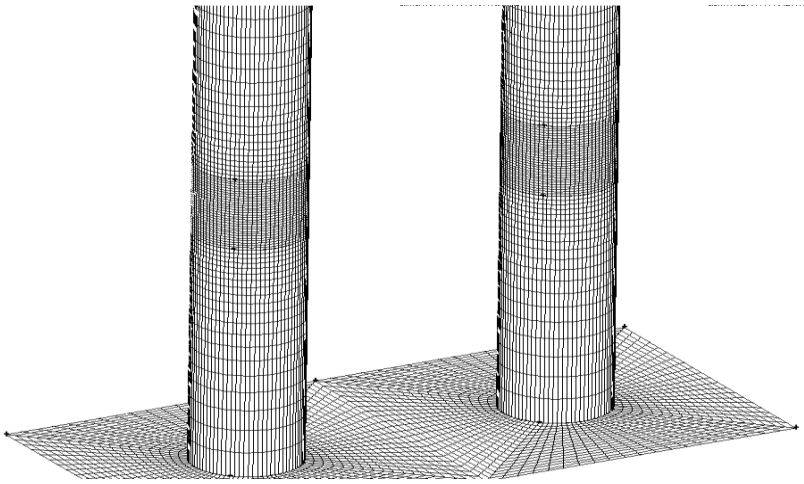

Figure 5.38 Detailed meshing configuration around the two cylinders

5.4.2 Sketch of Numerical Test Set-up

Figure 5.39 shows the sketch of the numerical test set-up. A total of 41 different wave gauges are used to measure wave elevations around the cylinder surfaces. Two cylinders with diameters of 0.812m are placed. The cylinder which is directly facing the waves is referred to as 'Cylinder 1'and the one on the backside is 'Cylinder 2'.

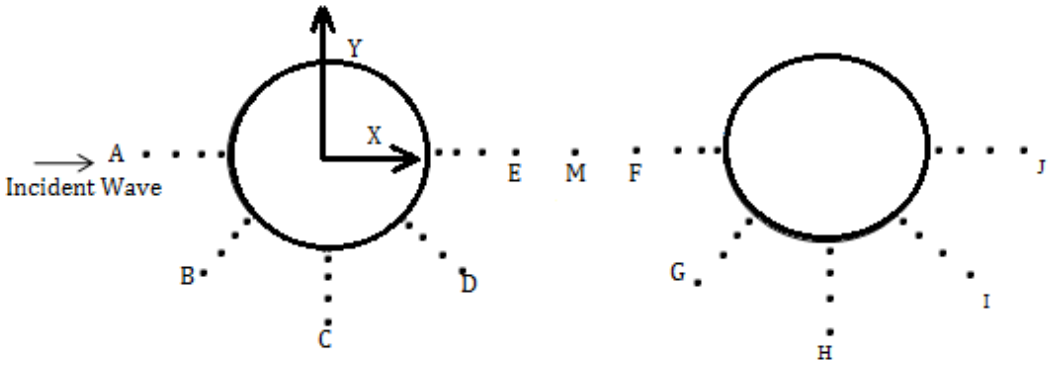

Cylinder 1 Cylinder 2

Figure 5.39 Sketch of numerical test set-up.

5.4.3 Input Freak Wave Parameter

The different cases allocated by different input parameters, including input wave steepness, frequency bandwidth, cylinder distance, and focused positions, are shown in Table 5.7. In case I4, the freak wave train focuses at the centre of cylinder 1 and the focal position of case I5 is the centre of cylinder 2. Among the other cases, the freak wave groups are all focusing at the middle position of the two cylinders. In cases J1, J2, J3 and J4, the distance between the two cylinders is 2.436m, but the distance between the two cylinders for all the other cases is 1.624m.

Table 5.7 Input freak wave parameters

Case	A (m)	Δf (Hz)	Cylinder centre distance (m)	Focused position
F	0.18	0.7	1.624 (2D)	Cylinder middle
G1	0.09	0.6	1.624 (2D)	Cylinder middle
G2	0.18	0.6	1.624 (2D)	Cylinder middle
G3	0.36	0.6	1.624 (2D)	Cylinder middle
H	0.18	0.5	1.624 (2D)	Cylinder middle
I1	0.09	0.3	1.624 (2D)	Cylinder middle
I2	0.18	0.3	1.624 (2D)	Cylinder middle
I3	0.36	0.3	1.624 (2D)	Cylinder middle
I4	0.18	0.3	1.624 (2D)	Front cylinder
I5	0.18	0.3	1.624 (2D)	Back cylinder
J1	0.18	0.7	2.436 (3D)	Cylinder middle
J2	0.18	0.6	2.436 (3D)	Cylinder middle
J3	0.18	0.5	2.436 (3D)	Cylinder middle
J4	0.18	0.3	2.436 (3D)	Cylinder middle

5.4.4 Results and Discussion

5.4.4.1 Wave Run-up Tendency

Concentrating on the phenomenon of freak wave run-up on a pair of cylinders, the maximum wave run-up ratio during the simulation time is shown in Figure 5.40, with case G3 used.

The wave run-up tendency in line a and line b is almost the same as in line f and line g, which are all in the upstream incident wave direction. The wave run-up ratio increases when the extreme wave train propagates to the cylinder surface. For both the front cylinder and the back cylinder, the maximum wave run-up happens at the wave measurement point in the upstream incident wave

direction closest to the cylinder surface place. In lines c, d, h and I, the wave run-up decreases when the extreme wave train propagates to the cylinder surface. In lines e and j, at the back of the cylinder surface, the wave run-up is almost maintained at the same level. Generally, the maximum wave elevations measured at wave gauges around the front cylinder are larger than the corresponding values measured around the back cylinder in case G3.

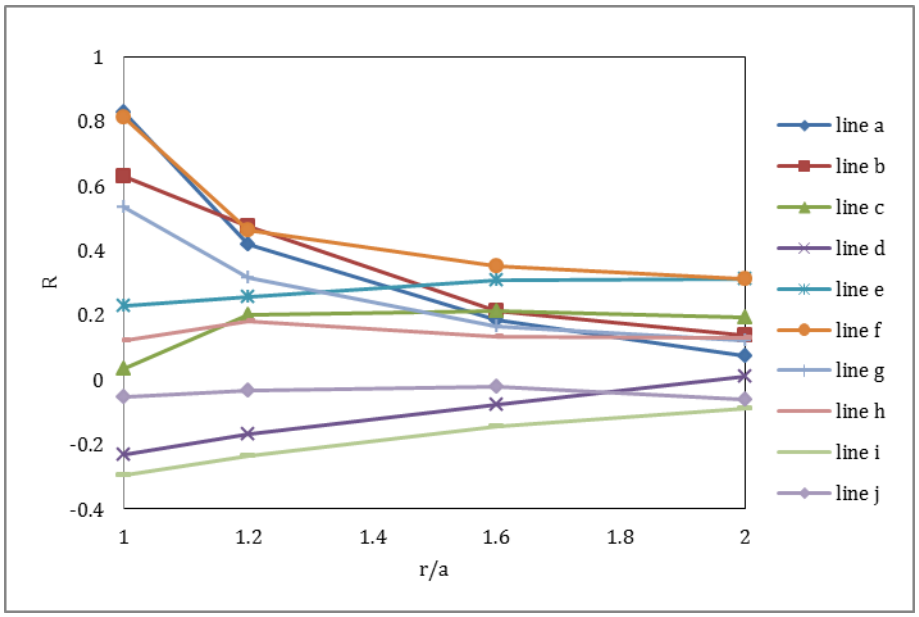

Figure 5.40 Maximum wave run-up ratio measured at all wave gauges for freak wave case G3

5.4.4.2 Wave Run-up around the Cylinder

After introducing the general tendency of a focused wave train running up a pair of cylinders, the research moves to comparing the maximum wave run-up around the cylinder surface.

5.4.4.2.1 Effect of Wave Steepness on the Wave Run-up

Figure 5.41 and Figure 5.42 illustrate the wave run-up around the two cylinders with varying degrees of wave steepness for freak wave case G and case I. The computational results show that the effect of wave steepness on the wave run-up depends on the wave elevation measuring positions around the cylinder surface.

The freak wave run-up tendency around cylinder 1 is similar to the numerical results obtained from the freak wave running-up a single cylinder case. The computational results show that the steeper the input wave amplitude, the larger the wave run-up at the cylinder front places at α =180° to 225° measured at wave gauges a4 and b4, and the smaller the wave run-up at position α =315° measured at wave measurement point d4. At the back side of the cylinder, at the position α =360° measured at wave gauge e4 with the increase of input wave steepness, the wave amplification increases dramatically. In case I3, the wave run-up ratio at wave point e4 is 0.52 and the corresponding ratio value measured in case I1 is 0.27.

Around the back of cylinder 2, the wave elevation measured at wave gauges f4, g4, h4 and i4 have the same wave run-up tendency as the front cylinder. However, at wave point j4, the measured wave run-up is almost maintained at the same level by different input amplitudes and the wave amplification phenomenon is not obvious.

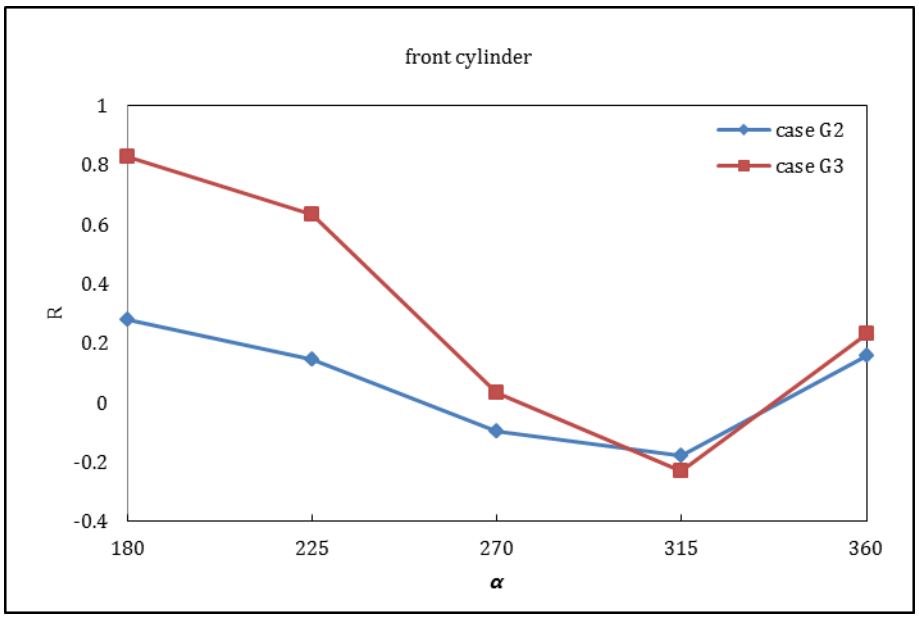

(a) Wave run-up around the front cylinder

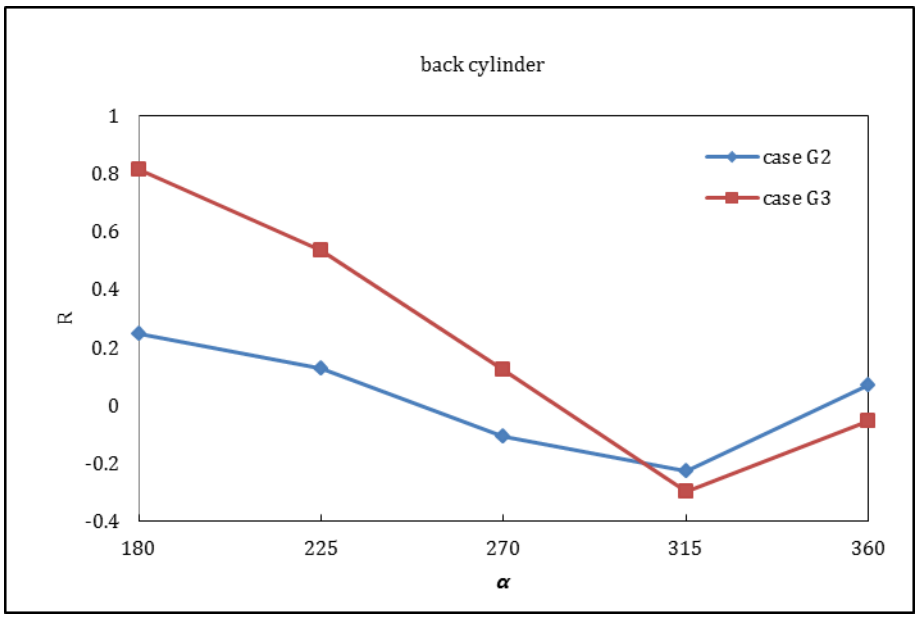

(b) Wave run-up around the back cylinder

Figure 5.41 Wave run-up around the two cylinders with varying degrees of wave steepness for freak wave case G

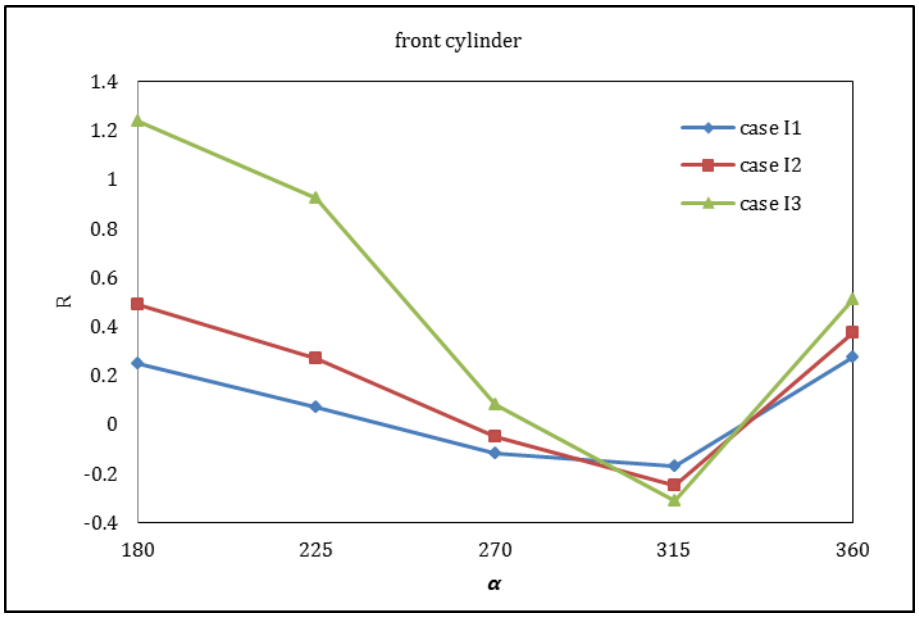

(a) Wave run-up around the front cylinder

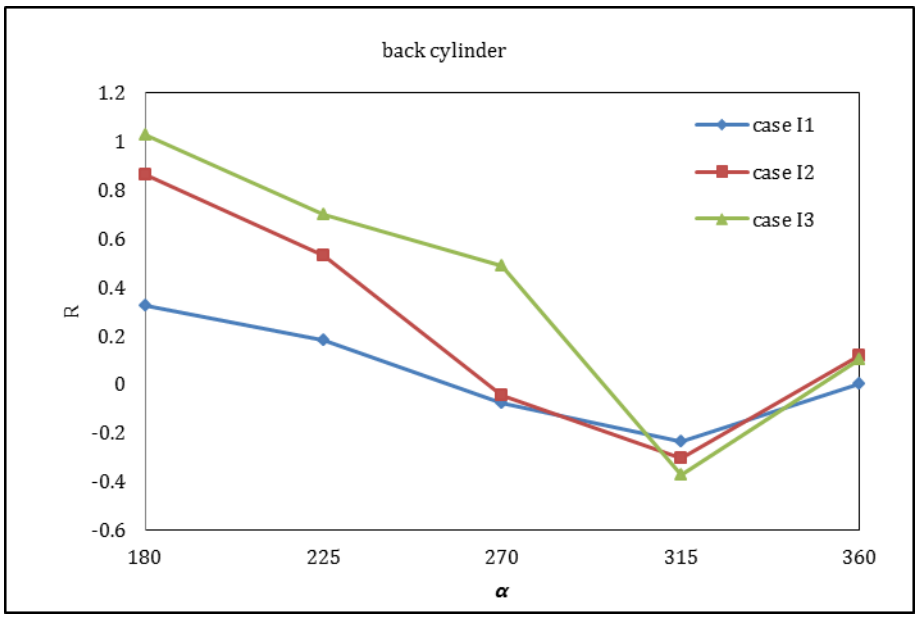

(b) Wave run-up around the back cylinder

Figure 5.42 Wave run-up around the two cylinders with varying degrees of wave steepness for freak wave case I

5.4.4.2.2 Effect of Focused Positon on the Wave Run-up

Figure 5.43 shows the variation of maximum wave run-up ratios to illustrate the effect of the focused position on the wave run-up around the two cylinders. Case I2, I4 and I5 are considered in this regard. The computational results show that when the freak wave group focuses at the centre of cylinder 1, the wave run-up measured at wave gauges a4, b4, c4 and d4 are the same as the computational results obtained from the freak wave single cylinder case D2. However, at wave point e4, as the distance between the two cylinders is small, the reflected wave from the back cylinder will disturb the flow regions at the back of the front cylinder area. The simulated wave run-up ratio in case I4 at wave point e4 is 0.33, which is much larger than the corresponding value measured in single cylinder case D2.

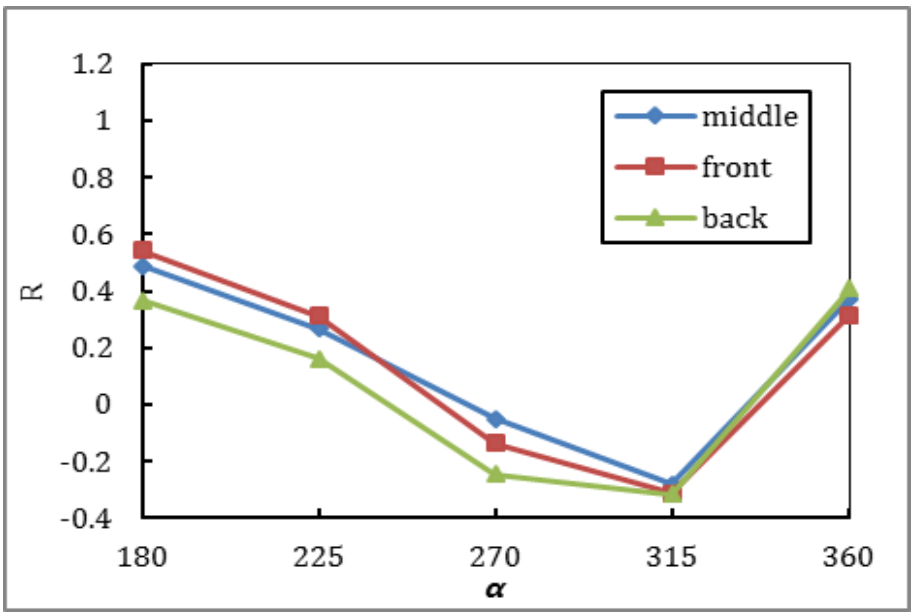

(a) Wave run-up around the front cylinder

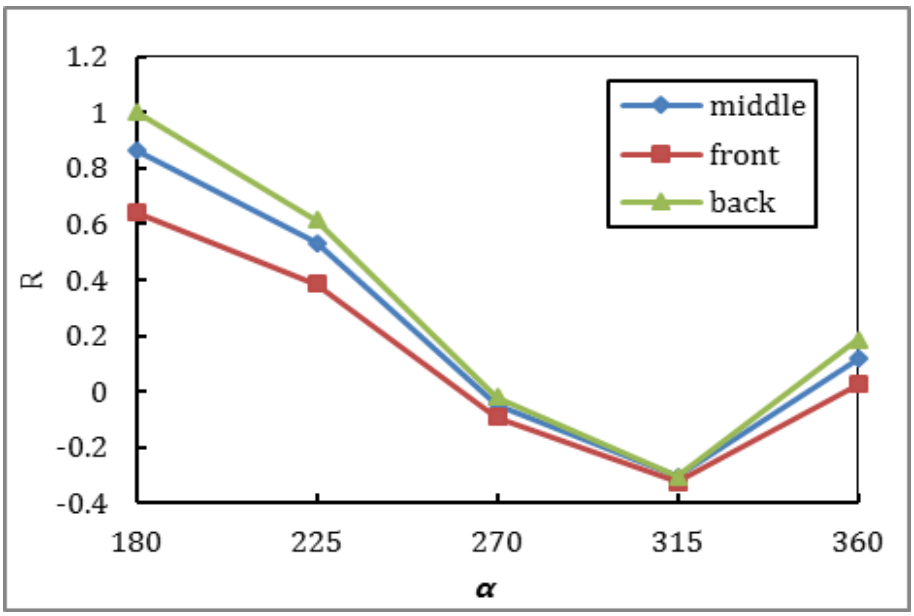

(b) Wave run-up around the back cylinder

Figure 5.43 Variation of wave run-up around the two cylinders with different wave focused positions for case I2, I4 and I5

It can be seen from Figure 5.43 (a) that around the front cylinder in the range α = [180°, 225°], the closer the wave group focused position moves to the front cylinder, the larger the wave run-up appears. However, at α = 360°, it has an

opposite tendency; the closer the wave group focused position moves to the front cylinder, the smaller the wave run-up appears.

In Figure 5.43 (b), the numerical results show clearly that around the back cylinder, in all the five wave elevation measurement points, the closer the wave group focused position moves to the back cylinder, the larger the wave run-up appears. At the incident wave facing point f4, the wave run-up ratio is 1 when the wave group focuses at the centre of the back cylinder. However, at the same point the measured wave run-up ratio is only 0.64 when the wave group is predetermined to focus at the centre of the front cylinder.

5.4.4.3 Horizontal Freak Wave Force

5.4.4.3.1 Effect of Frequency Bandwidth on Freak Wave Force

To analyse the effect of frequency bandwidth on the horizontal wave force on a pair of cylinders, Figure 5.44 shows the variations of non-dimensional horizontal focused wave forces for the freak wave groups with different frequency bandwidths. The numerical results show that for all the cases illustrated in this section, the decreased frequency bandwidth results in an obvious increase in non-dimensional horizontal focused wave force for both cylinders. This is because when the frequency bandwidth in a wave group decreases, the nonlinear behaviour of this wave group becomes stronger, which will further result in a larger wave impact force. This phenomenon is much more obvious when the frequency bandwidth declines from 0.5Hz to 0.3Hz. On the front cylinder, when the incident focused wave group changes from case freak wave case H to freak wave case I2, the non-dimensional wave force increases from 4.23 to 5.45 with an increase of 30%. On the back cylinder, this increase is 48%.

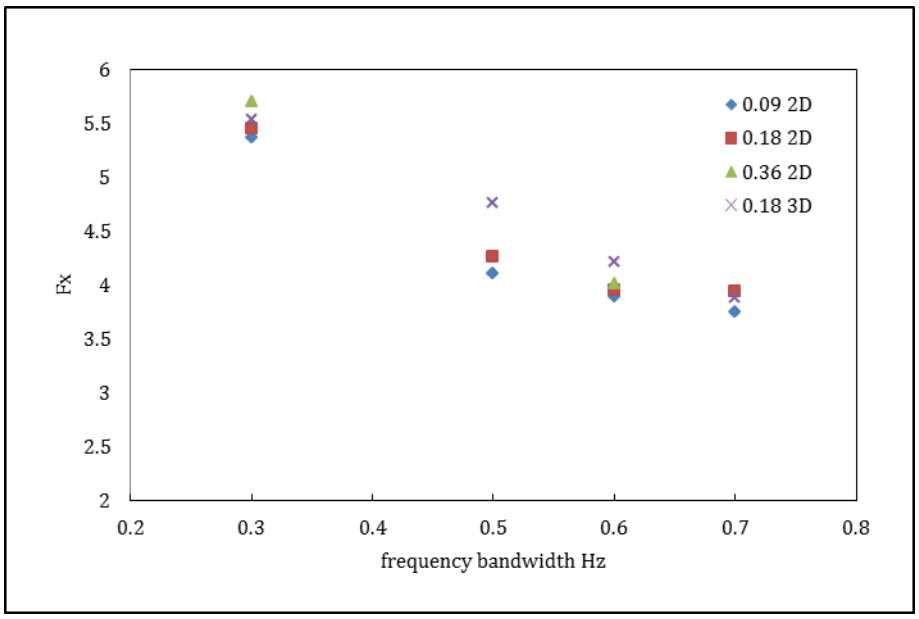

(a) Freak wave force on front cylinder

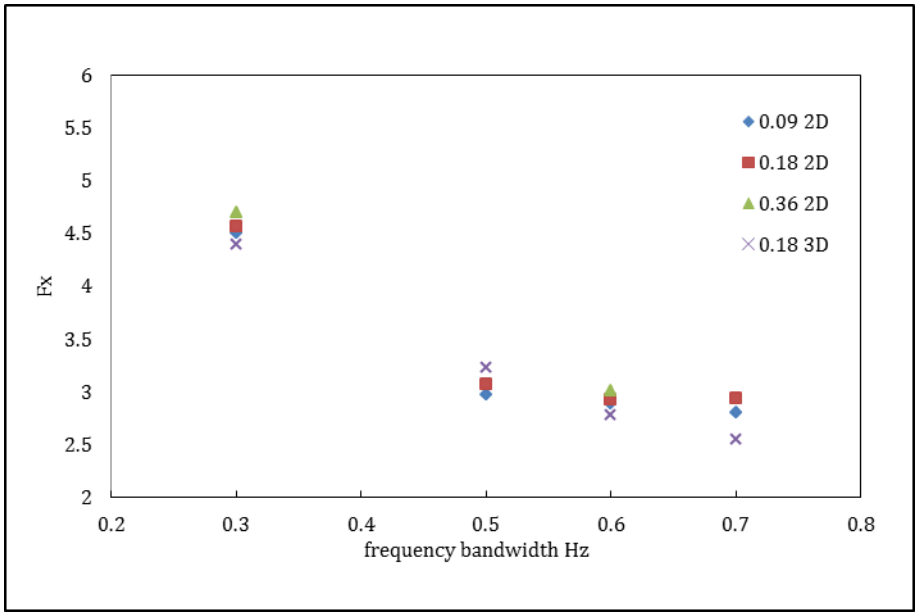

(b) Freak wave force on back cylinder

Figure 5.44 Variations of non-dimensional horizontal focused wave force for the freak wave groups with different frequency bandwidths

5.4.4.3.2 Effect of Focused Position on the Wave Forces

To illustrate the effect of focused position on wave forces, Figure 5.45 and Figure 5.46 show a comparison of time histories of focused wave force on a pair of cylinders for cases I2, I4 and I5. The computational results show that on the

front cylinder, when the focal positon of the wave group moves from the centre of cylinder 1 to the centre of cylinder 2, the maximum positive horizontal wave force impacting on the cylinder increases, while the maximum negative force decreases. For the back cylinder, the effect of the focused positon on the focused wave horizontal force is the same as the front cylinder 1. When the focal positon of the wave group moves from the centre of the front cylinder to the centre of the back cylinder, the maximum positive horizontal wave force increases, however the maximum negative force decreases on the cylinder.

Figure 5.46 also shows that the time history of the focused wave force profile is not symmetric around the focal time, which is unlike the wave run-up profile. On the back cylinder, after a large slamming force happens around the focal time, another large wave force appears. This two-peak wave force situation will result in large damage to offshore structures. Comparing the impact of focused wave force on a pair of tandem cylinders in the three cases, both cylinders will suffer larger freak wave horizontal forces when the incident wave group focuses around the centre of the back cylinder.

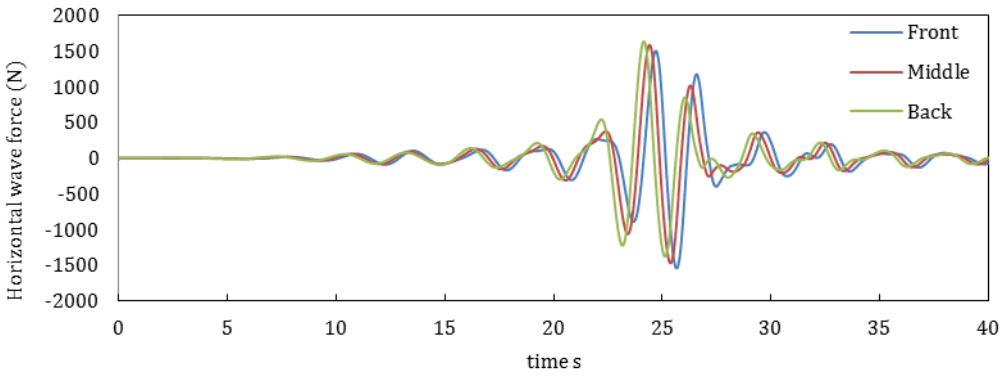

Figure 5.45 Time history of horizontal wave force on front cylinder for three different focusing positions

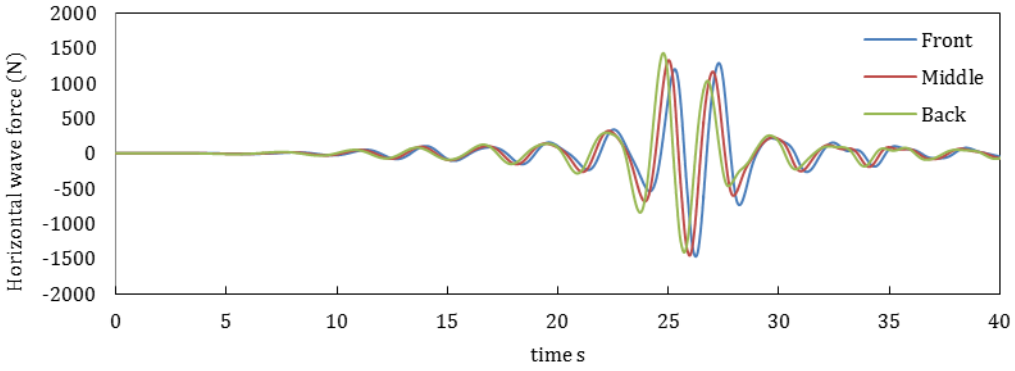

Figure 5.46 Time history of horizontal wave force on back cylinder for three different focusing positions

5.4.4.4 Wave Field around the Cylinder

Figure 5.47 shows a visualization of freak wave case I3 run-up around the two cylinder surfaces at the focused time. The jet-like wave run-up and high nonlinear wave structure interaction behaviour can be clearly observed.

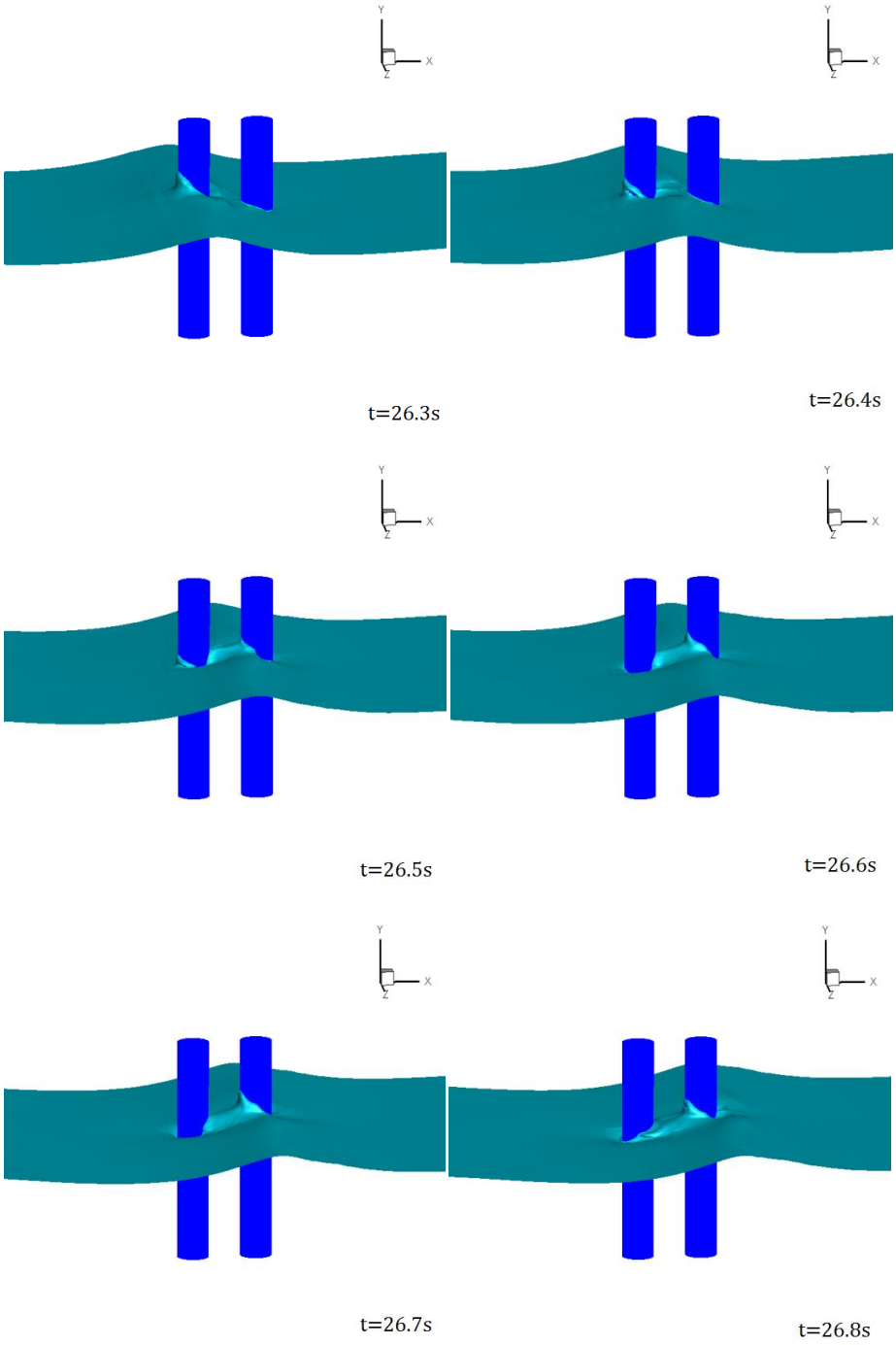

Figure 5.47 A visualization of the wave run-up around a cylinder at the focused time

5.5 Conclusions

In this chapter, the freak wave run-up and wave impacting force on a vertical cylinder and a pair of cylinders are investigated numerically. Several freak wave parameters are considered, such as wave steepness, frequency bandwidth and focused position.

At first, the experiment conducted by Nielsen (2003) to investigate regular wave run-up on vertical cylinder problems is reproduced numerically. The wave run-up results are compared with the experimental data, and the regular wave forces are compared with the results derived from Morrison's equation. The present CFD simulation and experimental wave run-up results around a vertical cylinder have a good agreement, and the first order diffraction theory underestimates the wave run-up dramatically.

Secondly, the freak wave run-up on a single cylinder is investigated numerically. 17 different freak wave conditions, such as wave steepness, frequency bandwidth and focusing position, are considered. The wave run-up tendency for all cases is almost the same. The maximum wave run-up appears at the front of the cylinder point a4 (α=180°), and the minimum wave run-up appears at the position α=315° close to the cylinder surface position d4. The increased wave steepness and decreased wave frequency bandwidth grow the nonlinear behaviour of the freak wave group, which increases wave run-up at wave point a4 and b4 further. At the same time, the increased wave nonlinear behaviour reduces the wave run-up level at wave point d4. The computational results also show that the increased nonlinear behaviour of the wave group raises the freak wave non-dimensional normal force slightly.

Finally, the freak wave run-up on a pair of cylinders is investigated numerically. The simulation results indicate that the maximum wave elevations measured at wave gauges around the front cylinder are larger than the corresponding values measured around the back cylinder. The numerical results show that the freak wave focusing position has a definite effect on wave run-up. The closer the wave focal position moves to the front cylinder, the larger the wave run-up appears in

the range α= [180°, 225°], and the smaller the wave run-up α=360° around the front cylinder. However, around the back cylinder, the closer the focal position moves to back cylinder, the larger the wave run-up appears in all the wave gauges. The numerical results also indicate that the horizontal freak wave force profile is not symmetric around the focal time, while the wave run-up profile is nearly symmetric with the incident freak wave profile.

6 Floating Structure under a Freak Wave Train

6.1 General Remarks

With the development of LNG production, the LNG sloshing excited by the ship motion has become one of the most important research interests in the field of ocean engineering. The coupling effect of sloshing tanks and ship motions under regular wave conditions have been investigated by many authors, both experimentally and numerically. In most of the numerical studies such as Zhao et al. (2014), Lee and Kim (2010) and Jiang et al. (2015), the ship motion is calculated from the potential boundary element method, which may underestimate the LNG ship motion under high nonlinear wave conditions. Therefore, it is essential to develop a new numerical tool to simulate the coupling effects of ship motions and tank sloshing under high nonlinear freak wave conditions.

At first, two validation cases are conducted. The experiment conducted by Liu and Lin (2008) to investigate liquid sloshing in a 2-D rectangular tank is reproduced numerically. The accuracy of the current numerical method in simulating a sloshing case under horizontal excitation should be proved. The second validation case is going to be done in a numerical wave tank, and the rolling response of a 2D rectangular body under regular waves are calculated and compared with the experimental data.

Secondly, three different freak waves are going to be generated in this numerical wave tank. After this, the rolling response of a rectangular structure under a freak wave train is going to be analysed, and the effect of focused wave factors, frequency bandwidth and peak frequency on the global floating body response will be analysed.

Finally, the coupling effects of the 2-D rectangular body rolling motion and tank sloshing are going to be investigated. In this present work, the research focuses on the global floating body response. Two different filling levels are considered. The numerical results are compared with those conditions without sloshing to

investigate the coupling effects on the rectangular body rolling motion under freak wave conditions.

6.2 Validation

To validate the developed numerical scheme, two models are considered in this section. At first, the accuracy of the current numerical method in simulating a sloshing case under horizontal excitation is proved by comparing the numerical and experimental results. To illustrate the accuracy of the present numerical scheme in simulating the rolling motion behaviour of a floating structure, the roll RAO (response amplitude operator) of a rectangular body is compared with an experiment result in the second case.

6.2.1 Sloshing under Horizontal Excitation

The experiment conducted by Liu and Lin (2008) to investigate liquid sloshing in a 2-D rectangular tank is reproduced numerically. The sketch of the sloshing experiment is shown in Figure 6.1. The tank length is 0.57m and tank height is 0.3m, and the static water depth is 0.15m. The lowest natural frequency (ω_o) of liquid motion in the tank is 6.0578s^{-1}. The tank is fixed on an oscillating sinusoidal motion $x = -a\sin(\omega t)$. The amplitude is 0.005m and the sloshing frequencies ω are $0.583\omega_o$ and $1.0\omega_o$, which correspond to non-resonant and resonant cases, respectively.

The dynamic mesh technique is used to control the tank movement. The no-slip wall condition is imposed on the entire boundary, and laminar flow is used for this numerical simulation. To investigate the grid convergence, three different meshes involving 56×60, 70×75 and 114×150 cells in the x- and z-directions are considered and shown in Table 6.1.

Figure 6.2 shows the results of the free surface elevation at Point H2 against time in three different mesh conditions. It can be seen that the numerical results with the different meshes approach the experimental results gradually. In addition, the values obtained by medium and fine grids lie closely to each other, which suggests that a convergent solution is achieved by the present model, and the mesh of 70×75 can be used in the following calculations.

The numerical wave elevation results are compared with the experimental data at H1, H2 and H3 for the two cases shown from Figure 6.3 to Figure 6.8. It can be seen that the numerical results and experimental results have a good agreement.

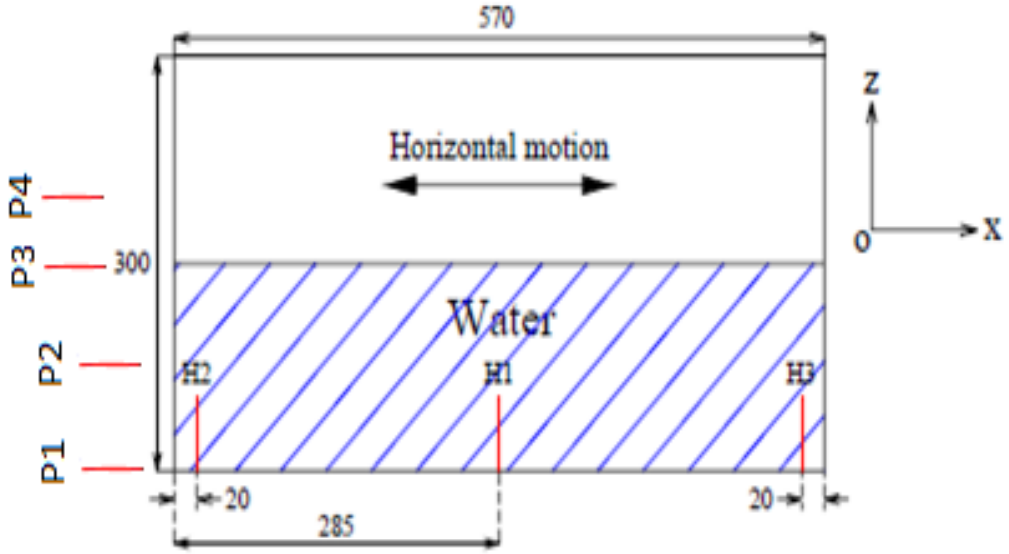

Figure 6.1 Sketch of the sloshing experiment

Table 6.1 Meshes conditions in the gird dependence study

Grid	x × z	δx	δz	Total elements number
Coarse	56×60	0.01	0.005	3360
Medium	70×75	0.008	0.004	5250
Fine	114×150	0.005	0.002	17100

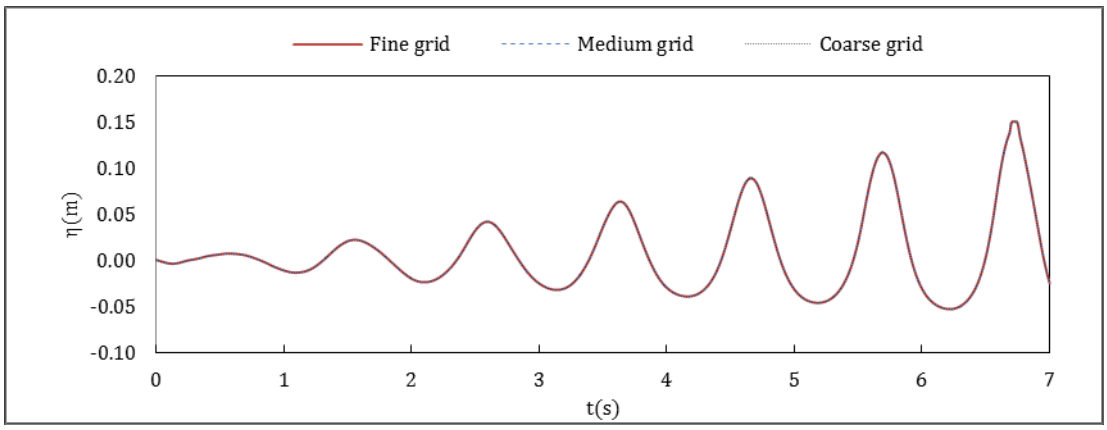

Figure 6.2 Free surface elevations at point H2 against time in three different mesh conditions

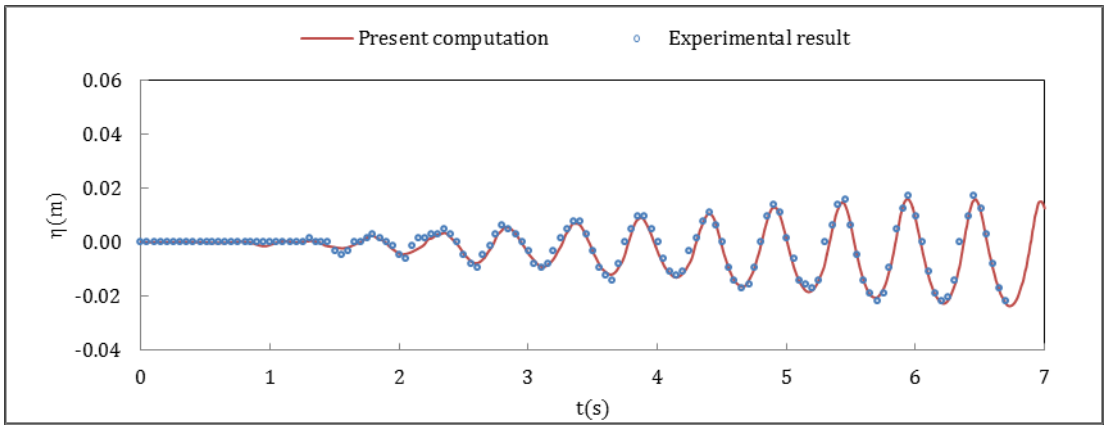

Figure 6.3 Wave elevation comparisons at H1 for case 1

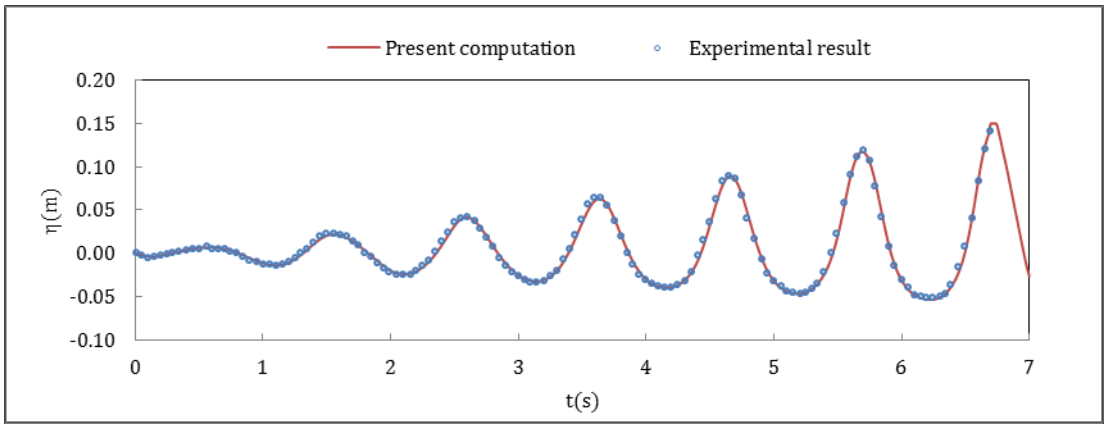

Figure 6.4 Wave elevation comparisons at H2 for case 1

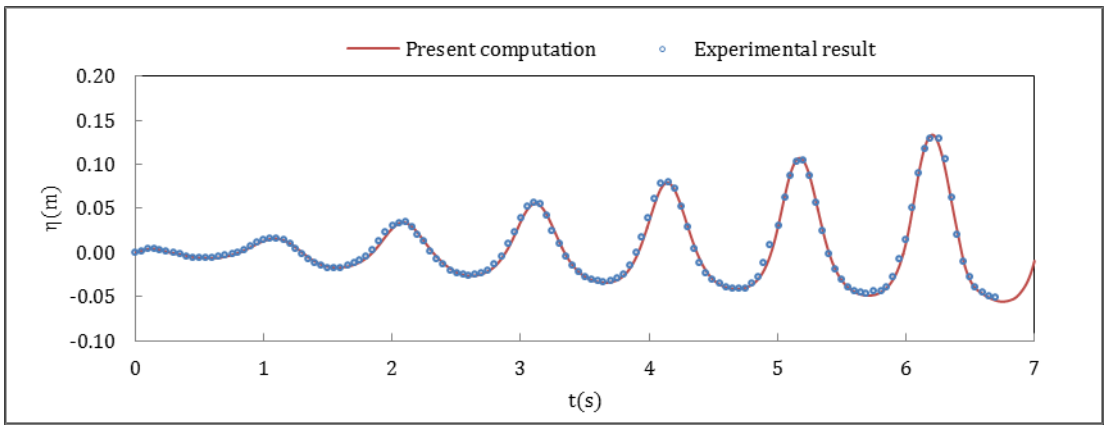

Figure 6.5 Wave elevation comparisons at H3 for case 1

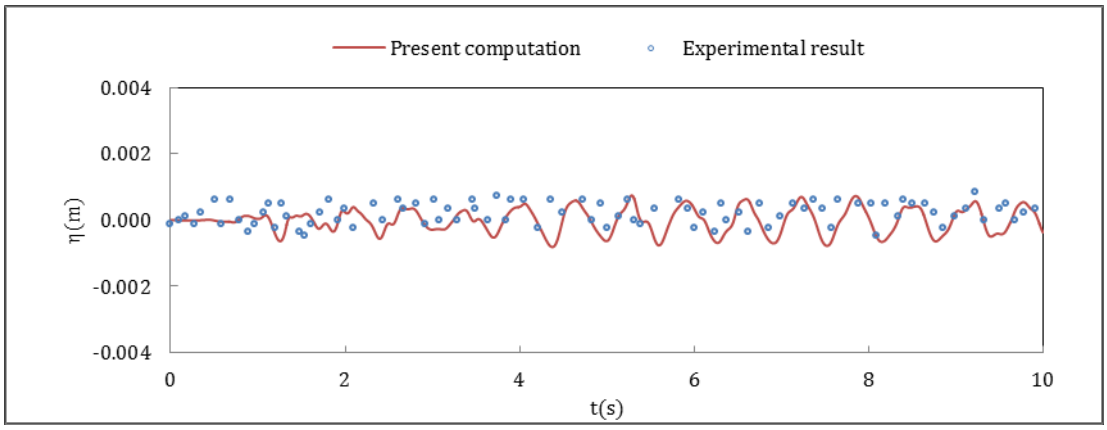

Figure 6.6 Wave elevation comparisons at H1 for case 2

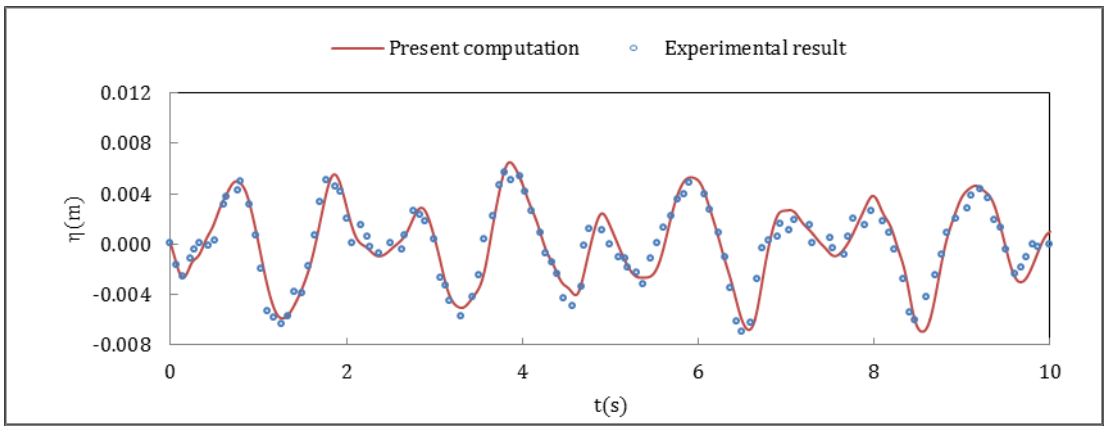

Figure 6.7 Wave elevation comparisons at H2 for case 2

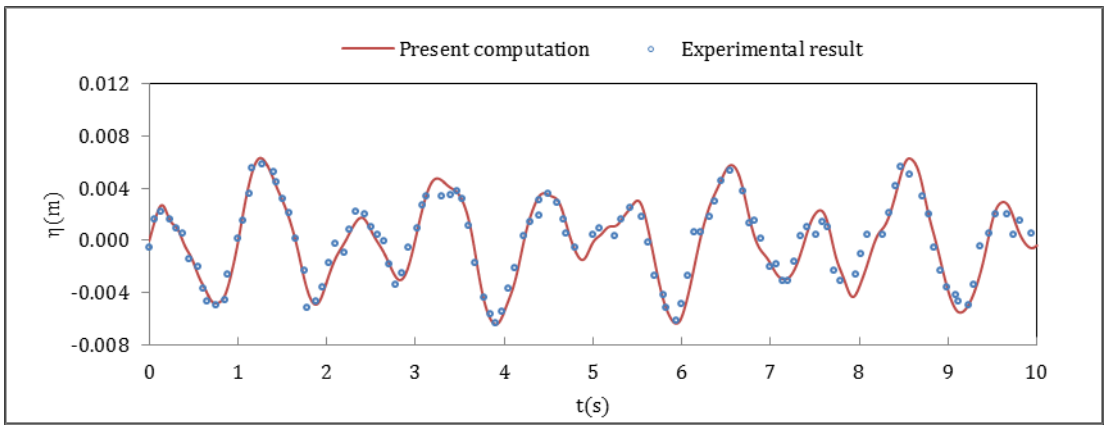

Figure 6.8 Wave elevation comparisons at H3 for case 2

6.2.2 Rectangular Body Roll Motion under Regular Waves

6.2.2.1 Experiment Set-up

The experiment conducted by Jung (2006) to investigate the rolling motion of a rectangular structure is reproduced numerically. The experiment was performed in a glass-walled wave tank. The tank is 35m long, 0.9m wide and 1.2m deep, and the sketch of the wave tank is shown in Figure 6.9. A dry back-flap type wave maker is installed at the left end of the tank.

The detailed set-up of free rolling structure is shown in Figure 6.10. A rectangular structure with dimensions of 0.900m long and 0.300m wide (B) was used as a scaled down barge in the experiments, as shown in Figure 6.10. In the experiment, the wave propagates from left to right. The structure was located at 20m from the wave maker with its width across the entire width of the wave tank, equivalent to the barge in a beam sea condition, so the flow can be treated as two dimensional. The water depth (h) was kept at 0.900m throughout the experiments. The structure was mounted on the tank walls with bars and a pair of hinges through the centre of gravity of the structure (0.05m from the keel). The hinges were adjusted so the axis aligned with the calm water level. Consequently, the structure floated at a draft D=0.05m. The hinges allowed the structure to roll and aligned with the water level, but restrained it from heaving and swaying motions.

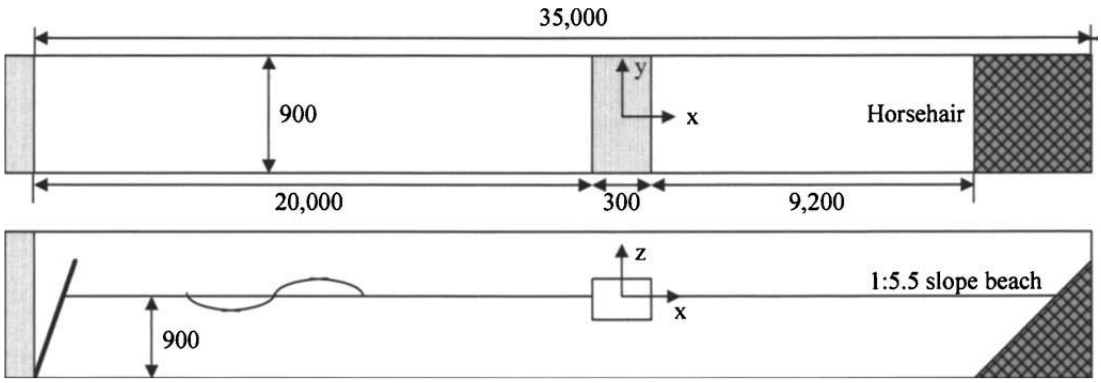

Figure 6.9 Sketch of wave tank by Jung (2006)

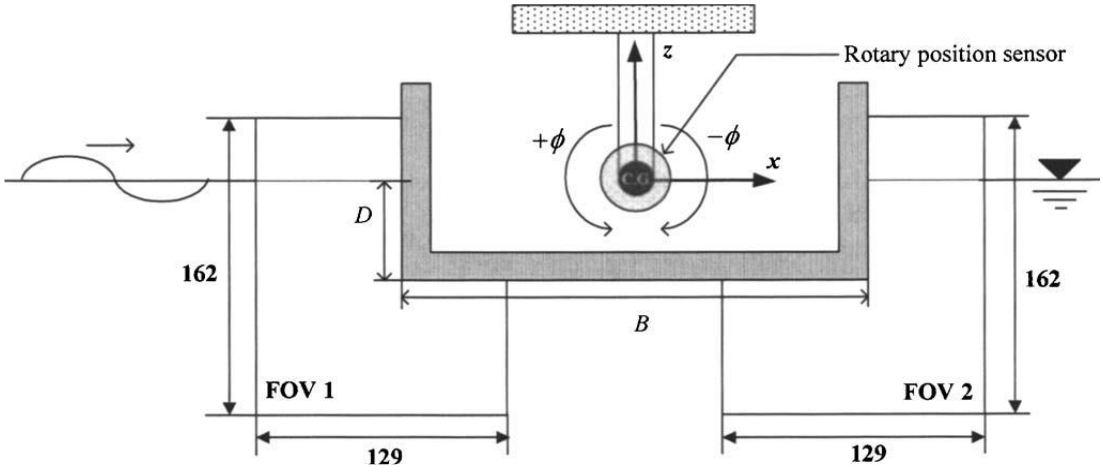

Figure 6.10 Setup of free rolling structure with coordinate system by Jung (2006)

6.2.2.2 Numerical Wave Tank Set-up

The sketch of the 2-D numerical wave tank is shown in Figure 6.11. In this part, the paddle wave making method is used for regular wave generation. The total wave tank length is 20m, and the wave damping domain is 5m long. The rectangular body with the same dimensions as the experimental one is located at x=7m, and the wave making paddle length below the free surface is 1m. The detailed meshing configuration around the paddle and near the free surface is shown in Figure 6.12. To simulate the paddle motion, the unstructured triangle mesh is used in the wave making domain, while the structured quadrilateral mesh is used in the working domain. The detailed meshing configuration around the rectangular body is shown in Figure 6.13. In the present work, the interface technique is used to simulate the body roll motion. The meshes in the

motion domain are moved with the rectangular body motion, while the meshes in the working domain remain stationary.

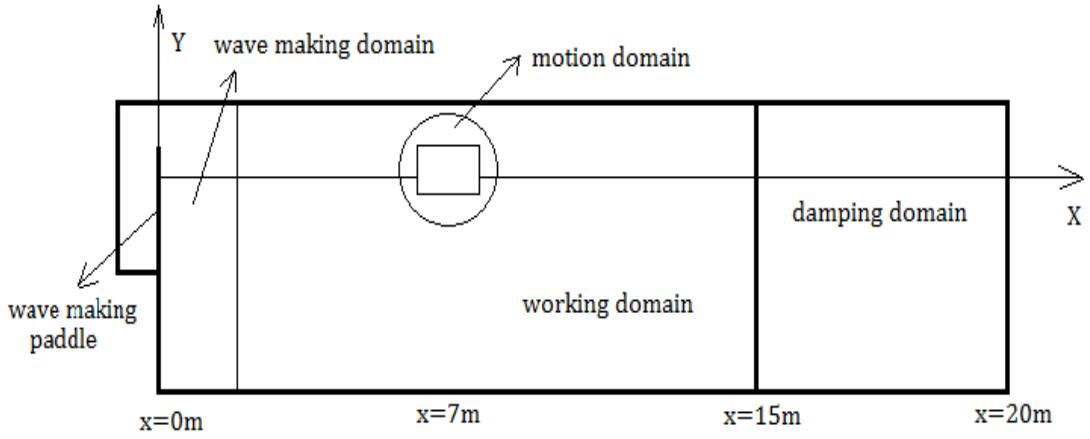

Figure 6.11 Sketch of the 2-D numerical wave tank

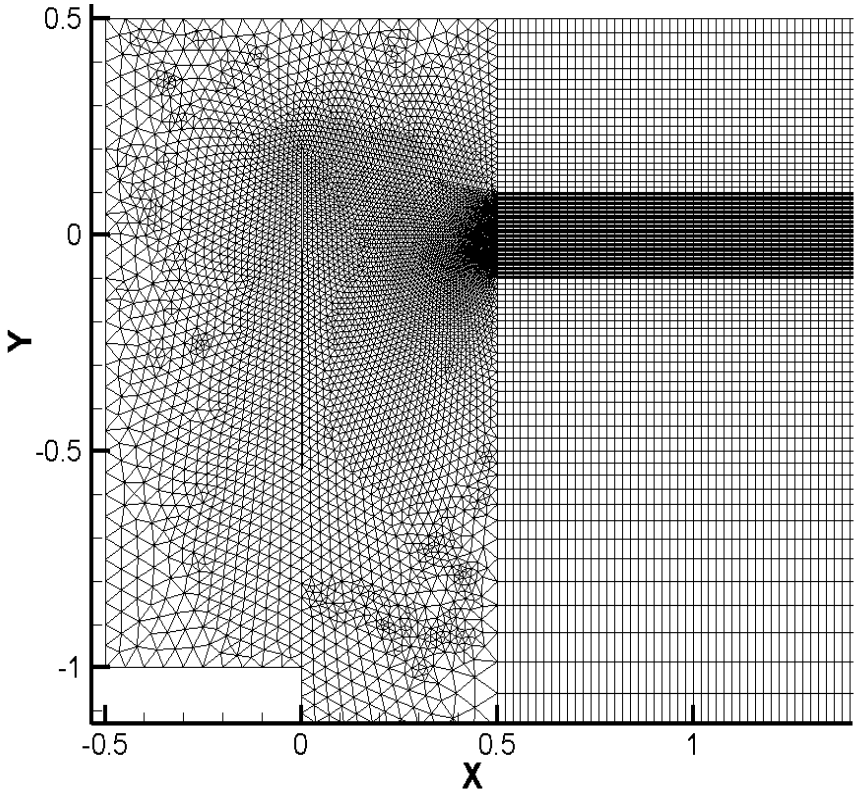

Figure 6.12 Detailed meshing configurations around the wave making paddle and free surface

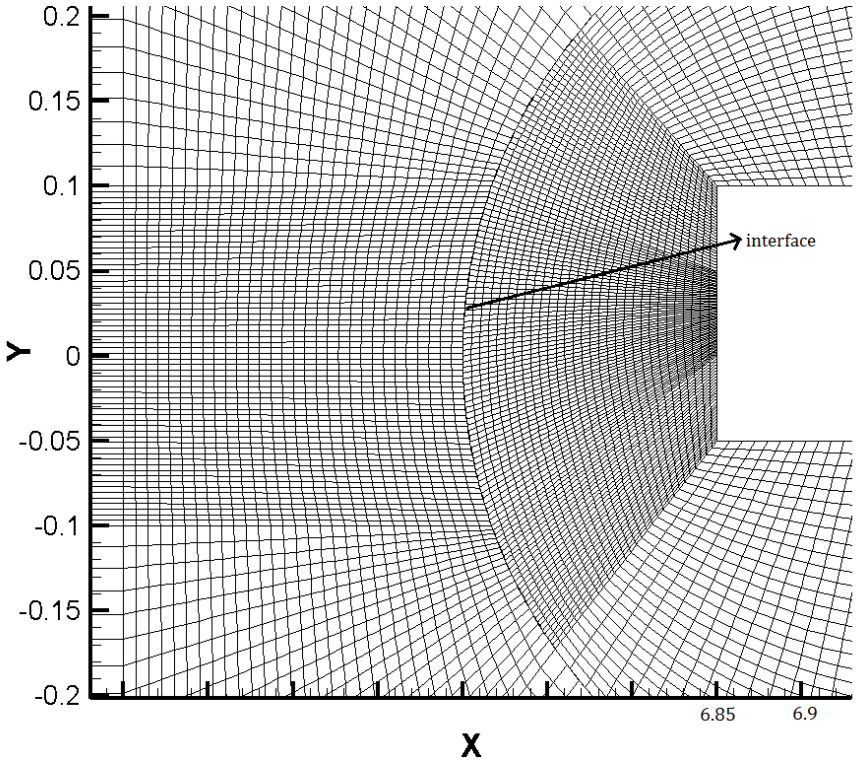

Figure 6.13 Detailed meshing configurations around the rectangular body

6.2.2.3 Results and Discussion

6.2.2.3.1 Decay Test

In the present numerical study, a decay test is conducted in the calm water condition with the time history of decaying roll amplitude records. The structure is initially inclined and released with an angle of 15°. The numerical roll motion decayed after each cycle due to the damping effects compared with the experimental data, as shown in Figure 6.14. The comparison results show that the numerical and experimental time histories of decayed roll motion have a good agreement.

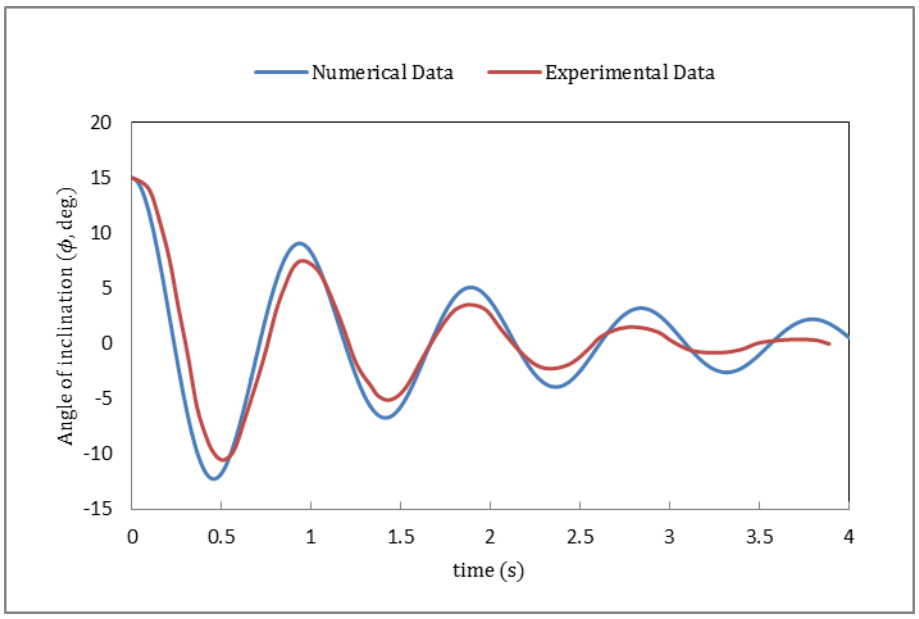

Figure 6.14 Decay test comparisons

6.2.2.3.2 Motion Response under Regular Waves

After validating the numerical decay test, the simulation of regular wave interaction with floating body is performed first. To understand the interactions between the rectangular structures and waves, regular waves with wave periods ranging from T=0.8s to T=1.6s, including the roll natural period (T_N=0.93s), are tested in the numerical wave tank. The numerical tested waves with corresponding wavelengths (λ) and wave heights (H) are listed in Table 6.2.

An example of numerical time history of rectangular body roll motion response under a regular wave with short wave length is shown in Figure 6.15. In this case, the selected regular wave has a wave period T=0.8s with wave height of 0.029m. The numerical results show that under the regular wave excitation, the rectangular structure rotates stably with an inclination angle of 5° approximately after a time t=11s. In Figure 6.16, another case of rectangular body rolling motion time history response is shown. In this case, the incident regular wave has the same wave period as the rectangular body rolling motion natural period T=0.93s. Although the incident regular wave has a small wave

height H=0.027m, the floating body begins to rotate at the large inclination angle 11°, approximately from time t=12s.

Table 6.2 Regular wave conditions

T(s)	ω(rad/s)	λ(m)	H(m)	kA
0.8	7.85	1	0.029	0.0912
0.93	6.76	1.35	0.027	0.0628
1	6.28	1.56	0.044	0.0887
1.2	5.24	2.22	0.06	0.0849
1.4	4.49	2.93	0.061	0.0653
1.6	3.93	3.65	0.06	0.0516

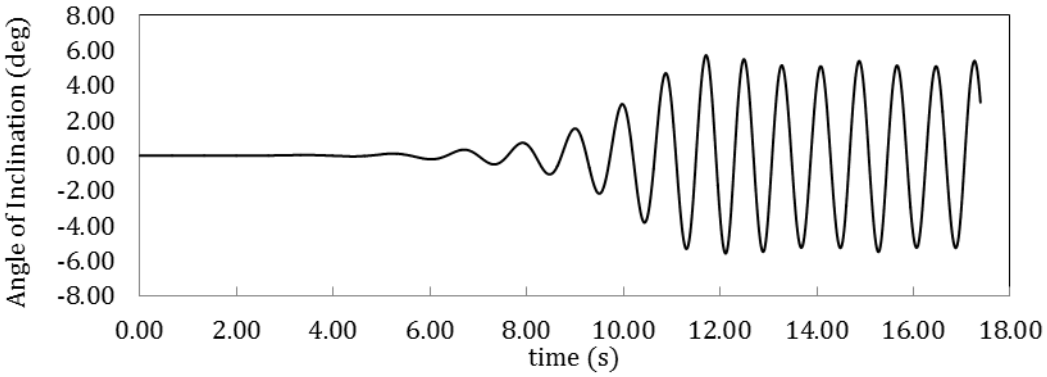

Figure 6.15 Time history of rectangular body response under regular wave of T=0.8s and H=0.029m

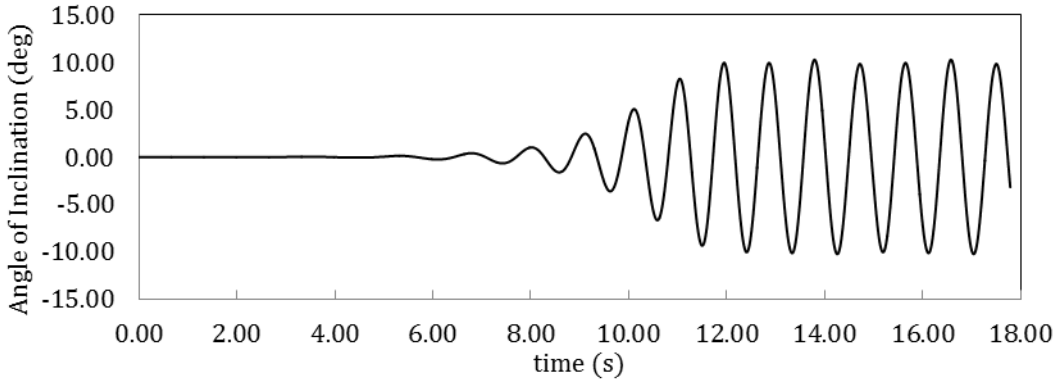

Figure 6.16 Time history of rectangular body response under regular wave of T=0.93s and H=0.027m

To prove the accuracy of the current numerical method in the research of hydrodynamic behaviour of a floating body under regular waves, the numerical response amplitude operators of the rectangular structure are compared with the experimental results in six different regular wave conditions, shown in Figure 6.17. Here, the response amplitude operator (RAO) is defined by a ratio ϕ/kA, and the frequencies in the figure are normalized by the floating structure roll natural frequency ω_n =6.76 rad/s. The results show that the numerical calculation of the rectangular roll motion has a good agreement with the experimental data in the six regular wave cases.

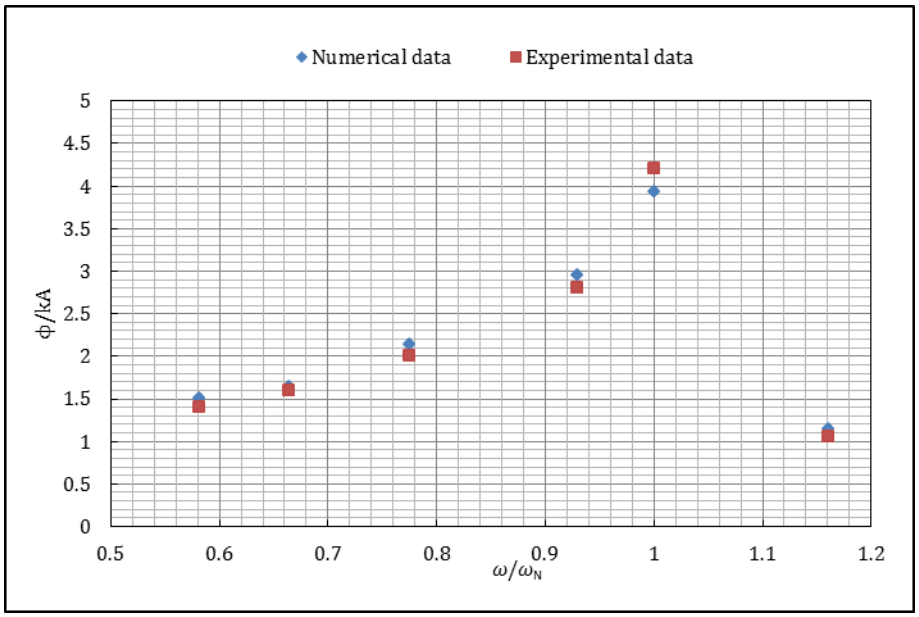

Figure 6.17 Comparisons of response magnification operator

6.3 Rectangular Body Roll Motion Response under Freak Wave

In this part, the extremely nonlinear interactions between freak wave and a floating body is investigated numerically. The paddle wave-making method is used to generate a freak wave train, and three different freak wave conditions are considered.

6.3.1 Freak Wave Generation

Before carrying out the freak wave and structure interaction problems, the validation of freak wave generation is conducted first. From different freak wave models introduced in Chapter 4, an efficient freak wave model, combining a freak wave and regular wave, is used to simulate a freak wave appearing in calm seas. To investigate the effect of peak frequency and frequency bandwidth on body motion, three different freak wave cases are considered. The detailed configurations are shown in Table 6.3. In all the three cases, the number of wave components is M=29 and the Joint North Sea Wave Project (JONSWAP) is selected. The detailed JONSWAP wave spectrum equation (4.2.2) is shown in Chapter 4.

Table 6.3 Freak wave configurations

Case	Frequency Bandwidth (Hz)	fp(Hz)	Hs(m)	Pr
1	0.6-1.6	1	0.03	0.3
2	0.8-1.3	1	0.025	0.33
3	0.4-1.4	0.8	0.025	0.33

In freak wave case 1, the significant wave height of the wave group is Hs=0.03m; the frequency bandwidth of the wave components is [0.6, 1.6], and the peak frequency f_p=1.0 Hz. The analytical transient wave amplitude A_f=0.041m. In freak wave case 2, the significant wave height of the wave group is Hs=0.025m; the frequency bandwidth of the wave components is [0.8, 1.3], and the peak frequency is the same f_p=1.0 Hz. The analytical transient wave amplitude A_f =0.033m. In case 3, the significant wave height of the wave group is Hs=0.025m;

the frequency bandwidth of the wave components is [0.4, 1.4], and the peak frequency f_p=0.8 Hz. The analytical transient wave amplitude A_f=0.033m.

Figure 6.18, Figure 6.19 and Figure 6.20 illustrate the numerical time history of freak wave elevation measured at wave gauge x=7m for three different freak wave cases compared with the wave surface profile derived from first order wave theory. The computational results show that the calculated wave elevation agrees well with the corresponding analytical data, and the nonlinear behaviour of the wave group is obvious. For the narrow-banded freak wave case 2, the wave crest measured at the focal position is much narrower and higher, and the adjacent wave troughs are much wider and shallower than the linear results.

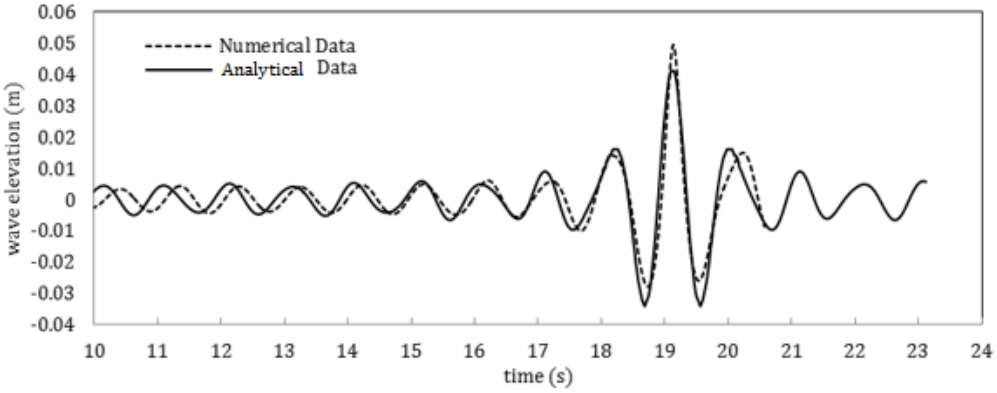

Figure 6.18 Wave elevation comparisons for freak wave case 1

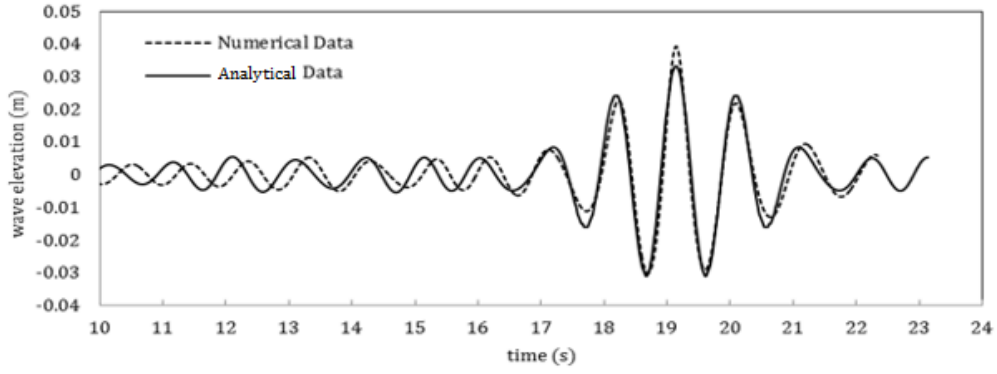

Figure 6.19 Wave elevation comparisons for freak wave case 2

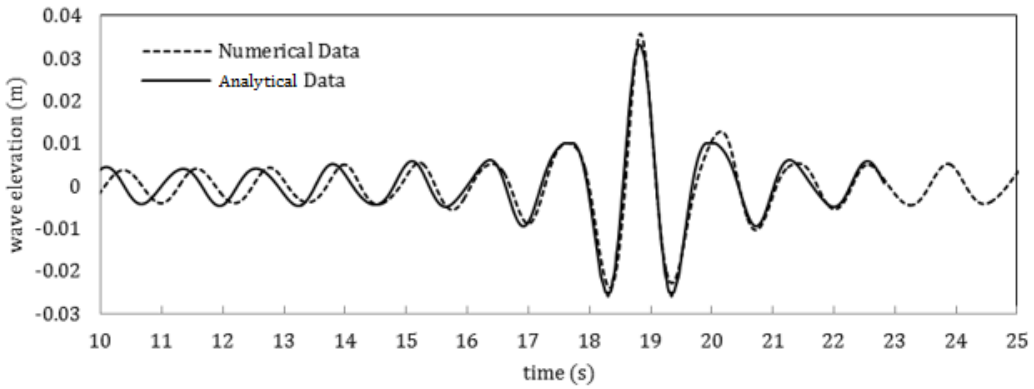

Figure 6.20 Wave elevation comparisons for freak wave case 3

6.3.2 Results and Discussion

The simulation results of the time history of rectangular body response under freak wave conditions are shown in Figure 6.21, Figure 6.22 and Figure 6.23 for the three different cases. The reason why the combing freak wave model is selected is to show what will happen to the body when it is subjected to freak waves in more realistic conditions. At the start of the simulation, the body shows regular response with the same phase of the surrounding regular wave. When all the wave components gather in the position where the rectangular body is placed, very large motion amplitude is observed in rolling response. When the focused wave passes, the body motion reduces gradually and remains at a regular motion. Compared with the rectangular body motion under a regular wave condition, the freak wave is more dangerous due to a sudden appearance of a large wave crest compared to the common sea states. The current numerical method can give a reasonable prediction of a floating body under large waves.

By comparing the computational results of freak wave case 1 and freak wave case 2, the peak frequency for the two cases is the same as fp=1Hz, and the corresponding peak period is also the same as Tp=1s, which is close to the natural frequency of the rectangular body in roll T_N=0.93s. In freak wave case 1, when the transient freak wave propagates to the floating body, the maximum freak wave amplitude reaches to 0.0493m and the rectangular body rotates with a maximum negative inclination angle -16.5°. In freak wave case 2, when

the transient freak wave propagates to the floating body, the maximum freak wave amplitude only reaches to 0.0392m, which is 25% smaller than the corresponding maximum wave amplitude in freak wave case 1. However, it is interesting to note that the floating structure suffers from a larger rolling response angle -19.5°, which results in a larger rolling response than the freak wave case 1 with inclination angle of -16.5°. Although in Jung (2006)'s work, it has been proven that the RAO magnification factors vary significantly with wave heights at natural periods and the response amplitude should increase with increased wave height, the complexity of a floating body interacting with focused freak waves have been presented here. When investigating the hydrodynamic behaviour of a floating body under focused freak waves, the frequency bandwidth in the freak wave group is an important factor. Comparing the computational results of a floating body rolling response under freak wave case 1 and freak wave case 2, it shows that the decreased frequency bandwidth gathers more wave energy together, and the high nonlinear behaviour of the freak wave group results in larger motion amplitude in roll further.

In the freak wave cases 2 and 3, the significant wave height is the same for the two cases Hs=0.025m. Ignoring the effect of frequency bandwidth on rectangular roll motion, the swift of the peak frequency of the wave energy spectrum results in a significant change of rectangular body roll motion behaviour dramatically. The computational results show that the roll motion profile is almost symmetric for freak wave case 2, and the maximum roll motion happens at t=20.04s with an inclination angle of -19.5°. When moving the peak frequency from 1Hz to 0.8Hz for freak wave case 3, the peak frequency of the freak wave spectrum is far away from the rectangular roll motion natural frequency. The simulated maximum roll motion of the rectangular body under freak wave is only 12°.

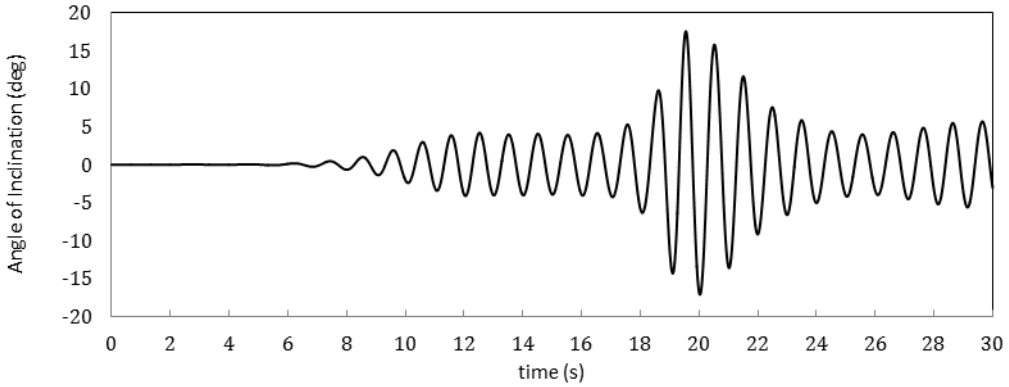

Figure 6.21 Time history of rectangular body roll response under freak wave case 1

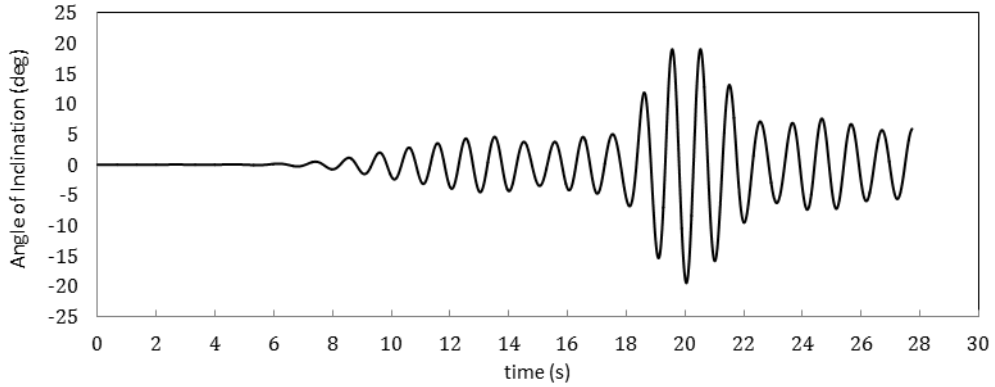

Figure 6.22 Time history of rectangular body roll response under freak wave case 2

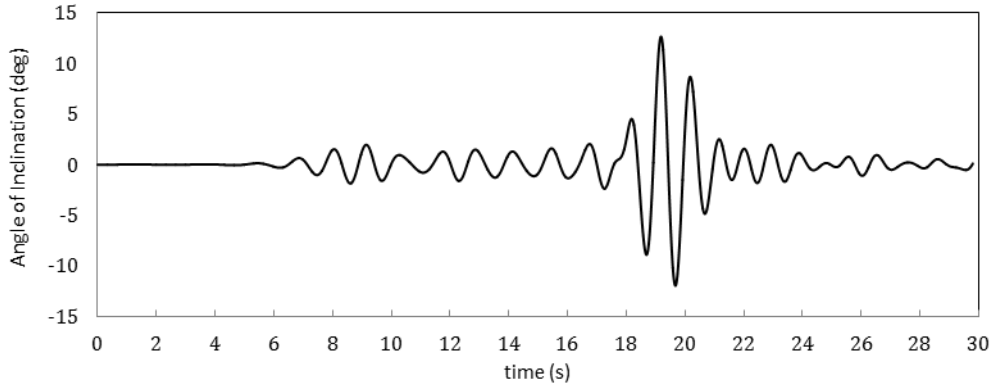

Figure 6.23 Time history of rectangular body roll response under freak wave case 3

6.3.3 Wave Field around the Floating Structure

When considering the time history of computational freak wave elevation shown in Figure 6.19, the wave free surface profile obtained from the narrow frequency bandwidth case 2 is different from the simulated results derived from board frequency bandwidth case 1 and case 3. As all the wave spectrum is gathered in a narrow frequency range, and besides a giant wave being generated at the predetermined focused time, the crests of the adjacent waves are also very large. The simulated maximum freak wave amplitude is 0.04m, and the wave amplitude of the wave before and after the giant wave is 0.025m approximately. In other words, a series of three freak waves is generated with a surrounding small amplitude regular wave for freak wave case 2.

Figure 6.24 shows the wave field around the floating body for freak wave case 2 during the time when the freak wave propagates to the rectangular position. The process of the freak wave impact on the floating body should be divided into several stages. At time t=18.85s, the first giant wave propagates to the rectangular body position. With the impact of the sudden large amplitude wave, the rectangular body suffers from a clockwise rotation 15.4°. After that, the anticlockwise torque rotates the floating body to an anticlockwise angle 19° at time t=19.55s. Then, the second giant wave with amplitude of 0.04m comes to the rectangular body surface. At time t=20.05s, the floating structure suffers the maximum clockwise rotation angle 19.5°, where violent nonlinear fluid-structure interactions can be observed. The nonlinear wave breakings and bubbles can be found around the rectangular surface. Finally, the rectangular body rotates with the impact of the third giant wave. Although the water free surface around the body is disturbed dramatically due to the nonlinear fluid-structure interactions, the response motion profile is almost symmetric.

(a) t=15s

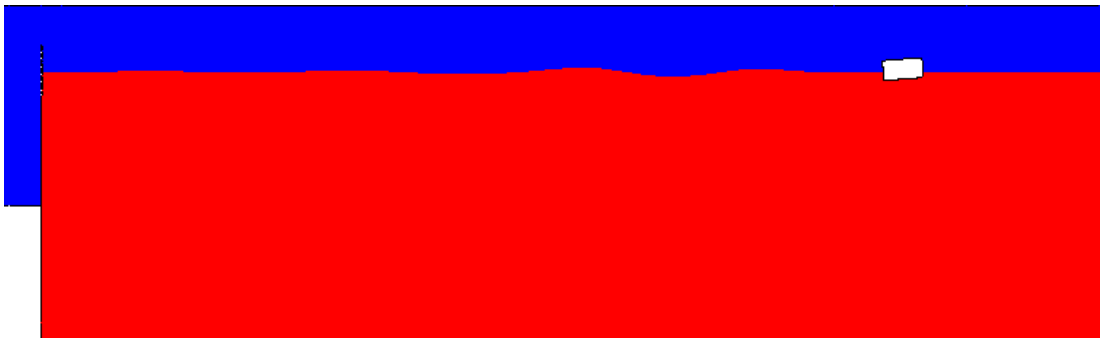

(b) t=16.55s

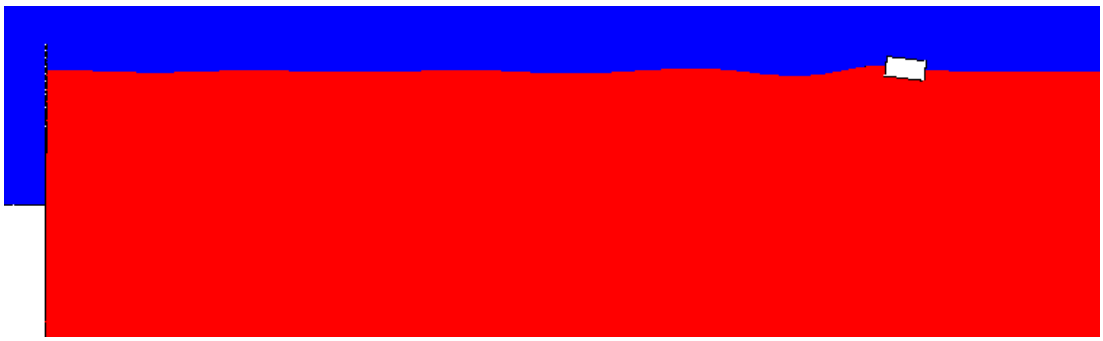

(c) t=18.1s

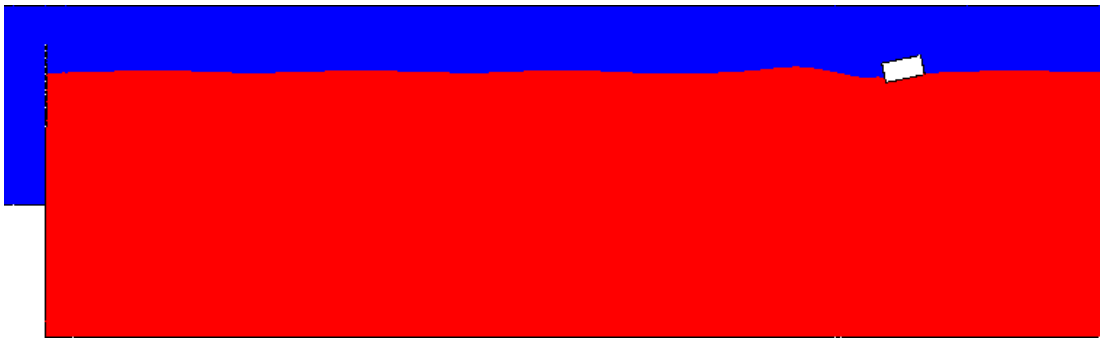

(d) t=18.6s

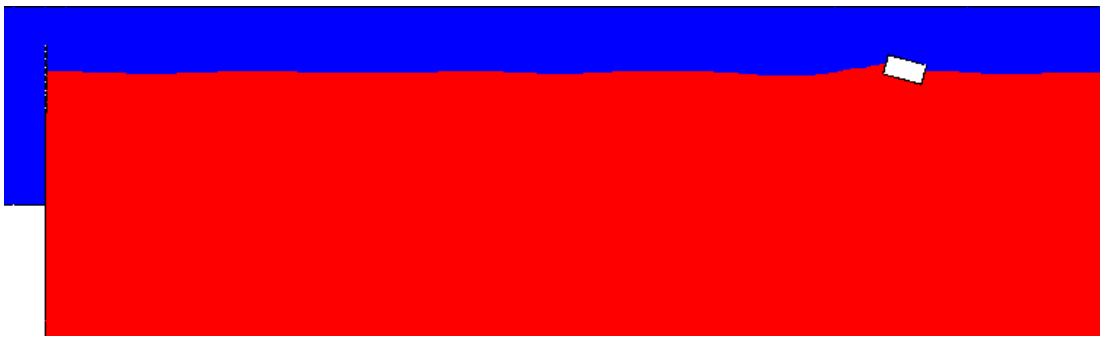

(e) t=19.1s

(f) t=19.5s

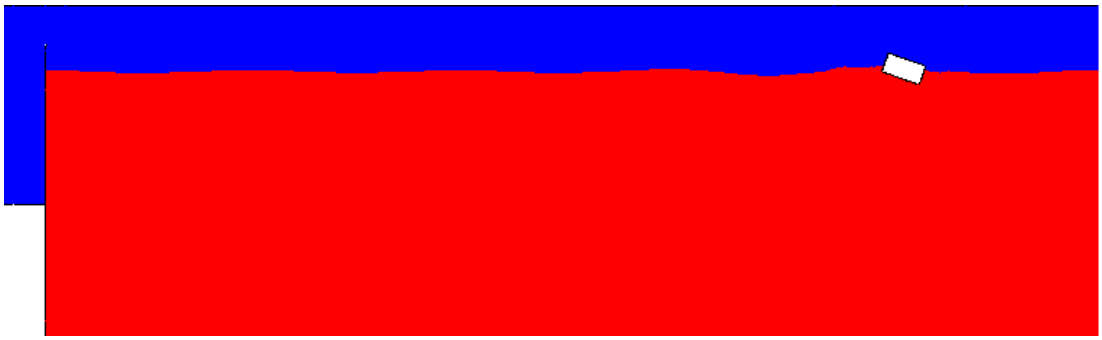

(g) t=20.03s

(h) t=20.53s

Figure 6.24 Wave field of the numerical wave tank for freak wave case C2

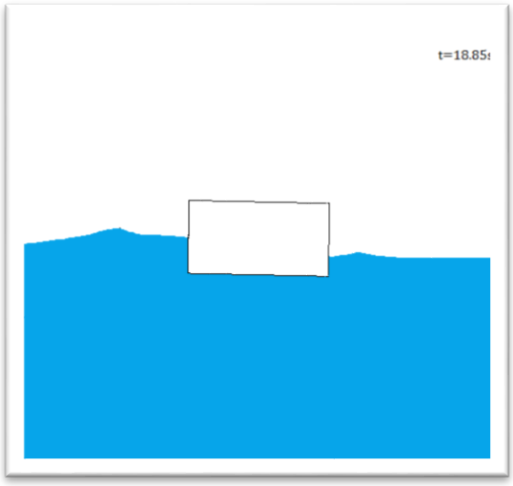
t=18.85s

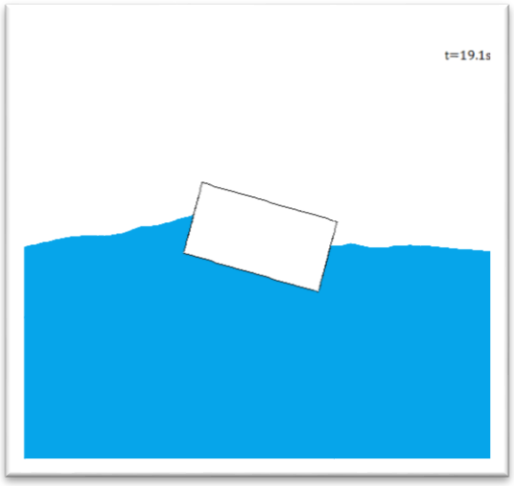
t=19.1s

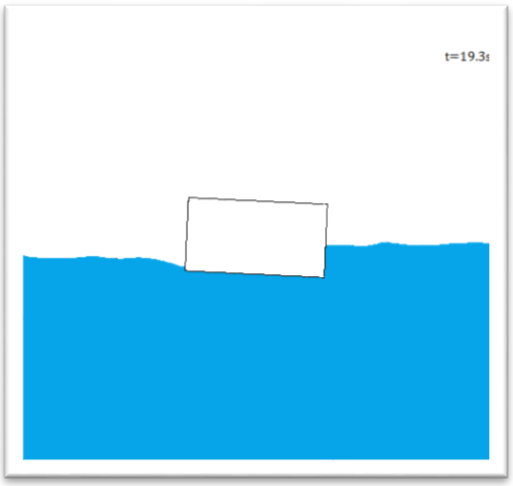
t=19.3s

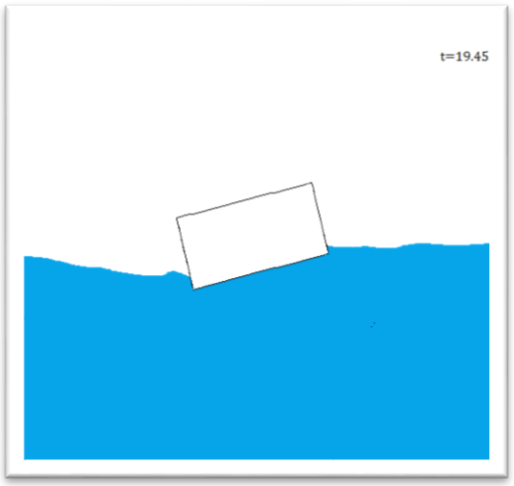
t=19.45

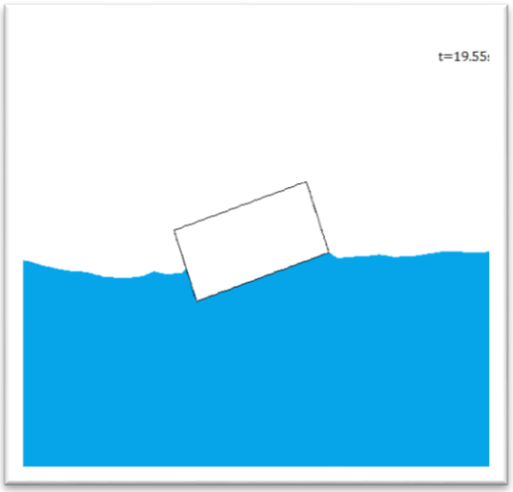
t=19.55s

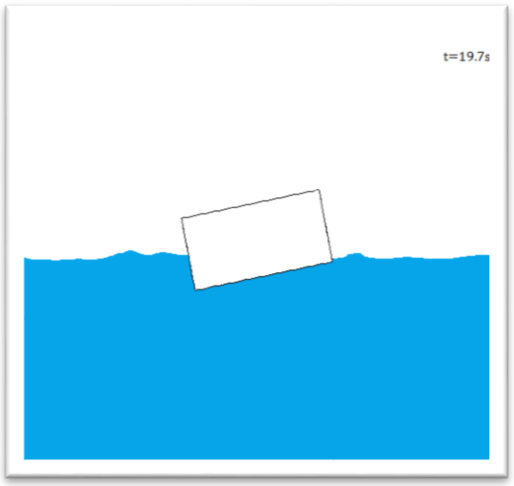
t=19.7s

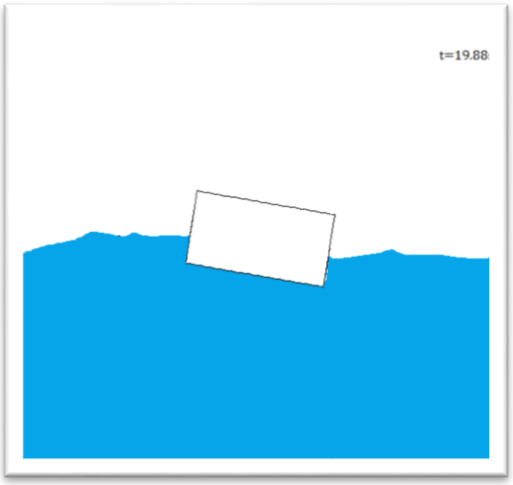
t=19.88

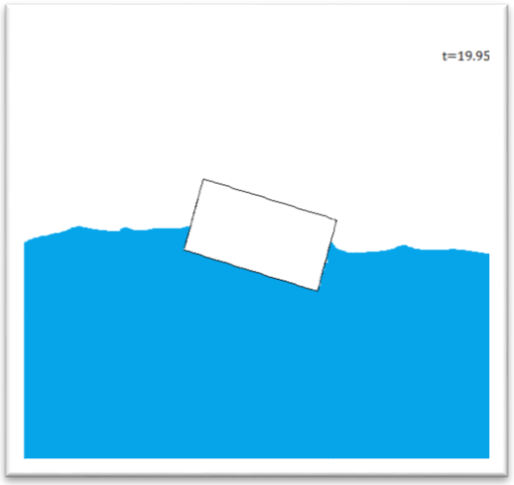
t=19.95

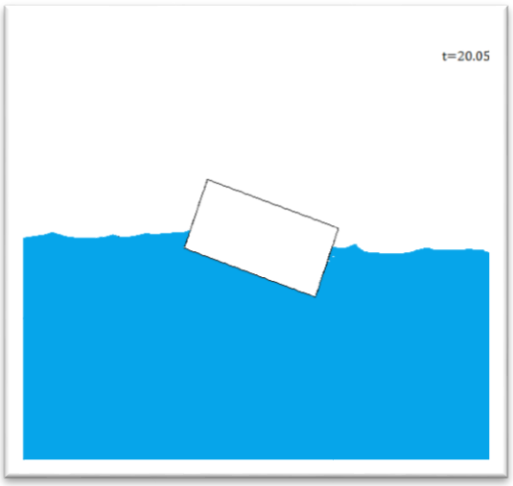
t=20.05

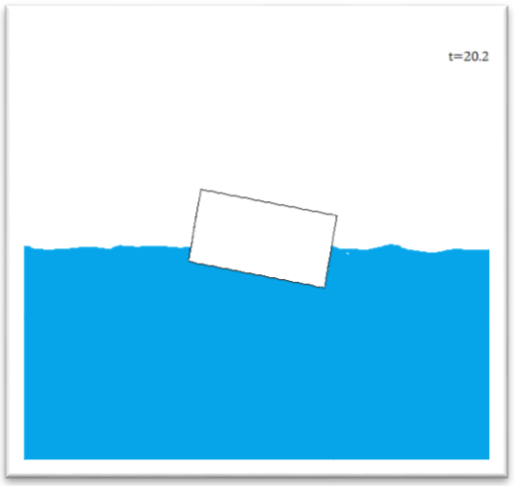
t=20.2

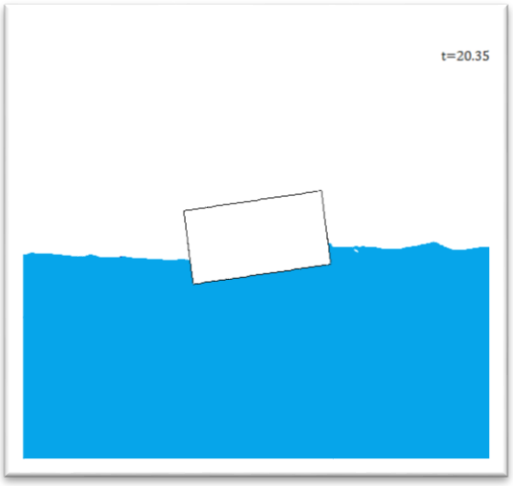
t=20.35

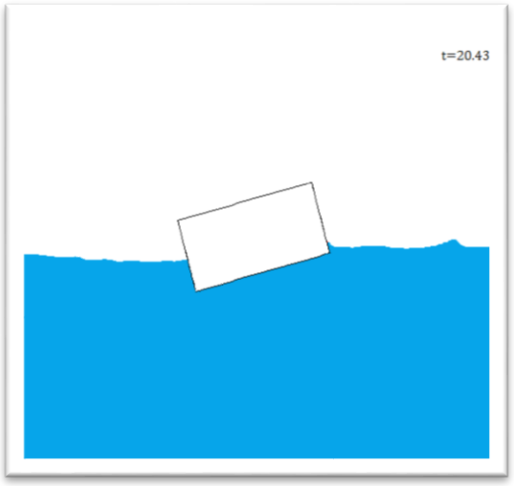
t=20.43

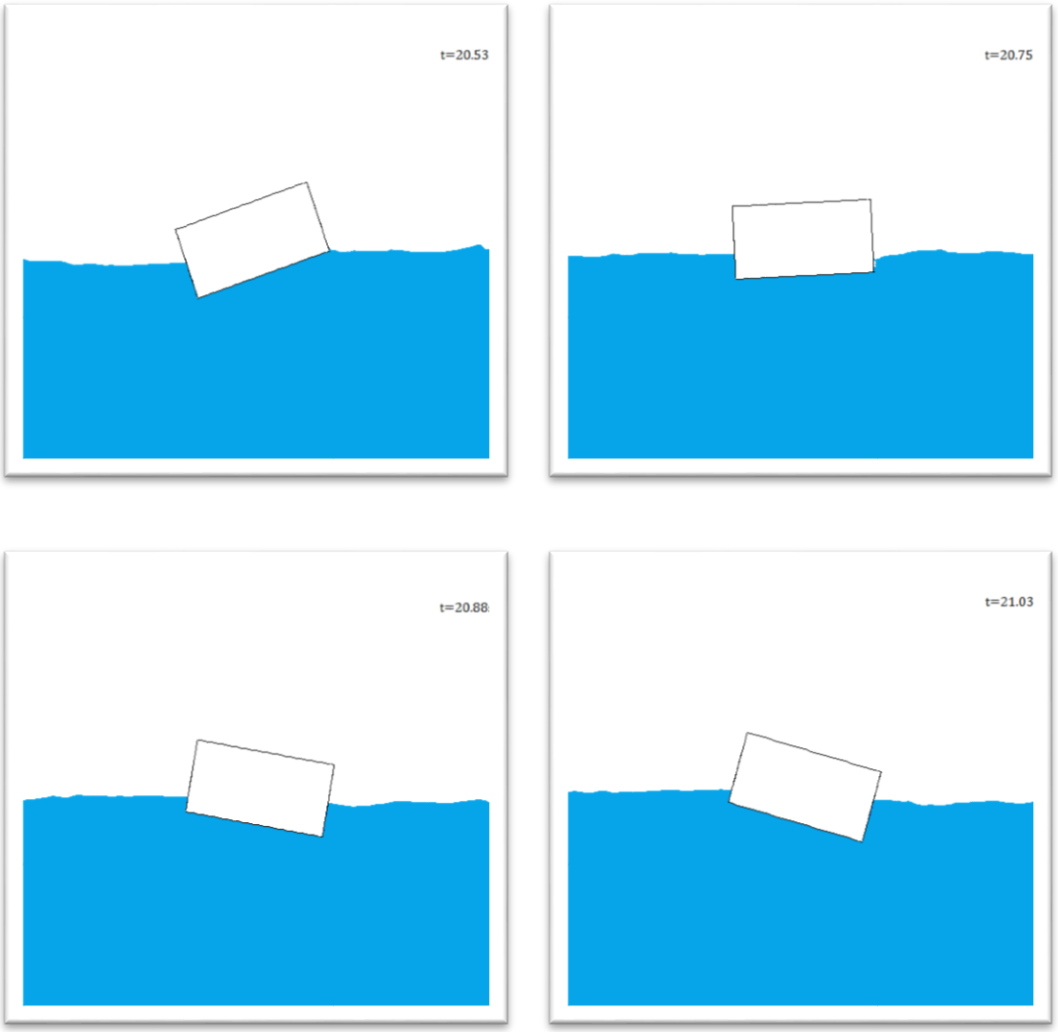

Figure 6.25 Wave field around the floating body for freak wave case 2

6.4 Coupling Effects on Rectangular Body Roll Motion under Freak Wave

In ships carrying liquid cargo, motion responses in waves are affected not only by external wave excitation but also by internal sloshing-induced forces and moments. In other words, the ship motion excites sloshing flow, and after that the sloshing flow affects the ship motions further. In this present study, the time-domain CFD method is used to investigate the coupling effects on the rectangular body motion under freak wave conditions.

The same rectangular structure is used and the main dimension for the internal tank is shown in detail. The gravity centre of the rectangular body is adjusted to keep water lines unchanged, and the moments of inertia are as the original

structure. Two different filling conditions, 25% and 75%, are studied in this section.

6.4.1 Decay Test and RAOs

Before investigating the rectangular body rotating under coupled wave excitation and sloshing induced excitation, the free decay tests should be conducted first. The same as the free decay test conducted for the no filling motion case, the structure is initially inclined and released with an angle of 15°. The numerical roll decay test with different filling conditions is shown in Figure 6.26. The computational results show that the decay motion behaviours of the rectangular body are affected, largely due to the internal sloshing flow. Compared with the free decay case without sloshing, the internal sloshing flows extend the roll motion natural periods for all the other two cases. Furthermore, in the first three cycles of rectangular free decaying, the anti-rolling effect of the low filling condition (25% filling) is obvious.

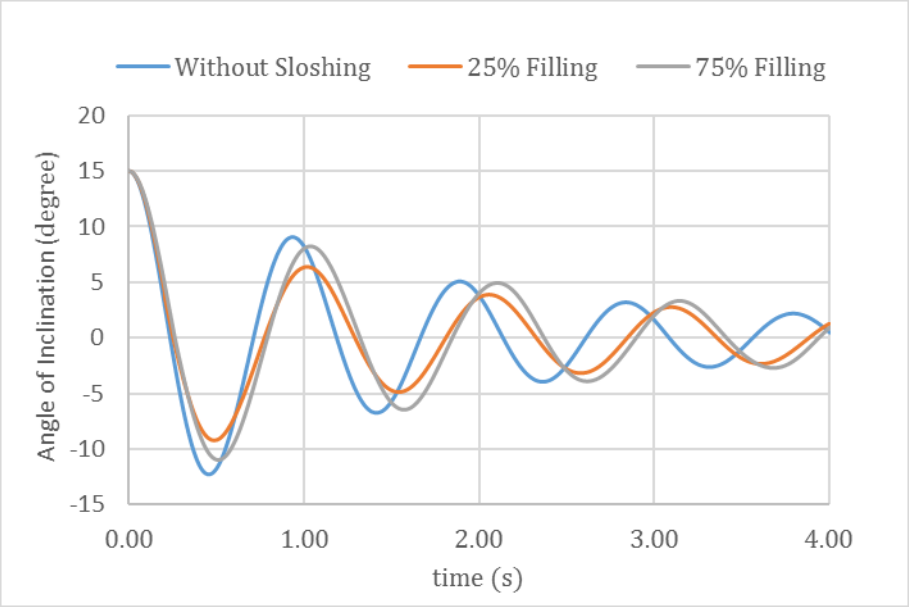

Figure 6.26 Free decay tests for three filling conditions

After comparing the roll motion time history of the decay test with different filling levels, the rectangular interaction with internal flow sloshing under regular waves is investigated. Six regular waves with different wave periods and wave heights are considered. Finally, the global roll motion RAOs of the coupled

floating body for different filling conditions are calculated and shown in Figure 6.27. When considering $\omega/\omega_N=1$, the anti-rolling behaviour of the internal flow sloshing is obvious, this anti-rolling behaviour of the coupling effects is dominant at low filling (25% filling level) conditions especially. Considering the regular wave, $\omega/\omega_N=0.93$, where the regular wave has a wave period T=1s, the effect of the internal flow excitations on the global ship motion presents a different characteristic compared with the natural frequency $\omega/\omega_N=1$ cases. For the low filling case (25% filling level) the internal flow excitation obviously reduces the global floating rectangular motion, and the anti-rolling effect still exists. However, under the high filling condition (75% filling level), the anti-rolling effect of the internal flow motion does not exist. The internal flow excitation largely increases the global floating body response. Looking at the response amplitude operator at $\omega/\omega_N=0.78$, when the corresponding regular wave has a large regular wave period T=1.2s, the coupling effect reduces the rectangular rolling response dramatically compared with the no sloshing case, and this phenomenon is presented in the low filling case most obviously.

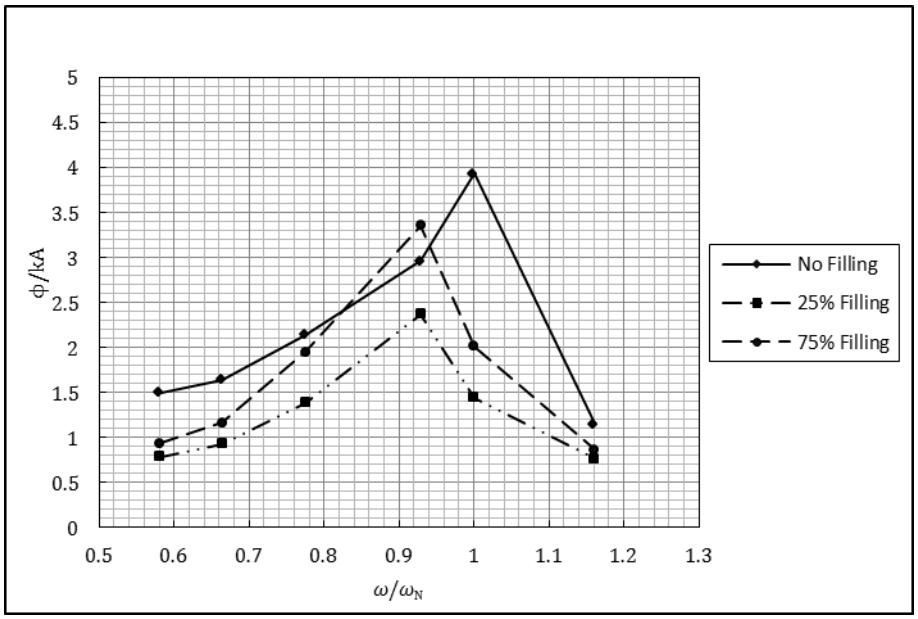

Figure 6.27 Comparisons of response magnification operator with different filling levels

6.4.2 Results and Discussion

Numerical investigations on coupling effects between ship motion response and internal liquid sloshing under freak wave excitations are carried out in this section. As aforementioned, three different freak wave conditions which have been validated are considered here, and three distinguished sloshing filling conditions are studied. The comparison of global rectangular body responses with and without sloshing effects is shown in detail.

The computational results illustrated in Figure 6.28 give the comparisons of time history of rectangular rotational angles for the no filling condition and two filling condition cases under freak wave conditions. In these freak wave cases, the peak frequency is selected 1Hz, which is close to the rolling natural frequency for both models. The anti-rolling effect, which is generated by the internal sloshing flow, can be observed clearly in the low filing case (25 % filling level). However, in the case of high filling conditions (75 % filling level), an insignificant coupling effect can be observed.

For the freak wave condition case 2, the peak frequency of the wave group is the same as case 1 that is 1Hz. The comparison of rectangular body rotation angles for no sloshing case, 25% filling case and 75% filling case are shown in Figure 6.29. Under the same peak spectrum of the wave group energy, the sloshing effect on the rectangular body motion is the same as the freak wave case 1. The coupling anti-rolling effect on the floating structure can be visualized in the low internal filling case. However, for the high filling condition case, the coupling effect on the rectangular rotation is not significant.

For the freak wave condition case 3, the peak frequency of the wave energy group is 0.8Hz, and the corresponding wave period is T=1.25s, which is far away from the model's rolling natural period T_N=0.93s. The computational time history of rectangular body rotation induced by internal flow sloshing is shown compared with the no sloshing case in Figure 6.30. The behaviour of sloshing effect on the rectangular body rotation is very different from the previous cases. For both the low filling case and the high filling case, the anti-rolling coupled effects are obvious.

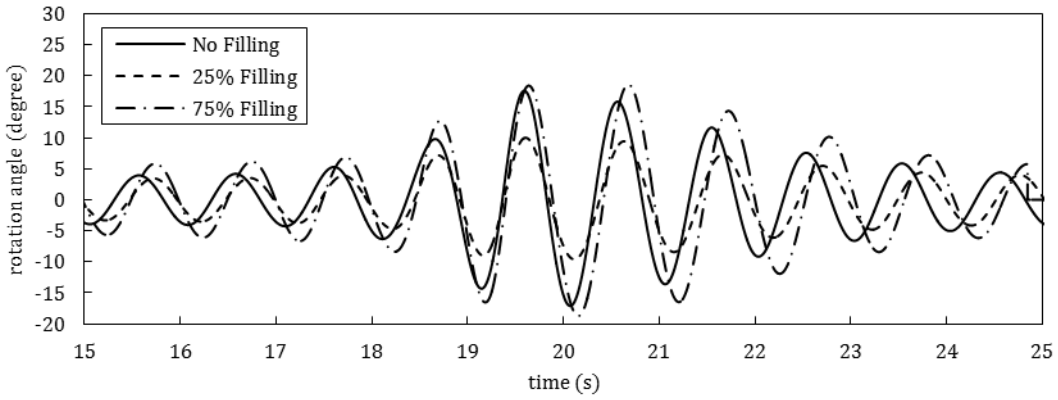

Figure 6.28 Comparisons of rectangular body rolling response freak wave case 1

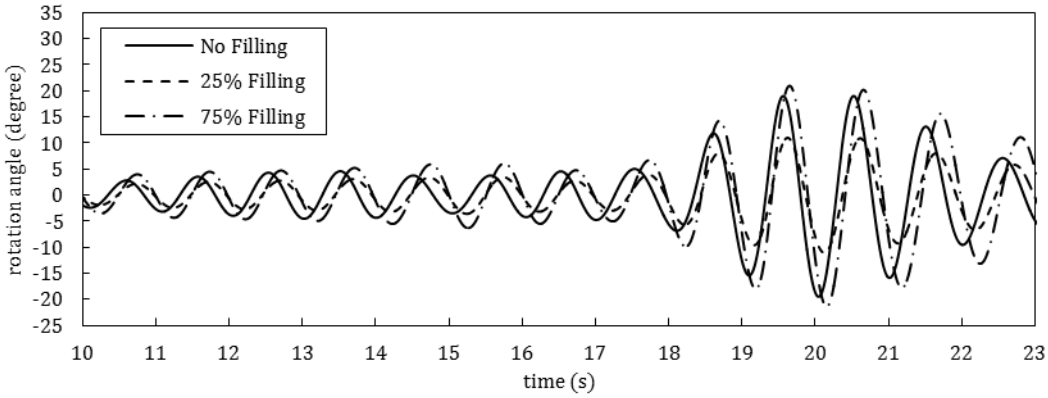

Figure 6.29 Comparisons of rectangular body rolling response freak wave case 2

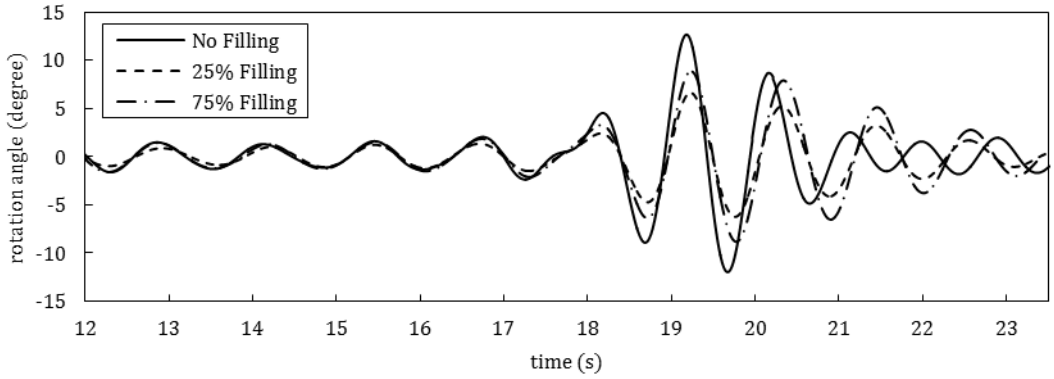

Figure 6.30 Comparisons of rectangular body rolling response freak wave case 3

6.4.3 Wave Field

Freak wave condition 2 is collected for example to illustrate the rectangular rotation under both the freak wave and internal flow excitations. The freak wave group is travelling from left to right. Figure 6.31 demonstrates the global

views of rectangular motion when the transient freak wave in the wave group interacts with the floating body. The high nonlinear behaviour of the internal flow sloshing can be seen in the low filling case (25 % filling level).

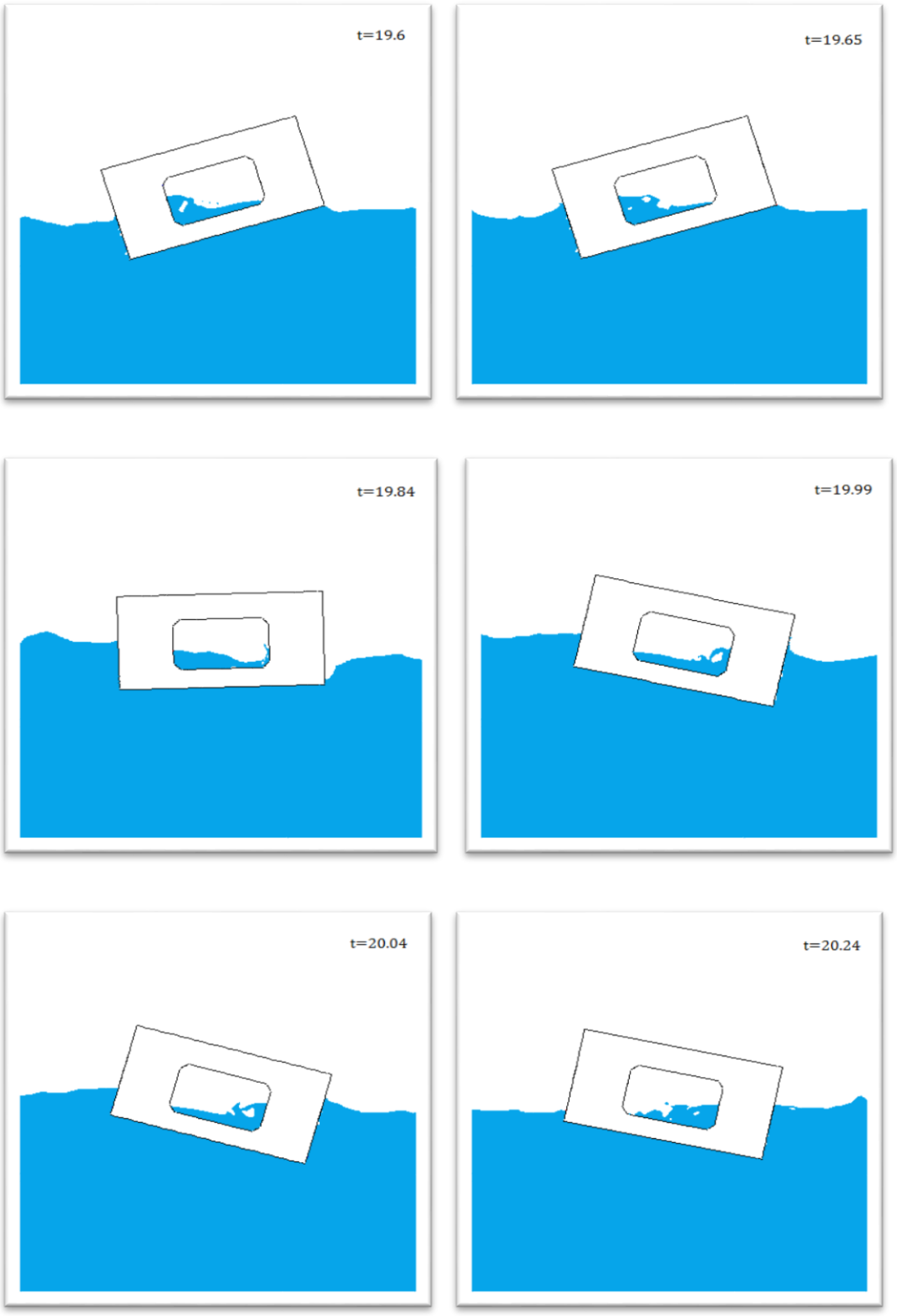

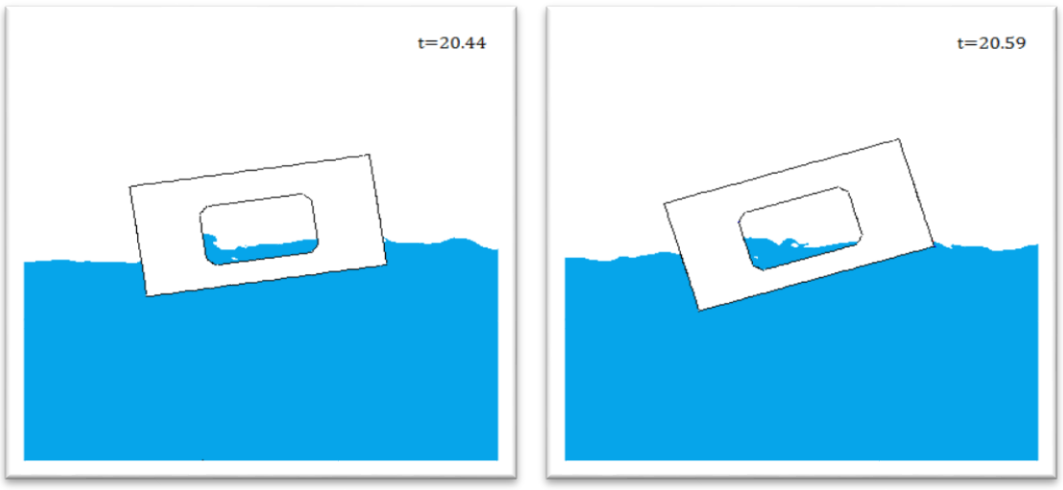

Figure 6.31 Rectangular body coupled motion for freak wave case 2 with low filling level during the freak wave period

6.5 Conclusions

In this chapter, a fully coupled numerical method is utilised to investigate the coupling effect on a 2-D rectangular body rotating under freak waves.

First, validation of sloshing under horizontal excitation is investigated, and the computational results indicate a good agreement with the experimental data.

Secondly, the rectangular structure roll response under regular waves is investigated in a numerical wave tank. The comparison of magnification factors for roll motions between the numerical results and the experimental data are given, and the results show that the numerical calculation of the rectangular roll motion under regular waves has a good agreement with the experimental data in the six cases.

Thirdly, three freak wave trains are generated by paddle wave making methods in the numerical wave tank for different wave spectrum peak frequencies and different frequency bandwidths. To simulate the rectangular body under real sea conditions, an efficient freak wave model is used by combining a transient giant wave and a surrounding regular wave. The computational results indicate that the freak wave train shows high nonlinear behaviour, and the nonlinearity is much more obvious in the highly significant wave height and narrow frequency bandwidth cases.

Further, the rolling motion responses of the rectangular body under three different freak wave conditions are investigated. At the start of the simulation, the body shows a regular response with the same phase of the surrounding regular wave. When all the wave components gather in the position where the rectangular body placed, very large motion amplitude is observed in roll. After the focused wave passes, the body motion reduces gradually and remains at a regular motion. The computational results demonstrate violent nonlinear fluid-structure interactions when the nonlinear behaviour of freak wave increases. The nonlinear wave breakings and bubbles can be found around the rectangular surface.

Following this, the global rolling RAOs of the coupled floating body for different filling conditions were obtained. The results indicate that the anti-rolling behaviour is obvious for the low filling case. However, for the high filling conditions, the coupling effect is not significant under the regular waves around the natural period.

Finally, the coupling effects on the rectangular body rolling motion under freak waves are investigated. The sloshing time history of rectangular rolling responses under freak waves is compared with the no sloshing case for different filling levels. The computational results indicate that the coupled rolling motion of a rectangular body under both internal flow sloshing and external freak wave excitation is a very complicated phenomenon. The peak frequency of a wave energy spectrum is an important factor to represent the characteristics of the selected wave spectrum. For freak wave case 1 and case 2, the coupling anti-rolling effect on the floating structure can be visualized in the low filling level cases, and the sloshing can be clearly observed inside the tanks. For freak wave case 3, the rectangular structure with high filling condition rolls more violently than the low filling level case.

7 Summary of conclusions and recommendations for further work

7.1 Conclusions

The freak wave is extremely dangerous to offshore structures due to its unexpectedly high wave height and strong nonlinearity. In this thesis, the freak wave is the research focus. At first, the freak wave was generated in a numerical wave tank. Following this, the freak wave run-up on a vertical cylinder and a pair of cylinders were investigated. Finally, a rectangular body rolling response under a freak wave train was investigated, and the effect of internal flow sloshing was also analysed. By investigating the hydrodynamic behaviour between freak waves and offshore structures, several important conclusions could be made.

1. The freak wave was simulated numerically in a 2-D numerical wave tank and 12 different freak wave cases were considered. The 12 cases were allocated by different input amplitudes and different frequency bandwidths. The main results and recommendations from the parametric studies indicated that:
   - The increased input amplitude and reduced frequency bandwidth could result in a growth of nonlinear behaviour of a freak wave group.
   - This increased nonlinear behaviour of a freak wave group would not only downstream shift the focal position, but also the focused time.
   - The wave-wave nonlinear interaction could change the wave surface profile compared with the linear analytical results. When the nonlinear behaviour increased, much more wave energy gathered in the higher order harmonic. This would result in a narrower and higher wave crest, and a wider and shallower wave trough.
2. For the freak wave running-up on vertical cylinders, this thesis applied a fully nonlinear CFD method for simulating the wave surface elevations around the cylinder and the hydrodynamic wave forces impacting on the cylinder body. The main observations were:

- The present CFD simulated regular wave run-up elevation around a vertical cylinder had a good agreement with the experimental results, however the analytical wave run-up results derived from the first order diffraction theory were underestimated dramatically.
- For the freak wave run-up on a single vertical cylinder case, the wave run-up tendency for all the cases was almost the same. The maximum wave run-up happened at the front of the cylinder point a4 (α=180°), and the minimum wave run-up appeared at the position α=315°, close to the cylinder surface position d4. The increased wave steepness and decreased wave frequency bandwidth grew the nonlinear behaviour of the freak wave group, which increased wave run-up at wave point a4 and b4 further. At the same time, the increased wave nonlinear behaviour reduced the wave run-up level at wave point d4. The computational results also showed that the increased nonlinear behaviour of the wave group raises the freak wave non-dimensional normal force slightly.
- For the freak wave running-up on a pair of cylinders, the simulation results indicated that the maximum wave elevations measured at wave gauges around the front cylinder are larger than the corresponding values measured around the back cylinder. The freak wave focusing position had a definite effect on wave run-up. The closer the wave focal position moved to the front cylinder, the larger the wave run-up appeared in the range α= [180°, 225°], and the smaller the wave run-up α=360° around the front cylinder. However, around the back cylinder, the closer the focal position moved to back cylinder, the larger the wave run-up appeared in all the wave gauges. The numerical results also indicated that the horizontal freak wave force profile is not symmetric around the focal time, while the wave run-up profile was nearly symmetric to the incident freak wave profile.

3. A fully coupled numerical CFD method was utilised to investigate the hydrodynamic behaviour of a 2-D rectangular body rolling response under a freak wave excitation. Before this, a decay test and rectangular floating

body response under six different regular waves were conducted, and compared with the experimental results. After that, the effect of internal flow sloshing on the global floating structure rolling response under freak waves was investigated. The main results and recommendations from the parametric studies indicated that:

- When investigating the hydrodynamic behaviour of a floating body under focused freak waves, the frequency bandwidth in the freak wave group was an important parameter. The decreased frequency bandwidth gathered more wave energy together, and the high nonlinear behaviour of the freak wave group resulted in larger rolling motion amplitudes.
- When considering the effect of internal flow sloshing on the global rectangular rolling response, the anti-rolling behaviour was obvious for the low filling level case. However, for the high filling conditions, the coupling effect was not significant on the floating body motion when the exerted regular wave periods were around the natural period.
- The coupled rolling motion of a rectangular body under both internal flow sloshing and external freak wave excitation was a very complicated phenomenon. The peak frequency of a wave energy spectrum was an important factor to represent the characteristics of the selected wave spectrum. In all the three freak wave conditions, the anti-rolling behaviour was obvious for the low filling case.

7.2 Recommendations

The freak wave damage, especially to the offshore structures, has drawn increasing research interests. To maintain the safety and the reliability of the offshore structures, more investigations should focus on the numerical generation of the freak wave and the freak wave structure interaction issues.

The water depth of the numerical wave tank needs to be calibrated to generate the shallow water freak waves to study the difference with deep water freak waves.

More breaking freak waves in shallow water need to be generated to investigate the shallow water freak wave running up on offshore structures, like the wind turbine support structure.

Further work is needed on the statistics of the likely freak wave slamming loads and dynamic pressure at a given point on the structure.

A 3-D model is needed to investigate the sloshing effect on the global LNG ship motion under freak wave events.

References

Baldock, T. and Swan, C. (1994). Numerical calculations of large transient water waves. Applied Ocean Research, Volume 16, Pages 101-112.

Baldock, T.E., Swan, C. and Taylor, P.H. (1996). A laboratory study of nonlinear surface waves on water. Philosophical Transactions of the Royal Society A: Mathematical, Physical and Engineering Sciences, Volume 354, Pages 649-676.

Barth, T.J. and Jespersen, D. (1989). The design and application of upwind schemes on unstructured meshes. Technical Report AIAA-89-0366.

Cao, H. and Wan, D. (2014). Numerical study of motion response of floating body in extreme wave. Proceedings of the 24th International Ocean and polar Engineering Conference.

Caretto, L.S., Gosman, A.D., Patankar, S.V. and Spalding, D.B. (1972). Two calculation procedure for steady three-dimensional flows with recirculation. Proceedings of 3rd International Conference of Numerical Methods Fluid Dynamics.

Chaplin, J. (1996). On frequency-focusing unidirectional waves. Journal of Offshore and Polar Engineering, Volume 6, Number 2.

Chorin, A.J. (1968). Numerical solution of Navier-Stokes Equations. Mathematics of Computation, Volume 22, Pages 745-762.

Christian, K. and Efim, P. (2003). Physical mechanisms of the rogue wave phenomenon. European Journal of Mechanics-B/Fluids, Volume 22, Issue 6, Pages 603-634.

Clauss, G. (1999). Task-related wave groups for seakeeping tests of simulation of design storm waves. Applied Ocean Research, Volume 21, Pages 219-234.

Clauss, G. and Kuhnlein, W. (1997). Simulation of design storm conditions with tailored wave groups. Proceedings of 7th ISOPE Conference, Pages 228-237.

Clauss, G. and Steinhagen, U. (1999). Numerical simulation of nonlinear transient's waves and its validation by laboratory data. Proceedings of 9th ISOPE Conference, Pages 1-8.

Clauss, G. F. (2002). Dramas of the sea: episodic waves and their impact on offshore structures. Applied Ocean Research, Volume 24, No 3, Pages 147-161.

Clauss, G.F., Schmitter, C. and Stutz, K. (2002). Time-domain investigation of a semisubmersible in rouge waves. Proceedings of 21st International Conference on Offshore Mechanics and Arctic Engineering,

Clauss, G.F., Schmitter, C. and Stutz, K. (2003). Freak wave impact on semisubmersibles time-domain analysis of motions and forces. Proceedings of the 13th International Offshore and Polar Engineering Conference.

Clauss, G.F., Schmitterner, C.E. and Robert, S. (2005). Numerical wave tank simulation of extreme waves for the investigation of structural responses. Proceedings of OMAE, 24th International Conference on Offshore Mechanics and Arctic Engineering.

Cox, D. and Ortega, J. (2002). Laboratory observation of green water overtopping a fixed deck. Ocean Engineering, Volume 29, Pages 1827-1840.

Danmeier, D.G., Seah, R.K.M., Finnigan, T., Abault, A., Vache, M. and Imamura, J.T. (2008). Validation of wave run-up calculation methods for a gravity based structure. Proceedings of the 27th International OMAE Conference.

Deng, Y., Yang, J., Zhao, W., Xiao, L. and li, X. (2015). An efficient focusing model of freak wave generation considering wave reflection effects. Ocean Engineering, Volume 105, Pages 125-135.

Galvin, C.J. and Hallermier, R.J. (1972). Wave run-up on vertical cylinders. Proceedings of 13th International Conference on Coastal Engineering.

Gingold, R.A. and Monagham, J.J. (1977). Smoothed particle hydrodynamics: theory and application to non-spherical stars. Journal of MNRAS, Volume 181, Pages 375-389.

Harlow, F.H. and Welch, J.E. (1965). Numerical calculation of time-dependent viscous incompressible flow with free-surface. Physics of Fluids, Volume 8.

Hirt, C.W. and Niichols, B.D. (1981). Volume of fluid (VOF) method for the dynamics of free boundaries. Journals of Computational Physics, Volume 39, Pages 201-225.

Issa, R.I. (1986). Solution of implicitly discretized fluid flow equations by operator-splitting. Journal of Computational Physics, Volume 62, Pages 40-65.

Iwanowski, B., Lefrane, M. and Wemmemhove, R. (2009). CFD simulation of wave run-up on a semi-submersible and comparison with experiment. Proceedings of the AMSE 28th International Conference on Ocean, Offshore and Artic Engineering.

Ji, X., Liu, S, Li, J. and Jia, W. (2015). Experimental investigation of the interaction of multidirectional irregular waves with large cylinder. Ocean Engineering, Volume 93, Pages 64-73.

Jiang, S.C., Teng, B., Bai, W. and Gou, Y. (2015). Numerical simulation of coupling effect between ship motion and liquid sloshing under wave action. Ocean Engineering, Volume 108, Pages 140-154.

Johannessen, T. and Swan, C. (1997). Nonlinear transient water waves Part 1. A numerical method of computation with comparisons to 2-D Laboratory Data. Applied Ocean Research, Volume 19, Pages 293-308.

Jung, K.H., Chang, K. and Jo, H.J. (2006). Viscous effect on the roll motion of a rectangular structure. Journal of Engineering Mechanics ASCE, Volume 132(2), Pages 190-200.

Khezzar, L., Seibi, A. and Goharzadeh, A. (2009). Water Sloshing in Rectangular Tanks – An Experimental Investigation & Numerical Simulation. International Journal of Engineering (IJE), Volume (3), Issue (2).

Kim, C., Randall, R., Boo, S. and Kraft, M. (1992). Kinematics of 2-D transient water waves using Laser Doppler Anemometry. Journal of Waterway, Port, Coastal, and Ocean Engineering, Volume 118, Pages 147-165.

Kim, C.H., Randall, R.E. and Krafft, M.J. (1990). Experimental study of kinematics of large transient wave in 2-D wave tank. Proceedings of the 22th Offshore Technology Conference, Pages 195-202.

Kim, Y., Nam, B.W., Kim, D.W. and Kim, Y.S. (2007). Study on coupling effects of ship motion and sloshing. Ocean Engineering, Volume 34, Pages 2176-2187.

Kim, Y., Shin, YS. And Lee, K.H. (2004). Numerical study on sloshi-induced impact pressures on three-dimensional prismatic tanks. Applied Ocean Research, Volume 26, Issue 5, July 2004, Pages 213-226.

Kriebel, D.L. (1992). Nonlinear Wave Interaction with a Vertical Circular Cylinder, Part II: Wave Run-up. Ocean Engineering, Volume 19, No. 1, Pages 75-99.

Kriebel, D.L. (1998). Nonlinear wave interaction with a vertical circular cylinder: wave forces. Journal of Ocean Engineering, Volume, 25, Number 7, Pages 597-605.

Kriebel, D.L. and Alsina, M.V. (2000). Simulation of extreme waves in a background random sea. Proceedings of 10th International Offshore and Polar Engineering Conference.

Lee, B. H., Park, J.C. and Kim, M.H. (2010). Two-dimensional vessel-motion/liquid- sloshing interactions and impact loads by using a particle method. Proceedings of the Conference on Ocean, Offshore and Arctic Engineering.

Lee, S.J. and Kim, M.H. (2010). The Effects of Inner-Liquid Motion on LNG Vessel Responses. Journal of Offshore Mechanics and Artic Engineering, Volume 132, 021101-1.

Lee, S.J., Kim, M.H., Lee, D.H., Kim J.W. and Kim, Y.H (2007). The effects of LNG-tank sloshing on the global motions of LNG carriers. Ocean Engineering, Volume 34, Issue 1, January 2007, Pages 10-20.

Leonard, B.P. (1979). A stable and accurate convective modelling procedure based on quadratic upstream interpolation. Computer Methods in Applied Mechanics and Engineering, Volume 19, Pages 59-98.

Li, J., Wang, Z. and Liu, S. (2012). Experimental study of interactions between multi-directional focused wave and vertical circular cylinder, Part 1: Wave run-up. Coastal Engineering, Volume 64, Pages 151-160.

Liang, X., Yang, J., Li, J. and Li, X. (2011). A numerical study on local characteristics of predetermined irregular wave trains. Ocean Engineering, Volume 38, Pages 651-657.

Liu, S. and Teng, B. (2001). Wave generation in computational domain using source function method. Proceedings of Asian and Pacific Coastal Engineering, Pages 358-368.

MacCamy, R.C. and Fuchs, R.A. (1954). Wave forces on piles: A diffraction theory. Technical Memorandum (United States. Beach Erosion Board), No. 69.

Monsters of the deep, huge freak waves may not be as rare as once thought. Economist Magazine, 2009.

Morison, J.R., O'Brien, M.P., Johnson, J.W. and Schaaf, S.A. (1950). The force exerted by surface waves on piles. Petroleum Transactions, Volume 189, Pages 149-154.

Morris-Thomas, M.T. and Thiagarajan K.P. (2004). The run-up on a cylinder in progressive surface gravity waves: harmonic components. Applied Ocean Research, Volume 26, Pages 98-113.

Niedzwecki, J.M. and Duggal, S.D. (1992). Wave run-up and forces on cylinders in regular and random waves. J. Waterway, Port, Coastal and Ocean Engineering, 118(6), Pages 615-634.

Nieland, H. (1998). New numerical methods for CFD applied to ship hull design. ERCIM NEWS, Number 33.

Nielsen, F.G. (2003). Comparative study on air-gap under floating platforms and run-up along platform columns. Marine Structures, Volume 16, Pages 97-134.

Osborne A. (1999). The random and deterministic dynamics of rouge waves in unidirectional deep-water wave trains. Proceedings of 3rd International Workshop on Very Large Floating Structures, Pages 14-22.

Peregrine, D.H. (1986). Approximately descriptions of the focussing of water waves. Proceedings of 20th International Conference on Coastal Engineering, Pages 675-685.

Peregrine, D.H., Skyner, D., Stiassnie, M. and Dodd, N. (1988). Nonlinear effects on focused water waves. Proceedings of 21st conference on Coastal Engineering.

Qin, H., Tang, W., Xue, H., Hu, Z. and Guo, J. (2017). Numerical study of wave impact on the deck-house caused by freak waves. Ocean Engineering, Volume 133, Pages 151-169.

Rajagopalan, Krishnakumar. And Nihous, Gerard. (2016). Study of the force coefficient on plates using an open source numerical wave tank. Ocean Engineering, Volume 118, Pages 187-203.

Rapp, R. and Melville, W. (1990). Laboratory measurements of deep water breaking waves. Mathematical. Physical and Engineering Sciences, Volume 331, Pages 735-800.

Repalle, N., Thiagarajan, K. and Morris-Thomas, M. (2007). CFD simulation of wave run-up on a spar cylinder. Proceedings of 16th Australian Fluid Mechanics Conference.

Shen, W. and Wan, D. (2012). Numerical simulations of Large-amplitude motions of KVLCC2 coupled with sloshing in waves. Proceedings of International Conference of Violent Flows.

Skourup, J., Andersen, K. and Hansen, N. (1996). Non-Gaussian extreme waves in the central North Sea. Proceedings of the 13th International Conference on Offshore Mechanics and Artic Engineering, ASME, Pages 25-32.

Stansberg CT. (1998). On the nonlinear behaviour of ocean wave groups. Proceedings of Ocean Wave Measurement and Analysis, ASCE, Pages 1227-1241.

Stansberg, CT, Kristiansen, T. (2006). Non-linear scattering of steep surface waves around vertical columns. Applied Ocean Research, Volume 27, Pages 65-80.

Stansberg, CT. (1993). On spectral instabilities and development of nonlinearities in propagating deep-water wave trains. Proceedings of 23rd International Conference on Coastal Engineering, Pages 658-671.

Sun, Z.C., Zhao, X.Z., Zhang, Y.F. and Shen, J.F. (2008). Focusing Models for Generating Freak Waves. Proceedings of the 8th International Offshore and Polar Engineering Conference, Vancouver, BC, Canada, 204-211.

Takewaki, H., Nishiguchi, A. and Yabe, T. (1985). The cubic-interpolated pseudoparticle (CIP) method for solving hyperbolic-type equations. Journal of Computer Physics, Volume 61, Page 261.

Taylor, P. and Haagsma, I. (1994). Focusing of steep wave groups on deep water. Proceedings of the International Symposium on Waves: Physical and Numerical Modelling, Pages 862-870.

Taylor, PH. (2007). The shape of the Draupner Wave of 1 January 1995. Department of Engineering Science, University of Oxford.

Trulsen, K. and Dysthe, K. (1997). Freak waves : a 3-D wave simulation. Proceedings of 21st International Symposium on Naval Hydrodynamics, Pages 550-558.

Vandoormaal, J.P. and Raithby, G.D. (1984). Enhancements of the SIMPLE method for predicting incompressible fluid flows. Numerical of Heat Transfer, Volume 7, Pages 147-163.

Versteeg, H.K. and Malalasekera, W. (2007). An introduction to computational fluid dynamics: the finite volume method. Pearson Education Ltd.

Westphalen, J., Greaves, D.M., Williams, C.J.K., Hunt-Rady, A.C. and Zang, J. (2012). Focused waves and wave-structure interaction in a numerical wave tank. Ocean Engineering, Volume 45, Pages 9-21.

White, B. and Fornberg, B. (1998). On the chance of freak waves at sea. J. Fluid Mechanics, Volume 335, Pages 113-138.

Yang, C., Löhner, C. and Lu, H. (2006). An unstructured-grid based volume-of-fluid method for extreme wave and freely-floating structure interactions. Journal of Hydrodynamics, Volume 18, Pages 415-422.

Yasuda, T. and Mori, N. (1994). High order nonlinear effects on deep-water random wave trains. Proceedings of the International Symposium on Waves: Physical and Numerical Modelling, Pages 823-832.

Young, D.L. (1982). Time-dependent multi-material flow with large fluid distortion. Numerical Methods for Fluids Dynamic, Academic Press.

Zhao, W., Yang, J., Hu, Z. and Tao, L. (2014). Coupled analysis of nonlinear sloshing and ship motions. Applied Ocean Research, Volume, 2014, Pages 85-97.

Zhao, X. and Hu, C. (2012). Numerical and experimental study on a 2-D floating body under extreme wave conditions. Applied Ocean Research. Volume 35, Pages 1-13.

Zhao, X., Ye, Z., Fu, Y. and Cao, F. (2014). A CIP-based numerical simulation of freak wave impact on a floating body. Ocean Engineering, Volume 87, Pages 50-63.

Appendix A Mathematical Formulation

A.1 General Remarks

Computational Fluid Dynamics (CFD) is applied in a wide variety of industrial settings, for example computation of water flow around ship hulls or air flow around the wind turbine.

CFD's founding father, John von Neumann, indulging him in speculations about the possibilities of the emerging digital computer, stated in 1946 that numerical models would eventually completely replace analytic solutions of fluid dynamics equations and even experimental fluid dynamics, Nieland (1998). As usual, the child did not exactly become what the father hoped for, analytic and experimental methods are still used, but by now CFD methods have become a prominent tool in many industrial settings and still form an active research field.

Finite volume methods (FVM) have been used extensively in recent years and the numerical algorithm exists of three main parts, Versteeg and Malalasekera (2007):

- Formal integration of the governing equations of fluid flow over all the (finite) control volumes of the solution domain.
- Discretization involves the substitution of a variety of finite-difference-type approximations for the terms in the integrated equation representing flow processes such as convection, diffusion and sources. This converts the integral equations into a system of algebraic equations.
- Solution of the algebraic equations by an iterative method.

The objective of this chapter is to present the numerical models which are used to carry out CFD calculations with numerical wave tanks. Following paragraphs will cover the subject areas fluid dynamics (governing equation of viscous fluid flows, boundary conditions, turbulence modelling).

A.2 Continuity and Momentum Equation

In Reynolds averaging, the solution variables in the instantaneous (exact) Navier-Stokes equations are decomposed into the mean (ensemble-averaged or time-averaged) and fluctuating components. For the velocity components:

$$u_i = \bar{u}_i + u_i' \tag{A.2.1}$$

where

$\bar{u}_i$ = the mean velocity component ($i = 1,2,3$)

u_i' = the fluctuating velocity component ($i = 1,2,3$)

Likewise, for pressure and other scalar quantities:

$$\phi = \bar{\phi} + \phi' \tag{3.2.2}$$

where

$\phi =$ a scalar such as pressure, energy, or species concentration.

Substituting expressions of this form for the flow variables into the instantaneous continuity and momentum equations and taking a time (or ensemble) average (and dropping the overbar on the mean velocity,$\bar{u}$) yields the ensemble-averaged momentum equations. They can be written in Cartesian tensor form as:

$$\frac{\partial \rho}{\partial t} + \frac{\partial}{\partial x_i}(\rho u_i) = 0 \tag{A.2.3}$$

$$\frac{\partial}{\partial t}(\rho u_i) + \frac{\partial}{\partial x_j}\left(\rho u_i u_j\right) = -\frac{\partial p}{\partial x_i} + \frac{\partial}{\partial x_j}\left[\mu\left(\frac{\partial y}{\partial x} + \frac{\partial y}{\partial x} - \frac{2}{3}\delta_{ij}\frac{\partial u_l}{\partial x_l}\right]\right. + \frac{\partial}{\partial x_j}\left(-\rho\overline{u_i' u_j'}\right) \tag{A.2.4}$$

The Reynolds-averaged Navier-Stokes (RANS) equations are shown above. They have the same general form as the instantaneous Navier-Stokes equation, with the velocities and other solution variables now representing ensemble-averaged (or time-averaged) values. Additional term now appear that represent the effects of turbulence. These Reynolds stress,$-\rho\overline{u_i'u_j'}$ must be modelled in order to close to Equation.

A.3 Turbulence Model

Most flows encountered in engineering practice are turbulent and become unstable above a certain Reynolds number. Flows at a low Reynolds number are laminar whereas flows at a high Reynolds number are turbulent. These turbulent flows characterised by fluctuations which create additional unknown variables in the modified governing equations in the velocity fields can be calculated with various methods. The shear-stress transport (SST) k-ω model is such a turbulence model and has been used frequently in practical engineering for flow calculations in the time since it was proposed by Versteeg and Malalasekera (2007) to effectively blend the robust and accurate formulation of the k-ω model in the near-wall region with the freestream independence of the k-ε model in the far field. To achieve this, the k-ε model is converted into a k-ω formulation.

A.3.1 Transport Equation for the SST k-ω Model

The SST k-ω model has a similar form to the standard k-ω model:

$$\frac{\partial}{\partial t}(\rho k) + \frac{\partial}{\partial x_i}(\rho k u_i) = \frac{\partial}{\partial}_j\left(\Gamma_k \frac{\partial k}{\partial x_j}\right) + G_k - Y_k + S_k \qquad \text{(A.3.1)}$$

And

$$\frac{\partial}{\partial t}(\rho \omega) + \frac{\partial}{\partial x_i}(\rho \omega u_i) = \frac{\partial}{\partial x_j}\left(\Gamma_\omega \frac{\partial \omega}{\partial x_j}\right) + G_\omega - Y_\omega + D_\omega + S_\omega \qquad \text{(A.3.2)}$$

where

G_k = the production of turbulence kinetic energy

G_ω = the generation of ω

Γ_k = the effective diffusivity of k

Γ_ω = the effective diffusivity of ω

Y_k = the dissipation of k due to turbulence

Y_ω = the dissipation of ω due to turbulence

D_ω = the cross-diffusion term

$S_k \; and \; S_\omega$ = the user-defined source terms

A.3.2 Modelling the Effective Diffusivity

The effective diffusivities for the SST k-ω model are given by

$$\Gamma_k = \mu + \frac{\mu_t}{\sigma_k} \tag{A.3.3}$$

$$\Gamma_k = \mu + \frac{\mu_t}{\sigma_k} \tag{A.3.4}$$

where

σ_k = the turbulent Prandtl number of k

σ_k = the turbulent Prandtl number of ω

The turbulent viscosity μ_t is computed as follows:

$$\mu_t = \frac{\rho k}{\omega} \frac{1}{max\left[\frac{1}{a^*}, \frac{SF_2}{a_1 \omega}\right]} \tag{A.3.5}$$

where

S = the strain rate magnitude

$$\sigma_k = \frac{1}{F_1/\sigma_{k,1} + (1 - F_1)/\sigma_{k,2}} \tag{A.3.6}$$

$$\sigma_\omega = \frac{1}{F_1/\sigma_{\omega,1} + (1-F_1)/\sigma_{\omega,2}} \tag{A.3.7}$$

The coefficient a^* damps the turbulent viscosity causing a low-Reynolds number correction. It is given by

$$a^* = a^*_\infty \left(\frac{a^*_0 + Re_t/R_k}{1 + Re_t/R_k} \right) \tag{A.3.8}$$

where

$$Re_t = \frac{\rho k}{\mu \omega} \tag{A.3.9}$$

$$R_k = 6 \tag{A.3.10}$$

$$a^*_0 = \frac{\beta_i}{3} \tag{A.3.11}$$

$$\beta_i = 0.072 \tag{A.3.12}$$

The blending functions, F_1 and F_2, are given by

$$F_1 = tanh(\Phi_I^4) \tag{A.3.13}$$

$$\Phi_I = min\left[max\left(\frac{\sqrt{k}}{0.09\omega y}, \frac{500\mu}{\rho\ ^2\omega} \right), \frac{4\rho k}{\sigma_{\omega,2} D_\omega^+ y^2} \right] \tag{A.3.14}$$

$$D_\omega^+ = max\left[2\rho \frac{1}{\sigma_{\omega,2}} \frac{1}{\omega} \frac{\partial}{\partial x_j} \frac{\partial \omega}{\partial x_j}, 10^{-10} \right] \tag{A.3.15}$$

$$F_2 = tanh(\Phi_2^2) \tag{A.3.16}$$

$$\Phi_2 = max\left[2\frac{\sqrt{k}}{0.09\omega y}, \frac{500\mu}{\rho y^2 \omega} \right] \tag{A.3.17}$$

where

$y =$ the distance to the next surface

$D_\omega^+ =$ the positive portion of the cross-diffusion term

A.3.3 Modelling the Turbulence Production

A.3.3.1Production of k

The term G_k represents the production of turbulence kinetic energy, and is defined in the same manner as in the standard k-ω model. From the exact equation for the transport of k, this term may be defined as

$$G_k = -\rho\overline{u_i' u_j'}\frac{\partial u_j}{\partial x_i} \tag{A.3.18}$$

To evaluate G_k in a manner consistent with the Boussinesq hypothesis,

$$G_k = \mu_t S^2 \tag{A.3.19}$$

Where

$S =$ the modulus of the mean rate-of-strain tensor.

$$S \equiv \sqrt{2S_{ij}S_{ij}} \tag{A.3.20}$$

A.3.3.2 Production of ω

The term G_ω represents the production of ω and is given by

$$G_\omega = \frac{\alpha}{V_t} G_k \tag{A.3.21}$$

The coefficient α is given by

$$\alpha = \frac{\alpha_\infty}{a^*}\left(\frac{\alpha_0 + {Re_t}/{R_\omega}}{1 + {Re_t}/{R_\omega}}\right) \tag{A.3.22}$$

where

$$R_\omega = 2.95 \tag{A.3.23}$$

A.3.4 Modelling the Turbulence Dissipation

A.3.4.1 Dissipation of k

The term Y_k represents the dissipation of turbulence kinetic energy is defined as

$$Y_k = \rho\beta^* f_{\beta^*} k\omega \tag{A.3.24}$$

where

$$f_\beta = 1 \tag{A.3.25}$$

and

$$\beta^* = \beta_i^*[1 + \zeta^* F(M_t)] \tag{A.3.26}$$

$$\beta_i^* = \beta_\infty^* \left[\frac{{}^4\!/_{15} + ({}^{R_{e_t}}\!/_{R_\beta})^4}{1 + ({}^{R_{e_t}}\!/_{R_\beta})^4} \right] \tag{A.3.27}$$

$$\zeta^* = 1.5 \tag{A.3.28}$$

$$R_\beta = 8 \tag{A.3.29}$$

$$\beta_\infty^* = 0.09 \tag{A.3.30}$$

A.3.4.2 Dissipation of ω

The term Y_ω represents the dissipation of ω is given by

$$Y_\omega = \rho\beta f_\beta \omega^2 \tag{A.3.31}$$

where

$$f_\beta = \frac{1 + 70\chi_\omega}{1 + 80\chi_\omega} \tag{A.3.32}$$

$$\chi_\omega = \left|\frac{\Omega_{ij}\Omega_{jk}S_{ki}}{(\beta^*_\infty\omega)^3}\right| \tag{A.3.33}$$

$$\Omega_{ij} = \frac{1}{2}\left(\frac{\partial u_i}{\partial x_j} - \frac{\partial u_j}{\partial x_i}\right) \tag{A.3.34}$$

The strain rate tensor, $S_{ij}$is defined as

$$S_{ij} = \frac{1}{2}\left(\frac{\partial u_j}{\partial x_i} + \frac{\partial u_i}{\partial x_j}\right) \tag{A.3.35}$$

and also,

$$\beta = \beta_i\left[1 - \frac{\beta_i^*}{\beta_i}\zeta^* F(M_t)\right] \tag{A.3.36}$$

A.3.5 Cross-Diffusion Modification

The SST k-ω model is based on both the standard k-ω model and standard k-ω model. To blend these two models together, the standard k-ε has been transformed into equations based on k and ω, which leads to the introduction of a cross-diffusion term. D_ω is defined as

$$D_\omega = 2(1 - F_1)\rho\frac{1}{\omega\sigma_{\omega,2}}\frac{\partial k}{\partial x_j}\frac{\partial \omega}{\partial x_j} \tag{A.3.37}$$

A.3.6 Model Constants

$$\alpha^*_\infty = 1 \tag{A.3.38}$$

$$\alpha_\infty = 0.52 \tag{A.3.39}$$

$$\alpha_0 = \frac{1}{9} \tag{A.3.40}$$

$$\beta^*_\infty = 0.09 \tag{A.3.41}$$

$$\beta_i = 0.072 \tag{A.3.42}$$

$$R_\beta = 8 \tag{A.3.43}$$

$$R_k = 6 \tag{A.3.44}$$

$$R_\omega = 2.95 \tag{A.3.45}$$

$$\zeta^* = 1.5 \tag{A.3.46}$$

$$\sigma_k = 2.0 \tag{A.3.47}$$

$$\sigma_\omega = 2.0 \tag{A.3.48}$$

$$\sigma_{k,1} = 1.176 \tag{A.3.49}$$

$$\sigma_{\omega,1} = 2.0 \tag{A.3.50}$$

$$\sigma_{k,2} = 1 \tag{A.3.51}$$

$$\sigma_{\omega,2} = 1.168 \tag{A.3.52}$$

$$a_1 = 0.31 \tag{A.3.53}$$

$$\beta_{i,1} = 0.075 \tag{A.3.54}$$

$$\beta_{i,2} = 0.0828 \tag{A.3.55}$$

A.4 Free Surface Flows-multiphase Flows

A.4.1 General Remarks

In nature and engineering fields a large number of flows are object to a mixture of phases. A phase is a region in the parameter space of thermodynamic variables in which the free energy is analytic. Between such regions there are abrupt changes in the propertied of the system, which correspond to discontinuities in the derivatives of the free energy functions. Such physical phase as gas, liquid or solid, can be defined as an identifiable class of material which has inertial response to and interaction with the flow and the potential field in which it is immersed.

There are two basic ways to model free surface flows: the Lagrangian method where the mesh follows the interface shape and the Eulerian method which treats different phases mathematically as interpenetrating continua. The concept of phasic volume fraction is a term describing that the volume of a phases cannot be occupied by other phases. The sum of the volume fraction is equal to one and it is assumed that the volume fraction is a continuous function of space and time. A suitable Euler-Euler multiphase model for free surface problems is the volume of fluid (VOF) model which will be explained in the following chapter.

A.4.2 Volume of Fluid (VOF) Model

The VOF model is a surface-capturing technique applied to a foxed Eulerian mesh. It is designed for two or more immiscible fluids or phases that are not interpenetrating and gives the position of the interface between the fluids. For each additional phase added to the model, a variable is introduced and a single set of momentum equations if shared by the fluids and the volume fraction of the phase in the computational cell is tracked throughout the domain. In each control volume, the volume fractions of all phases sum to unity. As long as the volume fraction of each of the phases is known at each location all variables and properties are shared by the phases and represent volume-averaged values. Hence, the variables and properties in any given cell are either representing one of the phases, or represent a mixture of the phases, depending upon the volume fraction values. That means that if q^{th} fluid's volume fraction in the cell is denoted as α_q, then the following three conditions are possible:

- $\alpha_q = 0$ The cell is empty (of the q^{th} fluid).
- $\alpha_q = 1$ The cell is full (of the q^{th} fluid).
- $0 < \alpha_q < 1$ The cell contains the interface between the q^{th} fluid and one or more other fluids.

Based on the local value of α_q, the appropriate properties and variables will be assigned to each control volume within the domain.

The tracking of the interface between the phases is accomplished by the solution of a continuity equation for the volume fraction of one or more of the phases where α_q evolves from the transport equation:

$$\frac{\partial \alpha}{\partial t} + div(\alpha v) = 0 \tag{A.4.1}$$

For the q[th] phase, the equation has the following form:

$$\frac{1}{\rho_q}\left[\frac{\partial}{\partial t}(\alpha_q \rho_q) + \nabla \cdot (\alpha_q \rho_q \overrightarrow{v_q})\right] = S_{\alpha_q} + \sum_{p=1}^{n} \left|(\dot{m}_{pq} - \dot{m}_{qp})\right| \tag{A.4.2}$$

where

$\dot{m}_{pq}$ = the mass transfer from phase p to phase q

$\dot{m}_{qp}$ = the mass transfer from phase q to phase p.

The volume fraction equation will not be solved for the primary phase; the primary-phases volume fraction will be computed based on the following constraint:

$$\sum_{q=1}^{n} \alpha_q = 1 \tag{A.4.3}$$

A.4.2.1 Implicit Scheme

When the implicit scheme is used for time discretization, standard finite-difference interpolation schemes, QUICK, Second Order Upwind and First Order Upwind and the Modified HRIC schemes are used to obtain the face fluxes for all cells including those near the interface.

$$\frac{\alpha_q^{n+1}\rho_q^{n+1} - \alpha_q^n \rho_q^n}{\Delta t} V + \sum_f (\rho_q^{n+1} U_f^{n+1} \alpha_{q,f}^{n+1}) = \left[S_{\alpha_q} + \sum_{p=1}^{n} (\dot{m}_{pq} - \dot{m}_{qp})\right] V \tag{A.4.4}$$

Since this equation requires the volume fraction values at the current time step (rather than at the previous step, as for the explicit scheme), a standard scalar transport equation is solved iteratively for each of the secondary-phase volume fractions at each time step. The implicit scheme can be used for both time-dependent and steady-state calculations.

A.4.2.2 Explicit Scheme

In the explicit approach, the standard finite-difference interpolation schemes are applied to the volume fraction values that were computed at the previous time step.

$$\frac{\alpha_q^{n+1}\rho_q^{n+1} - \alpha_q^n \rho_q^n}{\Delta t} V + \sum_f (\rho_q^n U_f^n \alpha_{q,f}^n) = \left[\sum_{p=1}^{n} (\dot{m}_{pq} - \dot{m}_{qp}) + S_{\alpha_q} \right] V \qquad \text{(A.4.5)}$$

where

$n + 1 =$ index for new (current) time step

$n =$ index for previous time step

$\alpha_{q,f} =$ face value of the qth volume fraction

$V =$ volume of cell

$U_f =$ volume flux through the face, based on normal velocity

This formulation does not require iterative solution of the transport equation during each time step, as is needed for the implicit scheme.

A.4.3 Interpolation near the Interface

A special interpolation treatment to the cells that lie near the interface between two phases is applied to be able to calculate the convection and diffusion fluxes through the control volume faces and to balance them with the control volume itself. Figure A.1 (a) shows an actual interface shape along with the interfaces assumed during computation by the geometric reconstruction scheme (Figure A.1 b) and the donor-acceptor scheme (Figure A.1 c).

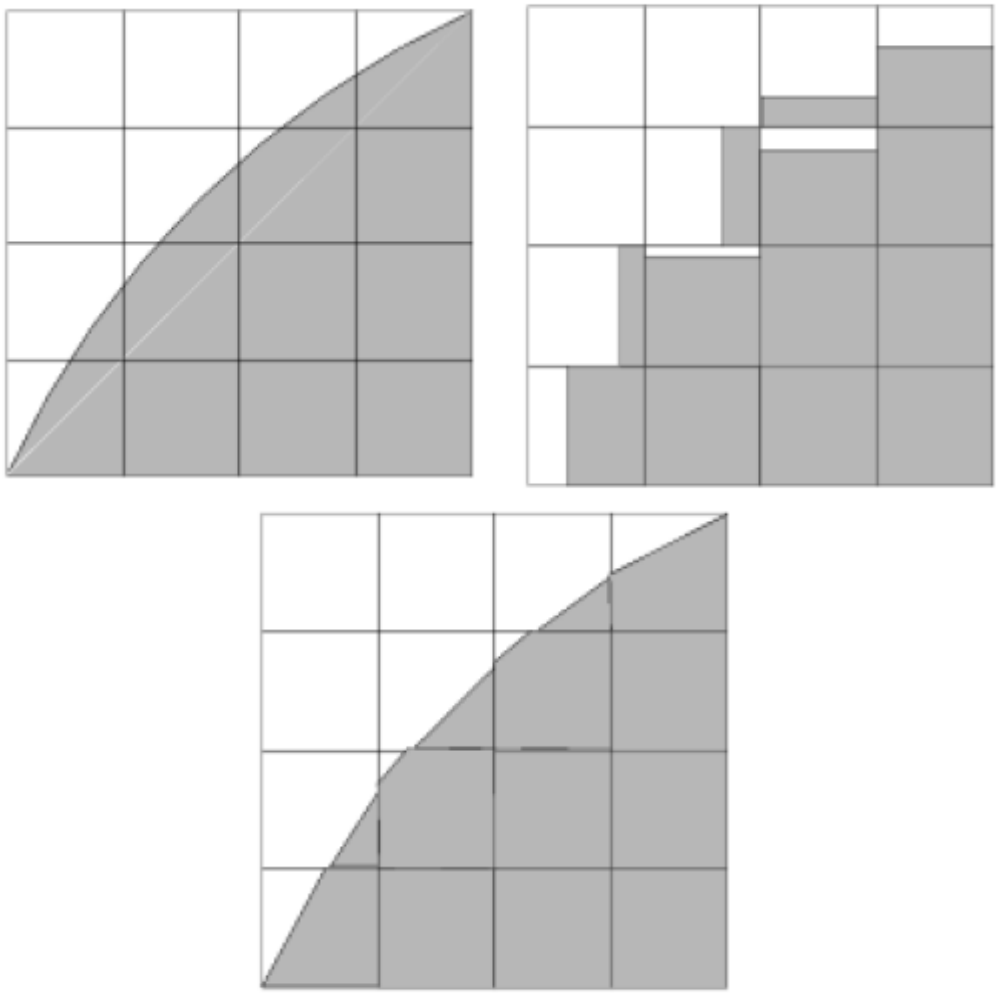

Figure A.0.1 The actual interface shape, the geometric reconstruction scheme and the donor-acceptor scheme

A.4.3.1 The Geometric Reconstruction Scheme

Whenever a cell is completely filled with one phases or another, the standard interpolation schemes are used in order to obtain the face fluxes. The geometric construction scheme is applied when two or more phases split a cell with its interface.

The geometric reconstruction scheme is also known as the piecewise-linear approach which represents the interface between fluids. This scheme is the most accurate and is applicable for general unstructured mesh which was a main achievement in the work of Young (1982). It is assumed that the interface

between two fluids has a linear slope within each cell; therefore, the advection of fluid through the cell faces can be computed by making use of this linear shape, see Figure A.1 (b).

The interpolation procedure is carried out in three steps: firstly, the position of the linear interface relative to the centre of each partially-filled cell is derived based on information about the volume fraction and its derivatives in the cell. The second step is calculating the advection amount of fluid through each face using the computed linear interface representation and information about the normal and tangential velocity distribution on the face. The third step is calculating the volume fraction in each cell using the balance of fluxes calculated during the previous step.

A.4.3.2 The Donor-Acceptor Scheme

In almost the same manner as in the geometric reconstruction scheme the standard interpolation schemes are used in order to obtain the face fluxes whenever a cell is completely flied with one phase or another. A donor-acceptor scheme is used, when the cell is near the interface between two phases, to determine the amount of fluid advected through the face, Hirt and Nichols (1981). This scheme identifies one cell as a donor of an amount of fluid from one phase and another neighbour cell as the acceptor of that same amount of fluid, and is used to prevent numerical diffusion at the interface. The amount of fluid from one phase that can be convected across a cell boundary is limited by the minimum of two values; the flied volume in the donor cell or the free volume in the acceptor cell.

The orientation of the interface is also used in determining the face fluxes. The interface orientation is either horizontal or vertical, depending on the direction of the volume fraction gradient of the q^{th} phase within the cell and that of the neighbour cell that shares the face in question. Depending on the interface's orientation as well as its maximum, flux values are obtained by pure upwinding, pure downwinding, or some combination of the two.

A.5 Dynamic Mesh

A.5.1 General Remarks

The dynamic mesh model allows moving the boundaries of a cell zone relative to other boundaries of the zone, and to adjust the mesh accordingly. The motion of the boundaries can be rigid, such as pistons moving inside an engine cylinder or a flap deflecting on an aircraft wing, or deforming, such as the elastic wall of a balloon during inflation or a flexible artery wall responding to the pressure pulse from the heart. In either case, the nodes that define the cells in the domain must be updated as a function of time, and hence the dynamic mesh solutions are inherently unsteady.

The dynamic mesh model can be used in flow cases where the shape of the domain, respectively the boundaries, is changing with time. These changes can either be prescribed motion with specified changes in linear and /or angular velocities about the centre of gravity or unspecified motions where the linear and angular velocities of the centre of gravity of a solid body are calculated based on the force balance on the body. This body can then move in six-degree-freedom. Each time step the volume mesh is updated with the new position of the boundaries. The volume mesh can be updated with one of the following methods or a combination of them:

- Smoothing methods
    - Laplacian smoothing
    - Spring-based method
- Dynamic layering
- Local remeshing

These smoothing methods and local remeshing will be explained in detail and some important equations will be discussed.

A.5.2 Conservation Equations

The integral form of the conservation equation for a general scalar ϕ on randomly chosen control volume V with a moving boundary can be written as

$$\frac{d}{dt}\int \rho\phi dV + \int \rho\phi(\vec{u}-\vec{u}_g)\cdot d\vec{A} = \int \Gamma\nabla\phi \cdot d\vec{A} + \int S_\phi dV \tag{A.5.1}$$

where

ρ = the fluid density

$\vec{u}$ = the flow velocity vector

$\vec{u}_g$ = the grid velocity of the moving mesh

Γ = the diffusion coefficient

S_ϕ = the source term of ϕ

Here ∂V is used to present the boundary of the control volume V.

The time derivation term in equation (A.5.1) can be written, using a first-order backward difference formula as

$$\frac{d}{dt}\int \rho\phi dV = \frac{(\rho\phi V)^{n+1} - (\rho\phi V)^n}{\Delta t} \tag{A.5.2}$$

where n denotes the respective quantity at the current time level and n+1 at the next time level. The $(n+1)^{th}$ time level volume V^{n+1} is computed from

$$V^{n+1} = V^n + \frac{dV}{dt}\Delta t \tag{A.5.3}$$

where

dV/dt = the volume time derivative of the control volume.

In order to satisfy the grid conservation law, the volume time derivative of the control volume is computed from

$$\frac{dV}{dt} = \int \vec{u}_g \cdot d\vec{A} = \sum_j^{n_f} \vec{u}_{g,j}\cdot\vec{A}_j \tag{A.5.4}$$

where

n_f = the number of faces on the control volume

$\vec{A}_j$ = the j face area vector

The dot product $\vec{u}_{g,j}\cdot\vec{A}_j$ on each control volume face is calculated from

$$\vec{u}_{g,j} \cdot \vec{A}_j = \frac{\delta V_j}{\Delta t} \tag{A.5.5}$$

where

$\delta V_j =$ volume swept out by the control volume face j over the time step Δt.

A.5.3 Dynamic Mesh Update Methods

A.5.3.1 Laplacian Smoothing Method

The Laplacian smoothing method is the simplest among the dynamic mesh update methods. It repositions each internal fluid node equidistant to the nodes connected to it, see Figure A.2.

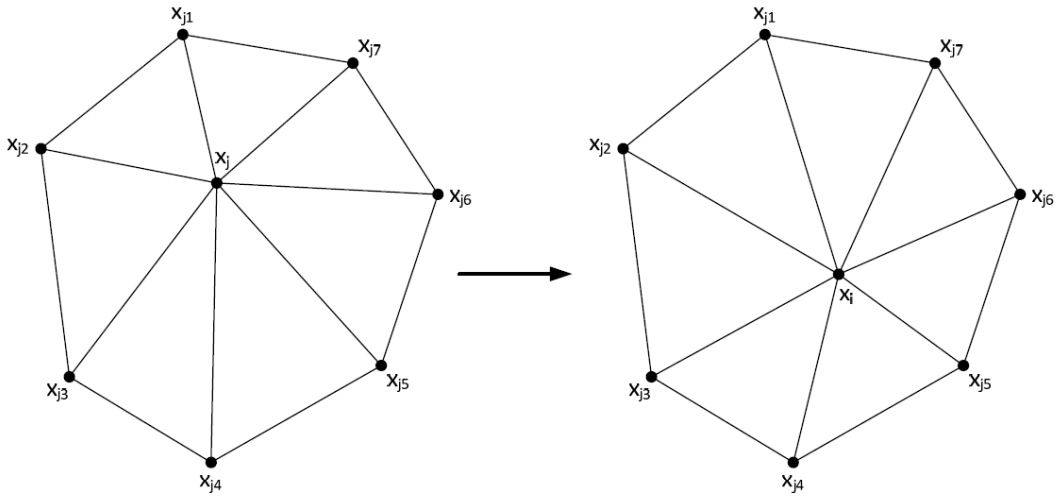

Figure A.0.2 Laplacian algorithm

Unfortunately, this method does not guarantee an improvement on the mesh quality but it is computationally inexpensive. The node position at the current time step is:

$$\overline{\vec{x}_i^m} = \frac{\sum_j^{n_i} \vec{x}_j^m}{n_i} \tag{A.5.6}$$

where

$\overline{\vec{x}_i^m}$ = the average node position of node i at iteration m

$\vec{x}_j^m$ = the node position of neighbour node $\vec{x}_i^m$ at iteration m

n_i = the number of nodes neighbouring node i.

The computation of the node position $\vec{x}_i^{m+1}$ at the next iteration works as follows:

$$\vec{x}_i^{m+1} = \vec{x}_i^m(1-\beta) + \overline{\vec{x}_i^m}\beta \tag{A.5.7}$$

where

β = the boundary node relaxation factor.

A.5.3.2 Spring-Based Smoothing Method

The spring-based smoothing method is a physics-based mesh updating procedure where the edge of the mesh is replaced with fictitious linear springs. It is assumed that the springs in the initial mesh ate in equilibrium. A displacement at a given boundary node will generate a force proportional to the displacement along all the springs connected to the node. The displacement of the nodes can be computed using the generalised Hook's Law and the force on a mesh node can be written as

$$\overrightarrow{F_i} = \sum_j^{n_i} k_{ij}(\Delta\,\overrightarrow{x_j} - \Delta\,\overrightarrow{x_i}) \tag{A.5.8}$$

where

$\overrightarrow{F_i}$ = the force vector

n_i = the number of neighbouring nodes connected to node i

k_{ij} = the stiffness between node i and its neighbour j

$\Delta\,\overrightarrow{x_i}$ = the displacement of node i

$\Delta\,\overrightarrow{x_j}$ = the displacement of node j

The stiffness k_{ij} of the spring connecting nodes i and j is chosen to be inversely proportional to the length of the edge and is defined as

$$k_{ij} = \frac{1}{\sqrt{|\vec{x}_i - \vec{x}_j|}} \tag{A.5.9}$$

The net force on a node due to all the springs connected to the node must be zero when it is assumed that the springs which connect the vertices in the unreformed mesh are in tension. The new nodal positions of the internal nodal points can be computed using:

$$[k]\{x\} = 0 \quad for\ x = \overline{x} \ \ on\ \Gamma_b \tag{A.5.10}$$

where

$x =$ the position vector

$\overline{x} =$ the known position vector of the moving boundaryΓ_b.

This condition results in an equation solved by the Jacobi sweep on all interior nodes:

$$\vec{x}_i^{m+1} = \frac{\sum_j^{n_i} k_{ij} \, \Delta \, \vec{x}_j^m}{\sum_j^{n_i} k_{ij}} \tag{A.5.11}$$

At convergence, the positions are updated such that

$$\vec{x}_i^{n+1} = \vec{x}_i^n + \Delta \, \vec{x}_i^{m,converged} \tag{A.5.12}$$

where

$n =$ the position at the current time step

$n + 1 =$ the position at the next time step

The spring-based smoothing is shown in Figure A.3 and Figure A.4 for a cylinder cell zone where one end of the cylinder is moving.

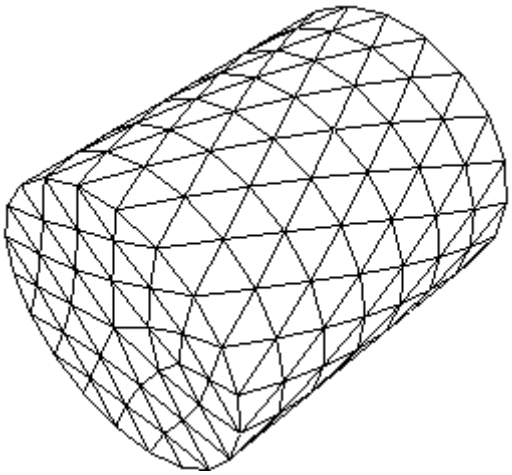

Figure A.0.3 Spring-based smoothing on interior nodes: start

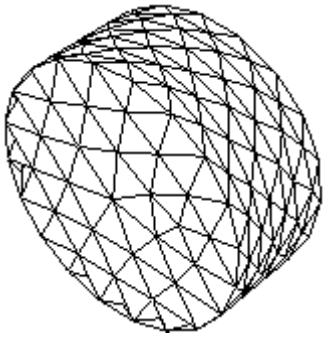

Figure A.0.4 Spring-based smoothing on interior nodes: end

A.5.3.3 Local Remeshing Method

The cell quality can be strongly influenced by large boundary displacements compared to the local cell size which can lead to negative cell volumes and in the end cause convergence problems. Therefore, areas with faces or cells that do not comply with size or skewness criteria will be locally updated with new cells. The skewness and size criteria that should be met to be updated are:

- It has a skewness that is greater than a specified maximum length scale.
- It is smaller than a specified minimum length scale.
- It is larger than a specified maximum length scale.
- Its length does not meet the specified length scale

Face region remeshing method: also, linear and triangular faces on a deforming boundary can be remeshed according to the minimum and maximum length

scale. A region of deforming boundary face is marked for remeshing; the remeshing algorithm replaces marked faces and adjacent cells with a regular mesh on the deforming boundary at the moving boundary, see Figure A.5. This method makes it possible to remesh domains with symmetric boundary conditions and across multiple face zones preserving all features within a face zone and between different face zones.

As an example: A simple tetrahedral mesh of a cylinder having a moving bottom wall is given, see Fig A.5. On the moving boundary, a single loop is generated at the bottom end of the cylinder because the notes are moving. Thereafter the height of the faces connected to the nodes on the loop is analysed and the faces are split or merged depending on the specified maximum or minimum length scale.

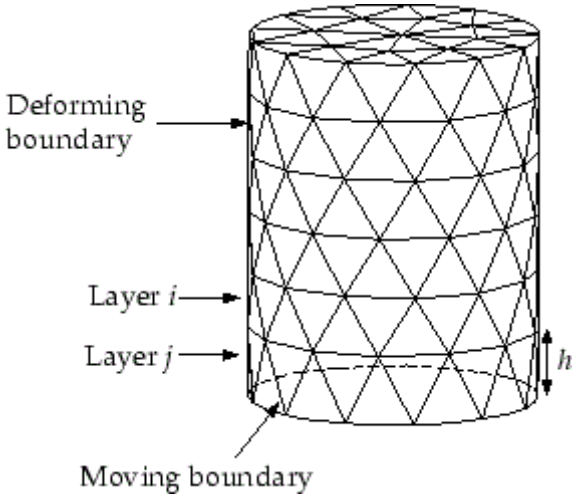

Figure A.0.5 Remeshing at a deforming boundary

If the faces in layer j are expanding, they are allowed to expand until the maximum length scale is reached; vice versa, if the layer j is contracting, faces are allowed to contract until the minimum length scale is reached.

When either of this condition is met, the compressed layer j of faces is merged into the layer I of faces above it, see Figure A.6 and Figure A.7.

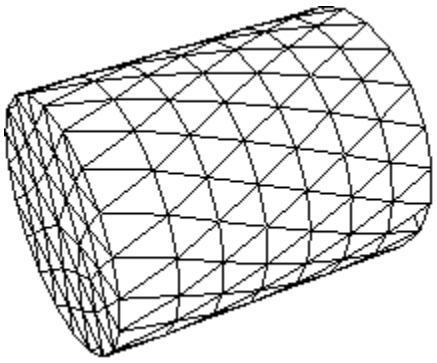

Figure A.0.6 Expanding cylinder before region face remeshing

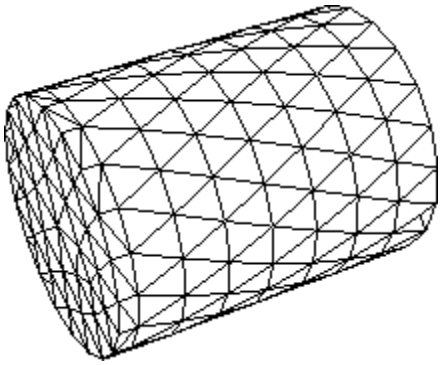

Figure A.0.7 Expanding cylinder after region face remeshing

Local Face Remeshing Method: In contrary to the local region remeshing method the local face remeshing method only applies to 3D geometries. Based on the face skewness on the deforming boundary the faces and adjacent cells are remeshed. Remeshing across multiple face zones is not allowed.

A.5.4 Sliding Mess Theory

The sliding mesh model is a special case of general dynamic mesh motion wherein the nodes move rapidly in a given dynamic meshes zones. Additionally, multiple cells zones are connected with each other through non-conformal interfaces. As the mesh motion is updated in time, the non-conformal interfaces are likewise updated to reflect the new positions each zone, it is important to note that the mesh motion must be prescribed such that zones linked through ono-conformal interfaces remain in contract with each other if we assume fluid to be able to flow from one mesh to the other.

The general conservation equation formulation for dynamic meshes, as expressed in Equation (A.5.1), is also used for sliding meshes. Because the mesh motion in the sliding mesh formulation is rigid, all cells retain their original shape and volume. Thus, the time rate of change of the cell volume is zero, and Equation (A.5.3) simplifies to:

$$V^{n+1} = V^n \tag{A.5.13}$$

And Equation (A.5.2) becomes:

$$\frac{d}{dt}\int \rho\phi dV = \frac{[(\rho\phi)^{n+1} - (\rho\phi)^n]V}{\Delta t} \tag{A.5.14}$$

Additionally, Equation (A.5.4) simplifies to:

$$\sum_j^{n_f} \vec{u}_{g,j} \cdot \vec{A}_j = 0 \tag{A.5.15}$$

Equation (A.5.1), in conjunction with the above simplifications, permits the flow in the moving mesh zones to be updated, if an appropriate specification of the rigid mesh motion is defined for each zone (usually this is simple linear or rotation motion, but more complex motions can be used). Note that due to the face that the mesh is moving, the solution to Equation (A.5.1) for sliding mesh applications will be inherently unsteady (as they are for all dynamic meshes.

A.5.5 Six DOF (6DOF) Solver Theory

The Six DOF Solver computes the translational and angular motion of the centre of gravity of a rigid body by taking its forces and moments into account. The mass centre translation is governed by Newton's law of motion, equation (A.5.16), which is written in the inertial coordinate system.

$$\dot{\vec{V}}_G = \frac{1}{m}\sum \vec{f} \tag{3.5.16}$$

where

$\dot{\vec{V}}_G =$ the translational acceleration of the centre of gravity

$m =$ the mass

$\vec{f} =$ the applied force vector through the centre of mass

The applied force vector has been broken into three components.

$$\vec{f} = \vec{f}_H + \vec{f}_E + \vec{f}_G \tag{A.5.17}$$

where

$\vec{f}_H =$ the hydrodynamic forces

$\vec{f}_E =$ the external forces

$\vec{f}_G =$ the forces due to gravity

Basically, these forces are determined by the gravitational force of the ship hull, the hydrostatic force of the floodwater the hydrodynamic force of the water surrounding the ship acting on the shell of the hull.

Newton's law can be integrated directly to give the position of the mass centre as a function of time. Holding $\vec{f}$ constant over the discrete physical time step (t^n, t^{n+1}) gives equation (A.5.18).

$$\vec{r}(t^{n+1}) = \frac{1}{2}\frac{\vec{f}}{m} \Delta\, t^2 + \vec{V}_G(t^n) \Delta\, t + \vec{r}(t^n) \tag{A.5.18}$$

It is easier to compute the angular acceleration of the object $\dot{\vec{\omega}}_B$, equation 1, by using body coordinates.

$$\dot{\vec{\omega}}_B = L^{-1}(\sum \overrightarrow{M_B} - \overrightarrow{\omega_B}) \tag{A.5.19}$$

where

$L =$ the inertia tensor

$\overrightarrow{M_B} =$ the moment vector of the body

$\overrightarrow{\omega_B} =$ the rigid body angular velocity vector.

The moments are transformed from inertial to body coordinates using

$$\overrightarrow{M_B} = R\overrightarrow{M_G} \tag{A.5.20}$$

where R is the following transformation matrix:

$$\begin{pmatrix} C_\theta C_\psi & C_\theta S_\psi & S_\theta \\ S_\phi S_\theta C_\psi - C_\phi S_\psi & S_\phi S_\theta S_\psi + C_\phi C_\psi & S_\phi C_\theta \\ C_\phi S_\theta C_\psi + S_\phi S_\psi & C_\phi S_\theta S_\psi - S_\phi C_\psi & C_\phi C_\theta \end{pmatrix}$$

where, in generic term, $C_\chi = cos(\chi)\ and\ S_\chi = sin(\chi)$. The angles $\phi, \theta\ and\ \psi$ are Euler angles that represent the following sequence of rotations:

- Rotation about the x-axis
- Rotation about the y-axis
- Rotation about the z-axis

After the angular and the translational accelerations are computed from Equation (A.5.16) and Equation (A.5.19), the rates are derived by numerical integration. The angular and translational velocities are used in the dynamic mesh calculations to update the rigid body position.

Appendix B Numerical Solution

Following the description of the mathematical model, the attention is turned to the numerical models involved on the CFD calculations. The object of this chapter is to present the numerical schemes that are used in the simulations. The following paragraphs will cover the algorithms, the discretization of the method, the coupling between the flow variables that are part of the problem and that are used for the application and the solution of fluid flow problems.

B.1 General Remarks

The CFD solver uses a finite volume method (FVM) to formulate the solution of the governing equation. The algorithm consists of three parts (Versteeg and Malalasekera, 2007):

- Formal integration of the governing equations of fluid flow over each and all the finite control volumes of the solution domain
- Discretization involving the substitution of a variety of approximations for the terms in the integrated equation representing flow processes such as convection, diffusion and sources. This converts the integral equations into a system of algebraic equations
- Solution of the algebraic equations by an iterative method

The numerical algorithm applied is the pressure-based solver. In the past, this solver was initially developed for low-speed incompressible flows, as opposed to the density-based solver, which was used for high speed compressible flows. Since then, both methods have been adapted and reformulated to operate on a wide range of flow conditions out with their original configuration.

In the pressure-based algorithm, the pressure field is obtained from the equation of state by solving a pressure or pressure correction equation (Poisson equation). The velocity fields are obtained from the momentum equations. Equations for the conservation of mass momentum and other scalars (e.g. turbulence) are solved using the control-volume approach implemented in Fluent that consists of:

- Division of the domain into discrete control volume using a computational grid
- Integration of the governing equations on the individual control volumes to construct algebraic equations for the discrete dependent variables ("unknowns") such as velocities, pressure, temperature and conserved scalars
- Linearization of the discretized equations and solution of the resultant linear equation system to yield updated values of the dependent variables

The governing equations of fluid flow are solved separately from each other. Two different pressure-based variants can be distinguished: the segregated and the coupled algorithm. In the current thesis, a segregated approach is used.
In the pressure-based segregated algorithm, the governing equations are solved sequentially, all solution variables one after another, because they are non-liner, in an iteratively wavy. This procedure makes the solution convergence process relatively slow. It consists of the following steps:

- Fluid properties are updated. Solution is initialised at first iteration
- The x-, y- and z- momentum equations are each solved using values for pressure and face mass fluxes, in order to update the velocity field
- Since the velocities obtained in step 2 may not satisfy the continuity equation locally, a Poisson equation for the pressure correction is derived from the continuity equation and the linearized momentum equations. This pressure correction equation is then solved to obtain the necessary corrections to the pressure and velocity fields and the face mass fluxes such that continuity is satisfied
- Equation for scalar, turbulence is solved using the previously updated values of the variables
- Convergence is checked. If successful, the solution ends. If not, the solution method restarts from step 1 and a loop is reinitiated.

On the other hand, the coupled algorithm solves a coupled system of equations implying the momentum equations and the pressure-based continuity equation.

All the other equations are solved in a decoupled manner similar to the segregated method. The solution convergence is improved and the process is accelerated.

B.2 Scalar-transport Equation

A control-volume based technique is used to convert the governing general scalar transport equation to an algebraic equation that can be solved numerically. This consists of integrating the governing equations about each control-volume. It results in discrete equations that conserve each quantity on a control-volume basis.

Discretization of the governing equations can be illustrated most easily by considering the unsteady conservation equation for transport of a scalar quantity ϕ. This is demonstrated by the following equation written in integral form for an arbitrary control volume V as follows:

$$\int_V \frac{\partial \rho \phi}{\partial t} dV + \oint \rho \phi \vec{v} \cdot d\vec{A} = \oint \Gamma_\phi \nabla \phi \cdot d\vec{A} + \int_V S_\phi dV \tag{B.2.1}$$

where

ρ = the density of the fluid

$\vec{v}$ = velocity vector

$\vec{A}$ = the surface area vector

Γ_ϕ = diffusion coefficient for ϕ

$\nabla \phi$ = gradient of ϕ

S_ϕ = source of ϕ per unit volume

Then, equation (B.2.1) is discretised and gives the following equation on any given cell:

$$\frac{\partial \rho \phi}{\partial t} dV + \sum_f^{N_{faces}} \rho_f \vec{v}_f \phi_f \cdot \vec{A}_f = \sum_f^{N_{faces}} \Gamma_\phi \nabla_{\phi f} \cdot \vec{A}_f + S_\phi V \tag{B.2.2}$$

where

N_{faces} = the number of faces enclosing the cell

ϕ_f = the value of ϕ convected through face f

$\rho_f \vec{v}_f$ = the mass flux through the face

$\vec{A}_f =$ the face area vector in 3D

$\nabla_{\phi f} =$ the gradient of ϕ at face f

$V =$ the cell volume

The diffusion terms are central-differenced and are always second-order accurate. The discretized scalar transport equation contains the unknown scalar variable ϕ at the cell centre as well as the unknown values in surrounding neighbour cells. This equation will, in general, be non-linear with respect to these variables. A linearized form of equation (B.2.2) can be written as:

$$a_p \phi = \sum_{nb} a_{nb} \phi_{nb} + b \tag{B.2.3}$$

where

$nb =$ neighbour cells

$a_p =$ the linearized coefficient for ϕ

$a_{nb} =$ the linearized coefficient for ϕ_{nb}

B.3 Discretization Methods

B.3.1 Discretization in Space (Spatial)

Discrete values of the scalar ϕ are usually stored at the cell centres. Face values ϕ_f are required for the convection terms in equation (B.2.2) and must be interpolated from the cell centre values. This is accomplished by an upwind scheme.

Upwind means that the face value ϕ_f is derived from quantities in the cell upstream, or "upwind", relative to the direction of the normal velocity v_n in equation (B.2.2)

B.3.1.1 First-Order Upwind Scheme

It is assumed that the cell centres values of any field represent a cell-average value. In other words, when the first-order upwind scheme is used the face value ϕ_f is equal to the cell centre value ϕ in the upstream cell.

B.3.1.2 Power-Law Scheme

The power-law discretization scheme interpolates the face value of a variable f using the exact solution to a one-dimensional convection-diffusion equation

$$\frac{\partial}{\partial x}(\rho u \phi) = \frac{\partial}{\partial x} \Gamma \frac{\partial \phi}{\partial x} \tag{B.3.1}$$

where $\Gamma \; and \; \rho u$ are constant across the interval ∂x. Equation (B.3.1) can be integrated in order to describe how $\phi \; varies \; with \; x$:

$$\frac{\phi(x) - \phi_0}{\phi_L - \phi_0} = \frac{exp\left(Pe\frac{x}{L}\right) - 1}{exp(Pe) - 1} \tag{B.3.2}$$

where

$Pe =$ the Peclet number

$$Pe = \frac{\rho u L}{\Gamma} \tag{B.3.3}$$

The variables of $\phi(x)$ between x=0 and x=L is illustrated in Figure B.1 for a range of values of the Peclet number. It shows that the values of ϕ at x=L/2 is approximately equal to the upstream value. When there is no flow or pure diffusion, $Pe = 0 \; and \; \phi$ may be interpolated using the linear average between the values at x=0 and x=L.

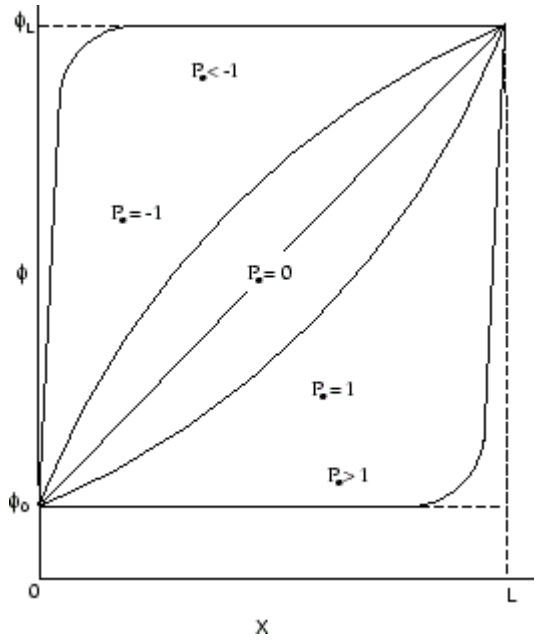

Figure B.0.1 Values ϕ between x=0 and x=L

The power-law differencing scheme is more accurate for ono-dimensional problems, because it attempts to represent the exact solution more closely.

B.3.1.3 Second-Order Upwind Scheme

The accuracy of hybrid and upwind schemes is only first-order in terms of Taylor series truncation error (TSTE). Thought the first-order schemes are very stable, they tend to become prone to numerical diffusion errors. Hence, such errors can be avoided by introducing higher order discretization which involve more neighbour points and bring in wider influence.

The second-order upwind scheme, a higher order differencing scheme, is based on the multidimensional linear reconstruction approach proposed by Barth and Jesperson (1989). The cell-centred solution about the cell centroid is interpolated to the cell face ϕ_f through a Taylor series expansion:

$$\phi_{f,SOU} = \phi + \nabla\phi \cdot \vec{r} \tag{B.3.4}$$

where

$\phi =$ the cell-centred value

$\nabla\phi =$ the gradient in the upstream cell

$\vec{r} =$ the displacement vector from the upstream cell centroid to the face centroid

B.3.1.4 Quick Scheme

Leonard (1979) developed a quadratic upstream interpolation for convective kinetics (QUICK) scheme which is based on a weight average of second-order-upwind and central interpolation of the variable. For face e in Figure B.2 following value can be determined if the flow is from left to right:

$$\phi_e = \theta\left[\frac{S_d}{S_c + S_d}\phi_P + \frac{S_c}{S_c + S_d}\phi_E\right] + (1-\theta)\left[\frac{S_u + 2S_c}{S_u + S_c}\phi_P - \frac{S_c}{S_u + S_c}\phi_W\right] \tag{B.3.5}$$

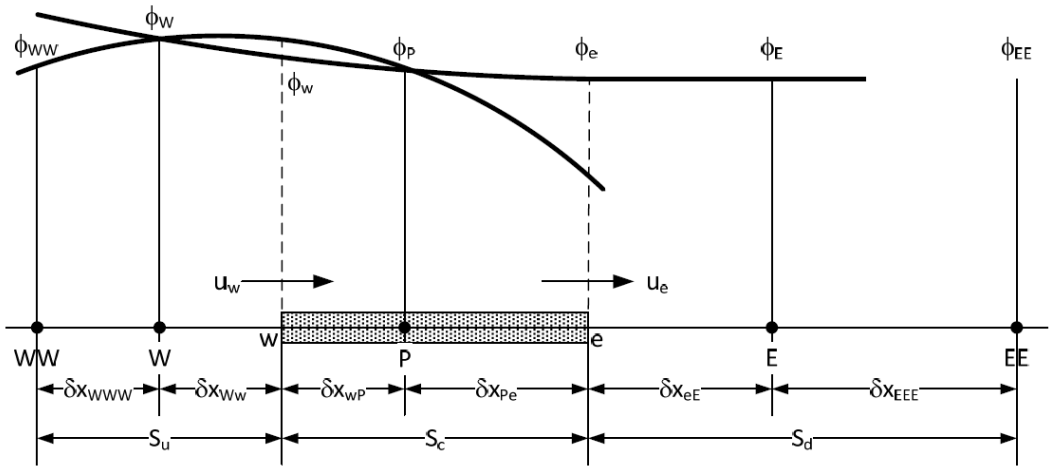

Figure B.0.2 Quick scheme

When $\theta = 0$, equation (B.3.5) results in a second-order upwind value, while when $\theta = 1$ a central second-order interpolation is provided. Usually θ is set to $1/8$ in the QUICK scheme.

B.3.2 Discretization in Time (Temporal)

For unsteady simulations, the governing equations must be discretized in both space and time. Temporal discretization involves the integration of every term in the differential equations over a time step ∆t. The integration of the transient terms is shown below.

A generic expression for the time evolution of a variable ϕ is given by:

$$\frac{\partial \phi}{\partial t} = F(\phi) \tag{B.3.6}$$

where the function F comprise any spatial discretization. The first-order accurate temporal discretization is given by:

$$\frac{\phi^{n+1} - \phi^{n}}{\Delta\, t} = F(\phi) \tag{B.3.7}$$

And the second-order is given by:

$$\frac{3\phi^{n+1} - 4\phi^{n} + \phi^{n-1}}{2\, \Delta\, t} = F(\phi) \tag{B.3.8}$$

where

$\phi =$ the scalar quantity

$n + 1 =$ the value at the next time level $t + \Delta\, t$

$n =$ the value at the current time level t

$n - 1 =$ the value at the previous time level $t - \Delta\, t$

When the time derivative has been discretised, $F(\phi)$ can be evaluated by using a future time level with implicit time integration:

$$\frac{\phi^{n+1} - \phi^{n}}{\Delta\, t} = F(\phi^{n+1}) \tag{B.3.9}$$

This is referred to as "implicit" integration since ϕ^{n+1} in a given cell is related to ϕ^{n+1} in neighbouring cells through $F(\phi^{n+1})$:

$$\phi^{n+1} = \phi^{n} + \Delta\, tF(\phi^{n+1}) \tag{B.3.10}$$

This stable approach can be solved iteratively at each time level before moving to the next time step. The advantage of the fully implicit scheme is that it is unconditionally stable with respect to time step size.

B.4 Gradients and Derivatives

Gradients are used to compute values of a scalar at a cell's faces. In addition, gradients such as $\nabla\phi$ can also be used for the calculation of secondary diffusion terms and velocity derivatives. The following two methods are considered in this thesis for the various simulations:

- Green-Gauss Cell-Based
- Green-Gauss Node-Based

Using the Green-Gauss theorem the gradient of the scalar ϕ at the cell centre c0 can be written as follows:

$$(\nabla\phi)_{c0} = \frac{1}{v}\sum_{f} \bar{\phi}_f\, \vec{A}_f \tag{B.4.1}$$

where

$\phi_f =$ the value of ϕ at the cell face centroid

The Green-Gauss Cell-Based approach enables the method where cell centre values are considered for comparing the gradient. The face values are taken from the arithmetic average of the values at neighbouring cell centres; this method is usually chosen for structured grids and is considered for the air foil simulations:

$$\bar{\phi}_f = \frac{\phi_{c0} + \phi_{c1}}{2} \tag{B.4.2}$$

On the other hand, the Green-Gauss Node-Based enables the face value to be calculated by the arithmetic average of the nodal values on the face; this method is preferred when using unstructured or hybrid meshes, such as the ones dealt in this thesis for the spheroid and the keel simulations:

$$\bar{\phi}_f = \frac{1}{N_f} \sum_{n}^{N_f} \bar{\phi}_n \tag{B.4.3}$$

where

N_f = the number of nodes on the face

B.5 Discretization of the Momentum Equation

The discretization of the momentum equation can be obtained by using the schemes introduced earlier in the chapter. The equation on its general form is expressed as:

$$a_P \phi = \sum_{nb} a_{nb}\, \phi_{nb} + \sum P_f A \cdot \hat{\imath} + S \tag{B.5.1}$$

The pressured field and faces mass fluxes are not known, a priori, and must be obtained as a part of the solution by using a pressure interpolation scheme, to compute the face values of pressure from the cell values. The scheme interpolates the values at the faces using momentum equation coefficients outlined by Rhie and Chow (1983):

$$P_f = \frac{\frac{P_{c0}}{a_{P,c0}} + \frac{P_{c1}}{a_{P,c0}}}{\frac{1}{a_{P,c0}} + \frac{1}{a_{P,c0}}} \tag{B.5.2}$$

Standard pressure interpolation scheme method works well with a consistent pressure variation between cell centres and cannot be used on momentum terms with jumps or large gradients which can cause high pressure gradients at the cell faces. If this scheme is used, the discrepancy shows up in overshoots and undershoots of cell velocity. Standard scheme is used for the large eddy simulation computations for all case studies.

When this becomes an issue, a higher scheme is applied for the pressure interpolation. The PRESTO (Pressure Staggering Option) scheme uses the discrete continuity balance for a "staggered" control volume about the face to compute the "staggered" *1. e., face) pressure. This procedure is similar in spirit to the staggered-grid schemes used with structured meshes (Patankar, 1980). The PRESTO scheme is available for all meshes and makes it more reliable than standard scheme for more complex problems. This was used for the detached eddy simulation runs.

B.6 Discretization of the Continuity Equation

The equation of the steady-state continuity integrated over a control volume will give the following:

$$\sum_{f}^{N_{faces}} J_f A_f = 0 \tag{B.6.1}$$

Where

J_f = the mass flux through face f

The face values of velocity must be related to the stored values of velocity at the cell centres. A linear interpolation of the cell-centre velocities to the face centroids by a momentum-weighted averaging algorithm is introduced, using weighting factors based on the a_P coefficients from equation (B.5.1). Using this procedure J_f can be written as:

$$\begin{aligned} J_f = \rho_f \frac{a_{P,c0} V_{n,c0} + a_{P,c1} V_{n,c1}}{a_{P,c0} + a_{P,c1}} \\ + d_f[(p_{c0} + (\nabla p)_{c0} \cdot \overrightarrow{r_0}) - (p_{c1} + (\nabla p)_{c1} \cdot \overrightarrow{r_1})] \\ = \hat{J}_f + d_f(p_{c0} - p_{c1}) \end{aligned} \tag{B.6.2}$$

where

p_{c0} *and* p_{c1} are the pressures, $V_{n,c0}$ *and* $V_{n,c1}$ are the normal velocities and d_f is a function of $\overline{a_P}$ which is the average of the momentum equation a_P coefficient for the cell on either side of the face f.

B.7 Pressure-Based Algorithm

The pressure-based algorithm evolved from a method called projection method proposed by Chorin (1968). In this method, the mass conservation of the velocity field is defined by the solution of a pressure or pressure correction equation which is derived from the continuity and momentum equations. The velocity field must satisfy the continuity.

Furthermore, it can be distinguished between two different pressure-based algorithms: the segregated and the coupled algorithm.

The governing equations in the pressure-based segregated algorithm are solved sequentially, all solution variables one after another, because they are non-linear and coupled and therefore carried out iteratively. This makes the solution convergence relatively slow.

Compared to the pressure-based segregated algorithm the pressure-based coupled algorithm is solved in a different manner. It solves a coupled system of equations implying the momentum equations and the pressure-based continuity equation. All the other equations are solved in a decoupled fashion line done in the segregated algorithm. The solution convergence is improved and the convergence process is sped up.

B.7.1 The Pressure- based Segregated Algorithm

B.7.1.1 The SIMPLE Algorithm

The SIMPLE algorithm by Caretto et al. (1972) uses pressure corrections to update the velocities and to obtain the pressure field.

The resulting face flux $\hat{J}_f^*$ from equation (B.6.2) does not satisfy the continuity equation of the momentum equation is solved with a presumed pressure field p^*:

$$J_f^* = \hat{J}_f^* + d_f(p_{c0}^* - p_{c1}^*) \tag{B.7.1}$$

Therefore, the correction term J_f' is added to the face flux J_f^* which gives the face flux:

$$J_f = J_f^* + J_f' \tag{B.7.2}$$

The SIMPLE algorithm implies that J' is:

$$J'_f = d_f(p'_{c0} - p'_{c1}) \tag{B.7.3}$$

where

p' = the cell pressure correction.

When substituting equation (B.7.2) and (B.7.3) into the continuity equation (B.6.1) the equation for the pressure correction p' can be written as:

$$a_p p' = \sum_{nb} a_{nb} p'_{nb} + b \tag{B.7.4}$$

Where

b = the net flow rate into the cell

$$b = \sum_{f}^{N_{faces}} J_f^* A_f \tag{B.7.5}$$

Equation (B.7.4) can be solved by using the algebraic multi grid (AMG) method, so that the cell pressure and the face flux are corrected using

$$p = p^* + \alpha_p p' \tag{B.7.6}$$

$$J_f = J_f^* + d_f(p'_{c0} - p'_{c1}) \tag{B.7.8}$$

where

α_p = the under-relaxation factor for pressure.

When during each iteration, the corrected face flux J_f satisfies the continuity equation.

B.7.1.2 The SIMPLEC Algorithm

There are various SIMPLE algorithms in literature. One of them is the SIMPLEC (SIMPLE-Consistent) algorithm described by Vandoormaal and Raithby (1984). The SIMPLEC procedure is very like the SIMPLE algorithm, but the flux correction J'_f is expressed differently. The equation (1.1.1) is the same as for the SIMPLE algorithm but the coefficient d_f is refined as a function of$(\overline{a_p - \sum_{nb} a_{nb}})$. This method considerably accelerates convergence problems where pressure-velocity coupling causes troubles to obtain a solution.

B.7.1.3 The PISO Algorithm

The PISO algorithm of Issa (1986) stands for Pressure Implicit with Splitting of Operators. It is a part of the SIMPLE family of algorithms and is based on the

higher degree of the approximate relation between the corrections for pressure and velocity. One of the limitations of the SIMPLEC algorithm is that new velocities and corresponding fluxes do not satisfy the momentum balance after the pressure-correction equation is solved. As a result, the calculation must be repeated until the balance is satisfied. To improve the efficiency of this calculation, the PISO algorithm performs an additional adjustment on top pf the skewness correction: the neighbour correction.

The main idea of the PISO algorithm is to move the repeated calculations required by SIMPLEC inside the solution stage of the pressure-correction equation. After one-or more additional PISO loops, the corrected velocities satisfy the continuity and momentum equations more precisely. This iterative process is called a momentum or neighbour correction. The PISO algorithm takes a little more CPU time per solver iteration, but it can decrease the number of iterations required for convergence, especially for transient problems.

B.7.2 The Pressure- based Coupled Algorithm

The coupled algorithm offer more advantages over the segregated or non-coupled algorithms, when the mesh is of poor quality or large time steps are used the coupled algorithm still gives robust and stable results for transient flows.

As previously mentioned, the Couples algorithm solves the momentum and pressure-based continuity equations together. A coupling is achieved by an implicit discretization of both, the pressure gradient terms in the momentum equations and the mass face flux. The pressure gradient for the components k in the moment equation can be written as:

$$\sum_{f} p_k A_k = -\sum_{j} a^{u_k p}\, p_j \tag{B.7.9}$$

Where

$a^{u_k p}$ = the coefficient computed from the Gauss divergence theorem and coefficients of the pressure interpolation schemes, see equation (B.5.2).

The discretised momentum equation for component u_k can then be defined as:

$$\sum_j a_{ij}^{u_k u_k} u_{kj} + \sum_j a_{ij}^{u_k p} p_j = b_i^{u_k} \tag{B.7.10}$$

By expressing the balance of fluxes in equation (B.6.1) with the flux in equation (B.6.2) results in the following:

$$\sum_k \sum_j a_{ij}^{p u_k} u_{kj} + \sum a_{ij}^{pp} p_j = b_i^p \tag{B.7.11}$$

After δ-transformation the system of equations (B.7.11) and (B.7.12) has this form:

$$\sum_j [A]_{ij} \vec{X}_j = \vec{B}_i \tag{B.7.12}$$

Where the influence of a cell i on a cell $j$has the form of the matrix:

$$A_{ij} = \begin{pmatrix} a_{ij}^{pp} & a_{ij}^{pu} & a_{ij}^{pv} & a_{ij}^{pw} \\ a_{ij}^{up} & a_{ij}^{uu} & a_{ij}^{uv} & a_{ij}^{uw} \\ a_{ij}^{vp} & a_{ij}^{vu} & a_{ij}^{vv} & a_{ij}^{vw} \\ a_{ij}^{wp} & a_{ij}^{wu} & a_{ij}^{wv} & a_{ij}^{ww} \end{pmatrix} \tag{B.7.13}$$

The unknown and residual vectors have the form

$$\vec{X}_j = \begin{bmatrix} p_i' \\ u_i' \\ v_i' \\ w_i' \end{bmatrix} \tag{B.7.14}$$

$$\vec{B}_i = \begin{bmatrix} -r_i^p \\ -r_i^u \\ -r_i^v \\ -r_i^w \end{bmatrix} \tag{B.7.15}$$

B.7.3 Under-Relaxation of Variables and Equations

Under-relaxation of variables is used to control the change of ϕ during each iteration step. The new value of the variable ϕ within a cell depends upon the old value ϕ_{old} and the change in ϕ and the under-relaxation factor α.

$$\phi = \phi_{old} + \alpha \, \Delta \, \phi \tag{B.7.16}$$

The under-relaxation of equation is used to stabilise the convergence behaviour of the non-linear iterations by introducing selective amounts of ϕ in the systems of discretised equations.

$$\frac{a_p \phi}{\alpha} = \sum_{nb} a_{nb} \phi_{nb} + b + \frac{1-\alpha}{\alpha} a_p \phi_{old} \tag{B.7.17}$$

The Courant-Friedrich-Lewy (CFL) number is a solution parameter in the pressure-based coupled algorithm and can be written in terms of α.

$$\frac{1-\alpha}{\alpha} = \frac{1}{CFL} \tag{B.7.18}$$

Appendix C Regular Wave Theory

C.1 Basic Functions

Figure C.1 shows a harmonic wave as seen from two different perspectives. Figure C.1 (a) shows what one would observe in a snapshot photo made looking at the side of a (transparent) wave tank; the wave profile is shown as a function of distance x along the flume at a fixed instant in time. Figure C.1 (b) is a time record of the water level observed at one location along the flume. Notice that the origin of the coordinate system is at the still water level with the positive z-axis directed upwards. The x-axis is positive in the direction of wave propagation. The water depth, h is measured between the sea bed and the still water level.

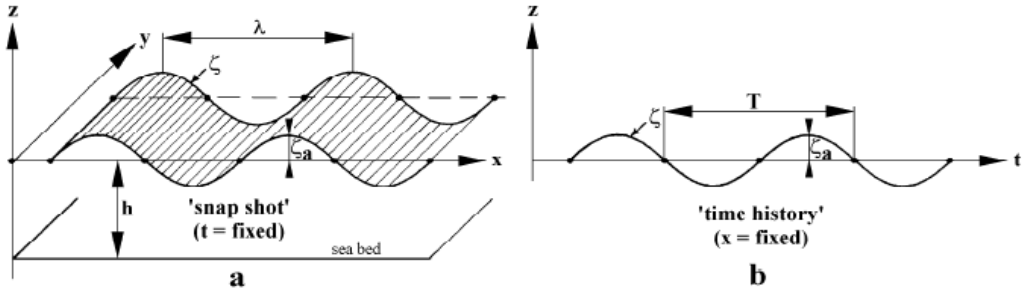

Figure C.0.1 a harmonic wave seen from two different perspectives (a) a snapshot of a wave tank; (b) a time record of water level

The highest point of the wave is called its crest and the lowest point on its surface is the trough. If the wave is described by a sine wave, then its amplitude a is the distance from the still water level to the crest, or to the trough for that matter. The wave height H is measured vertically from wave trough level to the wave crest level. The relation between wave amplitude and wave height is

$$H = 2a \qquad \text{For a sinusoidal wave} \qquad (C.2.1)$$

The horizontal distance which is measured in the direction of wave propagation between any two successive wave crests is the wave length, λ. The distance along the time axis is the wave period, T. The ratio of wave height to wave length is often referred to as dimensionless, H/ λ.

Since the distance between any two corresponding points on successive sine waves is the same, wave lengths and periods are usually actually measured between two consecutive upward (or downward) crossing of the still water level. Such points are also called zero-crossings, and are easier to detect in a wave record.

Since sine or cosine waves are expressed in terms of angular arguments, the wave length and period are converted to angles using:

$$k\lambda = 2\pi \tag{C.2.2}$$

$$\omega T = 2\pi \tag{C.2.3}$$

where

$k =$ the wave number (rad/m)

$\omega =$ the circular wave frequency (rad/s)

The wave form moves one wave length during one period so that its speed or phase velocity, c, is given

$$c = \frac{\lambda}{T} = \frac{\omega}{k} \tag{C.2.4}$$

If the wave moves in the positive x-direction, the wave profile from the form of the water surface can be expressed as a function of both space x and time t:

$$\zeta = acos(kx - \omega t) \tag{C.2.5}$$

C.2 Potential Theory

The water surface slope is very small. This means that the wave steepness is so small that terms in the equations of the waves with a magnitude in the order of the steepness-squared can be ignored. Using the linear theory, the harmonic displacement, velocity, acceleration of the water particle and the harmonic pressure will have a linear relation with the wave surface elevation.

The profile of a simple wave with a small steepness looks like a sine or a cosine and the motion of a water particle in a wave depends on the distance below the still water level. This is reason why the wave potential is written as:

$$\phi_w(x,z,t) = P(z) \cdot sin(kx - \omega t) \tag{C.2.6}$$

where $P(z)$ is an unknown function of z.

The velocity potential $\phi_w(x,z,t)$ of the harmonic waves must fulfil four requirements:

- Continuity condition or Laplace equation
- Sea bed boundary condition
- Free surface dynamic boundary condition
- Free surface kinematic boundary condition

C.2.1 Continuity Condition and Laplace Equation

The velocity of the water particles (u,v,w) in the three translational directions follow from the definition of the velocity potential ϕ_w:

$$u = \frac{\partial \phi_w}{\partial x} \qquad v = \frac{\partial \phi_w}{\partial y} \qquad w = \frac{\partial \phi_w}{\partial z} \tag{C.2.7}$$

Since the fluid is homogeneous and incompressible, the Continuity Condition:

$$\frac{\partial u}{\partial x} + \frac{\partial v}{\partial x} + \frac{\partial w}{\partial x} = 0 \tag{C.2.8}$$

Results in the Laplace Equation for potential flows:

$$\nabla^2 \phi_w = \frac{\partial^2 \phi_w}{\partial x^2} + \frac{\partial^2 \phi_w}{\partial y^2} + \frac{\partial^2 \phi_w}{\partial z^2} = 0 \tag{C.2.9}$$

Water particles move here in the x-z plane only, as in the equations above:

$$v = \frac{\partial \phi_w}{\partial y} = 0 \qquad \text{And} \qquad \frac{\partial v}{\partial y} = \frac{\partial^2 \phi_w}{\partial y^2} = 0 \tag{C.2.10}$$

Taking this into account, a substitution of equation (C.2.6) in equation (C.2.9) yields a homogeneous solution of this equation:

$$\frac{d^2P(z)}{dz^2} - k^2P(z) = 0 \qquad \text{(C.2.11)}$$

With as solution for $P(z)$*:*

$$P(z) = C_1e^{+kz} + C_2e^{-kz} \qquad \text{(C.2.12)}$$

Using this result from the first boundary condition, the wave potential can be written now with two unknown coefficients as:

$$\phi_w(x,z,t) = (C_1e^{+kz} + C_2e^{-kz}) \cdot sin(kx - \omega t) \qquad \text{(C.2.13)}$$

where

$\phi_w(x,z,t) =$ wave potential (m^2/s)

$C_1\ and\ C_2 =$ undetermined constants (m^2/s)

$k =$ wave number ($1/m$)

$x =$ horizontal distance (m)

$z =$ vertical distance(m)

$\omega =$ wave frequency ($1/s$)

C.2.2 Sea Bed Boundary Condition

The vertical velocity of water particles at the sea bed is zero:

$$\frac{\partial\phi_w}{\partial z} = 0 \qquad For: z = -h \qquad \text{(C.2.14)}$$

As given in Figure C.2.

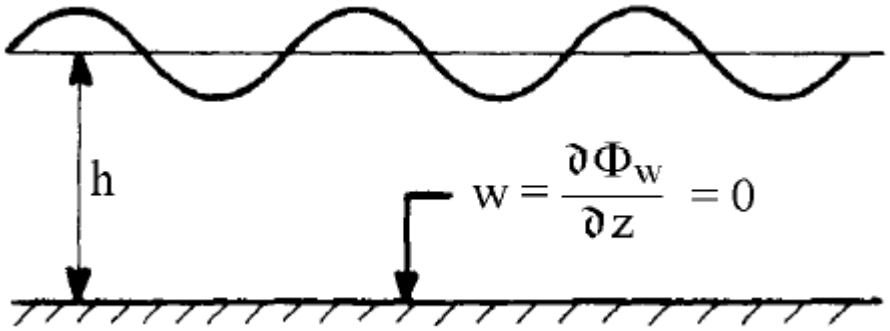

Figure C.0.2 The vertical velocity of water particles at the sea bed

Substituting this boundary condition in equation (C.2.13) provides:

$$kC_1e^{-kh} - kC_2e^{+kh} = 0 \tag{C.2.15}$$

Or:

$$C_1e^{-kh} = C_2e^{+kh} \tag{C.2.16}$$

By defining:

$$\frac{C}{2} = C_1e^{-kh} = C_2e^{+kh} \tag{C.2.17}$$

Or:

$$C_1 = \frac{C}{2}e^{+kh} \qquad \text{and} \qquad C_2 = \frac{C}{2}e^{-kh} \tag{C.2.18}$$

It follows that $P(z)$ in equation (C.2.12) can be worked out to:

$$P(z) = \frac{C}{2}\left(e^{+k(h+z)} + e^{-k(h+z)}\right) = C\,cosh\,k(h+z) \tag{C.2.19}$$

And the wave potential with only one unknown becomes:

$$\phi_w(x,z,t) = C \cdot cosh\,k(h+z) \cdot sin(kx - \omega t) \tag{C.2.20}$$

In which C is an unknown constant.

C.2.3 Free Surface Dynamic Boundary Condition

The pressure p at the free surface of the fluid $z = \zeta$ is equal to the atmospheric pressure p_0. This requirement for the pressure is called the dynamic boundary condition at the free surface which is shown in Figure C.3.

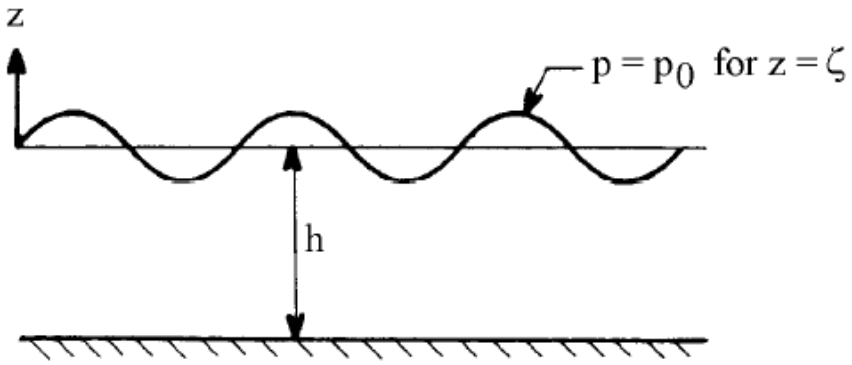

Figure C.0.3 The dynamic boundary condition at the free surface

The Bernoulli equation for an unstationary irrational flow (with the velocity given in terms of its three components) is in its general form:

$$\frac{\partial \phi_w}{\partial t} + \frac{1}{2}(u^2 + v^2 + w^2) + \frac{p}{\rho} + gz = C^* \qquad \text{(C.2.21)}$$

In two dimensions, $v = 0$ and since the waves have a small steepness (u and w are small), this equation becomes:

$$\frac{\partial \phi_w}{\partial t} + \frac{p}{\rho} + gz = C^* \qquad \text{(C.2.22)}$$

At the free surface this condition becomes:

$$\frac{\partial \phi_w}{\partial t} + g\zeta = 0 \qquad \textit{For: } z = \zeta \qquad \text{(C.2.23)}$$

The potential at the free surface can be expanded in a Taylor series, keeping in mind that the vertical displacement ζ is relatively small:

$$\{\phi_w\,(x,z,t)\}_{z=\zeta} = \{\frac{\partial \phi_w(x,z,t)}{\partial t}\}_{z=0} + O(\varepsilon^2) \qquad \text{(C.2.24)}$$

which yields for the linearized form of the free surface dynamic boundary condition:

$$\frac{\partial \phi_w}{\partial t} + g\zeta = 0 \qquad For: z = 0 \tag{C.2.25}$$

With this, the wave profile becomes:

$$\zeta = -\frac{1}{g} \cdot \frac{\partial \phi_w}{\partial t} \qquad For: z = 0 \tag{C.2.26}$$

A substitution of equation (C.2.20) in equation (C.2.26) yields the wave profile:

$$\zeta = \frac{\omega C}{g} \cdot cosh\, kh \cdot cos(kx - \omega t) \tag{C.2.27}$$

Or:

$$\zeta = a \cdot cos(kx - \omega t) \qquad with: a = \frac{\omega C}{g} \cdot cosh\, kh \tag{C.2.28}$$

With this the corresponding wave potential, depending on the water depth h is given by the relation:

$$\phi_w = \frac{ag}{\omega} \cdot \frac{cosh\, k(h+z)}{cosh\, kh} \cdot sin(kx - \omega t) \tag{C.2.29}$$

C.2.4 Free Surface Kinematic Boundary Condition

The relation between T and λ follows from the boundary condition that the vertical velocity of a water particle at the free surface of the fluid is identical to the vertical velocity of that free surface itself. This is a kinematic boundary condition.

Using the equation of the free surface (C.2.28) yields for the wave surface:

$$\frac{dz}{dt} = \frac{\partial \zeta}{\partial t} + \frac{\partial \zeta}{\partial x} \cdot \frac{dx}{dt} = \frac{\partial \zeta}{\partial t} + u \cdot \frac{d\zeta}{dx} \qquad For: z = \zeta \tag{C.2.30}$$

The second term in this expression is a product of two values, which are both small because of the assumed small wave steepness. This product becomes even smaller (second order) can be ignored.

This linearization provides the vertical velocity of the wave surface:

$$\frac{dz}{dt} = \frac{\partial \zeta}{\partial t} \qquad For: z = \zeta \qquad \text{(C.2.31)}$$

The vertical velocity of a water particle in the free surface is then:

$$\frac{\partial \phi_w}{\partial z} = \frac{\partial \zeta}{\partial t} \qquad For: z = \zeta \qquad \text{(C.2.32)}$$

Analogous to equation (C.2.25) this condition is valid for $z = 0$ too, instead of for $z = \zeta$ only. A differentiation of the free surface dynamic boundary condition with respect to t provides:

$$\frac{\partial^2 \phi_w}{\partial t^2} + g\frac{\partial \zeta}{\partial t} = 0 \qquad For: z = 0 \qquad \text{(C.2.33)}$$

Or after re-arranging terms:

$$\frac{\partial \zeta}{\partial t} + \frac{1}{g} \cdot \frac{\partial^2 \phi_w}{\partial t^2} = 0 \qquad For: z = 0 \qquad \text{(C.2.34)}$$

C.2.5 Dispersion Relationship

The information is now available to establish the relationship between ω and k referred to above. A substitution of the expression for the wave potential equation (C.2.29) in equation (C.2.34) gives the dispersion relation for any arbitrary water depth h :

$$\omega^2 = kg \cdot tanh\, kh \qquad \text{(C.2.35)}$$

In deep water ($tanh\, kh = 1$), equation (C.2.29) degenerates to a quite simple form which can be used without difficulty:

$$\omega^2 = kg \qquad \text{(deep water)} \qquad \text{(C.2.36)}$$

And the deep water relation between T and λ becomes:

$$T = \sqrt{\frac{2\pi}{g}} \cdot \sqrt{\lambda} \quad or \quad \lambda = \frac{g}{2\pi} \cdot T^2 \qquad \text{(deep water)} \qquad \text{(C.2.37)}$$

In shallow water, the dispersion relation is found by substituting $tanh\, kh = kh$ in equation (C.2.35):

$$\omega = k \cdot \sqrt{gh} \qquad \text{(shallow water)} \qquad \text{(C.2.38)}$$

C.3 Water Particle Kinematics

The kinematics of a water particle is found from the velocity components in the x- and z- directions, obtained from the velocity potential given in equation (C.2.29) and the dispersion relation given in equation (C.2.35).

C.3.1 Velocities

The resulting velocity components can be expressed as:

$$u = \frac{\partial \phi_w}{\partial x} = \frac{dx}{dt} = a \cdot \frac{kg}{\omega} \cdot \frac{cosh\, k(h+z)}{cosh\, kh} \cdot cos(kx - \omega t)$$

$$w = \frac{\partial \phi_w}{\partial z} = \frac{dz}{dt} = a \cdot \frac{kg}{\omega} \cdot \frac{sinh\, k(h+z)}{cosh\, kh} \cdot sin(kx - \omega t) \qquad \text{(C.2.39)}$$

Based on the dispersion relation, a substitution of the velocity components can be provided as:

$$u = a \cdot \omega \cdot \frac{cosh\, k(h+z)}{cosh\, kh} \cdot cos(kx - \omega t)$$

$$w = a \cdot \omega \cdot \frac{sinh\, k(h+z)}{cosh\, kh} \cdot sin(kx - \omega t) \qquad \text{(C.2.40)}$$

C.3.2 Accelerations

The water particle accelerations follow directly from a differentiation of the velocity components equation (C.2.39).

$$\dot{u} = a \cdot \omega^2 \cdot \frac{\cosh k(h+z)}{\cosh kh} \cdot sin(kx - \omega t)$$

$$\dot{w} = a \cdot \omega^2 \cdot \frac{\sinh k(h+z)}{\cosh kh} \cdot cos(kx - \omega t) \qquad \text{(C.2.41)}$$

Relative to the velocity components, the accelerations have amplitudes which have been multiplied by ω. Their phases have been shifted by 90 degrees as well.

C.3.3 Pressure

The pressure p in first order wave theory follows from the linearized Bernoulli equation (C.2.22):

$$\frac{\partial \phi_w}{\partial t} + \frac{p}{\rho} + gz = 0 \; or \; p = -\rho gz - \rho \frac{\partial \phi_w}{\partial t} \qquad \text{(C.2.42)}$$

With the wave potential from equation (C.2.29) the expression for the linearized pressure becomes:

$$p = -\rho gz + \rho ga \cdot \frac{\cosh k(h+z)}{\cosh kh} \cdot cos(kx - \omega t) \qquad \text{(C.2.43)}$$

For deep water, the linearized pressure becomes:

$$p = -\rho gz + \rho ga \cdot e^{kz} \cdot cos(kx - \omega t) \qquad \text{(deep water)} \qquad \text{(C.2.44)}$$

In shallow water, the dynamic pressure behaves hydrostatically so that:

$$p = -\rho gz + \rho ga \cdot cos(kx - \omega t) \qquad \text{(shallow water)} \qquad \text{(C.2.45)}$$